



Faculty of Technology  
Department of Energy and Sustainable Development

---

# Numerical Wind Resource Assessment in Urban Environments

## PhD THESIS

Rallou Dadioti

*Submitted in partial fulfilment of the requirements  
for the degree of Doctor of Philosophy*

January, 2017

*I dedicate this thesis to my son, Pavlos, who has grown into a wonderful one and a half years old in spite of his mother spending so much time away from him.*



## Acknowledgements

I wish to express my gratitude to my supervisor, Dr Simon Rees, for the incredible amount he has taught me during the course of this thesis, his professional guidance and assistance, as well as for the offer of this PhD program, without which this thesis would not have been produced.

My appreciation goes to Dr Paul Cropper and Dr Birgit Painter for their role of first and second supervisors.

To my husband Giorgos, who has shared the many uncertainties, challenges and sacrifices, I am eternally grateful for his patience and unfailing support.

Most importantly, I would like to express my gratitude to my parents, none of this would have been possible without their love, patience and support.

Krishna Nama Manjunatha, Dr Nare Gabrielyan, Dr Konstantina Saranti, Salah Maswoud, Dr Mian Usman Mazhar and Linda Toledo your friendship is thankfully acknowledged.

I would also like to acknowledge the industrial collaborator Sarah Brown at Infoterra Ltd, who produced the geometry data for Leicester. Without her involvement this project would not have been able to progress.

Finally, I am thankful to De Montfort University for their financial support of my studentship.



# Abstract

This thesis leads to a framework for micrositing, the process through which the specific location for mounting micro wind turbines in urban environments is determined. It can be used as a guidance on how to model an area of interest, find the optimum location for micro wind turbines installation and calculate the annual energy production, commenting on the accuracy that can be expected from the results. Essentially, it is composed of three parts, each one deals with different set of tasks associated with model development and simulation.

The first part investigates the computational practices to the fields of turbulence in urban environments implemented in the open-source CFD library OpenFOAM. It examines the performance of a turbulence model, known as DES, which has not been previously used for external flows in complex urban environments and concludes that this approach offers improved robustness and accuracy over a range of wind conditions. It offers improved prediction of flows in wake regions compared to RANS methods and is less computationally demanding than full LES approaches. The validity of DES implementation is tested using data sets derived from both wind tunnel experiments and field measurements.

In the second part, a procedure is developed to identify the optimum location for mounting wind turbines, based on the spatial variations in mean annual wind speed and the corresponding annual energy production (AEP). The procedure utilizes one year of measured wind data for one site to extrapolate (using the ‘Wind Atlas Methodology’) the annual

wind speed at the site of interest. Then combining the climate data with the CFD results and the power characteristics of the micro wind turbines, it estimates the mean wind speed and the annual energy yield. Essentially, this methodology leads to the formation of three dimensional fields of the average annual wind speed and the AEP (3d wind maps), which will enable identification of the effects of the complex urban topography on the wind flow, and the potential locations for micro wind turbines installation.

The third part examines the accuracy that can be expected from the annual energy production estimation techniques and provides guidelines on the calculations. In particular, it investigates the validity of the standard power curves for the site-specific air density and evaluates their effect on the annual energy production estimations. Differences of the order of  $10^{-3}$  between the default and the site specific mean air density ( $\rho$ ), do not change substantially the energy production. However, for higher discrepancies of the order of  $10^{-2}$  the power output can differ more than 10%. Turbulence affects the wind energy in two ways: through power performance impacts and through effects on turbine loads and fatigue. In the operational range of each turbine, TI increases the output at low wind speeds, while in the transition region to rated power it decreases the power output.

In the context of this study, the DES approach was implemented to examine the flow at the De Montfort university campus in Leicester. The 3d wind maps for the mean wind speed and the annual energy production were developed and the optimum locations for micro wind turbines installation were identified. Although the rooftops of the higher buildings have mostly the potential for wind energy applications, the effect

of the urban topography on the wind potential is not always apparent. Lower building can occasionally have higher potential for micro wind turbines installation than taller and roofs of the same height and close each other may differ substantially in their predicted energy output. Using the field measurements by two 3d ultrasonic anemometers placed in the campus, the site specific air density and turbulence intensity were considered to correct the energy yield estimations and evaluate their effect on the results.





# Contents

<b>Contents</b>	<b>ix</b>
<b>List of Figures</b>	<b>xvii</b>
<b>List of Tables</b>	<b>xxvii</b>
<b>Nomenclature</b>	<b>xxxvi</b>
<b>1 Introduction</b>	<b>1</b>
1.1 Preamble . . . . .	1
1.2 Research Aims and Objectives . . . . .	4
1.2.1 Analysis of wind flow in urban environment . . . . .	5
1.2.2 Identification of the optimum location for micro wind turbines	5
1.2.3 Estimation of the annual energy production (AEP) . . . . .	5
1.3 Thesis outline . . . . .	6
1.4 Accomplishments . . . . .	8
<b>2 Literature Review</b>	<b>9</b>
2.1 Introduction . . . . .	9
2.2 The wind resource . . . . .	11
2.2.1 Nature of the wind . . . . .	11
2.2.2 Atmospheric Boundary Layer (ABL) . . . . .	12
2.2.2.1 Static Stability of the ABL . . . . .	13

2.2.2.2	Surface roughness . . . . .	14
2.2.2.3	Urban Boundary Layer (UBL) . . . . .	15
2.2.2.4	Turbulence . . . . .	17
2.2.3	Wind Power . . . . .	19
2.2.3.1	Atmospheric density . . . . .	19
2.2.3.2	Wind velocity . . . . .	20
2.3	Wind flow analysis . . . . .	20
2.3.1	In-situ measurements . . . . .	22
2.3.2	Wind tunnel tests . . . . .	23
2.3.3	Analytical methods . . . . .	23
2.3.4	CFD methods . . . . .	24
2.4	Computational Fluid Dynamics . . . . .	26
2.4.1	CFD numerical models . . . . .	27
2.4.1.1	Direct Numerical Simulation (DNS) models . . . . .	28
2.4.1.2	Large Eddy Simulation (LES) models . . . . .	29
2.4.1.3	Reynolds Average Navier-Stokes (RANS) models . . . . .	30
2.4.1.4	Unsteady Reynolds-Averaged Navier Stokes (URANS) models . . . . .	32
2.4.1.5	Detached Eddy Simulation (DES) models . . . . .	32
2.4.2	Turbulence modelling . . . . .	33
2.4.2.1	Spalart-Allmaras (SA) based DES turbulence model . . . . .	33
2.4.2.2	Wall functions . . . . .	36
2.4.3	Best-practice guidelines for Wind Engineering applications . . . . .	36
2.4.3.1	Computational Domain . . . . .	37
2.4.3.2	Computational mesh . . . . .	38
2.4.3.3	Boundary conditions . . . . .	38
2.4.4	OpenFOAM . . . . .	40
2.5	Wind measurements and instrumentation . . . . .	42

2.5.1	Wind speed measurements . . . . .	43
2.5.2	Wind direction measurements . . . . .	44
2.5.3	Temperature measurements . . . . .	44
2.5.4	Barometric Pressure measurements . . . . .	44
2.6	Wind Energy Convertor (WEC) . . . . .	45
2.6.1	Types of wind turbines . . . . .	45
2.6.1.1	Built-environment Wind Turbines (BWT) . . . . .	47
2.6.1.2	Drag type WEC . . . . .	47
2.6.1.3	Lift type WEC . . . . .	47
2.6.1.4	Horizontal Axis Wind Turbines (HAWT) . . . . .	50
2.6.1.5	Vertical Axis Wind Turbines (VAWT) . . . . .	50
2.6.2	Power performance . . . . .	51
2.6.2.1	Air density correction . . . . .	53
2.6.2.2	Turbulence Intensity correction . . . . .	53
2.7	UK wind trials in urban areas . . . . .	54
2.8	Summary . . . . .	56
2.8.1	Barriers . . . . .	56
2.8.2	Actions . . . . .	57
2.8.3	Strategy . . . . .	58
<b>3</b>	<b>Validation of DES implemented in OpenFOAM</b>	<b>59</b>
3.1	Introduction - Chapter overview . . . . .	59
3.2	Test Case A: High rise building . . . . .	60
3.2.1	General description of the experiment . . . . .	60
3.2.2	Turbulence models . . . . .	60
3.2.3	Computational domain and mesh . . . . .	63
3.2.4	Boundary Conditions . . . . .	66
3.2.4.1	Basic boundary conditions . . . . .	66
3.2.4.2	Turbulent properties for RANS . . . . .	67

3.2.4.3	Turbulent properties for DES . . . . .	69
3.3	Test Case B: Actual Urban Area . . . . .	70
3.3.1	General description of the experiment . . . . .	70
3.3.2	Turbulence models . . . . .	72
3.3.3	Computational domain and mesh . . . . .	72
3.3.4	Boundary conditions . . . . .	75
3.4	Results - Test Case A . . . . .	75
3.4.1	Comparison between RANS models . . . . .	75
3.4.1.1	Reattachment lengths . . . . .	75
3.4.1.2	Distribution of velocity . . . . .	79
3.4.1.3	Distributions of turbulent kinetic energy . . . . .	79
3.4.2	Comparison between DES and standard k- $\epsilon$ model . . . . .	84
3.4.2.1	Mesh sensitivity study . . . . .	84
3.4.2.2	Reattachment lengths . . . . .	86
3.4.2.3	Distribution of time-averaged velocity . . . . .	89
3.4.3	Conclusions for Test Case A . . . . .	89
3.5	Results - Test Case B . . . . .	92
3.5.1	Mesh sensitivity study . . . . .	93
3.5.2	Distribution of velocity . . . . .	93
3.6	Conclusions . . . . .	100
<b>4</b>	<b>De Montfort university CFD model</b>	<b>103</b>
4.1	Introduction - Chapter overview . . . . .	103
4.2	Description of the DMU campus and surroundings . . . . .	104
4.3	Full-scale measurements . . . . .	108
4.4	Computational domain and mesh . . . . .	113
4.5	Turbulence model . . . . .	117
4.6	Boundary conditions . . . . .	119
4.7	CFD simulations and validation . . . . .	120

4.8	Conclusions . . . . .	126
<b>5</b>	<b>Meteorological data collection and analysis</b>	<b>127</b>
5.1	Introduction . . . . .	127
5.2	Meteorological data . . . . .	128
5.2.1	East Midlands airport weather station . . . . .	128
5.2.2	De Montfort university campus measurements . . . . .	129
5.2.3	Correlation between the wind speed data at two remote meteorological stations . . . . .	130
5.3	Extrapolation of meteorological data . . . . .	132
5.3.1	Terrain related contributions . . . . .	137
5.3.2	CFD contributions . . . . .	139
5.3.3	Predicted vs calculated amplification factors . . . . .	139
5.3.4	Discussion . . . . .	142
5.4	Conclusions . . . . .	146
<b>6</b>	<b>Micrositing</b>	<b>149</b>
6.1	Introduction - Chapter overview . . . . .	149
6.2	Processing the regional climate data . . . . .	150
6.3	Processing the CFD results . . . . .	151
6.4	Mean annual wind speed - 3d map . . . . .	155
6.5	Annual energy production (AEP) - 3d map . . . . .	157
6.6	Case study: DMU campus . . . . .	160
6.6.1	Processing the regional climate data . . . . .	160
6.6.2	Processing the CFD results . . . . .	166
6.6.3	Mean annual wind speed - 3d map . . . . .	171
6.6.4	Annual energy production - 3d map . . . . .	178
6.7	Discussion - Conclusions . . . . .	182
<b>7</b>	<b>Site specific power curves and corrected AEP</b>	<b>185</b>

7.1	Introduction - Chapter overview . . . . .	185
7.2	Site specific power curves . . . . .	186
7.2.1	Air-density correction . . . . .	187
7.2.1.1	Methodology . . . . .	187
7.2.1.2	Case study of the DMU campus . . . . .	189
7.2.2	Turbulence intensity correction . . . . .	198
7.2.2.1	Methodology . . . . .	198
7.2.2.2	Case study of the DMU campus . . . . .	202
7.3	Discussion - Conclusions . . . . .	211
<b>8</b>	<b>Conclusions and Future work</b>	<b>215</b>
8.1	Summary of achievements . . . . .	215
8.2	Recommendations for future work . . . . .	220
	<b>References</b>	<b>223</b>
<b>A</b>	<b>Near wall treatment - Wall functions</b>	<b>251</b>
A.1	Log-law wall functions . . . . .	253
A.1.1	Smooth surfaces . . . . .	253
A.1.2	Rough surfaces . . . . .	254
<b>B</b>	<b>Two-equation turbulence models</b>	<b>257</b>
B.1	Boussinesq approximation . . . . .	257
B.2	Standard $k-\epsilon$ turbulence model . . . . .	258
B.3	Realizable $k-\epsilon$ turbulence model . . . . .	258
B.4	Standard $k-\omega$ turbulence model . . . . .	260
<b>C</b>	<b>OpenFOAM settings</b>	<b>263</b>
C.1	Test Case A: High rise building . . . . .	263
C.1.1	fvSchemes . . . . .	263
C.1.2	fvSolution . . . . .	265

---

C.2	Test Case B: Actual urban area . . . . .	269
C.2.1	fvSchemes . . . . .	269
C.2.2	fvSolution . . . . .	270
C.3	Case study: DMU campus . . . . .	273
C.3.1	fvSchemes . . . . .	273
C.3.2	fvSolution . . . . .	274
<b>D</b>	<b>Mean Absolute Error</b>	<b>277</b>





# List of Figures

2.1	Time and space scales of atmospheric motion [Spera, 1994]. . . . .	12
2.2	Schematic diagram of Urban Boundary sub-layers [Barlow, 2014]. . . . .	15
2.3	Turbulence energy spectrum [Villiers, 2006]. . . . .	18
2.4	Mean streamline patterns about a building [Peterka et al., 1985; Woo et al., 1977] . . . . .	21
2.5	Validation process [Oberkampf and Trucano, 2002]. . . . .	42
2.6	Drag (D) and lift (L) forces on airfoil [Mathew, 2006]. . . . .	46
2.7	Types of wind turbines in terms of their rotor axis [The Scottish government]. . . . .	46
2.8	Types of BWTs. . . . .	48
2.8	Types of BWTs. . . . .	49
2.9	Savonius and Darrieus wind turbines [Óskarsdóttir, 2014]. . . . .	51
2.10	Typical wind turbine power curve [WINDPOWER software]. . . . .	52
2.11	Typical impact of turbulence on power curves [Kaiser et al., 2007]. . . . .	54
3.1	Test Case A: 2:1:1 shaped building geometry [Yoshie et al., 2007a]. . . . .	61
3.2	Test Case A - Wind tunnel experiment. (a) Measuring points in vertical cross-section ( $y = 0$ ). (b) Measuring points in horizontal plane ( $z = 0.125b$ and $1.25b$ ) [Yoshie et al., 2007a]. . . . .	62
3.3	Test case A: Computational domain and grid discretization. . . . .	64
3.4	Test Case A: Mesh resolution. . . . .	65

3.5	Inflow boundary condition for computation of $k-\epsilon$ models [Tominaga et al., 2008a]. . . . .	66
3.6	Building complexes in urban area of Shinjuku [Yoshie et al., 2007a] that define the geometry of Test Case B. . . . .	71
3.7	Test case B: measuring points and building heights. . . . .	71
3.8	Computational domain. . . . .	73
3.9	Refinement regions around the buildings. . . . .	74
3.10	Vertical distribution of velocity vectors around the roof for (a) the standard $k-\epsilon$ model, (b) the realizable $k-\epsilon$ model and (c) the $k-\omega$ SST model. . . . .	77
3.11	Vertical distribution of velocity vectors in the wake for (a) the standard $k-\epsilon$ model, (b) the realizable $k-\epsilon$ model and (c) the $k-\omega$ SST model. . . . .	78
3.12	Wind velocity at (a) a vertical plane and (b,c) two horizontal planes .	80
3.13	Wind velocity on a vertical plane above the roof. . . . .	81
3.14	Turbulent energy in (a) a vertical plane and (b,c) two horizontal planes.	82
3.15	Turbulent energy above roof . . . . .	83
3.16	Wind velocity at (a) a vertical plane and (b,c) two horizontal planes.	85
3.17	Mean horizontal velocity at an horizontal plane ( $z = 0.125b$ ) for (a) the coarse mesh and (b) the medium mesh. . . . .	86
3.18	Vertical distribution of velocity vectors around the roof for (a) the DDES-SA model and (b) the standard $k-\epsilon$ model. . . . .	88
3.19	Vertical distribution of velocity vectors in the wake for (a) the DDES-SA model and (b) the standard $k-\epsilon$ model. . . . .	88
3.20	Wind velocity at (a) a vertical plane and (b,c) two horizontal planes.	90
3.21	Wind velocity (a,b) above roof and (b,c) at the side on an horizontal plane part way up the building. . . . .	91

3.22	Comparison of predicted wind speed ratios for various mesh resolutions at the reference measuring points for the West wind direction.	93
3.23	Comparison of predicted and measured wind speed ratios at the reference measuring points. . . . .	95
3.23	Comparison of predicted and measured wind speed ratios at the reference measuring points. . . . .	96
3.23	Comparison of predicted and measured wind speed ratios at the reference measuring points. . . . .	97
3.23	Comparison of predicted and measured wind speed ratios at the reference measuring points. . . . .	98
3.24	Comparison of wind speed ratio at reference measuring points with wind direction South. . . . .	99
3.25	Vectors of the wind velocity at a plane 10 m above the ground for the DDES-SA model (left) and the standard k- $\epsilon$ model (right). . . . .	100
4.1	Position of the De Montfort university campus in Leicester city (yellow line). . . . .	104
4.2	The area of the De Montfort university campus (red line) and surrounding buildings (yellow line). . . . .	105
4.3	De Montfort university campus and the surrounding buildings indicating the average building heights. . . . .	106
4.4	De Montfort university campus indicating the abbreviated building names and the average building heights. . . . .	107
4.5	The geometry of De Montfort university campus in (a) reality and in (b) the model. . . . .	109
4.6	The geometry of the surroundings building in reality (left) and in the model (right). . . . .	110
4.7	Surroundings of the simulated area at each compass direction. . . . .	111
4.8	Plan view of the wider surroundings of the simulated area. . . . .	112

4.9	Position of wind measurements at De Montfort university campus. . . . .	114
4.10	3D ultrasonic anemometers at De Montfort university campus. . . . .	115
4.11	Roof of the highest building (Old Fletcher) at De Montfort university.	116
4.12	CAD data of De Montfort university and the surrounding buildings. . . . .	116
4.13	Computational domain. . . . .	117
4.14	Refinement regions around the buildings. . . . .	118
4.15	Comparison between numerical and experimental (10 degree interval) wind speed ratios ( $U/U_{ref}$ ) in the locations of anemometers for four wind directions -North (N), East (E), South (S), West (W). . . . .	123
4.16	Wind speed mean in the position (red point) of SM1 for North wind direction at (a) xz plane and (b) at yz plane. . . . .	124
4.17	Comparison between numerical and experimental (10 degree interval) angle deviation between the locations of anemometers and the refer- ence wind ( $\Delta_\phi = \phi - \phi_{ref}$ ) for four wind directions -North (N), East (E), South (S), West (W). . . . .	125
4.18	Comparison between numerical and experimental (10 degree interval) angle deviation of wind direction between the location of anemome- ters at KL and the reference wind at EM ( $\Delta_\phi = \phi - \phi_{ref}$ ) for four wind directions -North (N), East (E), South (S), West (W). . . . .	125
5.1	East Midlands weather station and target area. . . . .	129
5.2	Pearson correlation coefficient ( $r$ ) between EMA wind data and wind measurements at DMU campus. . . . .	132
5.3	Graphical representation of the wind speed at the meteorological sta- tion ( $U_{MET}$ ), the wind speed at the inlet of the building site ( $U_{ref}$ ) and the wind speed at the target area ( $U$ ). . . . .	133

5.4	Wind speed time series (a) at East Midlands airport meteorological station and on the roof of the Edith Murphy building at De Montfort university for the year 2015 and (b) at East Midlands airport meteorological station and on the roof of the Library at De Montfort university for the year 2015. . . . .	135
5.5	Wind roses for (a) East Midlands airport wind data during the wind measurements in Edith Murphy building (b) Edith Murphy data (c) East Midlands airport data during the wind measurements in Kimberlin Library and (d) Kimberlin Library wind data. . . . .	136
5.6	Schematic diagrams of the wind atlas methodology implemented in the current work, <a href="#">Millward-Hopkins et al. [2013b]</a> (modified). . . . .	137
5.7	Terrain surrounding the target area with a radius of 25km for estimating aerodynamic roughness lengths $y_0$ . The white area in the middle represents the building area used in this study. . . . .	139
5.8	Comparison between calculated ( $\gamma$ ) and predicted ( $\gamma'$ ) amplification factors between the EMA weather station and the location of the anemometers at EM for four wind directions -North (N), East (E), South (S), West (W). . . . .	141
5.9	Comparison between calculated ( $\gamma$ ) and predicted ( $\gamma'$ ) amplification factors between the EMA weather station and the location of the anemometer at KL for four wind directions —North (N), East (E), South (S), West (W). . . . .	141
5.10	De Montfort university campus indicating (a) the position and (b) the height of Edith Murphy (EM) and Kimberlin Library (KL) buildings where the anemometers are located. . . . .	143

5.11	Wind flow at Edith Murphy (EM) for four directions. The right images zoom in the area captured by the black circle as indicated at the left image and the black symbol ‘x’ specifies the location where the measurements carried out. . . . .	144
5.12	Wind flow at Kimberlin Library (KL) for four directions. The right images zoom in the area captured by the black circle as indicated at the left image and the black symbol ‘x’ specifies the location where the measurements were carried out. . . . .	145
6.1	Rotation of the mesh of each case (directions North, East and South) to the same direction (West) in order to be comparable and the corresponding points have the same coordinates. . . . .	152
6.2	MapField utility maps the fields related to the mesh of each case (directions North, East and South) onto the corresponding fields associated to the mesh for the direction they were all rotated to (West direction). . . . .	154
6.3	Reduction factors for each direction. . . . .	155
6.4	Illustration of the methodology to calculate the annual mean wind speed at each point of the domain (3d map). The applications used at each step are mentioned at the right side of each step. . . . .	156
6.5	Illustration of the methodology to calculate the annual energy production at each point of the domain (3d map) as it is explained step by step in Section 6.5. The applications used at each step are also mentioned. . . . .	159
6.6	Wind speed hourly data in the DMU region for the year 2015, transferred from the East Midlands airport weather station. . . . .	160
6.7	Wind roses for DMU wind data for the year 2015. . . . .	161
6.8	Average wind speed at DMU region for various periods of the year 2015. . . . .	162

6.9	Wind speed distribution in terms of wind speed (bins of 1m/s) and direction (four wind directions: N, E, S and W) for the year 2015 . . .	164
6.10	Wind speed distribution in terms of wind speed (bins of 2m/s) and direction (four wind directions: N, E, S and W) for the year 2015 . . .	165
6.11	Rotation of the mesh of each case (directions North, East and South) to the same direction (West) in order to be comparable and the corresponding points have the same coordinates. . . . .	167
6.12	MapField utility maps the fields related to the mesh of each case (directions North, East and South) onto the corresponding fields associated to the mesh for the direction they were all rotated to (West direction). . . . .	168
6.12	MapField utility maps the fields related to the mesh of each case (directions North, East and South) onto the corresponding fields associated to the mesh for the direction they were all rotated to (West direction). . . . .	169
6.13	Maps of the velocity field and the corresponding reduction factor field for the West wind direction CFD model. . . . .	170
6.14	Wind speed distribution at (a) EM and (b) KL. . . . .	172
6.15	Reduction factors at EM and KL for each wind direction . . . . .	173
6.16	Annual mean wind speed at the DMU campus; (a) at EM (black ‘x’ symbol) and the nearby buildings in a xz plane (red and yellow ‘x’ symbols) and (b) at KL (black ‘x’ symbol) and the nearby buildings in a xz plane (red ‘x’ symbol). . . . .	174
6.17	Annual mean wind speed at the DMU campus; (a) at EM (black ‘x’ symbol) and the nearby buildings in a xz plane (red and yellow ‘x’ symbols) and (b) at KL (black ‘x’ symbol) and the nearby buildings in a xz plane (red ‘x’ symbol). . . . .	175



6.18 (a) Mean annual wind speed at Old Fletcher building and (b) the wind speed distribution. . . . .	176
6.19 (a) Mean annual wind speed at the taller building (office building (OB) in city center) and (b) the wind speed distribution. . . . .	177
6.20 Power curve of a 5 kW HAWT [Vermeir and Runacres, 2015]. . . . .	179
6.21 Energy yield at EM. . . . .	179
6.22 Energy production at KL. . . . .	180
6.23 Energy production at (a) OF at the DMU campus and (b) at OB in the city center. . . . .	181
6.24 AEP estimated at various locations for wind speed bins of 1 m/s and 2 m/s. . . . .	182
7.1 Illustration of the standard power curve at 1.225 kg/m <sup>3</sup> air density (black line) and the corrected power curves for 1.0 kg/m <sup>3</sup> air density using the IEC 61400-12 standard (green line) and the new approach by Svenningsen [2010a] (blue line). It also represents the true power curve based on field measurements (red dots) [Svenningsen, 2010b]. . . . .	188
7.2 Standard power curve at the reference air density (1.225 kg/m <sup>3</sup> ) and the corrected power curves at 1.0 kg/m <sup>3</sup> , 1.1 kg/m <sup>3</sup> and 1.3 kg/m <sup>3</sup> air densities. . . . .	189
7.3 Histograms for the wind speed data at (a) Kimberlin Library and (b) Edith Murphy. . . . .	191
7.4 Time-series (hourly data) of air-density, air temperature and barometric pressure at DMU for the time period we have wind measurements at Edith Murphy. . . . .	192
7.5 Time-series (hourly data) of air-density, air temperature and barometric pressure at DMU for the time period we have wind measurements at Kimberlin Library. . . . .	193
7.6 Ratio of moist air to dry air [Thogersen, 2000]. . . . .	197

7.7	Computation method of the simulated power output [ <a href="#">Power Curve Working Group, 2014</a> ]. . . . .	200
7.8	Turbulence intensity at a) EM and b) Kimberlin library as calculated from the 10 min averages, excluding the TI values which correspond to wind speeds lower than 3.5 m/s (cut-in wind speed). . . . .	204
7.9	Turbulence intensity as a function of wind speed at a) EM and b) KL.	205
7.10	Corrected power curve for the 10 minute averaged wind speed and turbulence intensity at a) Edith Murphy b) Kimberlin library. . . . .	207
7.11	Corrected power curve for constant turbulence intensity at a) 18% and b) 5%. . . . .	208
7.12	Corrected power curve for the mean turbulence intensity at a) Edith Murphy b) Kimberlin library. . . . .	210
7.13	Energy yield calculated for the 10 min averages and the mean TI at EM and KL. . . . .	211
A.1	Composite regions of the turbulent boundary layer [ <a href="#">LEAPs Computational Fluid Dynamics</a> ]. . . . .	252



# List of Tables

1.1	Technology breakdown (TWh) for central view of deployment in 2020 in UK [ <a href="#">Department of Energy and Climate Change, 2011</a> ]. . . . .	3
2.1	Typical roughness ( $z_0$ ) of homogeneous zones in urban areas, ordered by height and density [ <a href="#">Grimmond and Oke, 1999</a> ] . . . . .	16
2.2	Recent CFD studies on evaluation of wind power in built environment.	25
2.3	List of constants for the Spalart-Allmaras turbulence model. . . . .	35
3.1	Standard Boundary Conditions in RANS models [ <a href="#">Yoshie et al., 2007a</a> ].	69
3.2	Boundary Conditions for DES calculations. . . . .	70
3.3	Boundary Conditions in Test Case B. . . . .	75
3.4	Reattachment lengths by RANS models. . . . .	76
3.5	Reattachment lengths by DES. . . . .	87
3.6	Statistics for various CFD codes. . . . .	99
4.1	Boundary conditions. . . . .	120
4.2	Wind speed ratios as calculated from the wind measurements clustered into 10 degrees, 45 degrees, 90 degrees and as calculated from CFD for four wind directions. . . . .	122
5.1	Weather data at East Midlands airport [ <a href="#">Met Office</a> ]. . . . .	129
5.2	The Strength of relationship based on the value of $r$ . . . . .	130

5.3	Pearson product-moment correlation coefficient ( $r$ ) between East Midlands airport wind data and Edith Murphy wind measurements. . . . .	131
5.4	Pearson product-moment correlation coefficient ( $r$ ) between East Midlands airport wind data and Kimberlin Library wind measurements. . . . .	131
5.5	Amplification factors ( $\gamma$ ) between EMA and DMU wind measurements based on the field measurements. . . . .	134
5.6	Design related contributions based on CFD results. . . . .	139
5.7	Predicted ( $\gamma'$ ) and calculated ( $\gamma$ ) amplification factors between East Midlands airport and Edith Murphy building at DMU campus. . . . .	140
5.8	Predicted ( $\gamma'$ ) and calculated ( $\gamma$ ) amplification factors between East Midlands airport and Kimberlin building at DMU campus. . . . .	140
6.1	Calculation procedure of F values. . . . .	150
6.2	Climate data divided in bins in terms of wind direction as well as wind speed; $f$ represents the number of occurrences the data are into the range of a wind speed bin for each direction. . . . .	151
6.3	F values for each wind direction as calculated for the climate data at DMU region for 2015. . . . .	163
6.4	Climate data at DMU region for 2015 divided in bins of 1 m/s in terms of four wind directions (North, East, South and West) as well as wind speed. . . . .	164
6.5	Climate data at DMU region for 2015 divided in bins of 2 m/s in terms of four wind directions (North, East, South and West) as well as wind speed. . . . .	165
7.1	Estimation of the energy yield (kWh) from a 5 kW wind turbine placed on Kimberlin Library (KL) and Edith Murphy (EM) buildings at standard air density ( $1.225 \text{ kg/m}^3$ ) and site specific air density for a period of 7.7 months and 2 months respectively. . . . .	194

7.2	Estimation of the energy yield (kWh) from a 5 kW wind turbine placed on Kimberlin Library (KL) and Edith Murphy (EM) buildings at standard air density ( $1.225 \text{ kg/m}^3$ ) and at $1.1 \text{ kg/m}^3$ and $1.3 \text{ kg/m}^3$ air density. . . . .	195
7.3	Convergence criteria . . . . .	201
7.4	Estimation of the energy yield (kWh) from a 5 kW wind turbine placed on Kimberlin Library (KL) and Edith Murphy (EM) buildings calculated at 10 min averages TI and at constant TI of 18% and 5%. In parenthesis, there is the rate of increase or decrease in power output in relation to the energy yield as calculated for the 10 min averages TI.	209
B.1	Standard k- $\epsilon$ constants . . . . .	258
B.2	Standard k- $\epsilon$ constants . . . . .	261



# Nomenclature

## Acronyms

ABL	Atmospheric Boundary Layer
AEP	Annual energy production
AIJ	Architectural institute of Japan
BADC	British academic data centre
BWT	Built-environment wind turbines
CAD	Computer-aided design
CFD	Computational fluid dynamics
DALR	Dry Adiabatic Lapse Rate
DDES	Delayed Detached Eddy Simulation
DES	Detached Eddy Simulation
DMU	De Montfort university
DNS	Direct Numerical Simulation
EAM	East Midlands airport



---

ELR	Environmental Lapse Rate
EM	Edith Murphy
GH	Gateway house
GHG	Greenhouse gas
HAWTs	Horizontal axis wind turbines
IEC	International Electrotechnical Commission
ISL	inertial sub-layer
KL	Kimberlin library
LES	Large Eddy Simulation
MAE	Mean absolute error
OB	Office building
OF	Old Fletcher
QB	Queen's building
RANS	Reynolds-Averaged Navier-Stokes
RF	Reduction factors
RSL	roughness sub-layer
SA	Spallart-Almaras
sd	Standard deviation
SGS	Sub-grid scale

SM	Short-term measurements
SST	Shear Stress Transport
SWT	Small Wind Turbine
TI	Turbulence Intensity
UBL	Urban Boundary Layer
UCL	Urban canopy layer
URANS	Unsteady Reynolds Averaged Navier-Stokes
VAWTs	Vertical axis wind turbines
WEC	Wind Energy Convertor
WEC	Wind energy converter
WWEA	World Wind Energy Association

### Greek Symbols

$\tau$	Stress tensor	$[kgms^{-1}]$
$\Delta$	Filter size, mesh related length scale	[m]
$\delta$	Boundary layer thickness	[m]
$\epsilon$	Turbulent energy dissipation	$[m^2s^{-3}]$
$\gamma$	Amplification factor	[-]
$\kappa$	Von Karman constant	[-]
$\mu$	Dynamic viscosity	$[kgm^{-1}s^{-1}]$

---

$\nu$	Kinematic viscosity	$[m^2s^{-1}]$
$\rho$	Density	$[kgm^{-3}]$
<b>Mathematical Symbols</b>		
$\nabla$	Nabla operator	
<b>Roman Symbols</b>		
$\mathbf{f}$	Body forces per unit volume	$[Nm^{-3}]$
$\mathbf{k}$	Wavenumber	$[m^{-1}]$
$\mathbf{u}, \mathbf{U}$	Velocity instantaneous and ensemble average	$[ms^{-1}]$
$\mathbb{E}(\mathbf{k})$	Energy density	$[m^2s^{-2}]$
$\nu_t$	Turbulent eddy viscosity	$[m^2s^{-1}]$
$\omega$	Vorticity	$[m]$
$\tilde{d}$	DES length scale	$[m]$
$C_{DES}$	Empirical constant	$[-]$
$u_\tau$	Shear velocity	$[ms^{-1}]$
$y_w$	Wall distance	$[m]$
$A$	Surface area magnitude	$[m^2]$
$b$	Width	$[m]$
$C, c$	Constant coefficient	$[-]$
$C_{v1}$	Constant coefficient	$[-]$

---

d	Displacement height	[m]
E	Wall function constant	[-]
e	Total specific internal energy	[ $m^2 s^{-2}$ ]
H	Height	[m]
k	Turbulent energy	[ $m^2 s^{-2}$ ]
$k_s$	Roughness height	[m]
L	Length	[m]
P	Power	[kW]
p	Pressure	[Pa]
q	Energy source term	[ $m^2 s^{-2}$ ]
R	Specific gas constant for dry air	[ $Jkg^{-1}K^{-1}$ ]
r	Pearson coefficient	[-]
Re	Reynolds number	[-]
T	Absolute temperature	[K]
t	Time	[s]
U	Wind speed	[ $ms^{-2}$ ]
u,U	Velocity	[ $ms^{-2}$ ]
$u^*$	Friction velocity	[ $ms^2$ ]
W	Width	[m]

---

$x,y,z$	Coordinate components	[m]
$X_F$	Reattachment length behind the building	[m]
$X_R$	Reattachment length on the roof	[m]
$z_0$	Roughness length	[m]

**Superscripts**

T	Transpose
---	-----------

# Chapter 1

## Introduction

### 1.1 Preamble

A noticeable increase in energy consumption over the last 100 years had a significant impact on environmental pollution and depletion of existing reserves. The current energy system (production, transformation and consumption) is unsustainable due to [\[European Commission, 2011\]](#):

- high greenhouse gas (GHG) emissions,
- supply risks related to:
  - dependence on sources of energy exploited by a limited number of suppliers,
  - gradual exhaustion of fossil fuel resources,
  - low resilience to adverse effects of climate change,
- high energy costs and underinvestment.

The transition of our energy system to a more secure and sustainable one is a long path and the decisions to set us on the right way should be made urgently. The

energy challenge for Europe is one of the greatest and demanding tests.

*‘People’s well-being, industrial competitiveness and the overall functioning of society are dependent on safe, secure, sustainable and affordable energy. The energy infrastructure which will power citizens’ homes, industry and services in 2050, as well as the buildings which people will use, are being designed and built now. The pattern of energy production and use in 2050 is already being set’*[[European Commission, 2012](#)].

#### *Energy roadmap 2050*

The European Union is committed to cut GHG emissions by 80-90% by 2050 when compared to 1990 levels [[European Commission, 2012](#)] and the UK aims to reducing its GHG emissions by at least 80% [[Department of Energy and Climate Change, 2013](#)]. The Energy Roadmap 2050 examines the development of the energy system in ways that would be consistent with the GHG target and results that about two thirds of the energy should come from renewable sources. Accordingly, by 2020, the part of renewable energy should come to 20% for EU and 15% for UK [[Department of Energy and Climate Change, 2011](#)]. For the short-term goal (2020), the analysis suggests that about 90% of the generation could be distributed to eight technologies (Table 1.1), which also determine the UK’s 2050 energy mix.

As illustrated in Table 1.1, onshore wind will play a significant role in the transition of the current conventional energy based system to a renewable energy based one.

The World Wind Energy Association (WWEA) has assessed the worldwide wind potential to be of the order of 95 TW, which could cover the world electricity demands when combined with other renewable technologies [[Hossain, 2015](#)]. For the United States, 20% of its electricity requirements could be generated from wind technology by 2030 [[Smith et al., 2012](#)].

Renewable technology	Central range (TWh)
Onshore wind	24-32
Offshore wind	33-58
Biomass electricity	32-50
Marine	1
Biomass heat (non-domestic)	36-50
Air-source and Ground-source heat pumps (non- domestic)	16-22
Renewable transport	Up to 48
Others (including hydro, geothermal, solar and domestic heat)	14
Estimated 15% target	234

Table 1.1: Technology breakdown (TWh) for central view of deployment in 2020 in UK [Department of Energy and Climate Change, 2011].

Large scale wind turbines have already made an impact on the world wide energy system, while small wind turbines designed for the built environment are catching up [Hossain, 2015]. The challenge for built-environment wind turbines (BWT) can be outlined as a need to understand the wind resource in the urban topography (e.g. turbulence, wakes, separation and reattachments zones), combined with a lack of measurements and validated model results to facilitate the development of specific guidelines for wind assessment [Smith et al., 2012].

Existing wind resource maps do not translate well to the built environment. The wind resource in urban areas is very site specific, there are large differences among sites with different topography and estimates for average wind speeds adequate for rural areas can not be applied in the urban complex environment.

*‘Understanding the wind resource (including annual averages, turbulence, and extremes) and developing better wind resource maps are considered high priorities to support BWTs’ [Smith et al., 2012].*



However, due to the complexity of the wind flow, the assessment of wind resources is not an easy task and limited knowledge exists. Crucial areas to be addressed include [Smith et al., 2012]:

- Turbulence and eddies in the built environment.
- Wakes, separation and reattachment zones.
- Three-dimensional wind speed profile and distribution.
- Annual averages.
- Wind resource maps.

In addition to increasing knowledge in each of these fields, the development of a rigorous and validated approach to wind energy assessment in complex urban environments is required.

## 1.2 Research Aims and Objectives

The main aim of this research is to offer a framework for wind resource assessment in the context of micro wind turbine applications in urban environments. As it attempts to offer an holistic approach, the research addresses the following issues:

1. analysis of the wind flow in urban environment,
2. identification of the optimum location for micro wind turbines,
3. estimation of the annual energy production of micro wind turbines.

This work could be of use to those interested in new or retrofit applications to particular projects, for planners, consultants, architects etc.

### **1.2.1 Analysis of wind flow in urban environment**

The main objectives of this part of the study are:

1. to evaluate the accuracy of computational fluid dynamics (CFD) modelling using a detached eddy simulation (DES) numerical model implemented in the open source CFD library OpenFOAM,
2. to evaluate the advantages of this approach over other CFD techniques,
3. to provide guidance on the use and reliability of the DES approach for external flows in the urban environment.

### **1.2.2 Identification of the optimum location for micro wind turbines**

The main objectives of this part of the study are:

1. to collect and analyse regional meteorological data,
2. to identify the effects of complex urban topography on the wind flow,
3. to provide guidance on the calculation of the average annual wind speed,
4. to analyse and visualise the results for practical applications.

### **1.2.3 Estimation of the annual energy production (AEP)**

The main objectives of this part of the study are:

1. to investigate the performance of micro wind turbines at the site of application,
2. to adjust the micro wind turbines' power curves to the site air density and turbulence intensity parameters,

3. to evaluate the accuracy of the results,
4. to provide guidance on the calculation and reliability of AEP estimation techniques.

This work is intended to make a substantial contribution to the assessment techniques of wind resource in urban areas. It is intended that the methods used for obtaining the results will offer guidance for others to investigate the feasibility of micro wind turbine applications. Some of the features of CFD and data analysis responsible for uncertainties in the assessment will be highlighted and improved and some others will be highlighted for further investigation.

### 1.3 Thesis outline

The structure of the thesis is arranged as follows:

**Chapter 1** provides the framework for understanding the role of renewable energy sources to the reduction of greenhouse gas emissions and consequently to climate change mitigation. It focuses on the contribution of wind energy and reports the areas requiring further investigation. In this context, it presents the scope of this study and describes the structure of the thesis.

**Chapter 2** surveys the current research literature in the field of wind energy in urban environment. It covers the theories and methodologies used and justifies the approach employed as part of the investigation. In particular, the following areas are reviewed: wind as a source of energy and wind characteristics, wind resource assessment methods, computational fluid dynamics (CFD), wind measurement and instrumentation, wind energy converter (WEC) systems for urban environments and power performance, .

**Chapter 3** deals with the selection of CFD numerical models for external flows in complex urban environments. It examines the performance of the DES turbulence model, implemented in the open source CFD library OpenFOAM using benchmark data sets. It offers validation evidence for DES approaches and evaluates their advantages over other numerical models.

In **Chapter 4** the DES approach is applied to examine the wind flow at the De Montfort university campus (DMU) in Leicester, U.K. It details the development of the CFD model starting with the description of the area and the surroundings, moving on to the selection of the computational parameters and finally to the validation of the CFD model using field measurements.

**Chapter 5** details the development of reliable meteorological data at the region of interest. It presents a method to extrapolate the annual hourly wind speed from available measurement sites, such as airport weather stations, for use at the site being assessed.

**Chapter 6** employs the findings from the CFD modelling of DMU, to investigate the effects of the complex urban topography on the wind flow and identifies the potential locations for micro wind turbines installation. The proposed assessment methodology is applied to identify preferred turbine sites and make estimates of AEP.

**Chapter 7** investigates the accuracy of AEP estimations based on the standard power curves. It illustrates how the site air density and turbulence intensity affect the turbine's power performance, provide guidance on power curves corrections and identifies areas for further research.

**Chapter 8** summarizes all findings and discusses the important points obtained during the validation and test cases. It summarises the knowledge gained and the contribution to the wind energy field and suggests areas of research that would benefit from future work.

**References** cited throughout the thesis are reported after Chapter 7.

**Appendices** A, B, C and D have been included at the end as a supplementary material to illustrate the use of CFD numerical models.

## 1.4 Accomplishments

This thesis endeavours to bring a better understanding and improved computational practices and data analysis methods to the fields of wind energy assessment in urban environments. It aspires to offer a framework for micro wind turbine application and guidance on how to model an area of interest, find the optimum location for micro wind turbines and calculate the annual energy production, commenting on the accuracy that can be expected from the results. Despite many questions related to the field of wind energy in urban environment were answered, many problems yet remain and in this context, this study tries to suggest directions for future research.

# Chapter 2

## Literature Review

### 2.1 Introduction

Wind energy will play a significant role in the transition of the current conventional energy based system to a renewable energy based system (Table 1.1). By 2050 two thirds of the energy in European union should come from renewable sources [European Commission, 2012] and by 2030 in the United States 20% of its electricity requirements should come from wind technology [U.S. Department of Energy, 2008]. The majority of this production will come from large wind farms. Nonetheless built-environment wind turbines have the potential to play a key role and influence people's perception about wind energy [Smith et al., 2012]. However, a large number of micro wind turbine installations have failed to produce the electricity expected and people are cautious about their efficacy [Tabrizi et al., 2014a].

To address this issue, representatives from academia and industry assembled in 2010 and developed the built-environment wind turbine roadmap [Smith et al., 2012], which identifies the barriers to wind turbine development in the built environment and suggested a strategic approach to overcome these obstacles. They distinguished five key areas for further investigation and development:

1. safety
2. wind resource
3. turbine technology
4. building interactions
5. non-technical obstacles

This thesis deals with the second and third points:

- understanding the wind resource in urban topography, and;
- investigating and improving wind turbine performance assessment.

These have been recognised as key reasons why urban wind turbines have failed to produce the electricity expected [[Smith et al., 2012](#)].

The following sections give a thorough review of the theories and methodologies used to analyse the wind resource in urban environments and justify the approach employed as part of the study presented in this thesis. Firstly, the nature of the wind and its characteristics in the built environment are described (Section [2.2](#)). Secondly, the existing methods to analyse the wind flow are presented and compared (Section [2.3](#)), focusing mainly on CFD approaches (Section [2.4](#)), which is the method used in this work. Thirdly, the role of the wind measurements and instrumentation is outlined (Section [2.5](#)), and the main aspects of wind turbine technology and performance are addressed (Section [2.6](#)). The most important UK wind trials in urban areas are presented in Section [2.7](#) and finally, Section [2.8](#) summarizes the barriers for built environment wind turbine application, the actions required and eventually the strategy followed in this study to address these issues.

## 2.2 The wind resource

In this section, the following topics are reviewed:

- the nature of the wind,
- the characteristics of the wind in the lower part of the atmosphere and particularly in the built environment, and;
- the parameters that influence the wind energy availability.

### 2.2.1 Nature of the wind

The sun and the rotation of the earth are the primary drivers of global wind flows. The spatial and temporal uneven heating of the earth's atmosphere creates atmospheric pressure gradients causing the air to move from higher to lower pressure regions. The generation and movement of the wind is also influenced by the Coriolis force (due to the earth's rotation) and the friction with the earth's surface. The weight of each factor on the wind flow characteristics depends on the scale of the motion examined [Manwell et al., 2010].

The time and space scales of the wind flows employed in wind engineering are illustrated in Figure 2.1 [Spera, 1994]. Inter-annual variations in wind speed can have a large effect on long-term wind turbine production [Manwell et al., 2010] as they help in estimating long-term mean wind at a site. Generally, 30 years of data are required to determine long-term values of weather or climate and it takes at least five years to arrive at a reliable average annual wind speed at a given location. Nevertheless, one year of wind data can be sufficient to predict long-term mean wind speeds within an accuracy of 10% with a confidence level of 90% [Aspliden and Elliot, 1986]. The wind speed variations during the year can be well characterized in terms of a probability distribution. Short-term wind speed variations of interest include variations



over time intervals of one second to ten minutes that have a stochastic character and represent turbulence and gusts. For wind energy applications, turbulent fluctuations in the flow should also be considered in wind turbine siting [Manwell et al., 2010]. Space variations are generally dependent on height above the ground. The movement of the wind in the lowest part of the atmosphere, where micro-wind turbines are usually located, is mainly controlled by the local geographical conditions —the terrain shape and the earth’s surface cover variations.

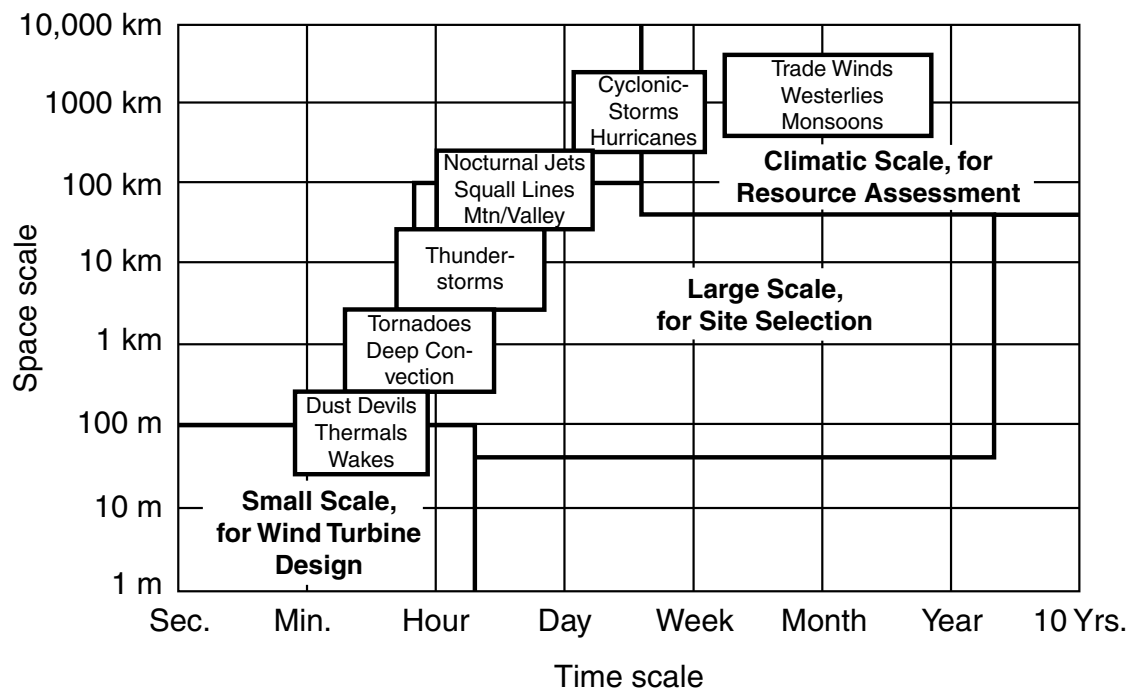


Figure 2.1: Time and space scales of atmospheric motion [Spera, 1994].

### 2.2.2 Atmospheric Boundary Layer (ABL)

The lowest layer of the atmosphere (about 1km thick) where the earth’s surface directly influences its characteristics, is called Atmospheric Boundary Layer (ABL) [Kaimal and Finnigan, 1994]. In the ABL the horizontal wind speed is zero at the earth’s surface and increases with height. The variation of the wind speed over vertical distances, known as vertical wind shear, arises from two main processes

[Cushman-Roisin, 2001]:

1. A thermal process that has its origin in the solar radiation and determines the static atmospheric stability.
2. A mechanical process which results from the friction exerted by the air against the earth's surface and depends on the surface roughness and terrain.

### 2.2.2.1 Static Stability of the ABL

The static atmospheric stability refers to the capacity of the atmosphere to enhance or suppress turbulent motions, generated due to the vertical temperature distribution by the radiative heating or cooling of earth's surface [Aral and Mustafa, 2010].

For a system with no energy transfer, the rate that temperature decreases with an increase in height, due entirely to pressure changes, is known as the Dry Adiabatic Lapse Rate (DALR) and is equal to  $-9.8^{\circ}\text{C}/\text{km}$ . The actual rate at which the air temperature decreases as it rises is known as Environmental Lapse Rate (ELR) [Barry and Chorley, 1987]. The ABL is characterised as stable when the temperature decreases with height less than the DALR ( $\text{ELR} > \text{DALR}$ ).

The stability of the ABL can be thought of by considering the motion of a parcel of dry air as follows. In a stable ABL the temperature of a dry rising air parcel will decrease (due to decompression) faster than its surroundings and consequently will sink back to its original position (subjected to a negative buoyancy force). In a statically unstable ABL the temperature decreases with height faster than the adiabatic lapse rate ( $\text{ELR} < \text{DALR}$ ). Then, the air parcel will be warmer than the surrounding atmosphere and it will continue to rise. The positive buoyancy of the air parcel will generate turbulence that works to eliminate the unstable condition. The ABL is considered to be neutral when the ELR is equal to the DALR and the

air parcel will maintain its new position [Battan, 1979].

In cities the turbulent characteristics of the flow mainly depend on the frictional shear stress (due to surface roughness) and less on the buoyancy force, and hence the ABL is commonly regarded as being near neutral [Yersel and Goble, 1986].

### 2.2.2.2 Surface roughness

The surface roughness describes the aggregated effect of the roughness elements and terrain surface and depends on their characteristics —geometry, spacing and arrangement [Brown and Hugenholtz, 2012; Garratt, 1994]. It is a measure of the drag exerted on the wind by the underlying surface, causing the steady deceleration of the wind approaching the ground in a neutral ABL [Sunderland et al., 2013]. It is expressed as a measure of roughness length ( $z_0$ ), which is the height above the ground at which the horizontal component of the wind speed approaches zero, measured logarithmically downward from the gradient wind level, where the free flowing winds are free of surface influences [Nicholas and Lewis, 1970].

To determine the roughness length by visual survey of the terrain, the updated Davenport classification of effective terrain roughness [Wieringa, 1992] is regarded as the best field-validated roughness classification to date to use. The roughness tables of Grimmond and Oke [1999] (Table 2.1) extend tables of Wieringa [1992] by recognizing four types of homogeneous urban roughness terrain, defined on the basis of the height and packing density of the roughness elements. However, in real urban environments the use of roughness estimates that do not account for the non-uniform building layouts and height variability, can cause significant discrepancies in wind regime predictions [Millward-Hopkins et al., 2011]. Millward-Hopkins et al. [2013c] have used a model [2011a] that accounts for the variability in building height. Then, comparing the results to the ranges given by the Grimmond and Oke [1999] tables, suggests that to accurately predict aerodynamic parameters of real urban

areas, detailed morphological data is required and the height variability must be considered in detail.

### 2.2.2.3 Urban Boundary Layer (UBL)

Variations of the aerodynamic parameters of a site can have a major impact on the behaviour of the wind near the earth's surface [Millward-Hopkins et al., 2012a]. Urban areas are characterised by high roughness length elements and as the wind approaches them the vertical wind shear changes [Paiva et al., 2009]. Analogous to ABL, the part of the atmosphere directly influenced by contact with the roughness elements is known as the Urban Boundary Layer (UBL).

The UBL is shaped as the wind passes over the urban area and its height grows with distance from the urban edge [Heath et al., 2007]. A neutral UBL can be subdivided into a series of sublayers as indicated in Figure 2.2.

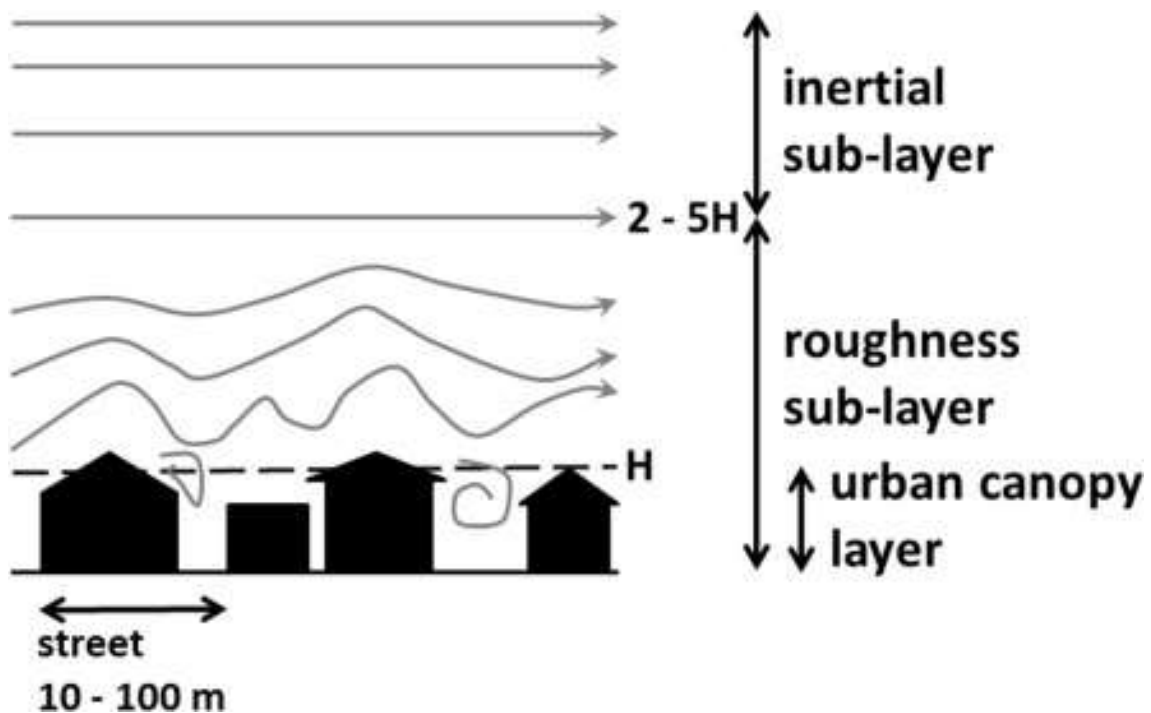


Figure 2.2: Schematic diagram of Urban Boundary sub-layers [Barlow, 2014].

The first layer from the ground up to the mean building height ( $H$ ) is the urban

	$z_0$ (m)	$z_d$ (m)
Urban surface form		
Low height and density.		
Residential one or two story single houses, gardens, small trees.	0.3-0.8	2-4
Mixed houses and small shops. Warehouse, light industrial, few trees.		
Medium height and density.		
Residential two and three story large or closely spaced, semidetached and row houses, large trees.	0.7 - 1.5	3.5-8
Less than five-story blocks of flats with open surroundings.		
Mixedhouses with shops, light industry, churches, schools.		
Tall and high density.		
Residential closely spaced < six-story row and block buildings or major facilities (factory, university, etc.), town center.	0.8 - 1.5	7-15
High-rise.		
Urban core or suburban nodes with multistory tower blocks in dense urban surroundings.	>2.0	>12
Major institutional complexes.		

Table 2.1: Typical roughness ( $z_0$ ) of homogeneous zones in urban areas, ordered by height and density [Grimmond and Oke, 1999]

canopy layer (UCL). The movement of the air into this layer is mainly controlled by the interactions among the roughness elements and their surfaces and is very complex [Romanic et al., 2015]. The wind speed is calculated using an exponential profile whilst accounting for the influence of height variation upon the wind profile [Emejemara and Tomlin, 2015]. The layer above the UCL is called roughness sub-layer (RSL) and extends to 2-5H [Raupach et al., 1991], the height up to which the wind flow is horizontally inhomogeneous and the airflow is influenced by the individual roughness elements. It is characterised by high turbulence and is of importance in wind resource assessment analysis as being the layer where the micro wind turbines are usually placed, on the roof of the buildings [Garratt, 1983; Romanic et al., 2015]. The mean wind velocity profile is highly spatially dependent but if the friction velocity is well known it can be expressed by a log law [Millward-Hopkins et al., 2012b], the same which applies to the outer layer of the UBL known as the inertial sublayer (ISL) or constant flux layer. In this layer, the airflow is only influenced by the average properties of the urban surface and turbulence is considered homogeneous [Heath et al., 2007].

#### 2.2.2.4 Turbulence

In neutral UBL, the building morphology and the roughness length of the urban surface are the important parameters that should be examined when the turbulence structure of the wind is examined for wind resource assessment purposes [Sunderland et al., 2013]. The roughness elements of each surface influence the turbulent content of the flow and turbulence will be present at different intensities and directions for each case. As a rule of thumb, turbulence at roof heights is characterised by small length scales which increase as the distance from the roof increases [Christen et al., 2007]. The large scale eddies are dominated by inertial effects and viscous effects are negligible. They contain the most turbulent kinetic energy which is transferred to the smaller eddies which only contribute a fraction of the total energy, until finally

the smallest scales are dissipated into heat by molecular viscosity [Villiers, 2006].

Figure 2.3 illustrates the energy spectrum, which is divided in three regions:

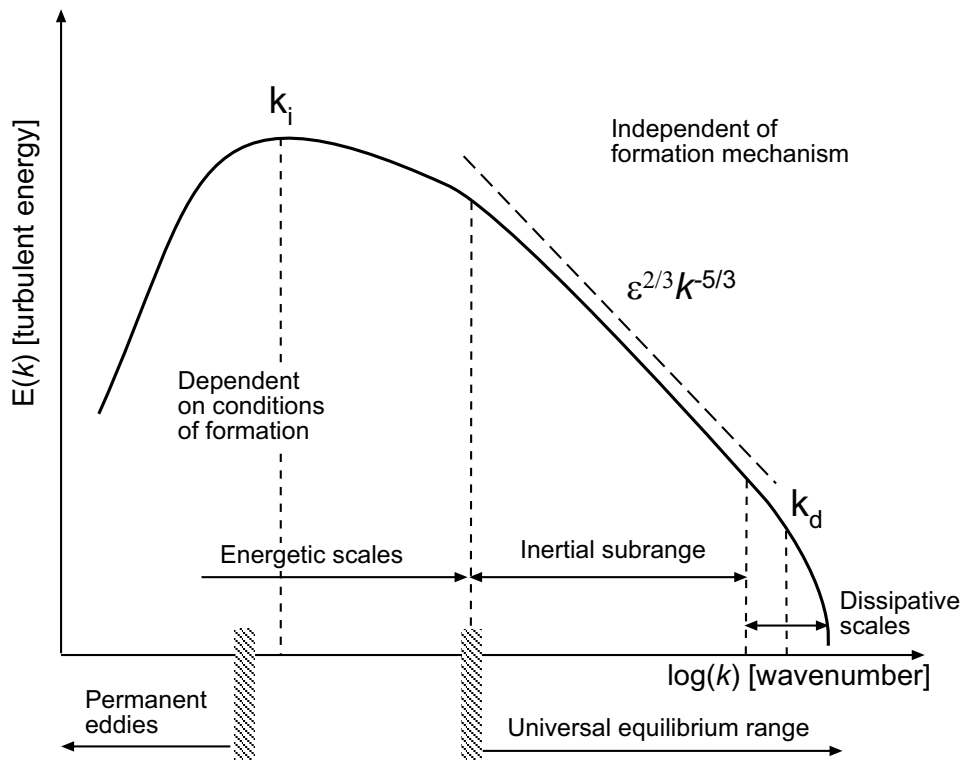


Figure 2.3: Turbulence energy spectrum [Villiers, 2006].

1. The first region represent the the large, energy-containing, or integral scales;  $k_i$ .
2. The second region, known as inertial subrange, contains the transitive scales which transfer energy from the large to the small scales. These scales obey Kolmogorov's law (indicated by the straight line):

$$\mathbb{E}(k) = C \cdot \epsilon^{(2/3)} \cdot \mathbf{k}^{(-5/3)} \quad (2.1)$$

where  $\mathbb{E}(k)$  is the turbulence energy ( $m^3s^{-2}$ ),  $C$  the Universal Kolmogorov constant ( $\simeq 1.5$ ),  $\epsilon$  the turbulence dissipation ( $m^2s^{-3}$ ) and  $\mathbf{k}$  the wavenumber ( $m^{-1}$ ).

3. The final region is the dissipative range which includes very small scales. Viscous effects dominate their behaviour and hence they are considered to be independent from the influence of boundaries and other forcing effects.

Turbulence intensity is the main measure to determine the turbulent content and it is defined as the ratio of wind speed standard deviation to the mean wind speed, determined from the same set of measured data samples of wind speed, and taken over a specified time [IEC, 2006]. The time period in wind energy engineering is usually equal to ten minutes and the sampling rate 1 Hz [Manwell et al., 2010].

### 2.2.3 Wind Power

Wind moving over the earth's surface constitutes a great resource of kinetic energy. The power available (Watts) in the flow through a wind turbine's rotor disc of area (A) is given by:

$$P = \frac{1}{2}\rho AU^3 \quad (2.2)$$

where  $\rho$  is the air density ( $\text{kg}/\text{m}^3$ ),  $U$  the air velocity (m/s) and  $A$  the rotor's disc area ( $\text{m}^2$ ) through which the wind passes normally.

As illustrated in Equation 2.2 the energy contained in the wind is proportional to the air density, the area swept by the rotor and the cube of the wind velocity. It will be shown later that not all the energy theoretically contained in the wind can be converted into useful energy.

#### 2.2.3.1 Atmospheric density

As the Equation 2.2 demonstrates, a factor influencing the available power in the wind is the air density. The density of dry air is given by the ideal gas law (Equation



2.3) and is equal to  $1.225 \text{ kg/m}^3$  at sea-level and at  $15^\circ\text{C}$ .

$$\rho = \frac{p}{R_{spec}T} \quad (2.3)$$

where  $\rho$  is the air density ( $\text{kg/m}^3$ ),  $p$  the absolute pressure (Pa),  $T$  the absolute temperature (Kelvin) and  $R$  the specific gas constant for dry air ( $287.058 \text{ J}/(\text{kgK})$ ).

The atmospheric temperature and pressure decrease with height and they also both vary as the weather patterns change (the temperature fluctuations due to the local weather conditions have a greater impact on air density than the daily pressure changes). Despite the fact that moist air is slightly less dense, the moisture content is rarely used for wind resource assessment purposes [Manwell et al., 2010].

### 2.2.3.2 Wind velocity

The effect of the wind speed variation is highly significant, due to its cubic relationship with power (Equation 2.2). Even a small difference in wind speed within a given area can have a big impact on the amount of energy a wind turbine can generate. Hence, the accuracy of the wind velocity predictions is crucial in wind power resource assessment studies for micro wind turbine installation. The factors affecting the prediction of the spatial and temporal variations in wind speed are discussed in the following sections of the chapter.

## 2.3 Wind flow analysis

In this section, the various methods to analyse the wind flow are presented and compared each other. The strengths and weaknesses of each technique are reported and some successful applications are demonstrated.

Calculation of external flows in complex urban environments is challenging. Fig-

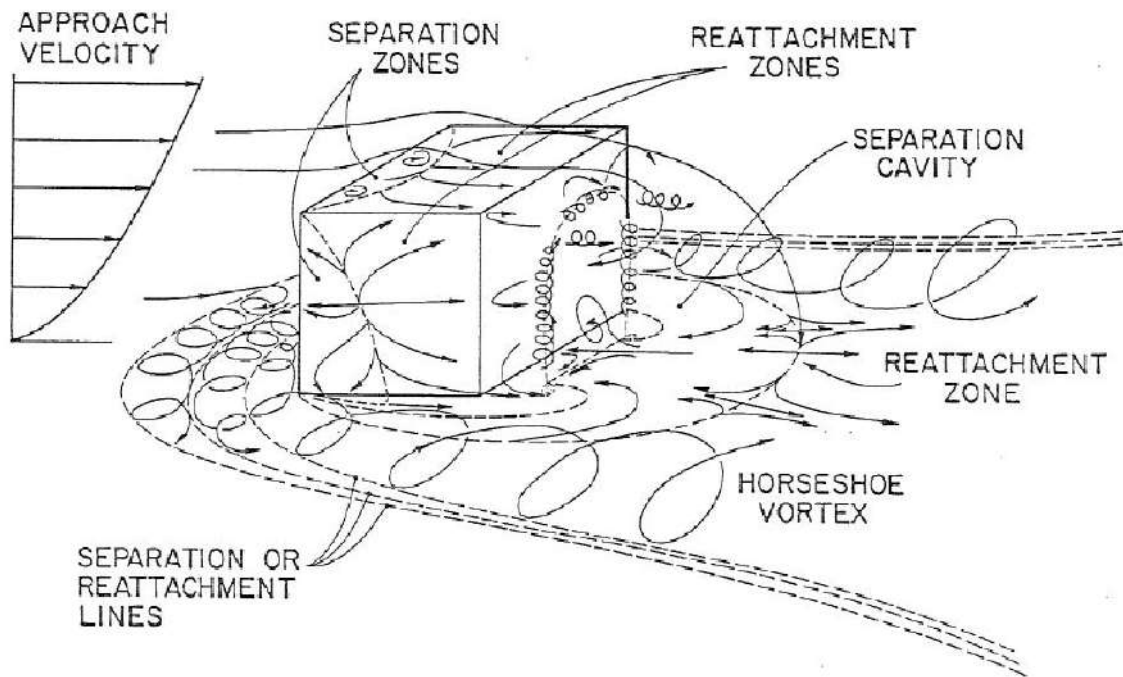


Figure 2.4: Mean streamline patterns about a building [Peterka et al., 1985; Woo et al., 1977]

Figure 2.4 shows a flow pattern about a single building. Separation on the top and sides of building, vorticity in this separated flow, a large vortex in front and around the building, horseshoe shaped vortices downwind, stagnation regions and reattachment zones are some of the effects of the interaction between wind flow and buildings. The unsteadiness of the flow after the wind strikes the building makes the evaluation of the wind flow very challenging. Evaluation of the flow is of great importance in the study of structural loads (e.g. Aly, 2013; Katz and Ag; Meroney et al., 2001; Mohotti et al., 2014; Vafaeihosseini et al., 2013), pedestrian comfort (e.g. Blocken et al., 2012; Blocken and Persoon, 2009; Blocken et al., 2008; Fadl and Karadelis, 2013; Janssen et al., 2013; Meroney et al., 2001; Planning and Building Department, 2014; Stathopoulos and Storms, 1986; Willemsen and Wisse, 2007), natural ventilation (e.g. Calautit and Hughes, 2014; Hooff and Blocken, 2010; Jiang et al., 2003; van Hooff et al., 2011a; Wang et al., 2011), contaminant dispersion (e.g. Coirier and Kim, 2006; Cui et al., 2016; Holmes and Morawska, 2006; Lateb et al., 2016; Vardoulakis et al., 2003), wind energy (Anjum, 2014; Gagliano et al., 2013; Irshad,

2012; Kalmikov et al., 2010; King, 2009; Mattuella et al., 2016; Milanese et al., 2011; Probst and Cardenas, 2010; Rasouli et al., 2014; Tabrizi et al., 2014b) and other problems (Huang and Li, 2010; Neofytou et al., 2006; Tominaga et al., 2011; van Hooff et al., 2011b). Little research has been carried out into urban wind speeds for micro wind turbine applications [?]. However, since the concerns about global warming have increased the interest in using renewable energy sources, it has gradually gained the interest of the research community [Emejamara and Tomlin, 2015; Gagliano et al., 2013; Karthikeya et al., 2016; Rodriguez-Hernandez et al., 2016; Romanic et al., 2015; Simoes and Estanqueiro, 2016; Weekes and Tomlin, 2013]. The main methods for prediction of urban wind flows and wind power production include:

1. In-situ measurements of wind speed.
2. Wind tunnel tests.
3. Analytical methods.
4. Computational Fluid Dynamics (CFD).

Each method has advantages and disadvantages depending on the type of analysis being considered.

### 2.3.1 In-situ measurements

In-situ measurements are considered [Plate, 1999] the most accurate method for wind resource assessment at a specific site, particularly in the case of energy retrofit of existing buildings [Gagliano et al., 2013]. However, it is a time consuming approach, as it requires data acquisition of months or years and it can only capture the flow characteristics at discrete points. The equipment used, cup anemometers or ultrasonic sensors, is expensive and this method is usually applied in research applications. Sonic anemometers are preferred over cup anemometers, as they can take

measurements of high temporal resolution and hence, they can capture turbulence phenomena. Usually, in-situ measurements are used as a means of the validation procedure of other methods such as wind tunnel tests and CFD. [Abohela et al., 2011].

### 2.3.2 Wind tunnel tests

Wind tunnel tests have been extensively used for the prediction of wind flows around buildings and they can produce reliable data under certain circumstances [Campos-Arriaga, 2009a]. However, they are not amenable to adjustments and remodeling requires significant time and effort. They usually capture the flow characteristics at discrete points using sensors the cost of which is a con to wider use other than in universities and large international companies [McAlpine, 1985]. Hence, planners and architects cannot implement wind tunnel tests at the design stage which limits the efficacy of their designs [Abohela et al., 2011]. Wind tunnel measurements are also used as a means of validating other methods; especially they are necessary to gain confidence in the CFD methodology [Jothiprakasham, 2014].

### 2.3.3 Analytical methods

Analytical methods for estimating the mean wind flow primarily consider variations as a function of height and are based on the use of the Wind Atlas methodology [Landberg et al., 2003]. The UK Met Office has adopted this approach as it is regarded as the de facto standard for countries with dense and long term wind observations. The method corrects the regional wind measurements for the roughness characteristics of the surface using the standard logarithmic profile:

$$U = \frac{u^*}{\kappa} \ln\left(\frac{z-d}{z_0}\right) \quad (2.4)$$

where  $z_0$  is the aerodynamic parameter of roughness length,  $d$  is the displacement height,  $u^*$  is the friction velocity,  $\kappa$  is the Von Karman constant ( $\simeq 0.4$ ), and  $z$  is the height above the ground. In particular, it scales the regional wind speed to the urban boundary layer, where the frictional effect of the surface on the flow is negligible and then it scales it back down to the hub-height, considering the aerodynamic parameters of the surface.

In urban areas, due to the influence of individual building aerodynamics on the wind flow and the approximations in estimating the aerodynamic parameters, analytical methods have large uncertainties (around 30%) and have usually failed to make accurate predictions [Millward-Hopkins et al., 2012b]. Sabatino et al. [2008] and Millward-Hopkins et al. [2013c, 2011] have increased the reliability of these methodologies. These approaches include the development of maps of surface aerodynamic parameters for a grid of neighbourhood regions by inputting detailed building data for the city into a morphological model [Millward-Hopkins et al., 2013c, 2011] and account for the effects of building height heterogeneity and wind direction [Millward-Hopkins et al., 2013a,b; Tomlin et al., 2012].

### 2.3.4 CFD methods

CFD techniques have been considered to constitute the most promising tool for future use in wind resource assessment in the built environment due to growing computational power and less time and investment required than the other methods [Clifford et al., 1997; Jones and Whittle, 1992]. However, it is an emerging field and very limited studies have evaluated wind energy considering the complexity of the built environment and validating the results using field measurements. Table 2.2 presents the recent micro-siting studies based on CFD [Yang et al., 2016]. The approach and the methods used are described in the next section.

Publication	Configuration	Turbulence modeling	Validation
Heath et al. [2007]	3D/urban landscape considered an array of cubes	Steady RANS	Wind tunnel
Kalmikov et al. [2010]	3D/simplified model of campus	Steady RANS	Field measurements
Ledo et al. [2011]	3D/an array of cubic buildings with different types of roofs	Steady RANS	Wind tunnel
Balduzzi et al. [2012]	2D/generic urban environment	Steady RANS	Wind tunnel
Khayrullina et al. [2013]	3D/2 simple parallel rectangular building blocks	Steady RANS	Wind tunnel
Abohela et al. [2013]	3D/an array of cubic buildings with different types of roof	Steady RANS	Wind tunnel
Tabrizi et al. [2014b]	3D/a rectangular building with a radius of 200m surrounding area	Steady RANS	Field measurements
Toja-Silva et al. [2015a]	3D/a rectangular building with inclined solar panels	Steady RANS	Wind tunnel
Toja-Silva et al. [2015b]	3D/a rectangular building	Steady RANS	Wind tunnel
Wang et al. [2015]	3D/2 perpendicular buildings	Steady RANS	Wind tunnel
Yang et al. [2016]	3D/generic urban environment	Steady RANS	Field measurements

Table 2.2: Recent CFD studies on evaluation of wind power in built environment.

## 2.4 Computational Fluid Dynamics

Computational Fluid Dynamics (CFD) is a numerical analysis approach in which computers are used to solve the equations describing the fluid flow (the laws of mass, momentum and energy conservation) [Irshad, 2012]. Different CFD models are used depending on the flow problem, the level of accuracy required, the computational resources and the turbulent problem [Irshad, 2012]. The currently available models include:

1. Direct Numerical Simulation (DNS).
2. Large Eddy Simulation (LES).
3. Reynolds Averaged Navier-Stokes (RANS).
4. Unsteady Reynolds Averaged Navier-Stokes (URANS).
5. Detached Eddy Simulations (DES).

Due to the booming growth in computing power Clifford et al. [1997] and Jones and Whittle [1992] foresaw that CFD will be the main tool for wind resource assessment in the urban environment for the purpose of micro wind turbine installation. Many researchers have acknowledged the advantages of CFD modeling. Stathopoulos [2006] reported that it is less expensive than in situ measurements and wind tunnel experiments. Furthermore, open source CFD libraries have the potential to make such calculations accessible and affordable. The models can be altered quickly and different scenarios can be tested in the design stage [Jones et al., 2004]. Versteeg and Malalasekera [2007] confirmed the advantage of comparing alternatives in a reasonable time and cost, while He and Song [1999]; Mochida et al. [1997]; Murakami et al. [1999]; Stathopoulos [2006] paid attention to its useful visualization techniques.

However, CFD modeling is not a straightforward process [Malkawi and Augenbroe, 2004] and the field of wind resource assessment for energy yield calculations in complex urban environment is not yet well established [Walker, 2011]. The unsteadiness of the flow after the wind strikes the buildings and the complex relationships between the variables makes the evaluation of the wind flow cumbersome [Stathopoulos and Baniotopoulos, 2007]. To produce reliable solutions, sensible knowledge of fluid dynamics, accurate modeling of the intended physics and relevant computational skills are required [Campos-Arriaga, 2009b]. In addition, the CFD codes should be validated using other wind assessment tools and for this purpose wind tunnel tests as well as field measurements are of value.

### 2.4.1 CFD numerical models

The basis of Computational Fluid Dynamics (CFD) is the fundamental governing equations of fluid flow, known as the Navier Stokes equations, named after Claude-Louis Navier and George Gabriel Stokes, that characterize the behaviour of a Newtonian fluid, including the turbulence effects. They are partial differential equations describing three basic physical principles: the conservation of mass (Equation 2.5), the conservation of momentum (Equation 2.6) and the conservation of energy (Equation 2.7) [Wendt et al., 1996].

$$\frac{\partial \rho}{\partial t} + \nabla \cdot \rho \mathbf{u} = 0, \quad (2.5)$$

$$\frac{\partial \rho \mathbf{u}}{\partial t} + \nabla \cdot (\rho \mathbf{u} \mathbf{u}) = -\nabla p + \nabla \cdot (\mu \nabla \mathbf{u}) + \mathbf{f}, \quad (2.6)$$

$$\frac{\partial \rho e}{\partial t} + \nabla \cdot (\rho \mathbf{u} e) = -\nabla p \mathbf{u} + \nabla \cdot (\mu \mathbf{u} \nabla \mathbf{u}) - \nabla q, \quad (2.7)$$



where  $\rho$  is the density,  $\mathbf{u}$  the flow velocity,  $\nabla$  the del operator,  $p$  the pressure,  $\mu$  the dynamic viscosity,  $\mathbf{f}$  the external forces,  $e$  the total energy and  $\mathbf{q}$  the heat flux.

Considering an incompressible flow and assuming the absence of gravity and body forces, results in the form of the Navier-Stokes equations as described in Equations 2.8 and 2.9. The energy equation can be omitted and only the unknown quantities of velocity and pressure remain.

$$\nabla \cdot \mathbf{u} = 0 \quad (2.8)$$

$$\frac{\partial \mathbf{u}}{\partial t} + \nabla \cdot (\mathbf{u}\mathbf{u}) = -\frac{\nabla p}{\rho} + \nabla \cdot (\nu \nabla \mathbf{u}) \quad (2.9)$$

The incompressibility of the flow is a common assumption for fluids at low Mach numbers ( $<0.3$ ), such as air flow at normal temperatures [Acheson, 1990]. In accordance with the neutral ABL approximation (Section 2.2.2.1), only isothermal flows are considered in this study and the body forces were neglected.

#### 2.4.1.1 Direct Numerical Simulation (DNS) models

A numerical integration of the Navier-Stokes equations that directly solves the flow without any turbulence modeling is known as Direct Numerical Simulation (DNS) [Orszag, 2006]. As all the spacial and temporal scales of the turbulence must be resolved, from the smallest dissipative scales up to the integral scale, it requires a high resolution grid and costs massive computing resources and time, preventing DNS from being used in wind engineering and in complex urban environment problems [Rudman and Blackburn, 2006].

### 2.4.1.2 Large Eddy Simulation (LES) models

Given this constraint, only the most important —geometry dependant and high energy containing— large eddies can be explicitly calculated, while modelling the influence of the more universal small scales [Moeng and Sullivan, 2015; Moin and Mahesh, 1998]. The LES approach spatially filters the Navier-Stokes equations (Equations 2.8, 2.9) to exclude small scales of the solution and resolve only the large scales. For incompressible flow the filtered equations of motion are the equations 2.10 and 2.11, where the large scales are indicated by the overbar.

$$\nabla \cdot \bar{\mathbf{u}} = 0 \quad (2.10)$$

$$\frac{\partial \bar{\mathbf{u}}}{\partial t} + \nabla \cdot (\overline{\mathbf{u}\mathbf{u}}) = -\frac{\nabla \bar{p}}{\rho} + \nabla \cdot \nu(\nabla \bar{\mathbf{u}} + \nabla \bar{\mathbf{u}}^T) \quad (2.11)$$

Hence, if the grid-spacing ( $\Delta$ ) is the filter width, the turbulent length scales larger than  $\Delta$  are retained in the flow field, whereas the smaller scales (Sub Grid Scales (SGS)) are modelled. In fact, since the small (dissipative) scales are not resolved, the SGS model is required to extract energy from the large scales (resolved scales) to imitate the turbulence energy cascade (Section 2.2.2.4). This is carried out by an SGS eddy viscosity model.

The Smagorinsky model [Smagorinsky, 1963] was the first developed relation for the SGS eddy viscosity and is based on the assumption that all the energy extracted from the resolved scales is dissipated entirely and instantaneously from the small scales which are in equilibrium. However, non equilibrium conditions characterise the free shear layers and separating and reattaching flows, wherefore the Smagorinsky model is not accurate [Villiers, 2006]. This can be handled by considering a history effect, such as a transport equation for the sub-grid scale eddy viscosity. Despite

the fact that the LES approach reduces computational demands, the simulation of atmospheric high Reynolds number flows is still expensive in the sense of the computational cost [Breuer et al., 2003]. Gagliano et al. [2013] have applied an LES (transient) solver to assess the wind potential in urban areas, but the use of a simple CFD code, like ‘Virtual Wind’, is not intended for high-end CFD analysis.

### 2.4.1.3 Reynolds Average Navier-Stokes (RANS) models

In order to make steady-state calculations and avoid resolving turbulent length scales explicitly, an alternative approach to averaging can be applied based on Reynolds decomposition; i.e. each instantaneous quantity is separated into its average part ( $\mathbf{U}$ ) to represent the statistically steady solution of the flow variable and its fluctuating component. This averaging approach applied to the Navier-Stokes equations, produces the RANS equations for incompressible flow:

$$\frac{\partial \mathbf{U}}{\partial x} = 0 \quad (2.12)$$

$$\frac{\partial \mathbf{U}}{\partial t} + \nabla \cdot (\mathbf{U}\mathbf{U}) = -\frac{\nabla P}{\rho} + \nabla \cdot [\nu(\nabla \mathbf{U} + (\nabla \mathbf{U})^T)] - \frac{1}{\rho} \nabla \cdot \boldsymbol{\tau} \quad (2.13)$$

$\mathbf{U}$  are the mean velocities in the coordinate directions  $x$ . The new variable  $\boldsymbol{\tau}$  ( $kgm^{-1}s^{-1}$ ), known as Reynolds stress tensor, represents the effects of the turbulent fluctuations and should be modelled to close the set of equations. Based on the number of additional differential equations required to close the system, the turbulence models are classified as:

1. one-equation model: e.g the Spalart-Allmaras (SA) model,
2. two-equation models: e.g. the commonly used standard k- $\epsilon$  [Launder and Spalding, 1974], the realizable k- $\epsilon$  [Shih et al., 1995], the k- $\omega$  SST [Menter,

1994].

3. Reynolds stress models (six additional equations for the Reynolds stresses):  
e.g. the Launder, Reece and Rodi (LRR) model.

There are several studies of assessing the wind potential in urban areas using RANS (steady state) models implemented with various turbulence models, that have been validated with field measurements [Campos-Arriaga, 2009a; Garg and Srikanth, 2013; Irshad, 2012; Kalmikov et al., 2010; Tabrizi et al., 2014b] and wind tunnel testing [Campos-Arriaga, 2009a]. However, even the most sophisticated turbulence models are not able to fully represent the turbulent characteristics of the flow field, resulting in an inadequate description of unsteady phenomena [Breuer et al., 2003; Franke et al., 2004].

The Reynold decomposition approach has limited ability to capture all flow details and represent a very wide range of scales using time averaged quantities [McDonough, 2007]. In the averaging process too much information is lost to be able to recover it by any statistical correlations. Cheng et al. [2003] compared the RANS approach with LES and concluded that RANS modelling gives significant uncertainties in flows dominated by large-scale features such as flows around building in urban environments. Cheng et al. [2003] found that the RANS results were considerably different from the LES calculations and the experimental data. The RANS model overestimated the recirculation zones in the wake of a cube obstacle [Cheng et al., 2003], over-predicted the separation length by about 35-110%, and complex features such as separation zones, vortex shedding and recirculation zones were better reproduced with LES than with RANS calculations [Rodi, 1997]. For RANS calculations, the turbulence model had significant impact on results and LES, although more computationally demanding, represented better the turbulent characteristics of the flow in complex terrain [Petry et al., 2015]. Steady-state RANS failed to capture the turbulent mixing of the flow field and did not produce consistent results [Salim

et al.].

#### 2.4.1.4 Unsteady Reynolds-Averaged Navier Stokes (URANS) models

In order to better capture the dynamics of turbulent complex flows using feasible computational costs, unsteady RANS (URANS) has been introduced. The Navier-Stokes equations for incompressible flow have to be time-filtered; all scales smaller than a characteristic time period ( $\Delta t$ ) are averaged and the unsteadiness accounts for time scales larger than  $\Delta t$ . In this ensemble averaging process the momentum is effectively averaged over each time step. For the averaging to make sense, the averaging period should be much smaller than the time scale of the unsteady mean motion and at the same time, the time period should be orders of magnitude higher than the time scale of the random fluctuations. However, in many fluid flow problems these requirements cannot be met simultaneously, leading to the so-called spectral problem [Sadiki et al., 2006].

#### 2.4.1.5 Detached Eddy Simulation (DES) models

To deal with the limitations of the numerical models, a new hybrid approach, known as Detached Eddy Simulation (DES), was created [Spalart et al., 1997]. It uses RANS turbulence modelling in the boundary layer and it employs LES in separated regions. It combines the one-equation eddy viscosity RANS model (Spalart-Allmaras (SA) model, Section 2.4.2.1) and LES outside boundary layer regions according to a length scale defined by:

$$\tilde{d} = \min(y_w, C_{DES}\Delta) \quad (2.14)$$

where  $y_w$  is the distance to the wall involved in the destructive term of the SA model,  $C_{DES} = 0.65$  and  $\Delta$  is the largest local grid-spacing. Its intention is to treat the whole boundary layer using the RANS model ( $y_w < C_{DES}\Delta$ ) and implement

an LES model at regions of separated flows ( $y_w > C_{DES}\Delta$ ). However, in thick boundary layers, when the grid spacing parallel to the wall  $\Delta_{\parallel}$  becomes less than the boundary thickness  $\delta$ , the DES approach in its original form, reverts to an LES model and it fails to behave as expected. In order to achieve the original intention of the DES, a modified version, called Delayed Detached Eddy Simulation (DDES), was developed, which preserves the RANS behaviour over the whole boundary layer regardless of the grid spacing and the boundary thickness size. This version of the Spalart-Allmaras DES model improves prediction of boundary layer separation points on aerofoils and flows dominated by boundary layer effects like pipe flows and channel flows. However, the precise position of the point of detachment is not a particular issue in building external flows as separation is generally forced by reverse right-angle features at roof and wall edges rather than curved surfaces. In aerodynamics and bluff body flows, where the boundary layer is small and the flows are dominated by large length scales and separation induced vortices, the initial DES model is anticipated to produce LES quality solutions at reduced costs in terms of computational resources [Villiers, 2006]. For the DES model, the Spalart-Allmaras (SA) one-equation eddy viscosity model [Spalart and Allmaras, 1992] constitutes the base RANS turbulence model. It has been tested at high Reynolds numbers conditions, similar to what can be calculated using well resolved LES ( $Re = 10^4$ - $10^6$ ) and it shows good accuracy for cases including large unsteady separation [Villiers, 2006].

## 2.4.2 Turbulence modelling

### 2.4.2.1 Spalart-Allmaras (SA) based DES turbulence model

DES was initially formulated for the Spalart-Allmaras one-equation model, in which the Reynolds stresses ( $\tau = -\overline{u_i' u_j'}$ ) are calculated by the Equation 2.15 and the turbulent eddy viscosity ( $\nu_T$ ) is calculated as a function of a modified turbulent

kinematic viscosity ( $\tilde{\nu}$ ) (Equation 2.16).

$$\boldsymbol{\tau} = 2\nu_T S_{ij} \quad (2.15)$$

$$\nu_T = \tilde{\nu} f_{v1} \quad (2.16)$$

where:

$$f_{v1} = \frac{\chi^3}{\chi^3 + c_{V1}^3}, \quad \chi = \frac{\tilde{\nu}}{\nu} \quad (2.17)$$

$c_{v1}$  is a constant (Table 2.3) and  $\nu$  the molecular viscosity. The viscosity-like variable ( $\tilde{\nu}$ ) satisfies a further transport equation for the modified turbulent viscosity to close the system of RANS equation and is given by:

$$\frac{D\tilde{\nu}}{Dt} = c_{b1}\tilde{S}\tilde{\nu} + \frac{1}{c_\sigma}(\nabla \cdot ((\nu + \tilde{\nu})\nabla\tilde{\nu}) + c_{b2}(\nabla\tilde{\nu})^2) - c_{w1}f_w\left(\frac{\tilde{\nu}}{y_w}\right)^2 \quad (2.18)$$

where  $y_w$  is the distance to the closest surface and:

$$\tilde{S} = S + \frac{\tilde{\nu}}{(\kappa y_w)^2} f_{v2}, \quad (2.19)$$

$$S = \sqrt{2\Omega_{ij}\Omega_{ij}}, \quad (2.20)$$

$$\Omega_{ij} = \frac{1}{2}\left(\frac{\partial u_i}{\partial x_j} - \frac{\partial u_j}{\partial x_i}\right), \quad (2.21)$$

$$f_{v2} = 1 - \frac{\chi}{1 + \chi f_{v1}}, \quad (2.22)$$

$$f_w = g \left[ \frac{1 + c_{w3}^6}{g^6 + c_{w3}^6} \right]^{1/6}, \quad (2.23)$$

$$g = r + c_{w2}(r^6 - r), \quad (2.24)$$

$$r = \frac{\tilde{\nu}}{\tilde{S} \kappa^2 y_w^2} \quad (2.25)$$

The wall boundary condition is  $\tilde{\nu} = 0$  and the constants are listed in Table 2.3.

$c_{v1}$	$c_{b1}$	$c_{b2}$	$c_{w1}$	$c_{w2}$	$c_{w3}$	$\kappa$	$c_\sigma$
7.1	0.135	0.622	$c_{b1}/\kappa^2 + (1 + c_{b2})/c_\sigma$	0.3	2	0.41	2/3

Table 2.3: List of constants for the Spalart-Allmaras turbulence model.

The transition from near-wall RANS based simulation to LES treatment is based on Equation 2.14. The  $y_w$  near wall distance is replaced by  $\tilde{d}$  and for  $y_w < \Delta$  it performs as an SA RANS model and for  $\Delta < y_w$  as an SGS model. The SA based DES models is considered one of the best known DES models, it has shown good results in cases of large unsteady separation and high Reynolds number ( $\text{Re} = 10^4 - 10^6$ ) and it is also valid over the whole range of dimensionless wall distance  $y^+$  ( $y^+ = (y u_T)/\nu$ , where  $u_T$  is the friction velocity at the nearest wall,  $y$  is the distance to the nearest wall and  $\nu$  is the local kinematic viscosity of the fluid), including the near-wall region [Van der Vorst, 1992]. Although modeling the entire boundary layer makes the approach inadequate for flows dominated by boundary layer effects, in aerodynamic and bluff body flows, where the thickness of the boundary layer is small compared to overall length scales and separation induced vortices, the model is anticipated to deliver LES quality results at vastly reduced costs [Villiers, 2006]. Wall functions can be also used in combination with SA based DES to further reduce



the calculation costs in applicable areas. The SA based DES approach is relatively young and to gain confidence more testing is required.

#### 2.4.2.2 Wall functions

In RANS calculations the inner boundary layer is not usually fully resolved by the mesh and a ‘wall function’ is used to treat the cells nearest the wall surfaces. Most wall functions are based on the standard logarithmic law of the wall and they require a minimum value for the dimensionless wall distance  $y_0^+ \approx 30$  (Appendix A.1). An advanced wall function is Spalding’s law (Equation 2.26) [Spalding, 1961], known as a ‘universal’ velocity profile, which is suitable for the laminar, buffer and logarithmic regions of an equilibrium boundary layer. Since the mesh point nearest the wall can be placed even in the viscous or buffer layer (i.e.  $y_0^+ < 30$ ) without any loss in the accuracy, the model can be used for fine resolution near the wall grids (locally refined grids).

$$y^+ = u^+ + \frac{1}{E} [e^{\kappa u^+} - 1 - \kappa u^+ - \frac{1}{2}(\kappa u^+)^2 - \frac{1}{6}(\kappa u^+)^3] \quad (2.26)$$

where  $\kappa = 0.42$  and  $E = 9.1$  are constants,  $y^+ = (y_0 u_T)/\nu$ ,  $u_+ = u_0/u_T$ . Knowing the values of  $y_0$  and  $u_0$  and using an iterative procedure for the resulting non linear equation for  $u_T$ , the wall shear can be calculated [Spalding, 1961].

### 2.4.3 Best-practice guidelines for Wind Engineering applications

A number of collaborative studies have been made [Franke et al., 2007; Menter et al., 2002; Tominaga et al., 2008b; Yoshie et al., 2007b] to develop best-practice guidelines for CFD applied to wind engineering problems. The main findings are

summarized below.

### 2.4.3.1 Computational Domain

In case of wind tunnel comparative studies, the dimensions of the computational domain should reproduce the geometry of the boundary layer wind tunnel testing as recommended by Best Practice guidelines [Franke et al., 2007]. For field measurements comparative studies in urban areas the height of the computational domain should include at least the height of the boundary layer as determined by the upstream terrain classification [Tominaga et al., 2008b] and  $5H_{\max}$  away from the tallest ( $H_{\max}$ ) building [Franke et al., 2007]. Such large dimensions avoid an artificial acceleration of the flow, since most boundary conditions prevent the flow out of the top of the domain. The lateral boundaries should be placed around  $5H_{\max}$  from the edges of the region of interest [Tominaga et al., 2008b], or even closer as recommended by [Franke et al., 2007]. In any case, testing two different configurations is preferable, since the impact of the lateral boundaries on the flow in the targeted buildings is highly case dependant. The inflow boundary should be located about  $5H_{\max}$  from the built area and the outlet about  $15H_{\max}$  behind it depending on outflow boundary conditions. For outflow boundary conditions, where the derivatives of all flow variables are forced to vanish the boundary should be placed far enough away to allow the flow redevelopment. Regarding surrounding buildings of the region of interest in urban areas, they should be explicitly reproduced if they are located less than  $6H_n$  away from the area of interest, where  $H_n$  is the height of the building. However, parametric simulations can be performed, with and without the distant features, in case of uncertainty regarding their influence on the flow in the area of interest. The boundary conditions applied always play a key role on the decisions for the geometry of the domain [Franke et al., 2007].

### 2.4.3.2 Computational mesh

In the urban environment the flow field around the buildings is characterised by separation near the walls and the roof. In order to capture these important phenomena a fine grid arrangement is required near the corners and a minimum of 10 cells per building side [Yoshie et al., 2007b]. In regions with high velocity gradients the grid should be almost equidistant or at least the stretching ratio remain less than 1.3 [Tominaga et al., 2008b]. As the grid resolution is highly case dependent, a sensitivity study with at least three systematically refined grids is recommended [Franke et al., 2007]. Although the use of wall functions is not recommended for the building surfaces, their influence is not important in the case of bluff bodies with sharp edges where the separating points do not depend on the Re numbers and are always formed at the leading edges. Regarding the shape of the cells, a hexahedral mesh is preferred to tetrahedra and the grid lines on the wall should be perpendicular to it [Menter et al., 2002].

### 2.4.3.3 Boundary conditions

The computational domain includes the region of interest and the surrounding features at some distance from it. The rest of the elements influencing the flow should be represented implicitly using the boundary conditions. Most often, the boundary conditions are not well known and the assumptions used introduce an uncertainty to the solution. Hence, the boundaries to the computational domain should be located far away from the targeted area to have a small effect on the results [Franke et al., 2007].

### Inflow boundary conditions

The vertical velocity profile is given either by a power law as suggested by [Tominaga et al. \[2008b\]](#) or a log law according to the [COST] recommendations [[Franke et al., 2004](#)] that use the formulas suggested by [Richards and Hoxey \[1993\]](#). The power law is given by the equation:

$$U(z) = U_s \left( \frac{z}{z_s} \right)^a \quad (2.27)$$

where  $U_s$  is the velocity at reference height  $z_s$  and  $a$  is the power-law exponent determined by terrain category [[Choi, 2009](#)]. The log law is given by the equation:

$$U(z) = \frac{U_{ABL}^*}{\kappa} \ln \left( \frac{z-d}{z_0} \right) \quad (2.28)$$

where  $\kappa$  is the Karman constant ( $= 0.4$ ) and  $U_{ABL}^*$  the atmospheric boundary layer friction velocity, which assumes a constant shear stress with height and hence the computational domain should be much lower than the atmospheric boundary layer [[Tominaga et al., 2008b](#)]. If wind tunnel data are available, they should be used.

### Top and lateral boundary conditions

In a large computational domain the top and lateral boundaries slightly influence the solution in the area of interest [[Mochida et al., 2002](#); [Yoshie et al., 2007b](#)]. When the top boundary is outside the boundary layer and the lateral boundaries far away from the built area the use of symmetry conditions which impose zero normal velocity, makes the computation more robust [[Tominaga et al., 2008b](#)]. If wind tunnel measurements are available and obtained within a closed test section, the top boundary should be classified as solid wall [[Franke et al., 2007](#)].

## Outflow boundary conditions

Outflow boundary conditions are usually used at the boundary downstream and all the derivatives of the flow variables are set to zero. Therefore, this boundary should be placed far enough away from the built area to allow the flow to fully redevelop.

## Ground surface and building wall

For the velocities at building and ground surfaces, the no-slip boundary condition is used. For the shear stress in urban areas the smooth wall condition is recommended by [Franke et al. \[2007\]](#). The rough wall condition usually leads to a bad resolution close to the wall, since the first calculation node of the wall must be placed at least  $k_s$  away from the wall [[Tominaga et al., 2008b](#)], where  $k_s$  is the roughness height. [Blocken et al. \[2012\]](#) have shown a method to use the wall roughness properties and circumvent this limitation using a commercial CFD code, but this leads to significant streamwise changes of the inflow profiles. In practice, the shear stress is estimated using the wall functions which apply a logarithmic velocity profile between the wall and the first computational node in the wall-normal direction. For the logarithmic profile to be valid, the first computational node should be placed at a non-dimensional wall distance of  $z^+$  between 30 and 500 for smooth walls [[Franke et al., 2007](#)].

### 2.4.4 OpenFOAM

The CFD code applied in this work was OpenFOAM. OpenFOAM is a free, open-source CFD software library, that makes use of the object oriented features of the C++ programming language [[Jasak et al., 2007](#)]. It was released in 2004 and since then, it has been further developed and gradually gained popularity in both com-

mercial and academic organisations, the reward of being free of charge, easily modifiable and adequate for a broad range of fluid dynamics applications. It also provides massive parallel computing capabilities and the possibility to easily implement customised solvers and functions [Ghione, 2012]. However, despite the considerable advantages, the downside of OpenFOAM is the lack of quality certification and documentation. The development of independent quality assurance data and documentation relies on the efforts of third parties. Some validation exercises where OpenFOAM models have been applied to wind flows have been published by Balogh et al. [2012]; Churchfield and Moriarty [2010]; Flores et al. [2014]; Lysenco et al. [2011]; Lysenko et al. [2013], but very few studies have been concerned with urban environments [Bahlouli and Bange, 2015; Balduzzi et al., 2012; Bianchi et al., 2013; Garcia-Sanchez et al., 2015]. The key validation procedure incorporates the comparison between computational results and experimental data (Figure 2.5).

The Working Group of the Architectural Institute of Japan (AIJ) [AIJ, 2009; Tominaga et al., 2008b; Yoshie et al., 2007b] performed cross comparisons between CFD calculations, field measurements and wind tunnel data for flow around a single high rise building and in an actual urban area [Tominaga et al., 2008a, 2004, 2005; Yoshie et al., 2007b] in order to identify the main factors influencing prediction accuracy. CFD studies of complex urban areas validated using field measurements are extremely limited in number. Tabrizi et al. [2014b] used the ANSYS-CFX software to model an area in Port-Kennedy, Western Australia. He used the RANS approach combined with a  $k-\epsilon$  turbulence model and the results were compared with experimental data. Yang et al. [2016] carried out simulations of the wind flow over the ITCB building on the National Taipei University of Technology campus, using the ANSYS-Fluent. He used RANS equations with the realizable  $k-\epsilon$  turbulence model and verified the results against on-site data. Kalmikov et al. [2010] considered the complex geometry of the Massachusetts Institute of Technology (MIT) campus in the USA to conduct CFD simulations. The ‘UrbaWind’ software solved the RANS

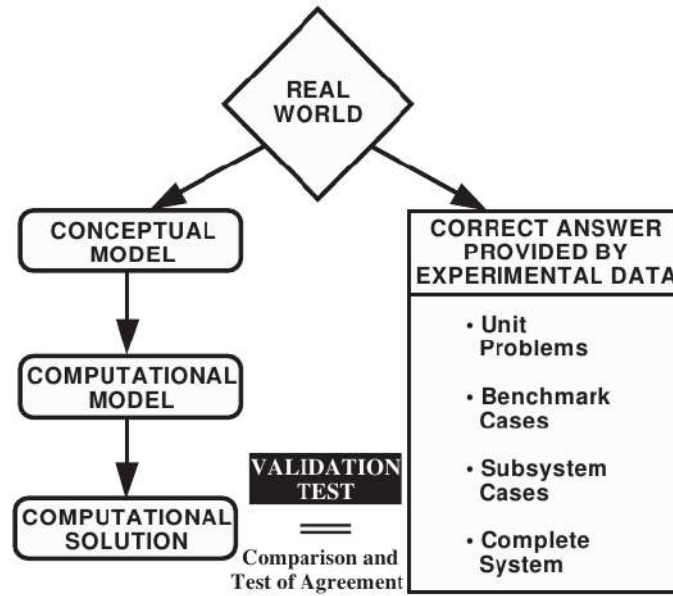


Figure 2.5: Validation process [Oberkampf and Trucano, 2002].

equations with the k-L model for the turbulent fluxes and local wind measurements were integrated for validating the model. One of the objectives of this thesis has been to carry out validation studies with OpenFOAM using the DES approach and field measurements.

## 2.5 Wind measurements and instrumentation

The use of reliable meteorological data is crucial in wind turbine installation planning. Wind speed and direction measurements are fundamental and the type of instrumentation required varies depending on the wind energy application. Typically for assessing the wind resource in the built environment the following measurements are used [Manwell et al., 2010]:

- wind speed,
- wind direction,
- ambient air temperature and

- air pressure.

Typical reported approaches to taking these measurements are described below and Section 4.3 describes the instrumentation used in this work.

### 2.5.1 Wind speed measurements

Wind speed measurements are the most important indicator for wind resource assessment and there is high demand for reliable sensors. The wind industry has introduced in the last few years the ultrasonic technology as an alternative to the traditional mechanical sensors. Mechanical (rotating cup and vane) and ultrasonic anemometers use different ways to measure the wind. Mechanical sensors have moving parts i.e. the ‘cups’ move with wind changes, while ultrasonic sensors have no moving parts and the wind speed is calculated from the time it takes the ultrasound to travel between a pair of transducers. Both sensors offer accurate measurements when averaged over time. However, mechanical sensors cannot always capture turbulence due to the physical limitations of moving parts to adapt immediately to the rapid changes in wind speed and direction (inertia). In contrast, ultrasonic technology is not affected by inertia and the rapid changes in wind speed and direction are measured in real time [Li et al., 2016]. This instrumentation allows for more accurate, high frequency (1 to 100 Hz), three-dimensional measurements of flow speed and turbulence properties. Therefore, the use of ultrasonic anemometers in the built environment—a highly turbulent and gusty environment—is more appropriate for wind energy assessment and model validation studies. Another aspect regarding the mechanical sensors is that they become unreliable or even inoperable in freezing conditions, as opposed to the ultrasonic sensors which are either heated or the ultrasonic prevent the transducers to freeze. Nevertheless, mechanical sensors are preferred in some applications due to their lower cost compared to ultrasonic technology.



### 2.5.2 Wind direction measurements

Wind direction measurements are important for identifying wind flow phenomena (turbulence, reattachment zones etc) and also influence the choice of wind turbine orientation and type —horizontal axis wind turbines (HAWTs) vs vertical axis wind turbines (VAWTs). The former are usually working for the prevailing wind direction when there is no yaw mechanism, while the later do not need to be pointed into the wind. As for the wind speed, ultrasonic sensors are able to measure the wind direction in real time as opposed to wind vanes with moving parts and inertia effects.

### 2.5.3 Temperature measurements

Air temperature is used to derive the air density, which affects the power performance of wind turbines. Ideally, it is measured near the hub-height and the sensor should not be exposed to direct sun light [Zhang, 2015].

### 2.5.4 Barometric Pressure measurements

Barometric pressure is also used to determine the air density and can improve estimates of annual energy production by 1% compared to assuming a constant density. When the instruments are placed near hub-height it is difficult to measure the barometric pressure accurately due to the windy environment and the dynamic pressures caused. To prevent condensation, it is also advisable to install the sensor in an environmentally protected enclosure, complete with desiccant, which should be changed at regular intervals [Campbell Scientific Inc, 2016]. The instruments which offer accurate and reliable measurements are quite expensive and for this reason most resource assessment studies use measurements taken by a nearby meteorological

station or they only use the air temperature and elevation data [Zhang, 2015].

## 2.6 Wind Energy Converter (WEC)

Wind turbine technology has been evolving substantially over the last few years, as wind energy is inherently available in almost every country and it can play a key role in mitigating climate change and providing energy security. The evolution of wind turbines has led to the development of reliable machines which can interface with the electricity grid [Hossain, 2015]. Although there is a tendency to large wind turbines, the interest for small wind turbines suitable for the built environment is growing and wind technology nowadays is developing for application in various areas of the world.

### 2.6.1 Types of wind turbines

Wind turbines are designed with various specifications and in various configurations, which affect their performance. They can be classified according to [Irshad, 2012]:

- the user applications; e.g. built-environment wind turbines (BWTs),
- the power output capacity, classified as micro (<10 kW), small (<25 kW), medium (25-100 kW), large (100-1000 kW) and very large (>1000 kW) WEC [Mathew, 2006],
- the driving aerodynamics force i.e. drag type and lift type wind turbines (Figure 2.6),
- the orientation of the rotation axis regarding the ground i.e. horizontal axis wind turbines (HAWTs) and vertical axis wind turbines (VAWTs) [Pagnini et al., 2015] (Figure 2.7).

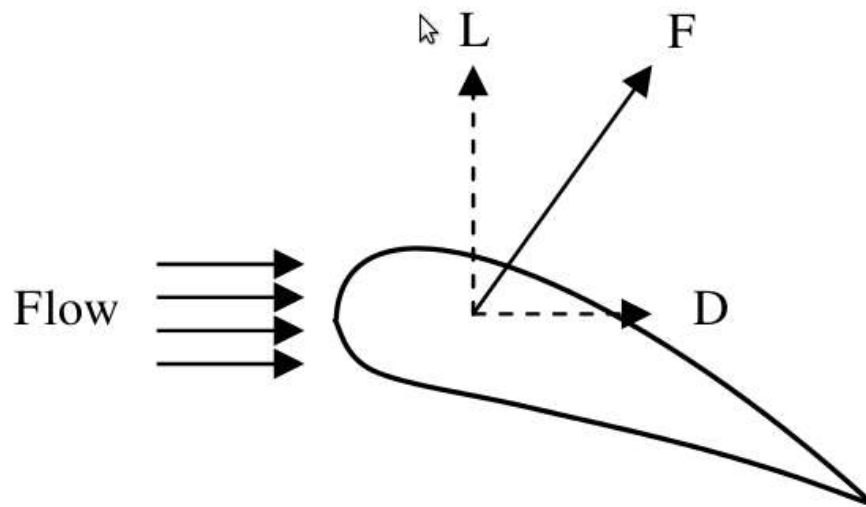


Figure 2.6: Drag (D) and lift (L) forces on airfoil [Mathew, 2006].

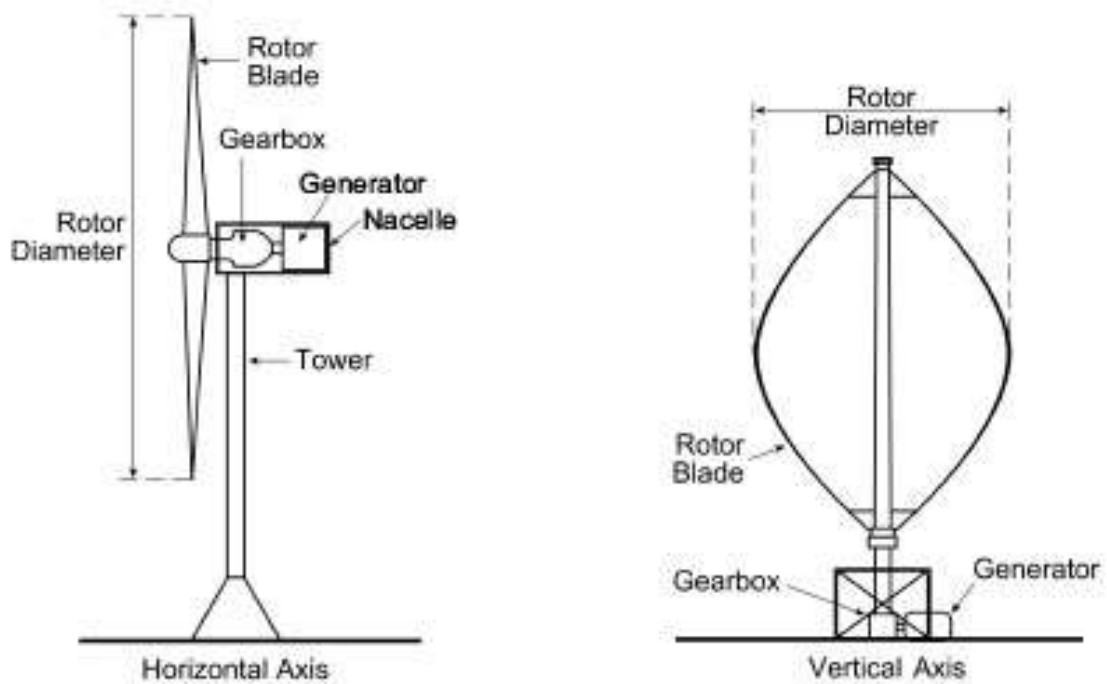


Figure 2.7: Types of wind turbines in terms of their rotor axis [The Scottish government].

### 2.6.1.1 Built-environment Wind Turbines (BWT)

Built-environment wind turbines are characterised as wind turbines which are designed to be located in an urban or suburban environment. Although they are small wind turbines (SWTs) ( $\leq 25$  kilowatts), not all SWTs are BWTs. SWT refers to their rated power, while BWT refers to their application. Most SWTs were developed for rural topography and not the built environment which is highly turbulent, the average wind speed is lower, there are frequent changes in wind direction and higher potential vertical flow. BWTs can be classified into four types [Smith et al., 2012] (Figure 2.8):

1. mounted on the roof of a building,
2. mounted on the side of a building,
3. building-integrated wind turbines and
4. ground-mounted.

### 2.6.1.2 Drag type WEC

Turbines that work principally by the drag force (Figure 2.6) are called drag machines. The drag force is parallel to the relative wind and pushes the blades. At the same time some blades must move into the wind and so induce drag forces. The speed of the blades cannot be greater than the wind speed and hence the efficiency of this type of turbine is limited [Irshad, 2012]. Therefore, there are a limited number of commercial drag-based wind turbines, like the Savonius VAWT.

### 2.6.1.3 Lift type WEC

Turbines that work predominately by the lift force (Figure 2.6) are called lift based wind turbines and produce a force perpendicular to the relative flow. Working with



(a) A VAWT mounted on the roof of the Leicester City College, UK.



(b) An HAWT mounted on the side of the Boston Museum of Science [Smith et al., 2012].

Figure 2.8: Types of BWTs.



(c) Building-integrated wind turbine at the Bahrain World Trade Center [Smith et al., 2012].



(d) Gound-mounted aeroturbine at the Randall Museum in San Francisco, California [Smith et al., 2012].

Figure 2.8: Types of BWTs.

lift force, the blades are able to move faster than the wind and hence they are more efficient than drag based machines in terms of aerodynamics [Irshad, 2012]. In particular, the optimum values for the tip speed ratio (ratio of the tip speed of the blade to the wind speed) is 7 for a lift machine (3-blade horizontal axis wind turbine) and 0.3 for a drag turbine. The conventional HAWTs and the Darrieus VAWT are lift-based machines.

#### 2.6.1.4 Horizontal Axis Wind Turbines (HAWT)

In urban areas the most common type of wind turbines are HAWTs which are able to produce more electricity than VAWTs from a given amount of wind [Saad and Asmuin, 2014]. However, they are very sensitive to turbulence phenomena and change of wind direction. Their rotors should be oriented into the wind direction by means of a tail or a yaw motor, otherwise they lose much of their efficiency [Gagliano et al., 2013]. Hence, due to the required repositioning of the turbine into the wind flow, this configuration is not very suitable for the complex urban environment with rapid changes of wind direction.

#### 2.6.1.5 Vertical Axis Wind Turbines (VAWT)

Although VAWTs have lower performance in smooth conditions, they are insensitive to wind direction and therefore are more convenient in urban environment [Carpman, 2011]. Besides, compared to HAWTs, they produce less aerodynamic noise due to their lower tip speeds, they require less maintenance and the generator and gearbox can be placed on the ground level making them easy to repair [Gagliano et al., 2013].

There are two general types of VAWTs, the Savonius design, a drag-based machine and the Darrieus design which uses the lift force (Figure 2.9). In fact, the Savonius turbine is not simply a drag-driven turbine, but it combines both drag and

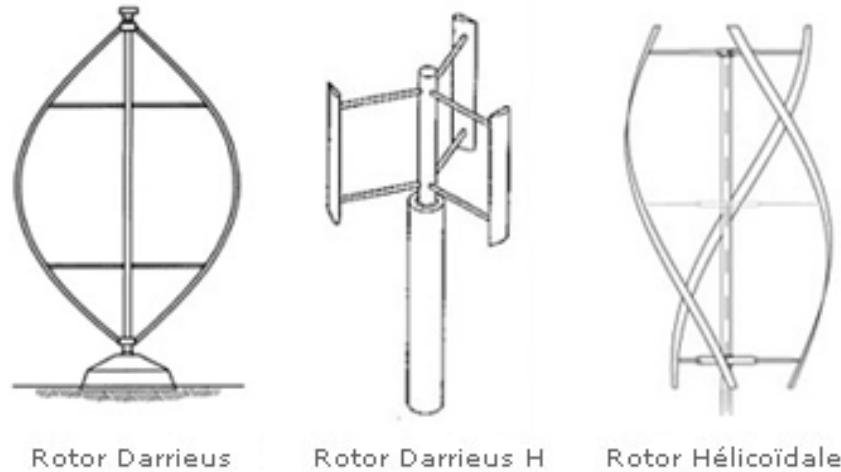


Figure 2.9: Savonius and Darrieus wind turbines [Óskarsdóttir, 2014].

suction forces and hence is more efficient than a pure drag turbine but has lower efficiency than lift-based turbines. The Darrieus machines have higher maximum efficiency than the Savonius as lift-based turbines, but they are less efficient than the conventional HAWTs in smooth wind conditions. However, in built environment, a highly turbulent environment with large fluctuations in wind direction, the Darrieus machines will run smoothly and they will counterbalance the higher efficiency of HAWT in an ideal undisturbed low turbulence wind environment [Bussel and Mertens, 2005].

## 2.6.2 Power performance

The kinetic energy in the wind is harnessed by wind turbines and converted into electrical energy [Ishugah et al., 2014]. In practice, only a fraction ( $C_p$ ) of the total power available in the wind can be harvested by wind turbines. For an ideal Horizontal Axis Wind Turbine (HAWT), it is equal to  $16/27 \simeq 59\%$  and is known as the Betz limit - after Albert Betz who published this result in 1920 [Betz, 1966]. The theory used to obtain the Betz limit cannot be applied directly to Vertical Axis Wind Turbines (VAWT), however experiments imply that the efficiencies of vertical



axis wind turbines seem to be lower than the equivalent HAWT. Furthermore, the real  $C_p$  for micro wind turbines is much lower than the Betz limit and values in the range of 0.2-0.25 can be assumed [Gagliano et al., 2013].

The power output as a function of hub-height wind speed for a single wind turbine is indicated by the power curve. Figure 2.10 illustrates an example of a power curve which is characterised by three key points: the cut-in wind speed, usually about 2 – 4 m/s, at which the turbine starts to operate, the rated speed, around 14 m/s at which the wind turbine produce its maximum power and the cut-off wind speed, approximately 25 m/s, at which the turbine is turned off for safety reasons [Carpman, 2011]. Most of the power curves are defined according to the industry standard IEC 61400-12-1 for default atmospheric conditions of i.e. air density, temperature, turbulence and vertical wind shear [Wan et al., 2010]. However, turbine performance is highly site-specific particularly in the built environment due to the complex wind flows [Gagliano et al., 2013]. Therefore, normalization procedures have been developed [IEC, 2006; Svenningsen, 2010b] and the standard power curves can be adapted to compensate the power curves for differences between the default atmospheric conditions and the actual conditions at the site of interest.

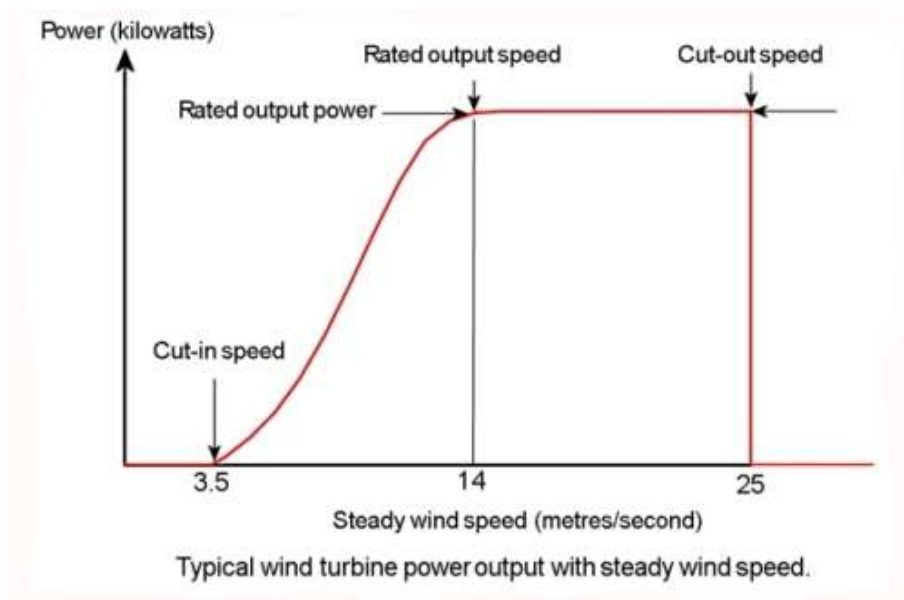


Figure 2.10: Typical wind turbine power curve [WINDPOWER software].

### 2.6.2.1 Air density correction

The IEC 61400-12 standard [IEC, 2006] includes a method to correct the standard power curve from the default air density to site-specific air densities. Since the temperature and air density are related (Equation 2.3) this method includes implicitly the temperature correction as well [Wagenaar and Eecen, 2011]. This method is based on the assumption that the efficiency of the wind turbine is fixed at all wind speeds, which is not fully achieved as indicated in the power coefficient ( $C_p$ ) curves. As a result, the calculated power output will be over-predicted for very low air densities for wind speeds near the rated power (where the power output is proportional to wind speed at a lower exponent than three) and under-predicted for higher air densities. To overcome the shortcomings of the IEC 61400-12 standard a new approach has been introduced by Svenningsen [2010b], which is similar to the IEC 61400-12 standard correction, adapted to incorporate the changes of wind turbines' efficiency as a function of wind speed.

### 2.6.2.2 Turbulence Intensity correction

For built environment wind turbines, TI is an important issue as they are located in the most turbulent area of the ABL and it affects the turbines power production. Wind turbines are designed to withstand specific external wind conditions, including turbulence.

The standard power curves are valid for a reference turbulence intensity, which may differ from the site-specific turbulence intensity. With increasing TI the turbines' power output increases at low wind speeds (cut-in), while in the transition region to rated power the TI decreases the power output [Kaiser et al., 2007; Tindal et al., 2008; Wagner et al., 2009] (Figure 2.11). Thus, for wind resource assessment purposes, the reference power curves should be normalised to the site-specific turbu-

lence intensity. Albers [2009a] have developed a methodology to modify the turbine's power curves for varying TI that is based on the hypothesis that the wind speed within an observation period is Gaussian distributed and hence can be fully determined by the average wind speed and the turbulence intensity. It also assumes that the wind turbine follows at each instant a certain power curve, which corresponds to zero turbulence intensity. The Alber's normalisation procedure has been incorporated into the draft of the second edition of the standard IEC 61400-12-1 [Albers and Windguard, 2014], which is going to be published in January 2017.

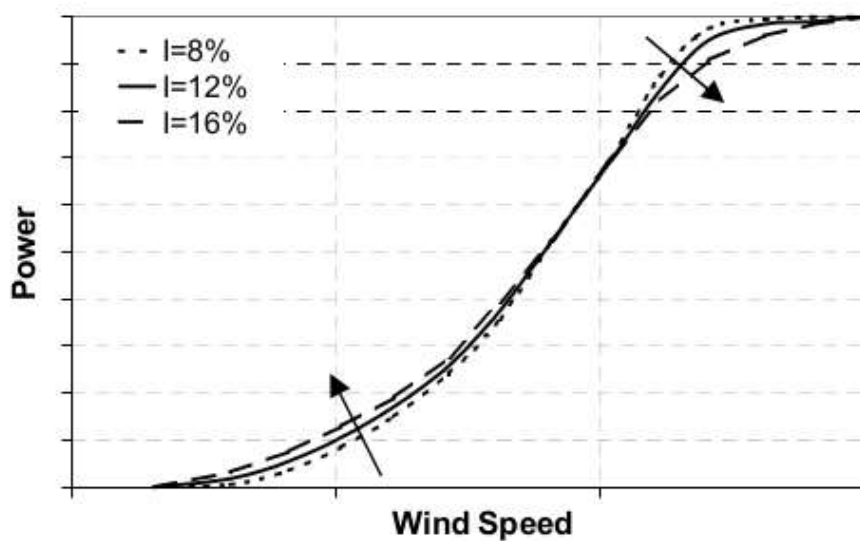


Figure 2.11: Typical impact of turbulence on power curves [Kaiser et al., 2007].

## 2.7 UK wind trials in urban areas

The UK has the best wind resource potential in Europe [Department of Energy and Climate Change, 2013]. Although large scale wind farms are well understood and it is easy to make accurate energy yield predictions, micro wind turbines (1-10 kW wind turbines) in urban areas is an emerging technology and there is limited knowledge on their performance.

In 2008-2009, the Energy Saving Trust undertook the UK's first large scale micro-wind trial, during which the performance of 39 turbines in urban, suburban and rural location were monitored [James et al., 2010; Sissons et al., 2011]. All the turbines were HAWTs due to the small number of VAWTs installed in the UK to date. It was found that the performance of the turbines was generally very poor with annual generation of less than 75 kWh/m<sup>2</sup> swept area. This was attributed mainly to the low wind resource at these turbine's locations and heights—all the recorded mean wind speeds were less than 4 m/s. Turbulence further affected their performance.

During the Warwick Urban Wind Trial Project [Encraft, 2009] small HAWTs were installed on the roofs of 26 households. The average energy generated per day was very low—628 Wh counting only the times when turbines were switched on, or 214 Wh including times when turbines were switched off—and significantly less than the manufacturers' performance predictions (sometimes less than 1/10 of the predictions). The power curves proved not to be always accurate, but the major factor for the overestimations was the accuracy of the predicted wind speeds. In both trials the measured average wind speeds at all sites were lower than the NOABL predictions—at some areas the wind speeds were 40% lower than NOABL [Encraft, 2009].

It was acknowledged that the development of a robust method to predict the average wind speed in urban areas was required and more accurate power curves should be published. Till today these demands remain [Yang et al., 2016]. In the following sections, the barriers, the actions and the strategy to address these issues are reported.

## 2.8 Summary

This literature review has demonstrated that the wind resource in urban environments is not well understood. Predictions of accurate wind speeds are required to avoid overestimations of turbine production and identify potential locations for mounting small wind turbines. Previous work also recognised the need for an industry standard that normalises the way in which manufacturers power curves are generated.

The following sections will explain the current barriers for built environment wind turbines application, the actions that should be made and finally the strategy followed in this study to address these issues.

### 2.8.1 Barriers

In short, one of the main barriers for built environment wind turbines application is the poor understanding of the wind resource in the urban environment and the lack of validated model results and field measurements to facilitate the development of guidelines for resource assessment.

The wind flow in urban areas is very complex as there are complex turbulent phenomena that are not well understood and hinder the identification of the most suitable wind turbine locations and the corresponding energy production estimates.

The wind resource is also site specific as huge differences exist among sites with different topography so that existing large-scale wind resource maps cannot be applied to the built environment in a meaningful and reliable manner [Smith et al., 2012]. They can be used for an initial prediction of the wind speed at high heights far away from obstacles, but they should at least be translated to the proposed hub heights.

The use of computational models is promising for wind speed estimates but limitations on computational resources and a lack of measurements for validation purposes prevents such models being widely used [Smith et al., 2012]. High resolution wind measurements in urban areas should be used to improve and validate the computational models. These models are also time consuming to apply, while simplified models have been proved inadequate for such simulations [Breuer et al., 2003; Franke et al., 2004].

Finally, even the most accurate wind speed predictions are not of value for annual energy production estimations if there are no reliable wind turbine performance characteristic data. Understanding the development of theoretical power curves and the parameters they are based on will also help to establish better energy production estimates.

## 2.8.2 Actions

There are several methods to model and predict the wind resource in urban environments. CFD and wind tunnel experimental methods are sometimes used, while field measurements are of major importance for studying the wind flow in major wind power projects as well as in the validation of model predictions. Each method has some success and limitations and investigation is required to identify their strengths and weaknesses.

With the growth of computer performance, CFD models have gained much more attention and today CFD packages are widely used for wind flow analysis. Nevertheless, the wind resource assessment in the built environment using CFD is an emerging area and validation is required through site measurements. The essential element for this action is the use of high quality, three dimensional data from sonic anemometers placed in adequate areas for BWT installation. Therefore, validation case studies will help to review the predictability and validity of CFD building

models, develop new models and create best practice.

Site measurements are also of use to review the wind turbines performance data and improve IEC-61400 [IEC, 2006], which is the basis for most wind turbine standards. This type of data should reflect the actual performance of a wind turbine at the specific location installed and providing recommendations to the IEC, the production estimates will be improved.

### 2.8.3 Strategy

To understand the wind resource in the built environment we should start with existing case studies, sites that have already been modelled, and compare the results—CFD, wind tunnel and field measurements—with each other. CFD software are increasingly available and open-source packages have gradually gained popularity in both commercial and academic organisations, but their development relies on the efforts of third parties. The key validation procedure incorporates the comparison between computational results and experimental data. For this purpose, high quality wind measurements are of value and sonic anemometers which can capture the three dimensional wind data should be used. These measurements will also help to develop the IEC standards in which the modelling of turbine performance is based on.

At the end, a robust methodology should be created to provide stakeholders with guidelines for assessing the wind resource in the built environment and estimate accurately the mean annual wind speed and the annual energy production (AEP).

# Chapter 3

## Validation of DES implemented in OpenFOAM

### 3.1 Introduction - Chapter overview

This chapter examines the performance of the DES turbulence model, implemented in the open source CFD library OpenFOAM, for external flows in complex urban environments. This is the numerical tool that will be used in the wind energy assessment methodology that is developed later in the thesis. Hence, it is necessary to examine its general ability to predict wind flows. For these purposes, a number of benchmark data sets developed by the Architectural Institute of Japan are revisited [AIJ, 2009]. Firstly, results are presented for analysis of the flow around a single high rise building and comparisons are made with wind tunnel data Secondly, predicted flows in a real urban environment are examined, using data derived from both wind tunnel experiments and field measurements. A number of studies have previously been reported that make use of these test cases [Tominaga et al., 2004; Yoshie et al., 2007a], but none has previously used a DES model.

The aim of this study is to offer some validation evidence for DES approaches applied



to external flows in urban environments and implemented with the OpenFOAM software [Weller et al., 1998]. It also aims to evaluate the advantages of DES approaches in these applications, as this has been reported in very few papers [Haupt et al., 2011]. As this work has been carried out in the context of a study and the development of CFD based methods for wind energy assessment in complex urban environments, it comments on modelling of building's wake conditions, rather than evaluation of surface pressures and forces or dispersion of contaminants.

## 3.2 Test Case A: High rise building

### 3.2.1 General description of the experiment

The first test case is a study of the flowfield around a high-rise building of 2:1:1 (height:width:depth) ratio, placed in a turbulent boundary layer (Figure 3.1). The wind tunnel scale model was 0.16 m high and 0.08 m square. The wind tunnel imposed an inlet condition approximating a power law velocity profile with an exponent of around 0.27 and the Reynolds number was  $2.4 \times 10^4$  (Figure 3.1).

Measurements were taken using a split-film probe for the instantaneous wind velocity in each direction and the average and standard deviation of fluctuating wind velocities were reported [Yoshie et al., 2007a]. Measurements of the velocities were made at a grid of points over a vertical cross-section and on horizontal planes indicated in Figure 3.2. The data used in our first validation study are that published by Meng and Hibi [1998].

### 3.2.2 Turbulence models

In applying the first of the Architectural institute of Japan (AIJ) test cases, the steady-state RANS solver `simpleFoam` for incompressible, turbulent flow from the

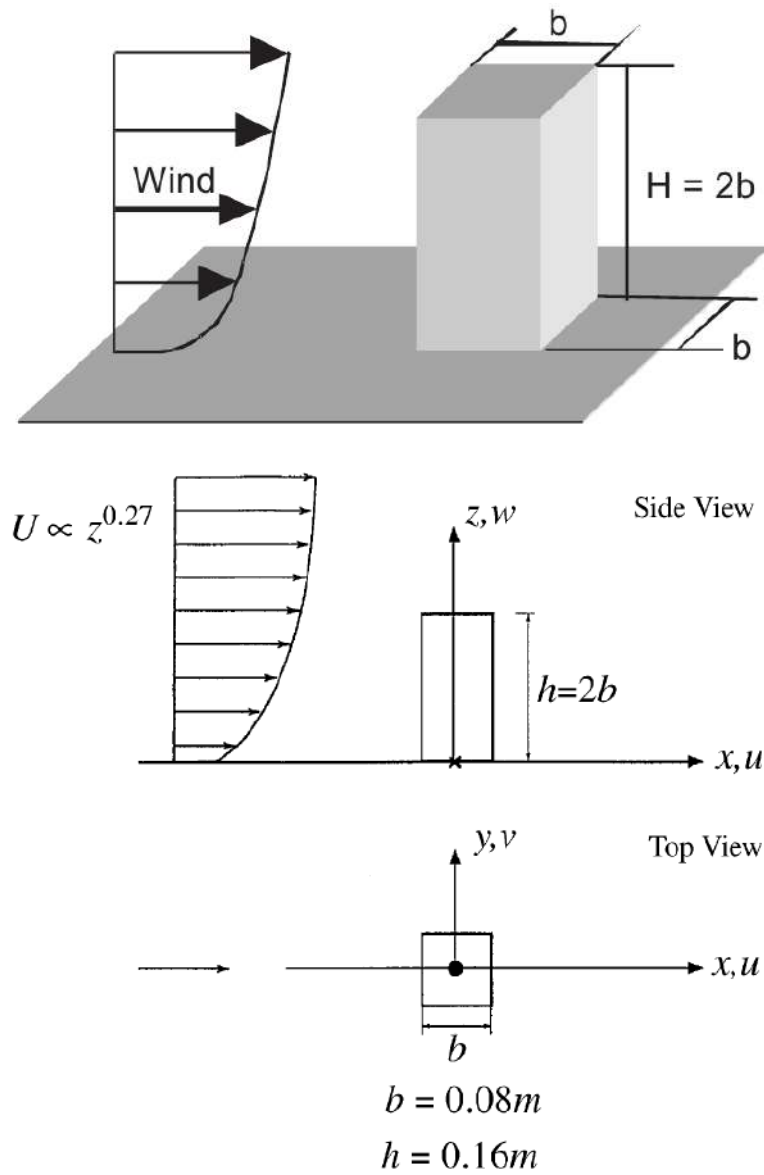


Figure 3.1: Test Case A: 2:1:1 shaped building geometry [Yoshie et al., 2007a].

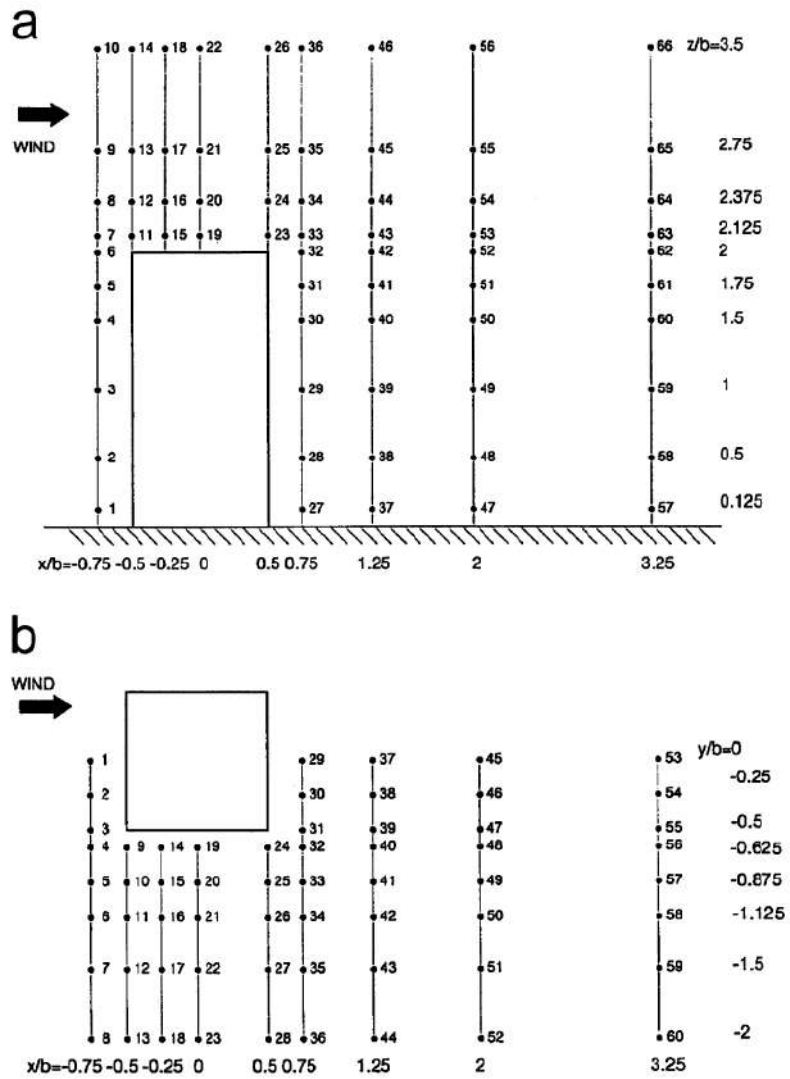


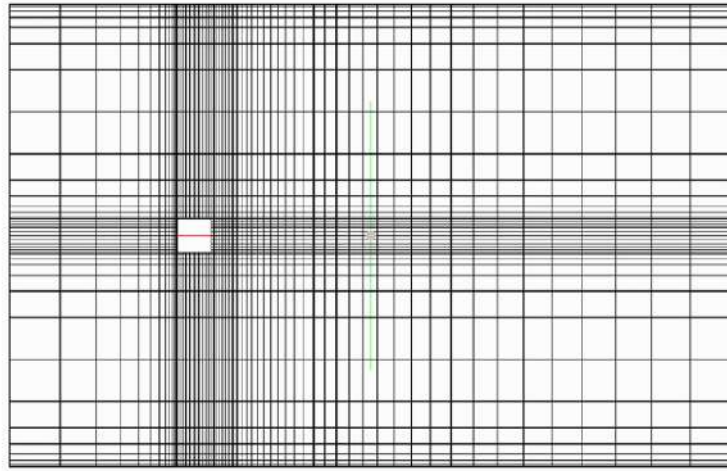
Figure 3.2: Test Case A - Wind tunnel experiment. (a) Measuring points in vertical cross-section ( $y = 0$ ). (b) Measuring points in horizontal plane ( $z = 0.125b$  and  $1.25b$ ) [Yoshie et al., 2007a].

OpenFOAM library (version 2.3.1) was used with the standard  $k-\epsilon$  (Appendix B.2),  $k-\omega$ -SST (Appendix B.4) and Realizable  $k-\epsilon$  (Appendix B.3) eddy viscosity turbulence models [Launder and Spalding, 1974; Menter, 1994; Shih et al., 1995]. For the DES calculations, the DDES-SA model [Spalart et al., 2006] was used with `pimpleFoam`, the large time-step transient solver for incompressible flow. As the DES model explicitly resolves the large scale turbulence and is a fully transient calculation, the flow should be fully developed ('spin-up' phase), before starting to average the data for adequate statistics and derivation of the mean flow field. In this study, the simulation time during which the data were averaged, was  $T = 2 \cdot T_0$ , where  $T_0$  is the time required for a cross-flow, preceded with a model spin-up time of  $T = 3 \cdot T_0$ . The solvers (`fvSolution` dictionary) and the numerical schemes (`fvSchemes` dictionary) for the DES calculations are presented in Appendix C.1.

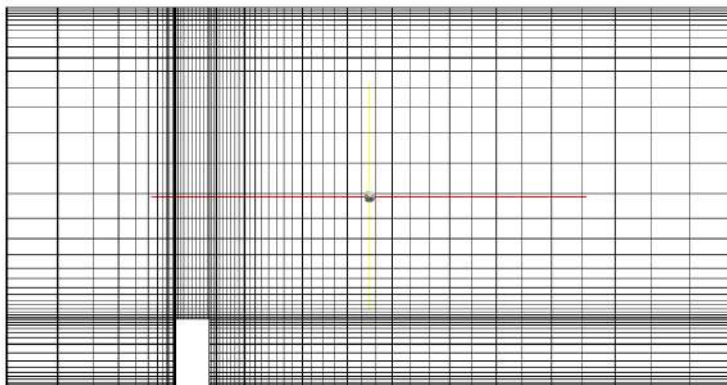
### 3.2.3 Computational domain and mesh

The dimensions of the computational domain are (Length) $\times$ (Width) $\times$ (Height) =  $21b \times 13.75b \times 11.25b$  (with  $b$  being the width of the building)(Figure 3.3) and replicate the geometry of the wind tunnel—as recommended in best practice guidelines by Franke et al. [2007]. The experimental parameters have been reported by Tominaga et al. [2008b] and are the standard conditions for the comparative studies with the wind tunnel data as well as the CFD results of other working groups. The mesh resolution for the RANS calculations was  $60(x) \times 45(y) \times 39(z)$  (105,300 cells) and the building was discretized into  $10 \times 10 \times 16$  cells. The minimum cell width is set to  $0.07b$  and is expanded towards the horizontal and the vertical directions (Figure 3.3). With this mesh configuration the first off the wall point lies in the logarithmic layer ( $y^+ = 30$ ) as required when the log-law wall functions applied (Appendix A) as described in section 3.2.4.2. This follows similar practice to other CFD studies of this case reported by Tominaga et al. [2008b].

For the DES calculations, the grid dependence was investigated by running simulations for three progressively finer grids: a coarse mesh (100,000 cells) same as for RANS calculations, a medium mesh (800,000 cells), twice the linear resolution of the RANS case and a fine mesh (2,700,000 cells), three times the linear resolution of the RANS case (Figure 3.4).

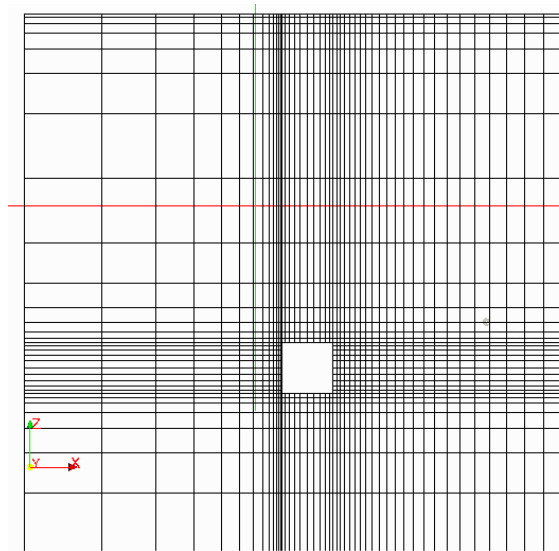


(a) Horizontal section (x-y)

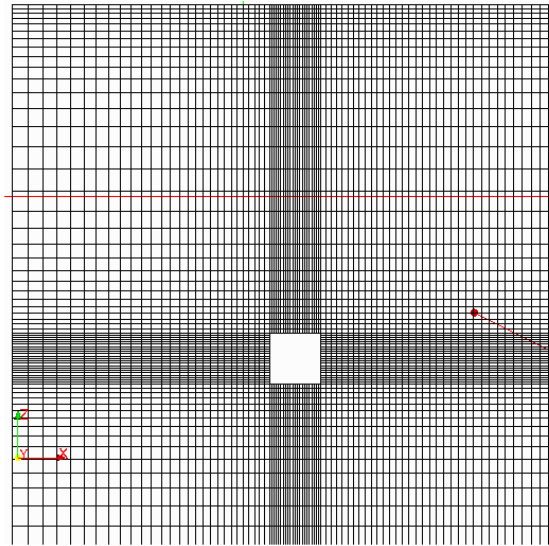


(b) Vertical section (x-z)

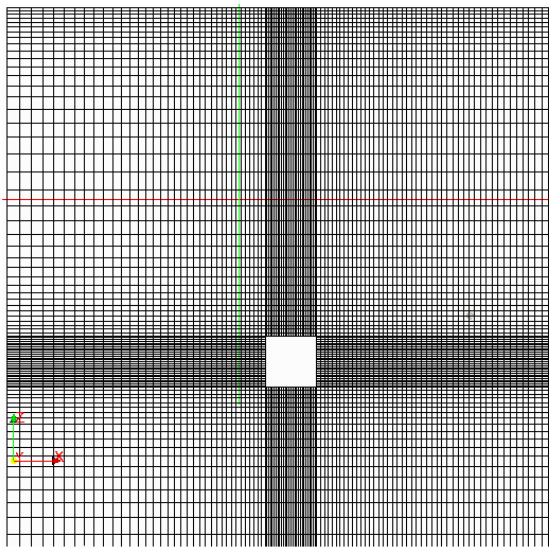
Figure 3.3: Test case A: Computational domain and grid discretization.



(a) Coarse mesh



(b) Medium mesh



(c) Fine mesh

Figure 3.4: Test Case A: Mesh resolution.

### 3.2.4 Boundary Conditions

#### 3.2.4.1 Basic boundary conditions

##### Fixed value

The fixed value boundary condition imposes a value of  $\phi_d$  for the value of an environmental variable on a certain boundary face (d) of the domain. It is used on the following conditions:

- inlet: Interpolated values of U from the experimental approaching flow (Figure 3.5). Non-uniform constant velocity:  $u = U(x,0,0)$ ,
- outlet: Uniform, constant pressure:  $p = 0$ ,
- walls: Uniform, constant velocity:  $u = (0,0,0)$ .

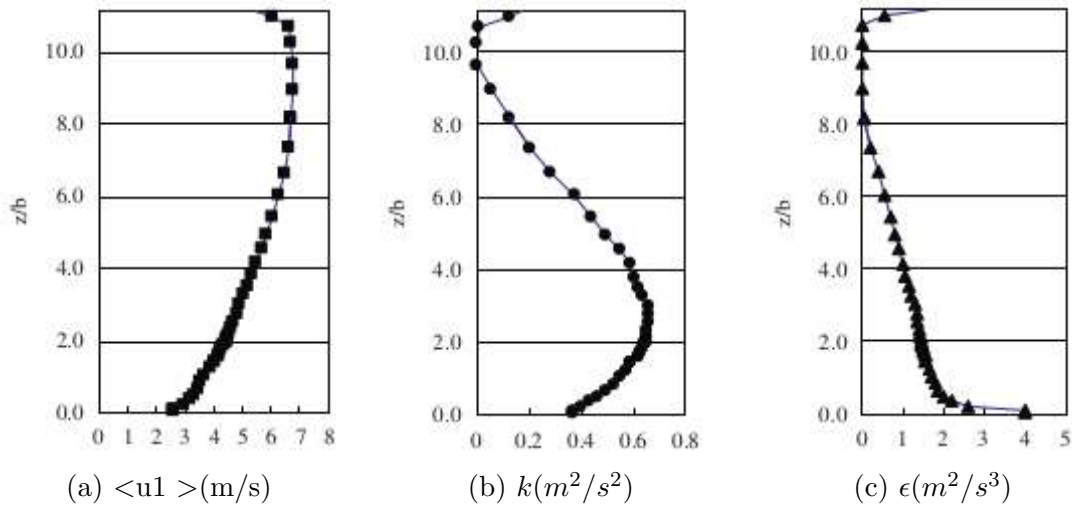


Figure 3.5: Inflow boundary condition for computation of k- $\epsilon$  models [Tominaga et al., 2008a].

##### Zero gradient

The zero gradient boundary condition imposes a value of zero for the normal gradient of a variable on the boundary face (d). It is used on the following conditions:

- inlet, walls: Uniform, constant pressure gradient:  $\frac{\partial p}{\partial n_d} = 0$ ,
- outlet: Uniform, constant velocity gradient:  $\frac{\partial \mathbf{U}}{\partial n_d} = (0, 0, 0)$ .

## Symmetry

The symmetry boundary condition imposes a fixed, zero value to the boundary normal component of a variable and zero gradient for the boundary parallel component.

### 3.2.4.2 Turbulent properties for RANS

The standard boundary conditions —following the practices reported by [Yoshie et al., 2007a](#)— have been selected for the RANS calculations as described below.

#### Log-law wall functions

The wall functions based on logarithmic law for a smooth wall (described in Appendix A.1), have been used for the building surfaces and the lateral and upper surfaces of the domain. For the ground surface the modified logarithmic law of the wall (Appendix A.1.1) have been applied to account for the roughness characteristics (roughness length:  $z_0 = 1.8 \cdot 10^4$  m). The wall functions (Section 2.4.2.2 and Appendix A) are used to derive the wall shear which is linked to the eddy viscosity according to the Boussinesq approximation (Appendix B.1).

#### k- $\epsilon$ turbulence model

Interpolated values of turbulent kinetic energy,  $k$ , from the experimental approaching flow have been applied in the inlet (Figure 3.5). The value of  $\epsilon$  is given from the



relation:

$$\epsilon = C_\mu^{1/2} k \frac{dU}{dz} \quad (3.1)$$

according to  $\epsilon = P_k$ , where  $C_\mu=0.09$ . At the outlet zero gradient conditions for  $k$  and  $\epsilon$  have been used in accordance to the conservation of momentum. The  $k$  is solved in the whole domain including the wall adjacent cells and the boundary condition at the walls is zero gradient ( $\frac{\partial k}{\partial n} = 0$ ) (k wall function in Openfoam act as a zero gradient condition). The  $\epsilon$  in the adjacent cells to the wall (`epsilonWallFunctions`) is computed by:

$$\epsilon = \frac{C_\mu^{3/4} k^{3/2}}{\kappa y} \quad (3.2)$$

where  $C_\mu = 0.09$  and  $\kappa$  the von Karmans constant.

### **k- $\omega$ turbulence model**

Just as in the  $k-\epsilon$  model calculations, interpolated values of  $k$  from the experimental approaching flow have been applied in the inlet, while the value of  $\omega$  is calculated from the relation:

$$\omega = \frac{\epsilon}{C_\mu k} \quad (3.3)$$

Zero gradient conditions, were set to satisfy the momentum equation at the outlet. At the solid boundaries, the wall function in OpenFoam acts as a zero gradient condition for  $k$  (`kqRWallFunction`) ( $\frac{\partial k}{\partial n} = 0$ ) and the  $\omega$  (`omegaWallFunction`) is given by:

$$\omega = \frac{\sqrt{k}}{C_\mu^{1/4} \kappa y} \quad (3.4)$$

where  $C_\mu = 0.09$  and  $\kappa$  the von Karmans constant.

Table 3.1 summarises the standard boundary conditions for the RANS calculations.

---

Inflow	<p>Interpolated values of U and k from the experimental approaching flow. The value of <math>\epsilon</math> is given from the relation <math>\epsilon = C_\mu^{1/2} k \frac{dU}{dz}</math> (<math>\epsilon = P_k</math>), <math>C_\mu = 0.09</math>.</p> <p>The value of <math>\omega</math> is given from the relation <math>\omega = \frac{\epsilon}{C_\mu k}</math>, <math>C_\mu = 0.09</math>.</p>
Outflow	Zero gradient condition
Lateral and upper surfaces of the domain	Wall functions based on logarithmic law for a smooth wall.
Ground surface	Wall functions based on logarithmic law with roughness length $z_0$ ( $z_0 = 1.8 \times 10^{-4}$ m).
Building surface	Wall functions based on logarithmic law for a smooth wall.

---

Table 3.1: Standard Boundary Conditions in RANS models [[Yoshie et al., 2007a](#)].

### 3.2.4.3 Turbulent properties for DES

#### Spalding wall functions

The ‘universal’ Spalding wall function (Section 2.4.2.2) was selected for the DES calculations and applied to the building and ground surfaces. (The lateral and upper surfaces, were defined as `SymmetryPlane` boundaries and symmetry conditions were applied).

#### Spalart Allamaras turbulence model

The SA viscosity ( $\tilde{\nu}$ ) is set to zero at all wall boundaries. The rest of the SA boundary conditions are identical to those applied to the eddy viscosity model and are summarised in Table 3.2.

---

Inflow	Interpolated values of U from the experimental approaching flow.
Outflow	Zero gradient condition.
Lateral and upper surfaces of the domain	Symmetry conditions.
Building and ground surfaces	Spalding's wall function.

---

Table 3.2: Boundary Conditions for DES calculations.

### 3.3 Test Case B: Actual Urban Area

#### 3.3.1 General description of the experiment

The second test case is a study of the flow field within a building complex in the Shinjuku sub-central area of Tokyo, Japan (Figure 3.6). A number of wind tunnel experiments as well as field measurements were carried out by various research institutions around the time of construction. In this and other reported studies the CFD simulations were performed for conditions recorded in 1977 [Yoshie et al., 2007a]. The case is of particular interest as it has a complex geometry with large variation in building heights. The data set has additional value as it includes field measurements as well as wind tunnel test data. In the field tests three cup anemometers were used, taking measurements at 10 m height from the ground for the points 1 to 36 and at 187 m and 237 m for the C and D points (10m above buildings) shown in Figure 3.7.

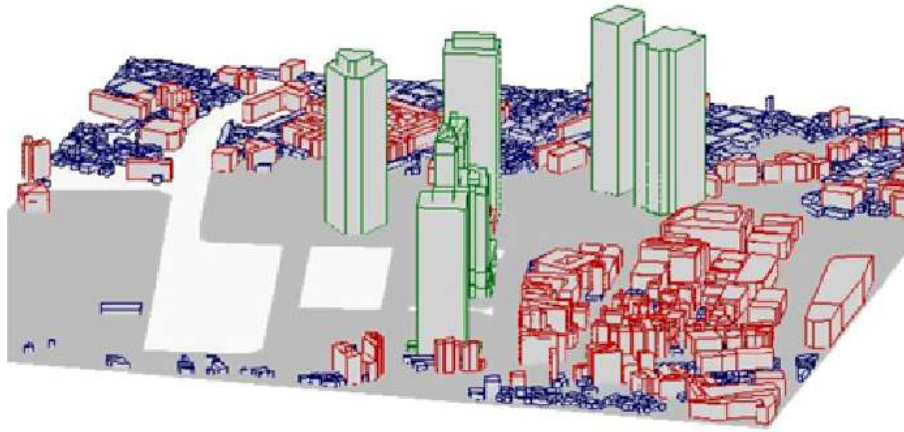


Figure 3.6: Building complexes in urban area of Shinjuku [Yoshie et al., 2007a] that define the geometry of Test Case B.

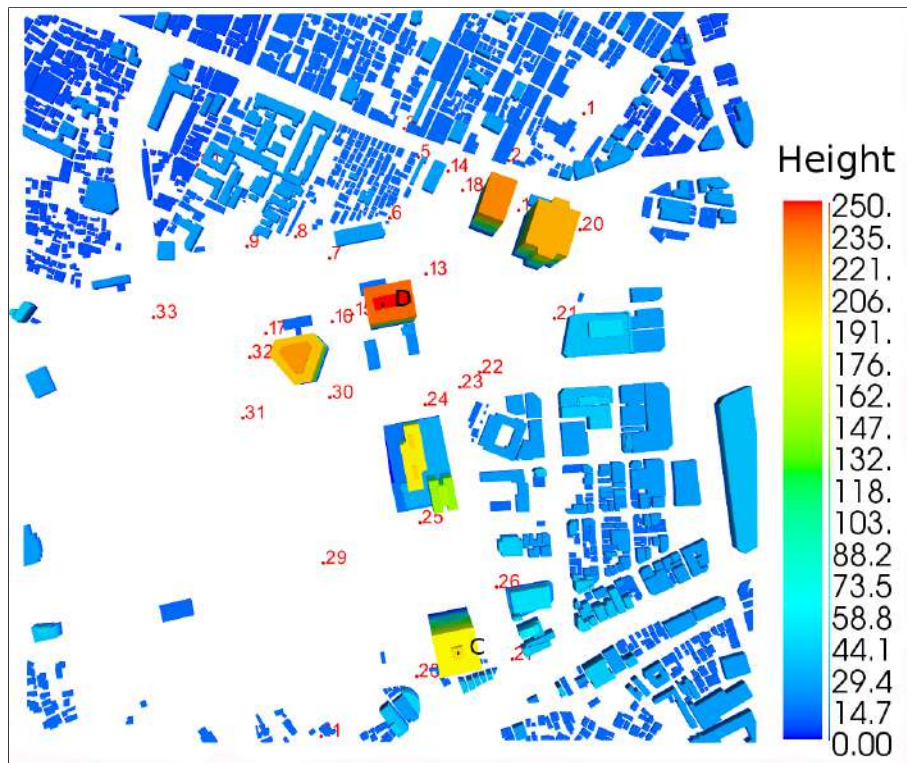


Figure 3.7: Test case B: measuring points and building heights.

### 3.3.2 Turbulence models

In the second test case involving a model of a real urban environment, the Standard  $k-\epsilon$  model for the RANS calculations was applied. For the DES calculations, it was applied the DDES-SA model [Spalart et al., 2006] with the `pimpleFoam` transient solver. In particular, the DES case was initialised using the RANS approach (the RANS results were used as inlet conditions for the DES calculations), then, a ‘spin-up’ time of  $T = 3 \cdot T_0$  ( $T_0$  the time required for a cross-flow) allowed the flow to be fully developed and the simulation time for averaging the data was  $T = 2 \cdot T_0$ . The turbulence and boundary conditions used were the same as those of Case A unless otherwise stated below. The solvers (`fvSolution` dictionary) and the numerical schemes (`fvSchemes` dictionary) for the DES calculations are presented in Appendix C.2.

### 3.3.3 Computational domain and mesh

The computational domain is firstly defined by CAD data representing  $1000 \times 1000$  m of the Shinjuku sub-central area (Figure 3.6). This building geometric data extends for approximately one block beyond the central region containing the measurement points (the exception being point 11 close to the south border) and this follows the AIJ guidance [Yoshie et al., 2007a]. The dimensions of the complete domain (Figure 3.8) are (Length) $\times$ (Width) $\times$ (Height) =  $5742 \times 3372 \times 1422$  m<sup>3</sup> accommodating an upstream length of  $5H$  (with  $H$  being the height of the highest building), a downstream subdomain length of  $15H$  and a height of  $6H$ . The lateral boundaries have been placed  $5H$  from the Shinjuku partition in accordance with best practice guidelines [Franke et al., 2007; Tominaga et al., 2008b].

This case study has geometric complexity representative of urban environments of practical interest and represents a challenge in terms of mesh generation. The

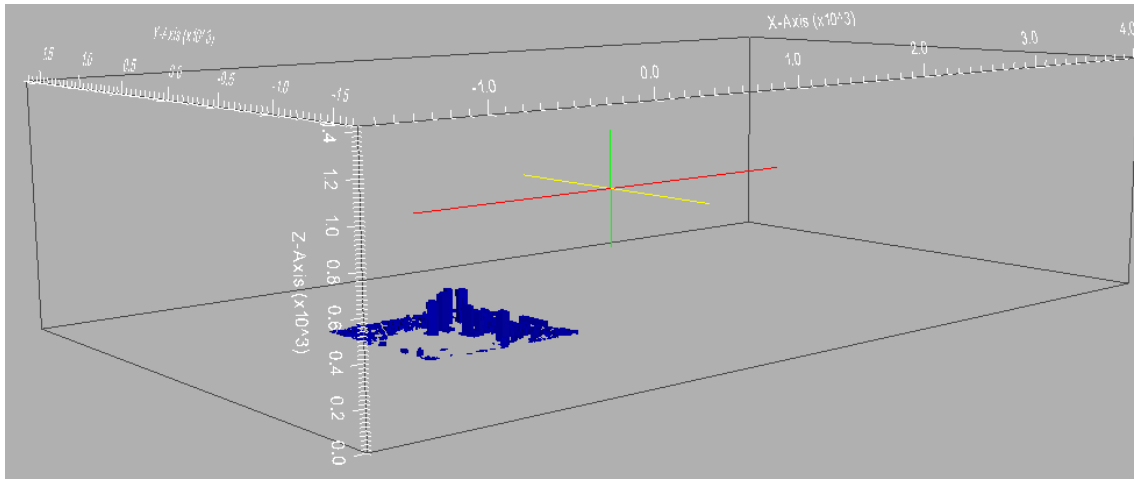
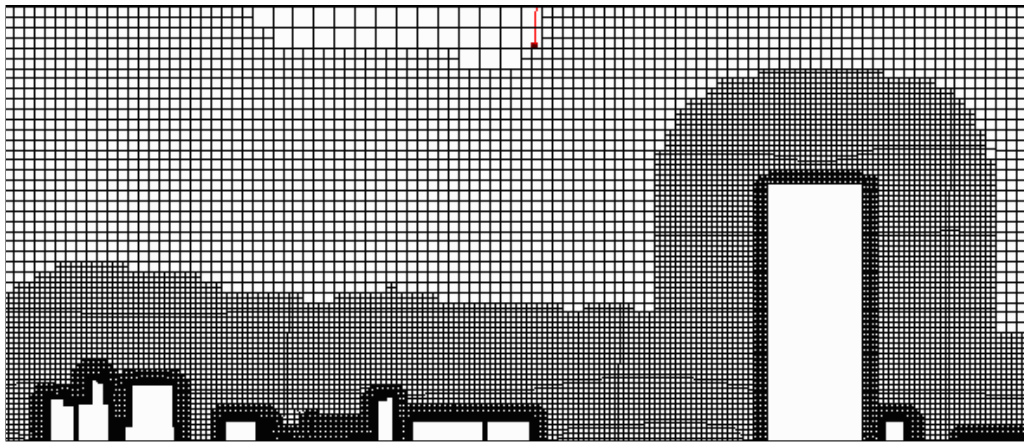


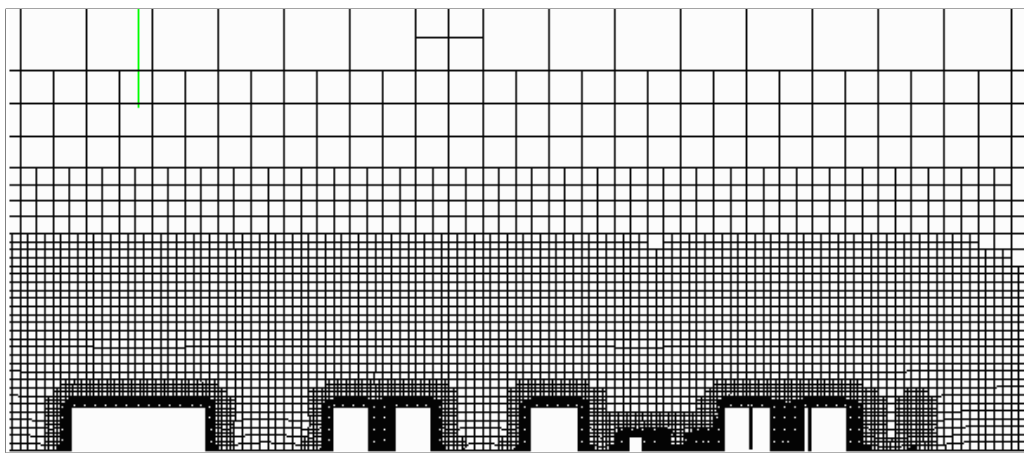
Figure 3.8: Computational domain.

OpenFOAM `snappyHexMesh` tool has proved able to mesh the case study geometry with a high degree of automation and good parallel efficiency. The tool generates hex-dominant meshes with an octree topology whereby a background cubic mesh is subdivided a number of times as the ground and building surfaces are approached. At the building surfaces the cells are modified to snap to the underlying CAD geometry (triangulated Stereolithography format in this case). Again, three progressively finer grids were generated to perform a grid study.

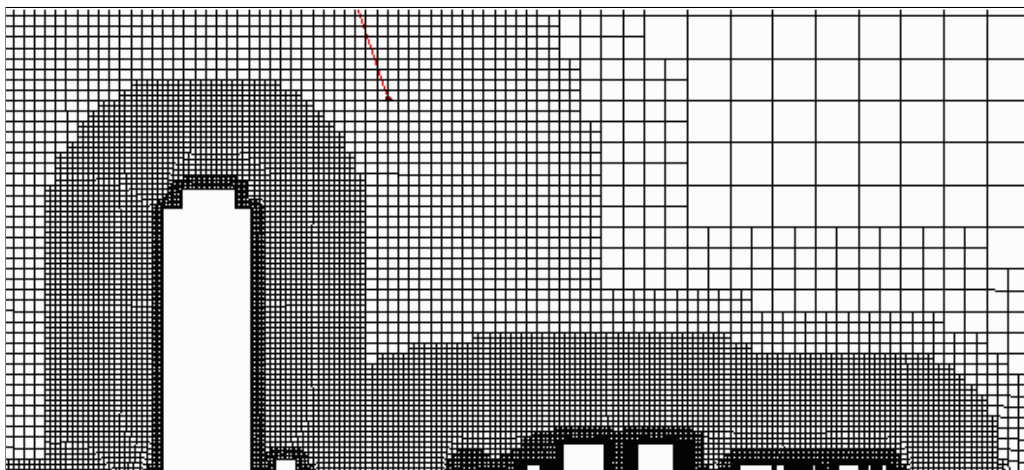
Parts of the medium computational grid are presented in Figure 3.9 to demonstrate the refinement regions around the buildings. The total number of cells for the whole domain was approximately 11.5 million for the west wind direction illustrated. Similar results were obtained by simply rotating the background mesh to obtain meshes for the other wind directions resulting in meshes with comparable numbers of cells.



(a)



(b)



(c)

Figure 3.9: Refinement regions around the buildings.

### 3.3.4 Boundary conditions

The boundary conditions for both RANS and DES calculations were treated in a similar manner to Test Case A and are shown in Table 3.3.

Inflow	Interpolated values of U from the experimental approaching flow.
Outflow	Zero gradient condition.
Lateral and upper surfaces of the domain	Symmetry conditions.
Building and ground surfaces	Wall functions.

Table 3.3: Boundary Conditions in Test Case B.

## 3.4 Results - Test Case A

### 3.4.1 Comparison between RANS models

#### 3.4.1.1 Reattachment lengths

The computed reattachment lengths on the roof ( $X_R$ ) and behind the building ( $X_F$ ) for RANS calculations utilizing different turbulence models are presented in Table 3.4. The results of the standard k- $\epsilon$  model calculated under the same conditions [Tominaga et al., 2008a] is added to the table for reference. In the results of the standard k- $\epsilon$  model, the reverse flow in the roof, which has been observed in the experiment, has not been reproduced. This has also been mentioned by other researchers [Murakami, 1993; Tominaga et al., 2008a; Tsuchiya et al., 1997] who have been working on the same case. In particular, RANS results show the flow attached



over part of the the roof ( $X_R/b = 0.25$ ), but there is no clear reversal of flow (Figure 3.10(a)). In the results of the realizable  $k-\epsilon$  model, the reverse flow appears, but it is a little larger than the experimental value (Figure 3.10(b)). For the  $k-\omega$  model the reverse flow does not reattach to the roof, since the separated region is too large (Figure 3.10(c)). In all cases the rear reattachment lengths are over predicted. Tominaga et al. [2004] presented 11 sets of results for this test case and also found  $X_F/b$  was larger than the experimental value. Lower values closer to the experimental result were only found using LES or DNS approaches in that study. The standard  $k-\epsilon$  and the  $k-\omega$  models are the most accurate, while the realizable  $k-\epsilon$  model greatly overestimates  $X_F$  (Figure 3.11).

CFD model	Turbulence model	$X_R/b$	$X_F/b$
RANS	$k-\epsilon$ (standard)	0.25	2.68
RANS	$k-\epsilon$ (realizable)	0.58	5.37
RANS	$k-\omega$ (SST)	$>1$	2.59
RANS	$k-\epsilon$ [Tominaga et al., 2008a]	-	2.70
	Experiment	0.52	1.42

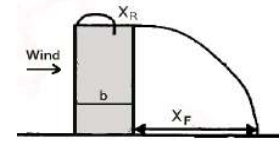


Table 3.4: Reattachment lengths by RANS models.

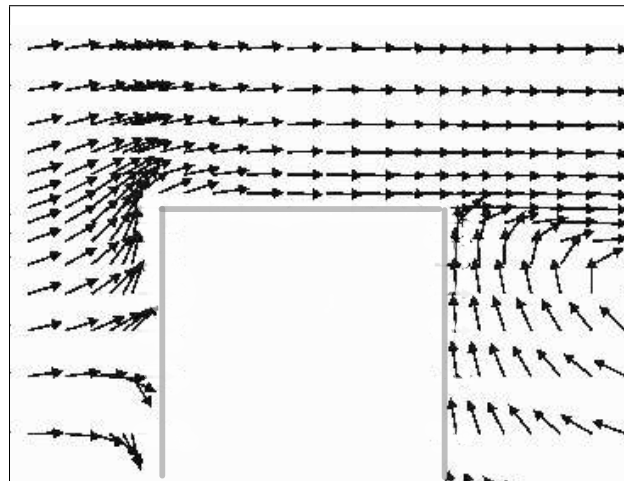
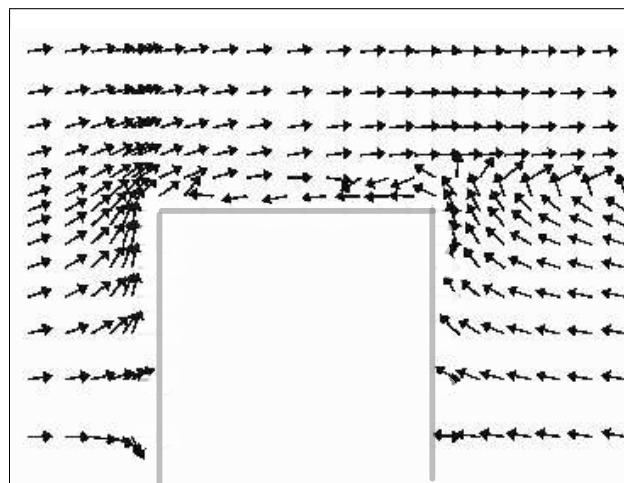
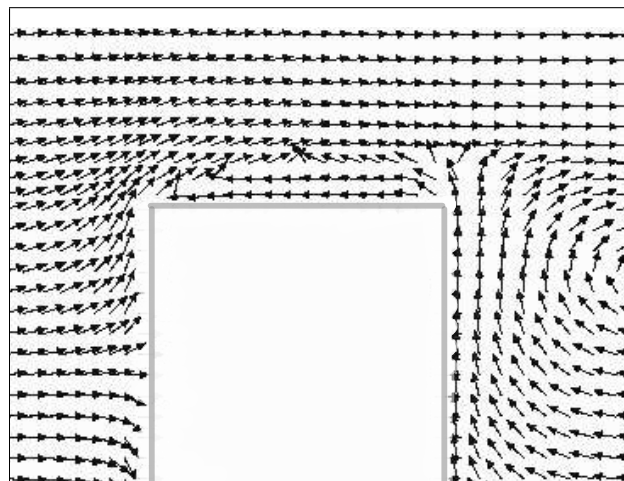
(a) Standard  $k-\epsilon$ (b) Realizable  $k-\epsilon$ (c)  $k-\omega$  SST

Figure 3.10: Vertical distribution of velocity vectors around the roof for (a) the standard  $k-\epsilon$  model, (b) the realizable  $k-\epsilon$  model and (c) the  $k-\omega$  SST model.

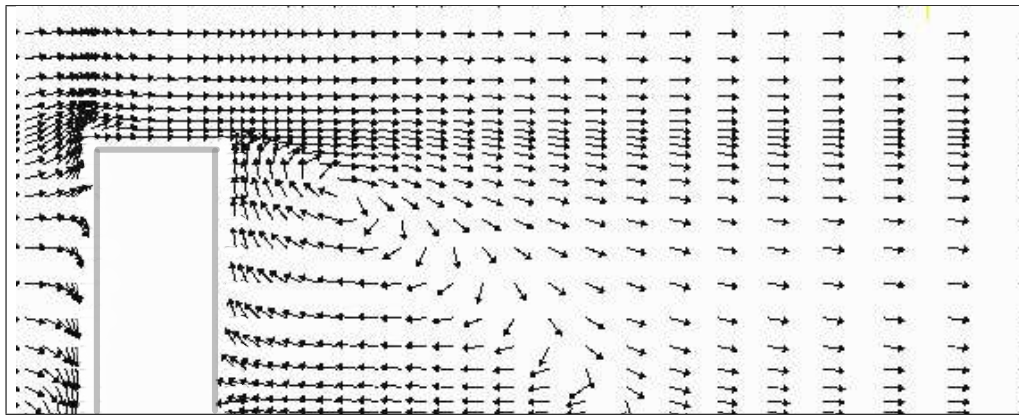
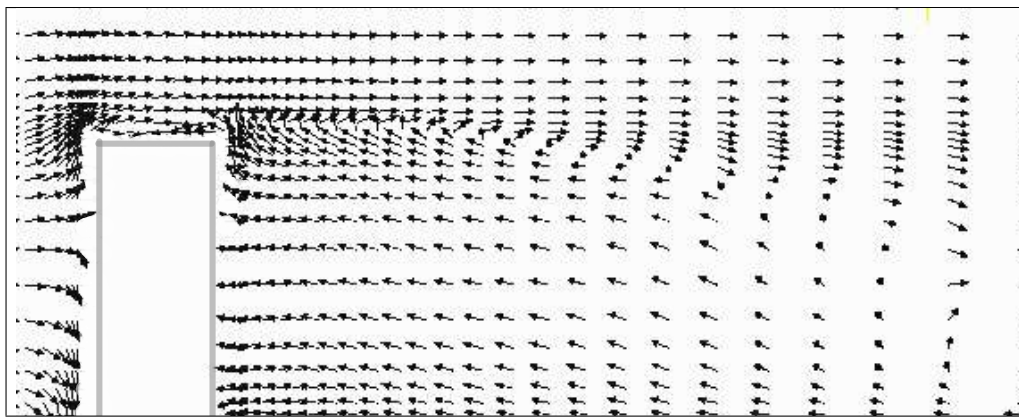
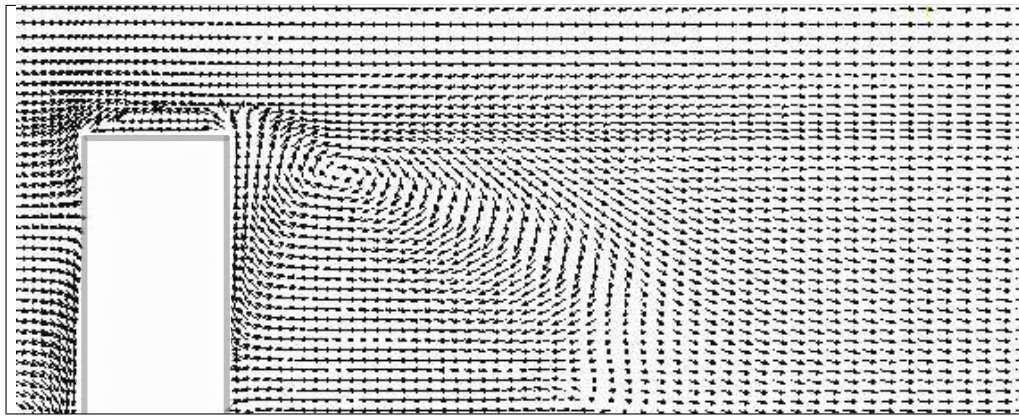
(a) Standard  $k-\epsilon$ (b) Realizable  $k-\epsilon$ (c)  $k-\omega$  SST

Figure 3.11: Vertical distribution of velocity vectors in the wake for (a) the standard  $k-\epsilon$  model, (b) the realizable  $k-\epsilon$  model and (c) the  $k-\omega$  SST model.

### 3.4.1.2 Distribution of velocity

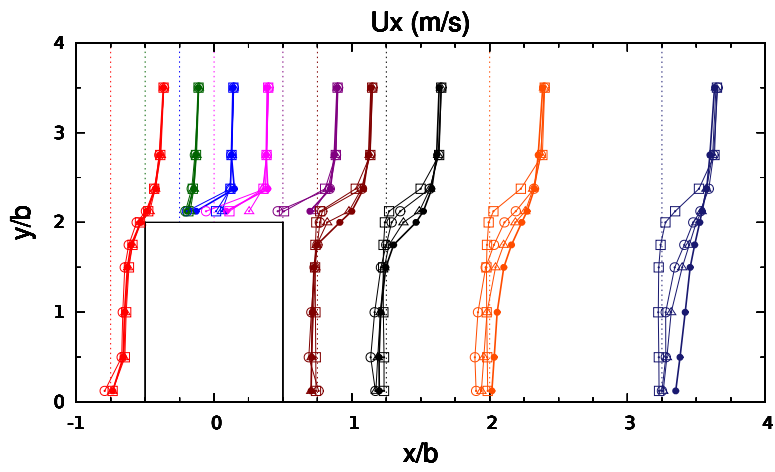
Figure 3.12 presents the distribution of the mean horizontal velocity ( $U_x$ ) on a vertical mid plane ( $y = 0$ ) and on two horizontal planes. One horizontal plane is near the ground ( $z = 0.125b$ ) and one part way up the building ( $z = 1.25b$ ). The positions of the measuring lines are illustrated with the dotted lines which also represent the origin for the calculated wind velocities i.e. positive values are plotted on the right side of the line, and negative values on the left side [Yoshie et al., 2007a].

In the wake region the standard  $k-\epsilon$  turbulence model results show best agreement with the experimental data, while the other models noticeably underestimate the horizontal velocities. Near the ground surface, the differences among the cases correspond to the difference in the reattachment length,  $X_F$ . In this region, the velocity in the reverse flow of the realizable  $k-\epsilon$  model shows larger negative values than the standard  $k-\epsilon$  and the  $k-\omega$  model.

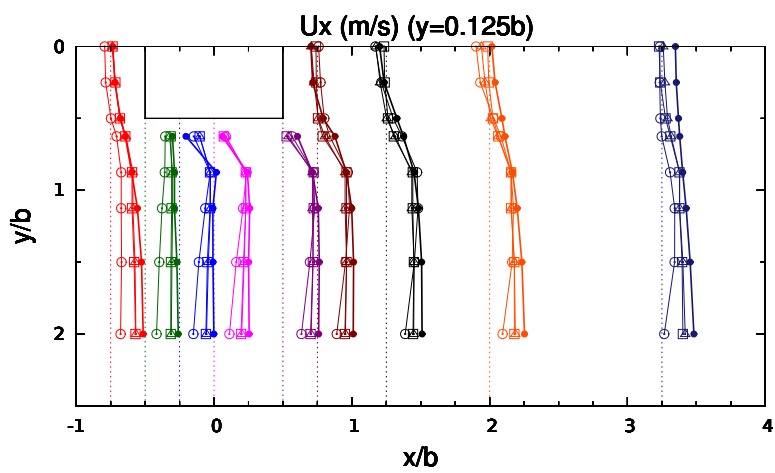
Above the roof, all models correspond well with the experimental values. However, the realizable  $k-\epsilon$  model, which reproduces the recirculation, is closer to the experimental data (Figure 3.13). The standard  $k-\epsilon$  model overestimates the horizontal velocity, thus, it does not show recirculation. The  $k-\omega$  model underestimates the streamwise component of velocity and explains why the reverse flow does not reattach to the roof. The differences among the velocity fields for the various turbulence models are closely associated to the computed turbulent energy, as discussed in the following section.

### 3.4.1.3 Distributions of turbulent kinetic energy

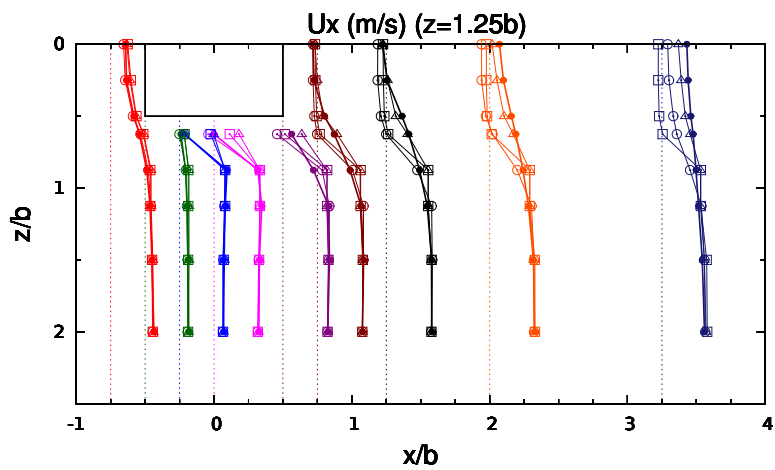
Figure 3.14(a) illustrates the vertical distribution of turbulent energy. The standard  $k-\epsilon$  model noticeably overestimates  $k$  at the upwind corner of the building



(a)



(b)



(c)

Wind Tunnel data	—●—	CFD, k- $\omega$ SST	—○—
CFD, Standard k- $\epsilon$	—△—	CFD, Realizable k- $\epsilon$	—□—

Figure 3.12: Wind velocity at (a) a vertical plane and (b,c) two horizontal planes

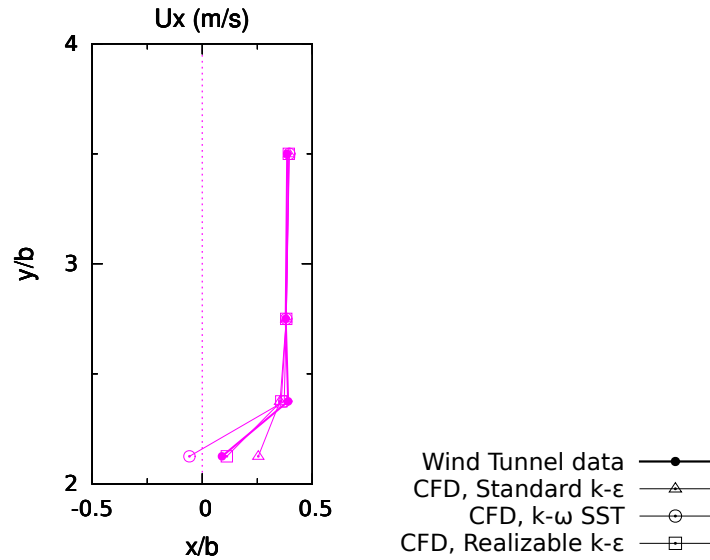
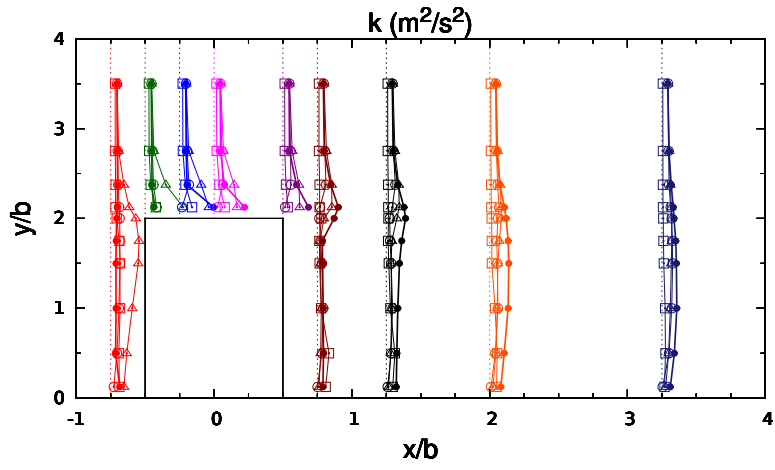


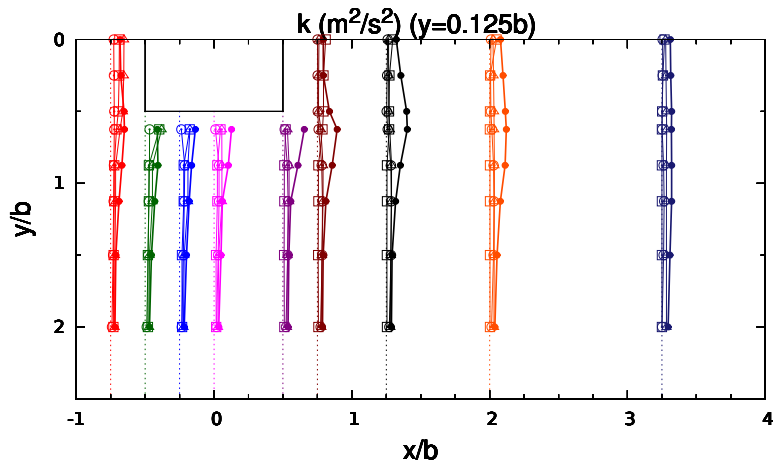
Figure 3.13: Wind velocity on a vertical plane above the roof.

(Figure 3.15(a)) as other researches have also observed [Murakami, 1993; Tominaga et al., 2008a; Tsuchiya et al., 1997]. This peak of  $k$  in front of the building explains why the reverse flow on the roof, which is observed in the experiment and the other models, is not reproduced in standard  $k$ - $\epsilon$  model. However, on the roof (Figure 3.15(b,c,d)) the standard  $k$ - $\epsilon$  model shows closer agreement with the experiment, while the realizable  $k$ - $\epsilon$  and the  $k$ - $\omega$  models underestimate  $k$  which makes the reverse flow on the roof rather large. Behind the building, as no velocity fluctuation due to vortex shedding is reproduced explicitly, the values of  $k$  are underestimated in all models, with those of standard  $k$ - $\epsilon$  model being closer to the wind tunnel data. This underestimation of  $k$  makes the reattachment lengths larger than in experiment, because the momentum diffusion in the lateral direction become small.

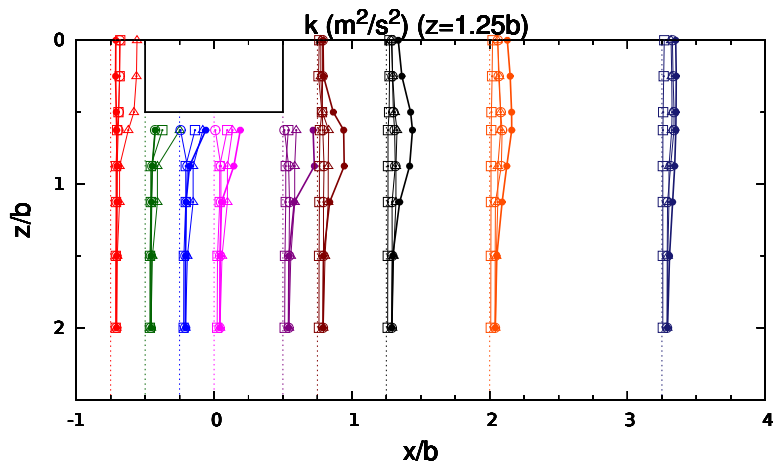
From the steady-state models compared here, the standard  $k$ - $\epsilon$  model reproduced the flowfield around the building quite well. However, it overestimates the reattachment length behind the building which seems to be related to the inability to reproduce the velocity fluctuation due to vortex shedding in the wake region. Thus, DES calculations have been conducted to illuminate the effect of the unsteady phenomena on reattachment length behind the building and the turbulent energy.



(a)



(b)



(c)

Wind Tunnel data	—●—	CFD, k- $\omega$ SST	—○—
CFD, Standard k- $\epsilon$	—△—	CFD, Realizable k- $\epsilon$	—□—

Figure 3.14: Turbulent energy in (a) a vertical plane and (b,c) two horizontal planes.

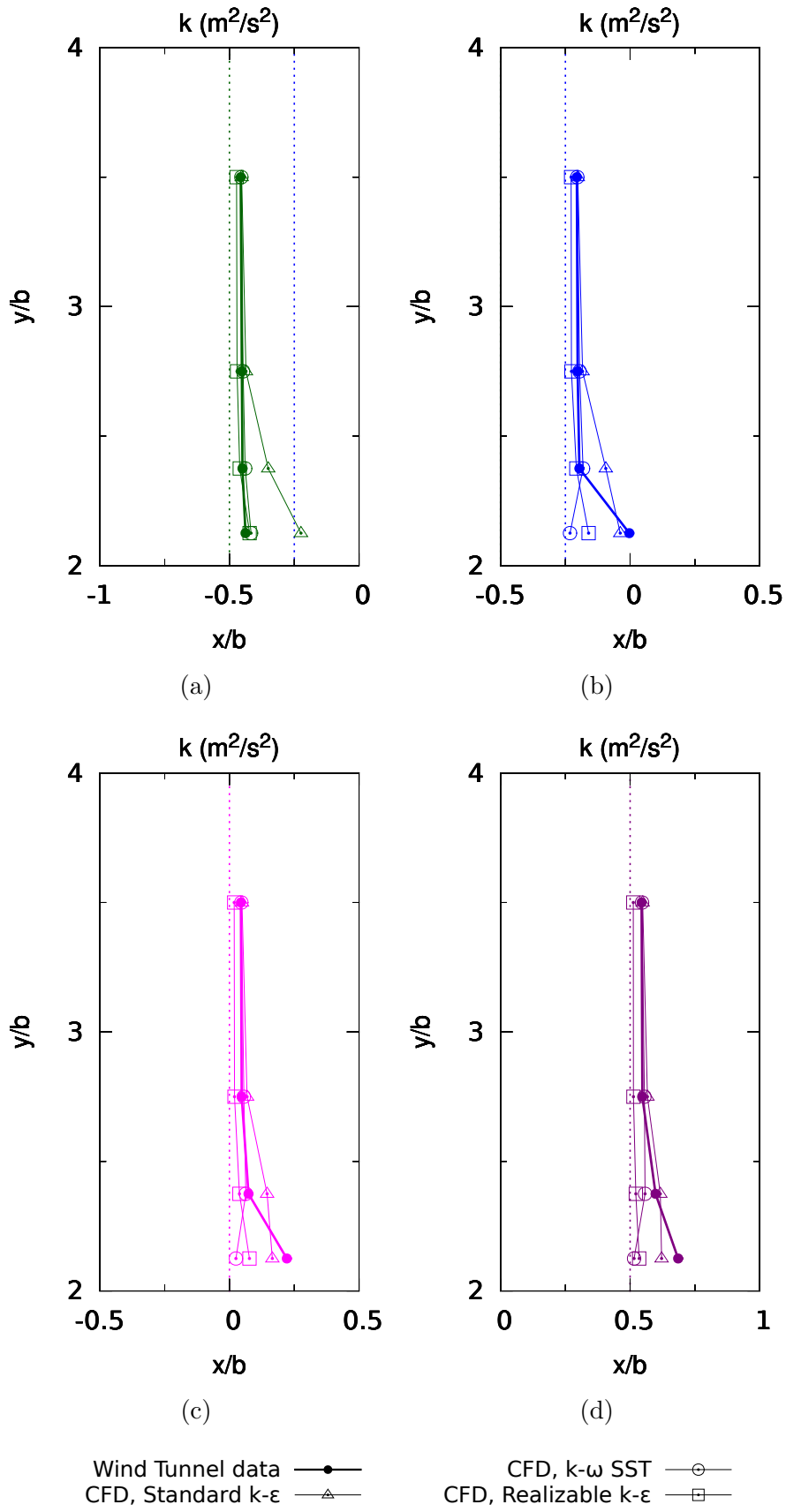


Figure 3.15: Turbulent energy above roof

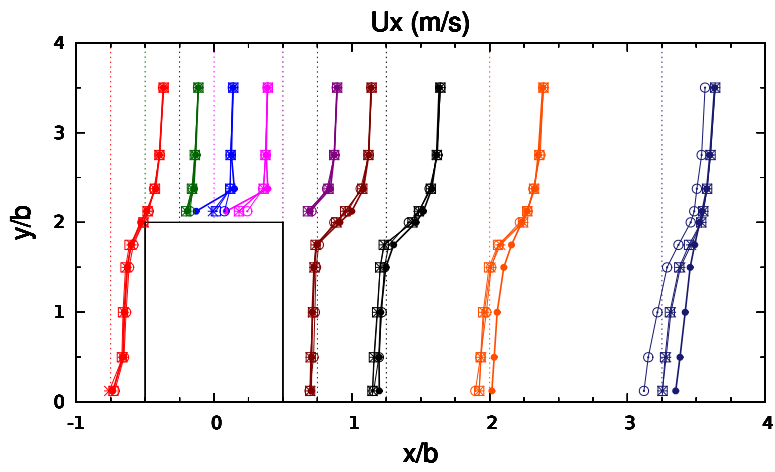


## 3.4.2 Comparison between DES and standard k- $\epsilon$ model

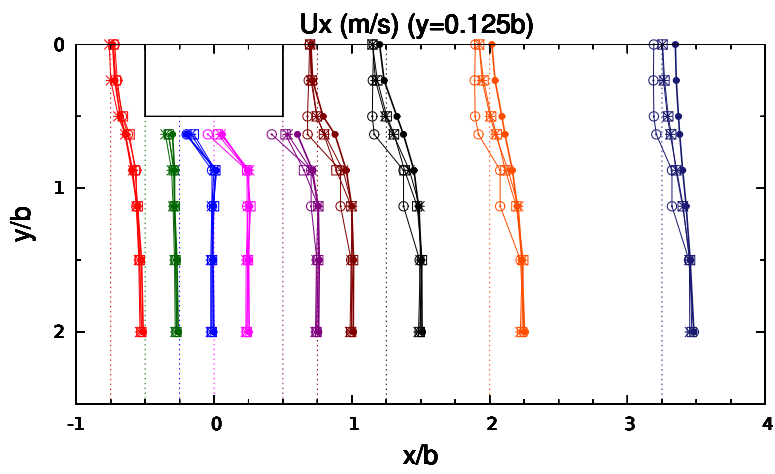
### 3.4.2.1 Mesh sensitivity study

Figure 3.16 presents the distribution of the mean horizontal velocity ( $\bar{U}_x$ ) on a vertical mid plane ( $y = 0$ ) and on two horizontal planes for the three progressively finer grids as well as the wind tunnel data. One horizontal plane is near the ground ( $z = 0.125b$ ) and one part way up the building ( $z = 1.25b$ ). The positions of the measuring lines are illustrated with the dotted lines which also represent the origin for the calculated wind velocities i.e. positive values are plotted on the right side of the line, and negative values on the left side [Yoshie et al., 2007a].

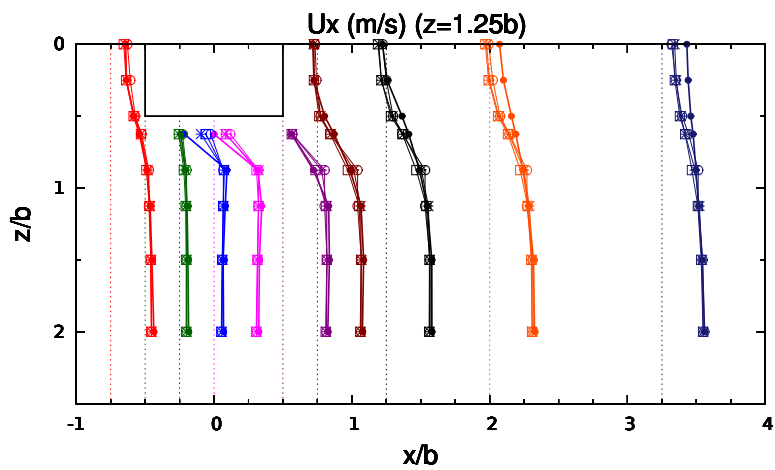
In general, the medium mesh gives similar results to the fine mesh and shows good agreement with the wind tunnel data. The velocity profiles predicted using the coarse mesh, although they maintain the same basic shape as the higher resolution DES runs, they vary significantly from them in the regions near the building surfaces and the edges of the wake. Moreover, the velocity field at the horizontal plane near the ground ( $z = 0.125b$ ) (Figure 3.17) shows that the flow patterns along the sides and in the wake of the building are not well reproduced by the coarse grid; the recirculation zone in the wake of the buildings is greatly overestimated and the backflow in the leeward side is poorly defined. Consequently, for a good match of the velocity field to the wind tunnel data, the coarse mesh is not adequate. However, the results obtained from the medium mesh are sufficient to provide a high fidelity solution since there was no improvement with the fine mesh resolution, and they were used in the following section for comparative studies and validation of the DES calculations.



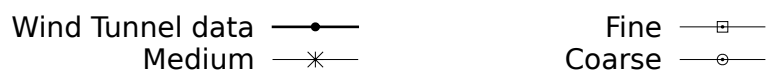
(a)



(b)



(c)



(d)

Figure 3.16: Wind velocity at (a) a vertical plane and (b,c) two horizontal planes.

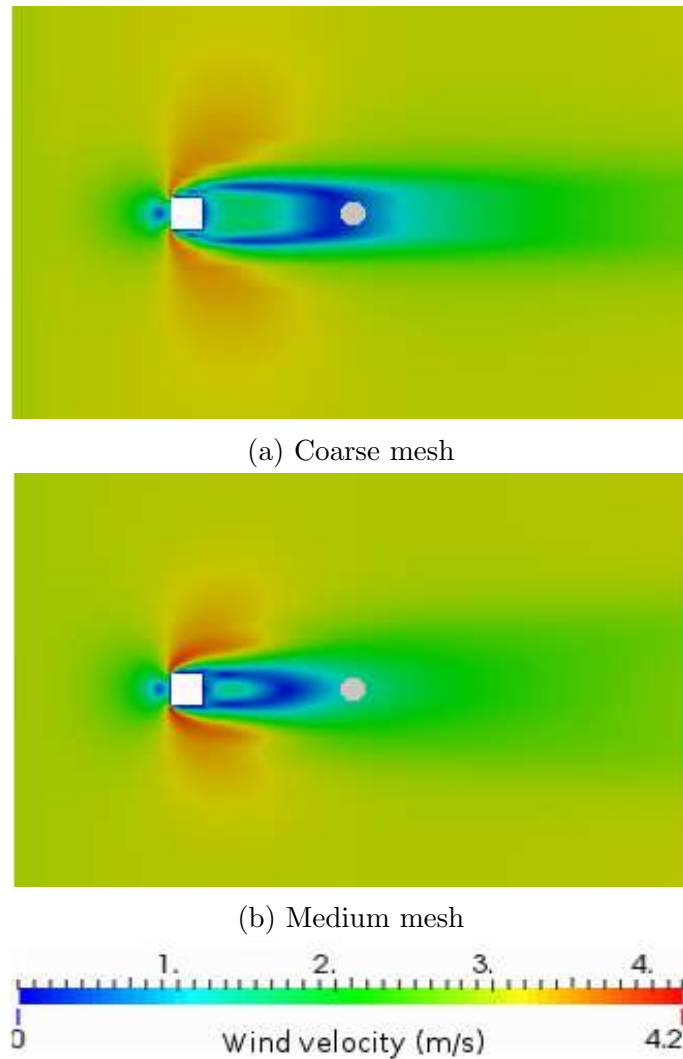


Figure 3.17: Mean horizontal velocity at an horizontal plane ( $z = 0.125b$ ) for (a) the coarse mesh and (b) the medium mesh.

### 3.4.2.2 Reattachment lengths

Table 3.5 presents the computed reattachment lengths on the roof ( $X_R$ ) and behind the building ( $X_F$ ) for DES calculations. The results of the standard  $k-\epsilon$  model, which shows the best agreement with the wind tunnel data, have also been included for comparison purposes. The DDES-SA calculations, similar to RANS results, show the flow attached over part of the the roof but no clear reversal of flow. However, the reattachment length for the DES model,  $X_R/b=0.44$ , is noticeably closest to the experimental value ( $=0.52$ ), than the reattachment length for the standard  $k-$

$\epsilon$  model ( $X_R/b=0.25$ ). This is further illustrated in Figure 3.18. As mentioned before, the reattachment length behind the building ( $X_F$ ) is overestimated in the standard  $k-\epsilon$  model. This inconsistency is improved in DES calculations, although the recirculation zone is still overestimated. The behaviour in the wake is further illustrated in Figure 3.19. This shows similar features in the standard  $k-\epsilon$  and DDES-SA flow near the reattachment point. However, there are further differences further downstream as the flow returns towards its undisturbed condition —unfortunately no wind tunnel measurements are available for this region. Visualisation of the instantaneous velocities calculated with the DDES-SA model have given some insight into the behaviour in the wake region. It appears that there are periods in the vortex shedding cycle where the wake is extended and the reattachment point is very mobile ( $X_F/b$  from 1.1 to 2.6). The aspect ratio of the building means that the eddy structures generated by the vertical leading edges dominate those generated at the leading edge of the roof. The largest eddy structures flowing from the roof are transported over the eddy structures near the ground at the leeward side of the building. The flow in the wake region accordingly seems more complex, with stronger mixing, than flows over cubes. This has also been pointed out by Tominaga et al. [2004].

CFD model	Turbulence model	$X_R/b$	$X_F/b$
DES	SA	0.44	2.37
RANS	$k-\epsilon$ (standard)	0.25	2.68
	Experiment	0.52	1.42

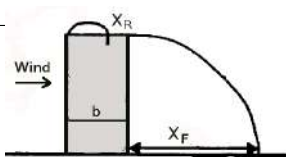


Table 3.5: Reattachment lengths by DES.

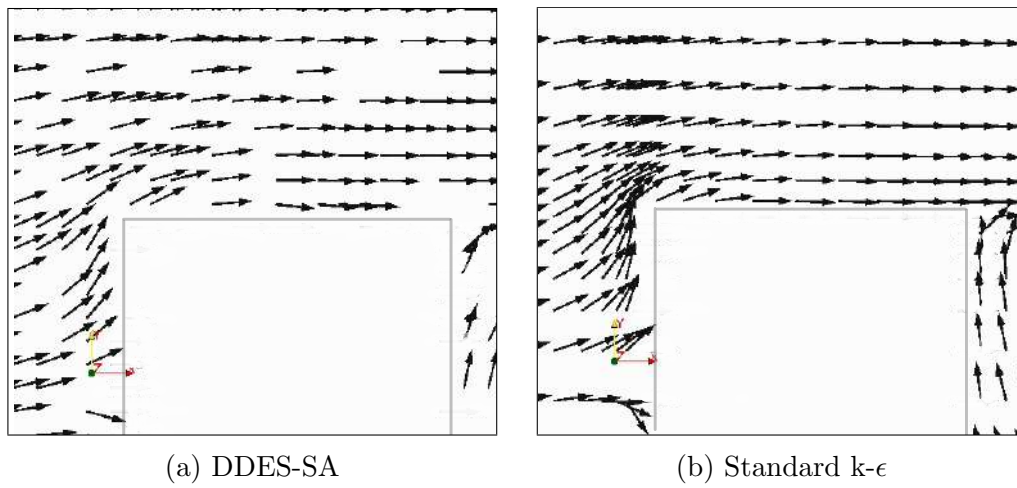


Figure 3.18: Vertical distribution of velocity vectors around the roof for (a) the DDES-SA model and (b) the standard  $k-\epsilon$  model.

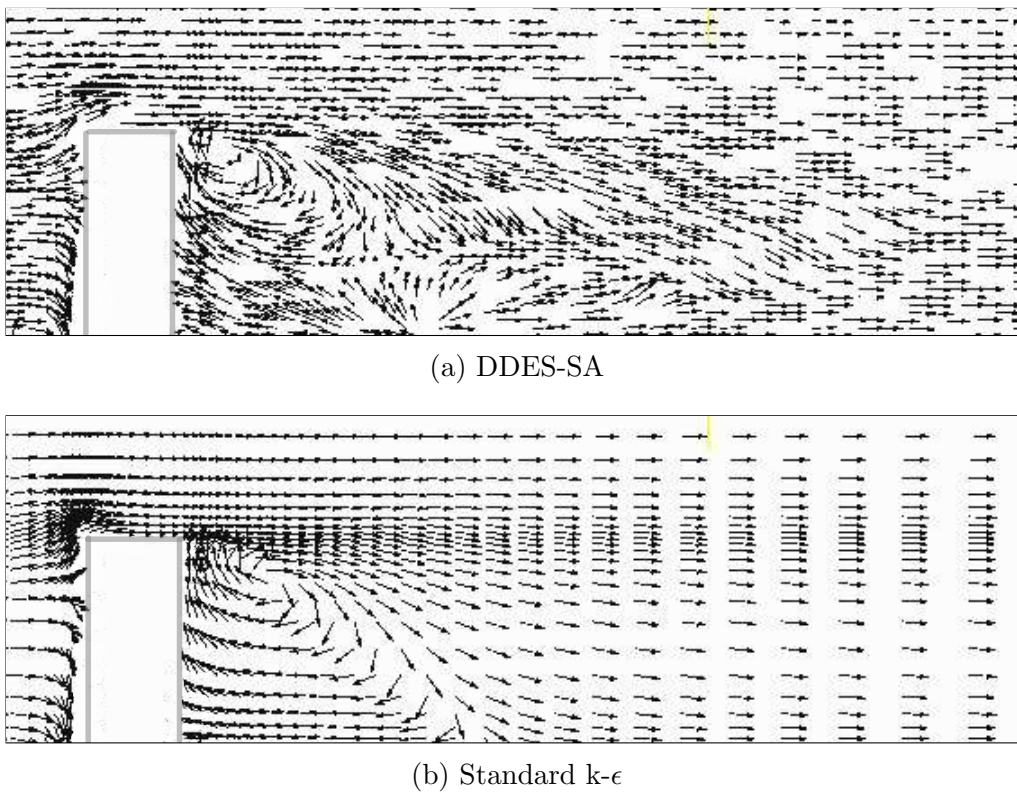


Figure 3.19: Vertical distribution of velocity vectors in the wake for (a) the DDES-SA model and (b) the standard  $k-\epsilon$  model.

### 3.4.2.3 Distribution of time-averaged velocity

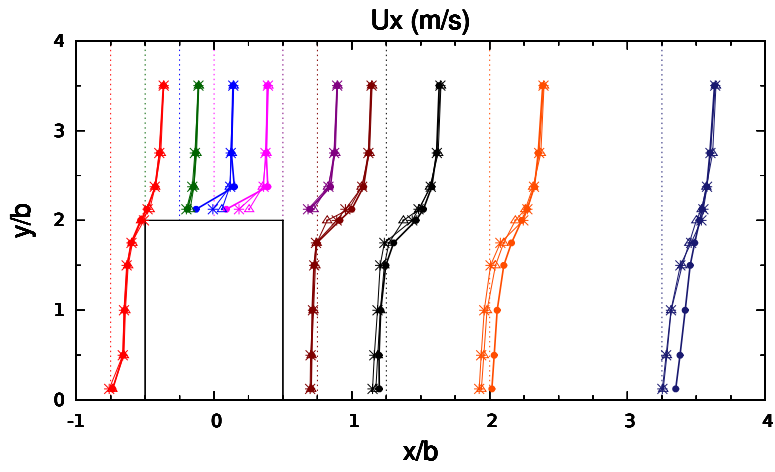
In general, where the mean velocities are compared at the measurement points (Figure 3.20) there is good correspondence between the CFD results (both DDES-SA and standard  $k-\epsilon$  model) and the wind tunnel data. The main differences in these velocity profiles are found near the building surfaces i.e. at locations of higher velocity gradient or rate of shear. Figure 3.21 shows the mean velocities above the roof(a,b) and at the sides on an horizontal plane part way up the building. Both the models overestimate the velocities, however the DDES-SA calculations are closer to the experimental values. This overestimation of  $U_x$  explains the underestimation of the reattachment length on the roof.

## 3.4.3 Conclusions for Test Case A

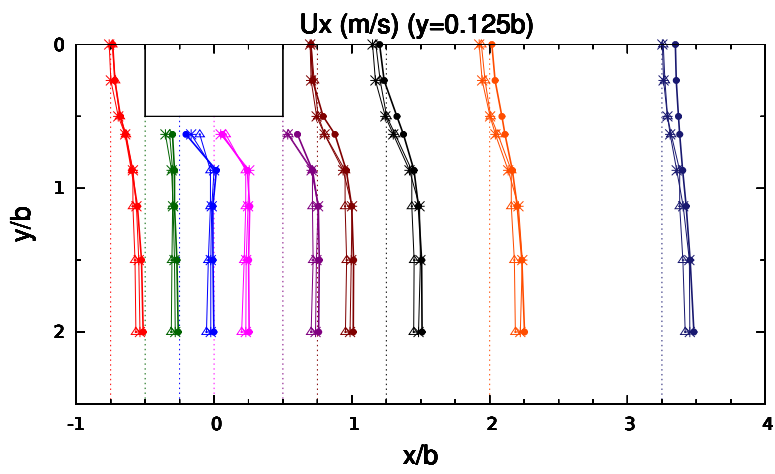
The standard  $k-\epsilon$  model could not reproduce the reverse flow on the roof. In particular, it shows the flow attached over part of the roof, but there is no reversal flow. This weakness does not appear in the realizable  $k-\epsilon$  model, however, it greatly overestimates the rear reattachment length in comparison with the standard  $k-\epsilon$  model. The  $k-\omega$  model predicts the reverse flow on the roof, but due to the large separated region, it does not reattach over the length of the roof. It shows similar features to  $k-\epsilon$  model near the reattachment point, but there are significant differences on the flowfield in the wake, with the standard  $k-\epsilon$  model being closer to the experimental results.

Summarising, for the flowfield regarded in this cross comparison, the standard  $k-\epsilon$  model showed the closest agreement with the experiment among the RANS models compared here.

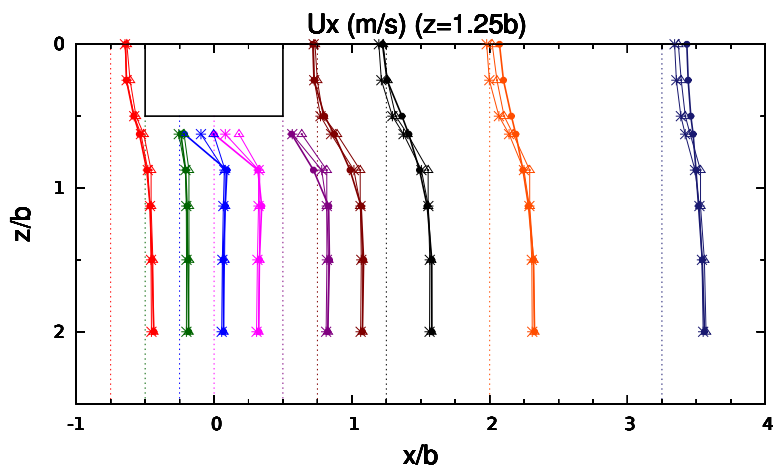
The overestimation of the rear reattachment length in standard  $k-\epsilon$  model was improved in the DDES-SA computations. This improvement is related to the repro-



(a)



(b)



(c)



Figure 3.20: Wind velocity at (a) a vertical plane and (b,c) two horizontal planes.

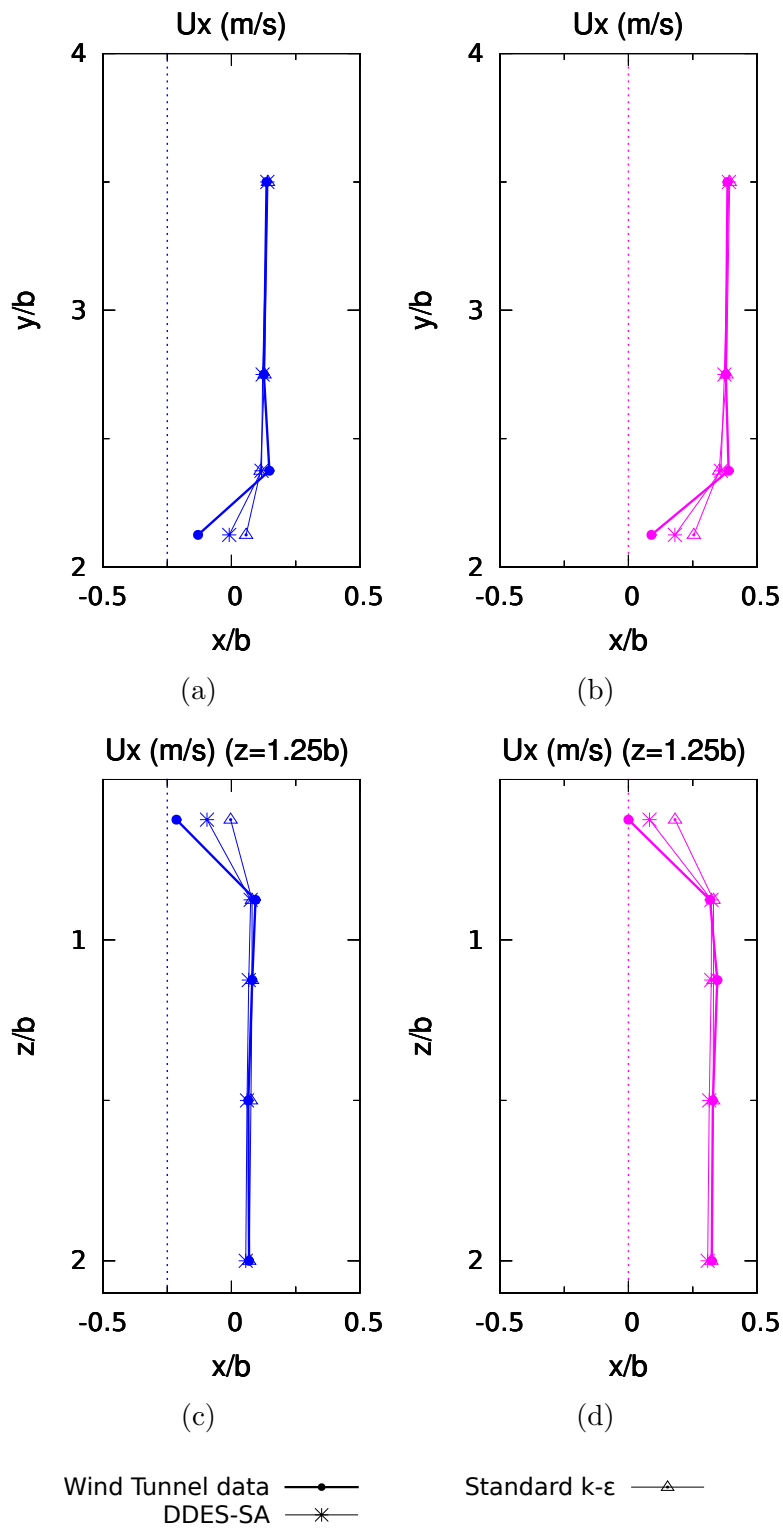


Figure 3.21: Wind velocity (a,b) above roof and (b,c) at the side on an horizontal plane part way up the building.



duction of the vortex shedding motion behind the building, which is reproduced in DDES-SA. Although both the models could not reproduce the reverse flow on the roof, the reattachment length for the DDES-SA model is noticeably closer to the experimental value compared to the predictions of the standard  $k-\epsilon$  model.

Generally, the results of the DDES-SA showed good agreement with the wind tunnel data in terms of the distributions of mean velocity and predicted reattachment lengths on the roof and in the wake. As this work has been carried out in the context of study and development of CFD based methods for wind energy assessment in complex urban environments, it comments on modelling of velocity distribution rather than evaluation of surface pressures and forces or dispersion of contaminants. The ability to deal satisfactorily with wake regions is particularly important in the context of wind energy production near groups of buildings.

The relation between the rear reattachment lengths and the reproduction of the vortex shedding motion should be investigated further. As pointed out by [Tominaga et al. \[2008a\]](#), the larger the velocity fluctuation behind the building, the larger the momentum diffusion in the lateral direction, the smaller the reverse flow due to such large diffusivity. Therefore, the influence of the vortex shedding cycle on the reattachment length and the mobility of the reattachment length in the vortex shedding cycle gives a starting point to a future study for potential improvement of the prediction capabilities of the DDES-SA model.

## 3.5 Results - Test Case B

To compare the CFD results with the field measurements the computational wind speed has been normalised by the wind speed at reference point D (the top of the Shinjuku Mitsui Building) at a height of 237 m for the wind directions NE-N-NW and point C (the top of the KDD Building) at 187 m height (Figure 3.7) for the

other wind directions as in previous studies [Yoshie et al., 2007a].

### 3.5.1 Mesh sensitivity study

Figure 3.22 presents the calculated DDES-SA wind speed ratios for the three progressively finer grids alongside the field measurements, at the measuring points for the West wind direction. The coarse mesh underestimates the wind velocity at most of the measuring points and most of the results fall outside but close to one standard deviation of the field measurements. The medium mesh shows significant improvement over the coarse mesh results and in 8 of the total 15 comparisons, results fall within one standard deviation, 6 lie close to this band and only one fall significantly out of one standard deviation. The fine mesh provide very similar results to medium mesh, hence the medium grid resolution is sufficient to provide a reliable solution.

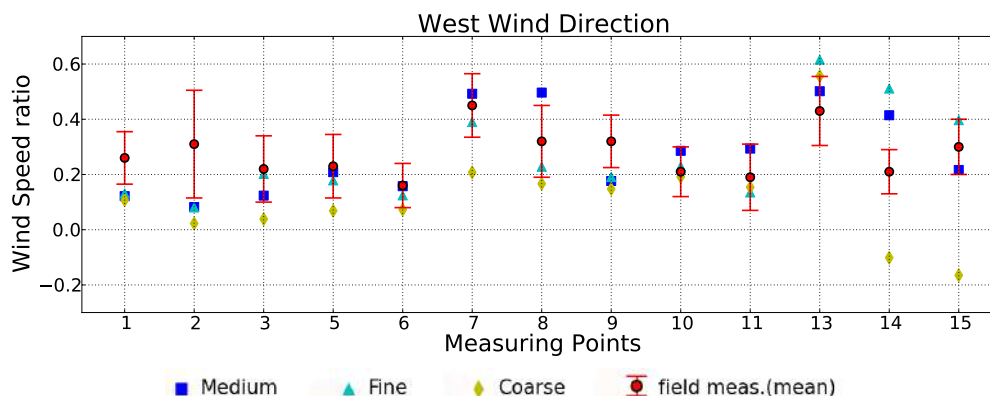


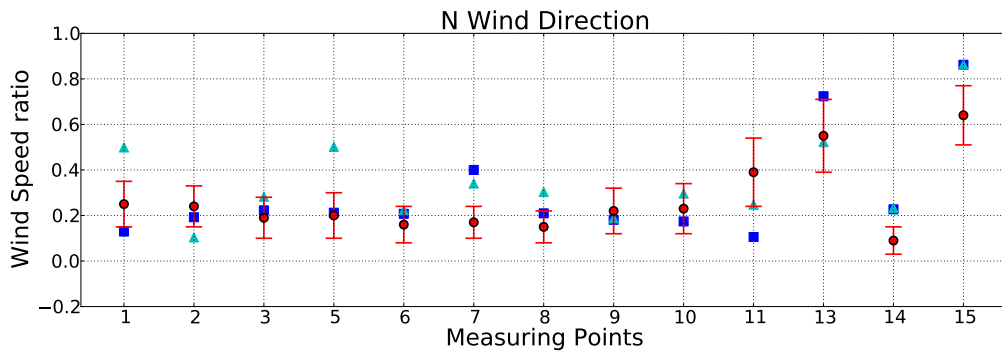
Figure 3.22: Comparison of predicted wind speed ratios for various mesh resolutions at the reference measuring points for the West wind direction.

### 3.5.2 Distribution of velocity

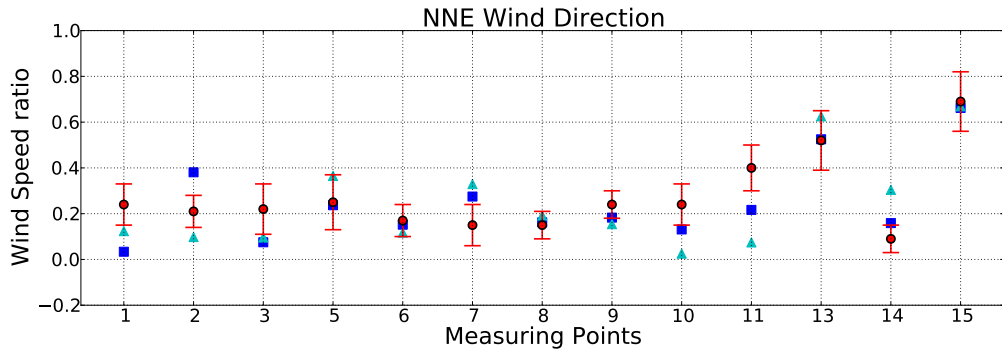
Figure 3.23 present the calculated wind speed ratios alongside the field measurements and the wind tunnel data (where available), at the measuring points for sixteen wind directions (north, north-northeast, northeast, east-northeast, east,

east-southeast, southeast, south-southeast, south, south-southwest, southwest, west-southwest, west, west-northwest, northwest, north-northwest). Only the measuring points where complete experimental data is available have been included. In 131 of the total of 208 comparisons, results for the DDES-SA model fall within one standard deviation (sd) of the field measurements and only 25 fall significantly outside this band. The RANS results fall within the one standard deviation band in 102 out of a total of 208 tests and 50 are significantly outside. In support of the above results, calculations of the Mean Absolute Error (MAE)(Appendix D) highlight also the improved performance of the DDES (MAE=0.10) over the RANS calculations (MAE=0.14) with its MAE being close to the mean standard deviation value (=0.10).

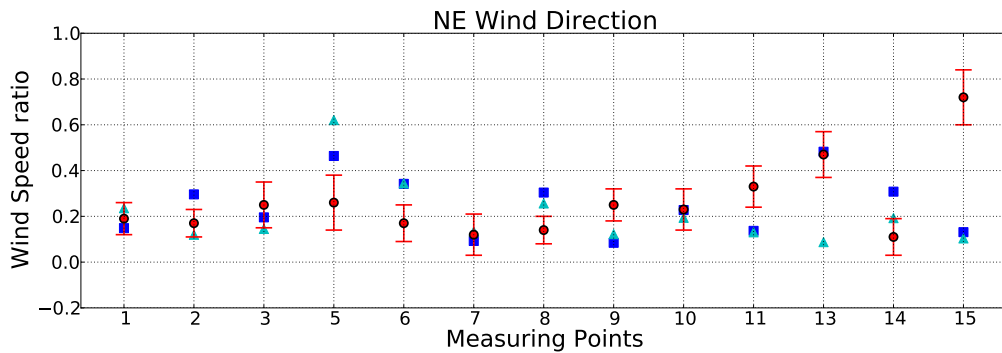
The superior performance of the DDES-SA model is also demonstrated in Figure 3.24, where the results are compared with the RANS results for other CFD codes published by a working group of the Architectural Institute of Japan [Tom-inaga et al., 2004]. Table 3.6 shows the statistics for all the models; in 6 out of a total of 10 comparisons, results for the DDES-SA model fall within one standard deviation of the field measurements and only 1 falls significantly outside this band. Although the standard k- $\epsilon$  model results fall within one standard deviation in 5 out of 10, showing the second better performance after DDES-SA calculations in terms of this feature, the corresponding MAE is the largest one, as the remaining 5 measurements are noticeably out of one standard deviation. The RANS CFD codes applied by a working group of the Architectural Institute of Japan have considerably lower performance than the DDES-SA in all the compared features.



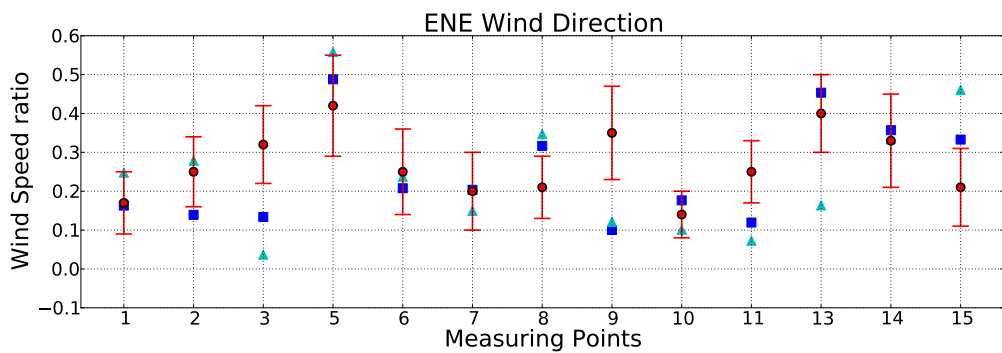
(a)



(b)



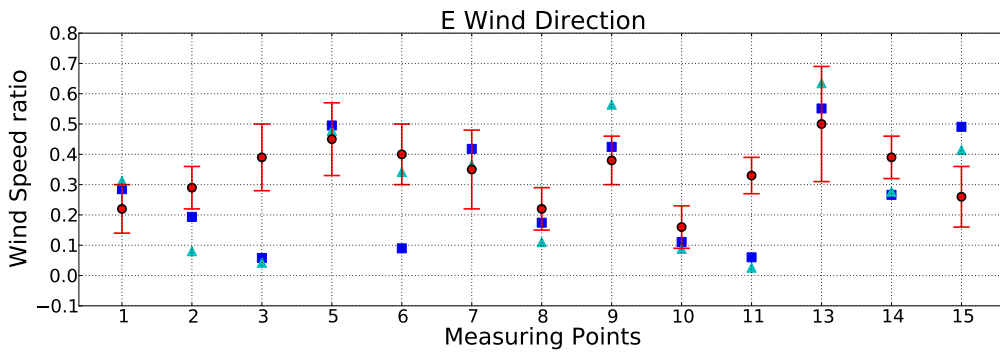
(c)



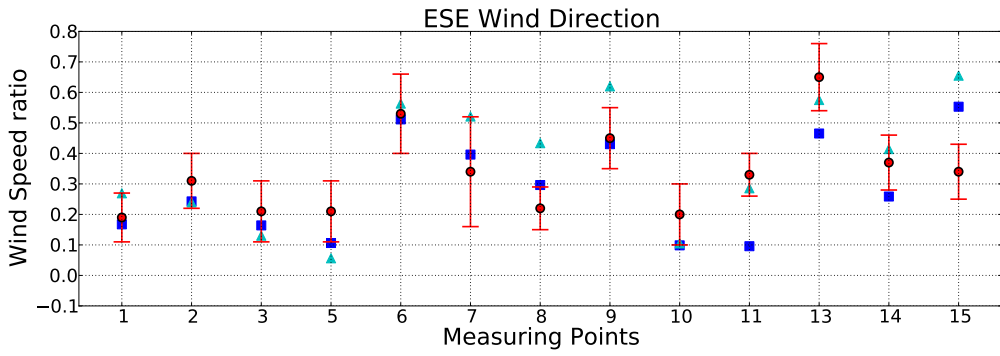
(d)

■ DDES    ▲ RANS    ● field meas.(mean)

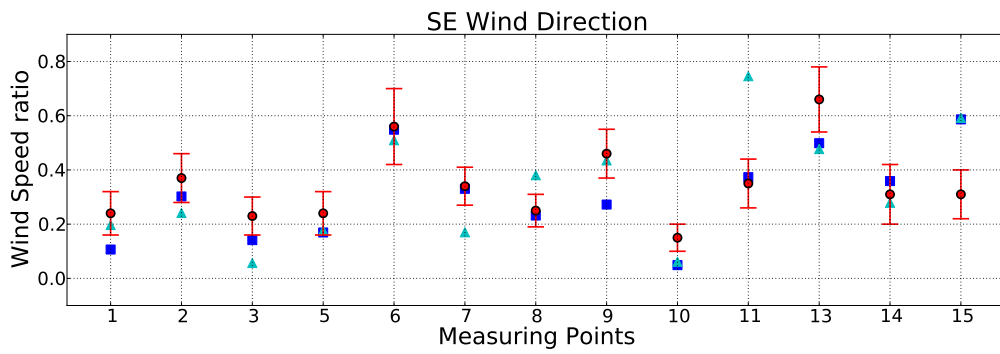
Figure 3.23: Comparison of predicted and measured wind speed ratios at the reference measuring points.



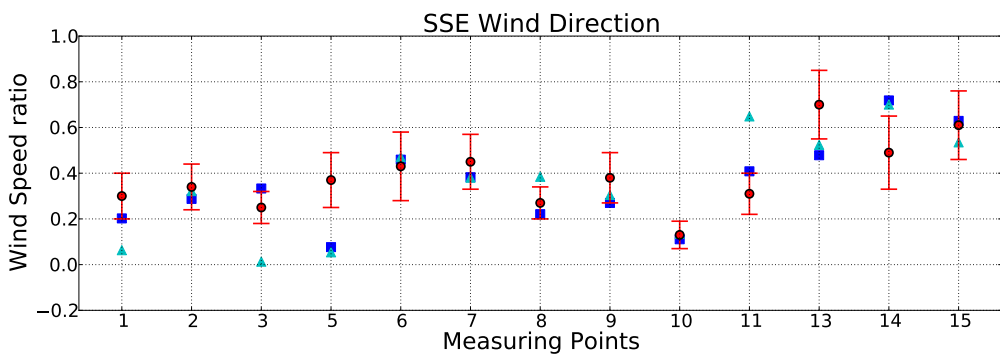
(e)



(f)



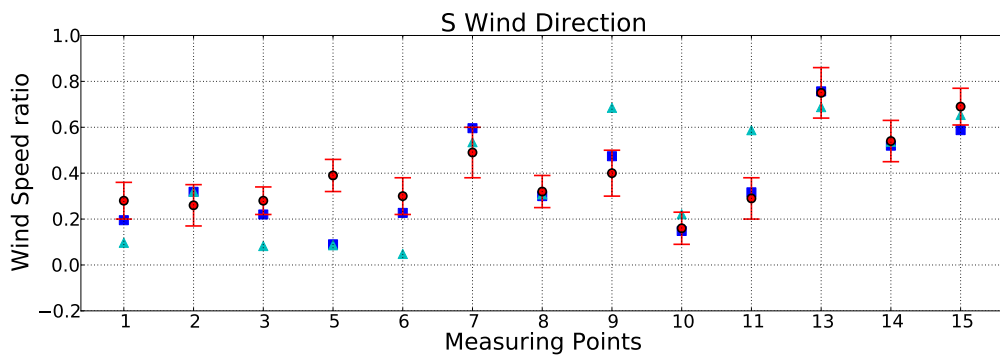
(g)



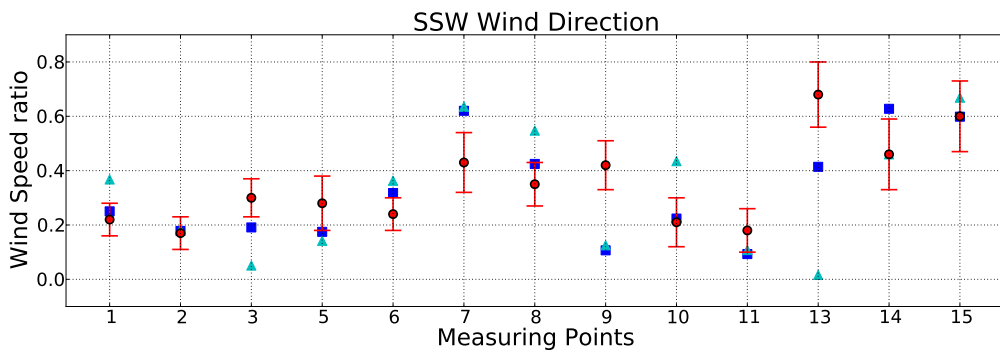
(h)

■ DDES    ▲ RANS    ● field meas.(mean)

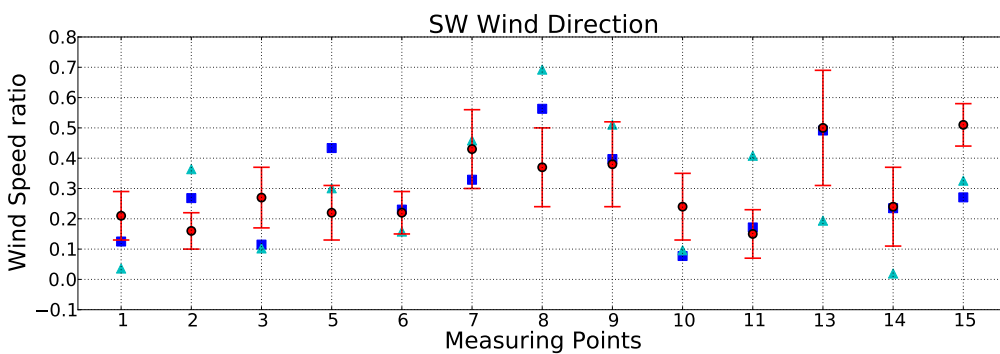
Figure 3.23: Comparison of predicted and measured wind speed ratios at the reference measuring points.



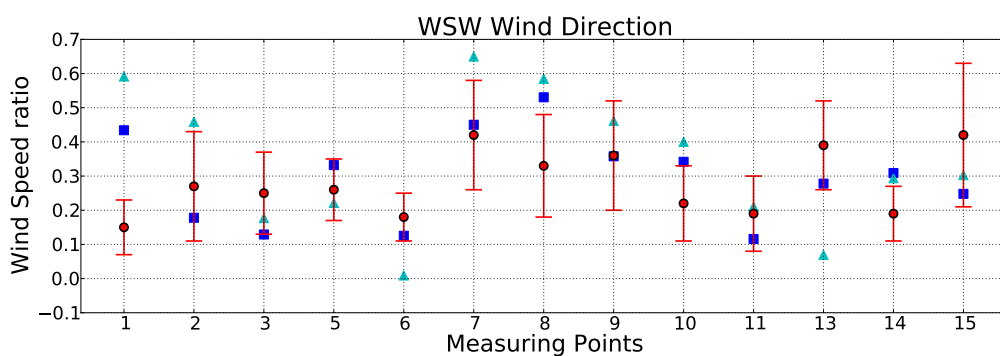
(i)



(j)



(k)



(l)

■ DDES    ▲ RANS    ● field meas. (mean)

Figure 3.23: Comparison of predicted and measured wind speed ratios at the reference measuring points.

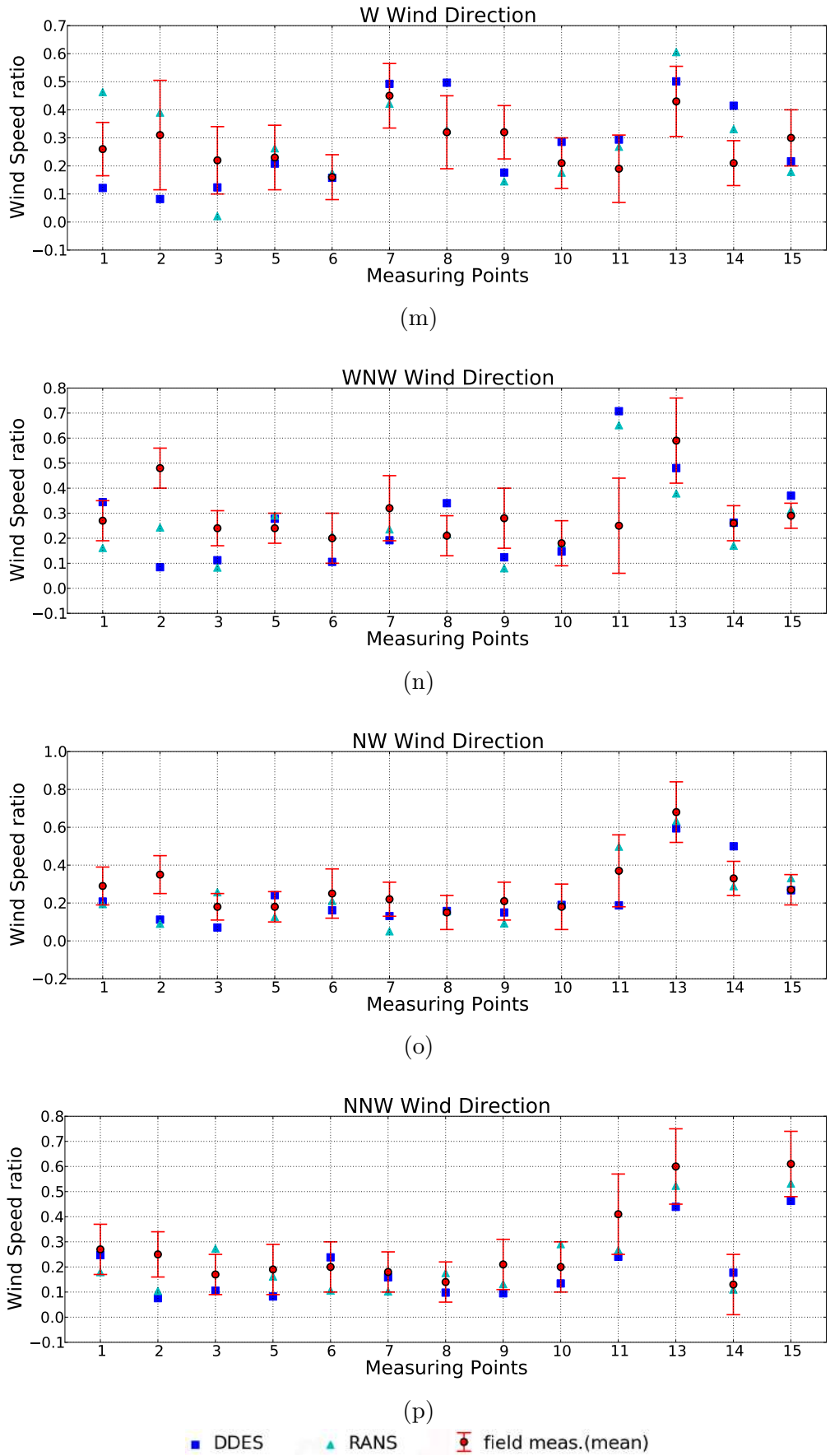


Figure 3.23: Comparison of predicted and measured wind speed ratios at the reference measuring points.

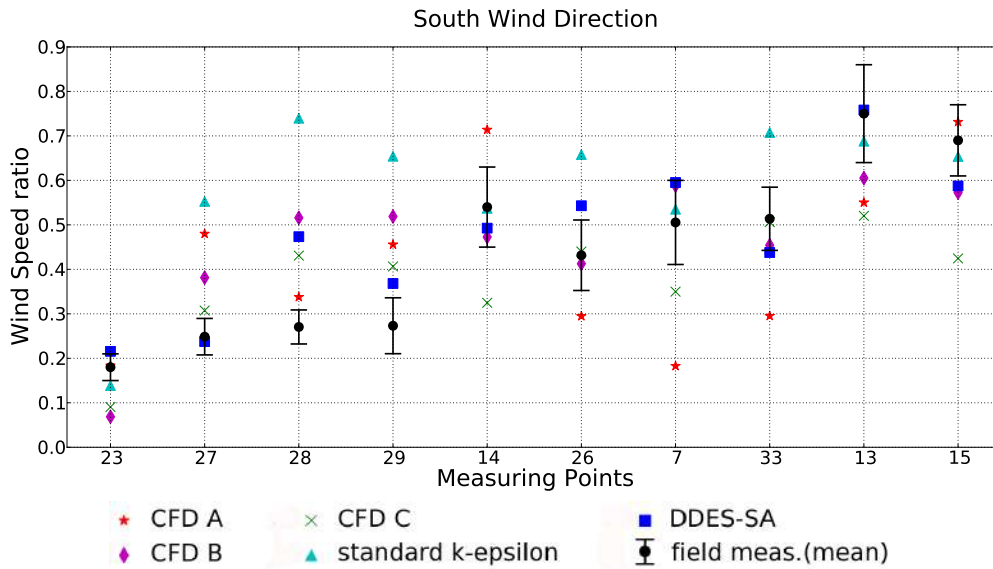


Figure 3.24: Comparison of wind speed ratio at reference measuring points with wind direction South.

CFD code	fall within 1 s.d.	significantly outside 1 s.d.	MAE
DDES-SA	6	1	0.08
standard k- $\epsilon$	5	5	0.17
CFD A	2	4	0.16
CFD B	4	3	0.12
CFD C	2	4	0.13

Table 3.6: Statistics for various CFD codes.

A qualitative review of the results (Figure 3.25) shows that the complex flow patterns of the interaction between the wind flow and building is well reproduced by the DDES-SA calculations (Figure 3.25 left), including such details as the horse-shoe vortex shape (h1, h2 and h3 regions) and the reattachment zones behind the buildings (r1, r2 and r3 regions). In the RANS results (Figure 3.25 right) these vortices are not as well defined and the size of the recirculation zone in the wake of



the buildings is overestimated.

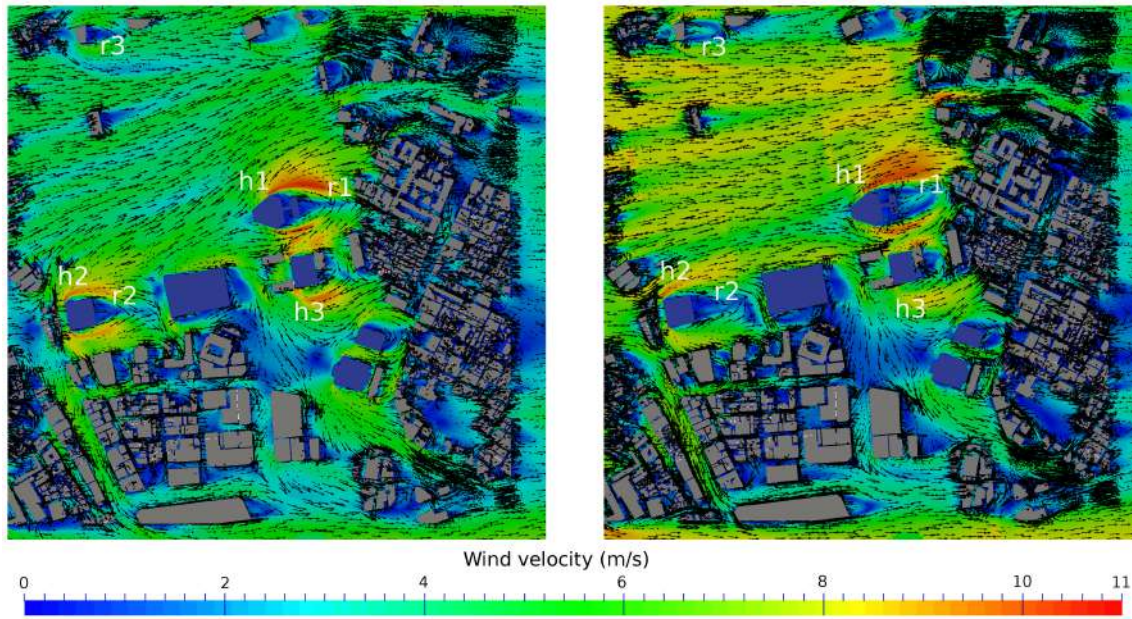


Figure 3.25: Vectors of the wind velocity at a plane 10 m above the ground for the DDES-SA model (left) and the standard  $k-\epsilon$  model (right).

## 3.6 Conclusions

The prediction capabilities of numerical models implemented using the OpenFOAM CFD library were investigated, revisiting two test cases developed by the Architectural Institute of Japan that provide benchmark data derived from wind tunnel testing and field measurements. The performance of both steady-state RANS approaches with some eddy-viscosity turbulence models as well as a hybrid RANS/LES approach with the Delayed Detached Eddy Simulation-Spalart Almaras (DDES-SA) turbulence model were examined. The test cases represent an idealized building with 2:1:1 aspect ratios and a real urban geometry with considerable geometric complexity. The tests have examined mean velocity predictions and boundary layer reattachment lengths. Calculations of wind flows around buildings using RANS approaches and two-equation turbulence models are known to have limitations, particularly in calculating conditions in wake regions. It was found this to be the case with the

models of this type which evaluated using OpenFOAM and that predictions were comparable with what has been published in earlier studies for these types of model. Results from applying DES approaches to these test cases have not been published before. The results obtained with the DDES-SA model have been noticeably better than those from the RANS models, particularly in wake regions, where LES is the mode of calculation. Consequently, this approach, although significantly more computationally demanding than RANS calculations, offers improved robustness and accuracy over a range of wind conditions. Accordingly, in the further study of wind flows at the De Montfort university campus, DES approaches using OpenFOAM are applied and further comparisons with high frequency anemometer data are made. This is discussed in the next chapter (Chapter 4).



# Chapter 4

## De Montfort university CFD model

### 4.1 Introduction - Chapter overview

In this chapter the DES approach is implemented to examine the flow at De Montfort university campus in Leicester, U.K., a real complex urban environment which includes a variation in buildings' height and geometry. The validity of DES implementation is tested using high frequency wind data recorded by three 3D ultrasonic anemometers installed at three disperse positions of various heights. Since this work has been carried out in the context of study and development of CFD based methods for wind energy assessment in complex urban environments for micro wind turbine applications, the pedestrian wind around buildings is not of importance and only the wind speeds above roof heights are studied. In addition, this work comments on modelling of wake conditions rather than evaluation of surface pressures and forces or dispersion of contaminants. The development of the CFD model and the computational parameters are explicitly reported.

## 4.2 Description of the DMU campus and surroundings

The De Montfort university campus is located near the centre of the city of Leicester in the U.K. (Figure 4.1). The area of the campus and surrounding buildings is shown in Figure 4.2. Figures 4.3 and 4.4 show the model geometry, indicating the average building heights and the abbreviated building names. The case is of particular interest as it has a complex geometry with large variation in building heights. The explicitly modelled buildings are the buildings at De Montfort university campus and the surrounding buildings in a radius of about 300 m around the campus, in agreement with the best practise guidelines [Franke et al., 2011].

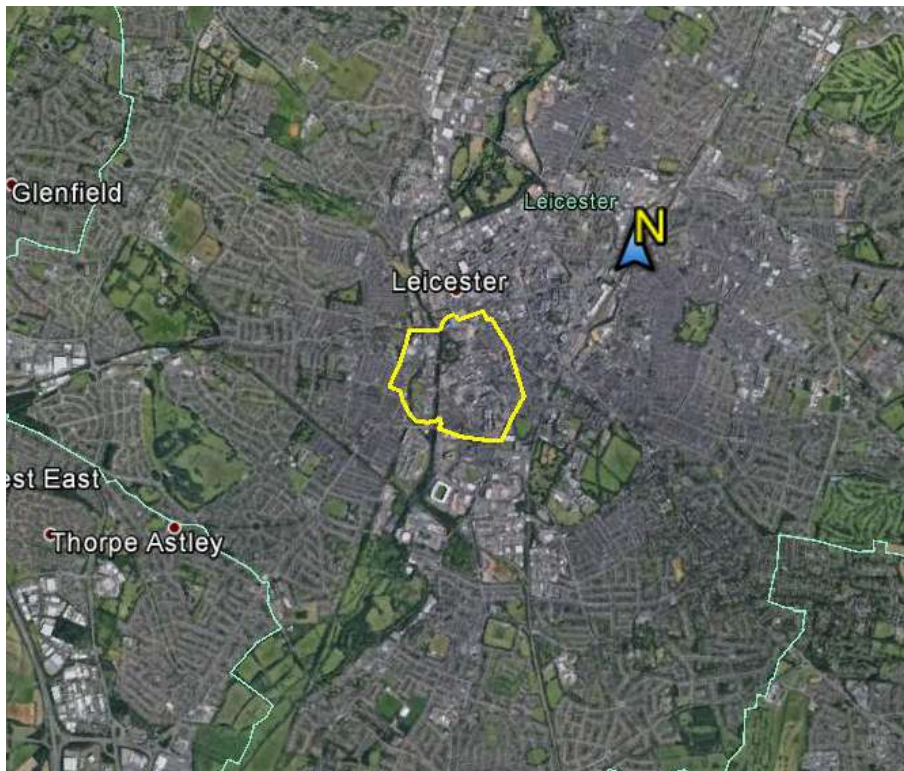


Figure 4.1: Position of the De Montfort university campus in Leicester city (yellow line).



(a)



(b)

Figure 4.2: The area of the De Montfort university campus (red line) and surrounding buildings (yellow line).

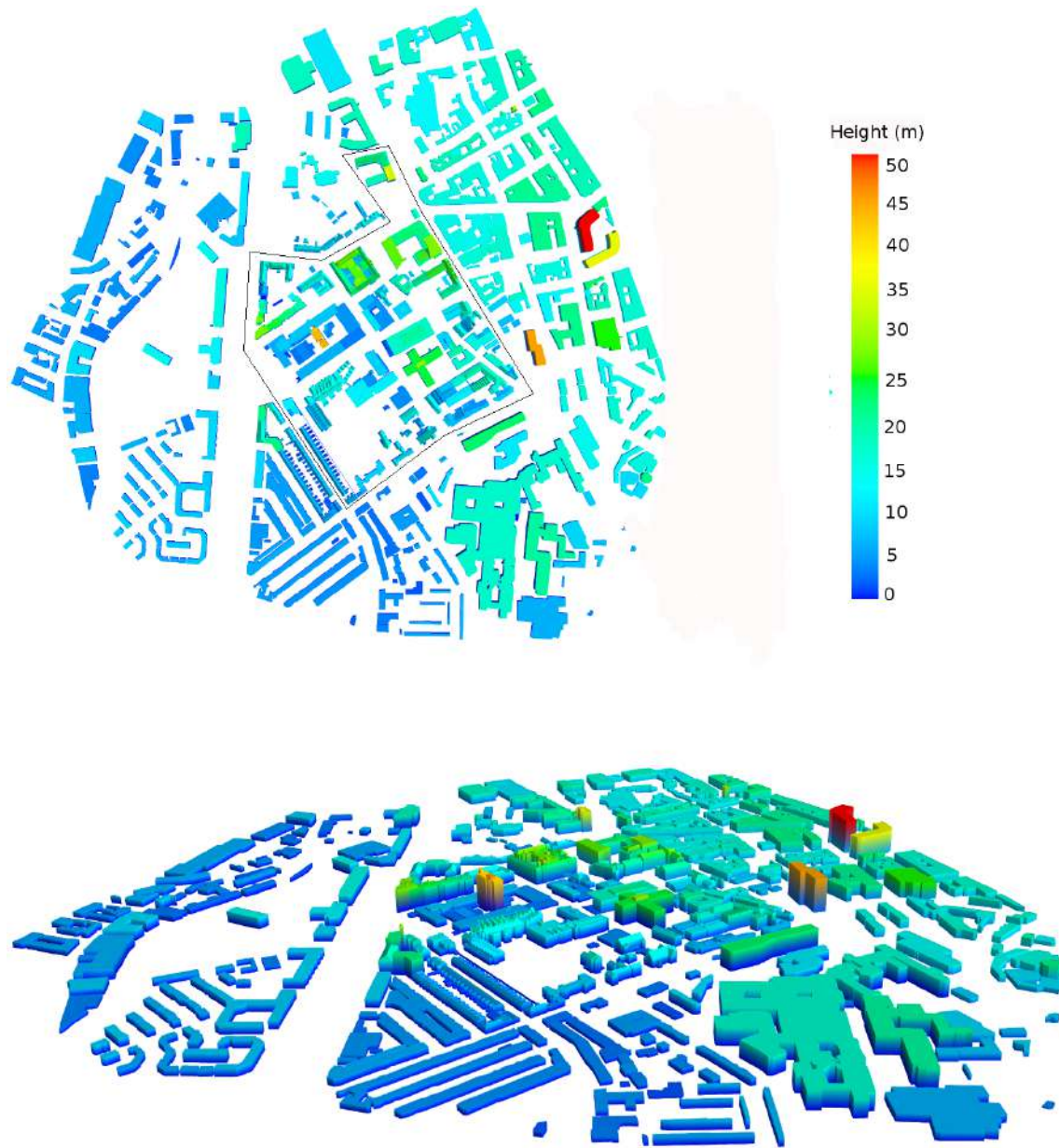


Figure 4.3: De Montfort university campus and the surrounding buildings indicating the average building heights.

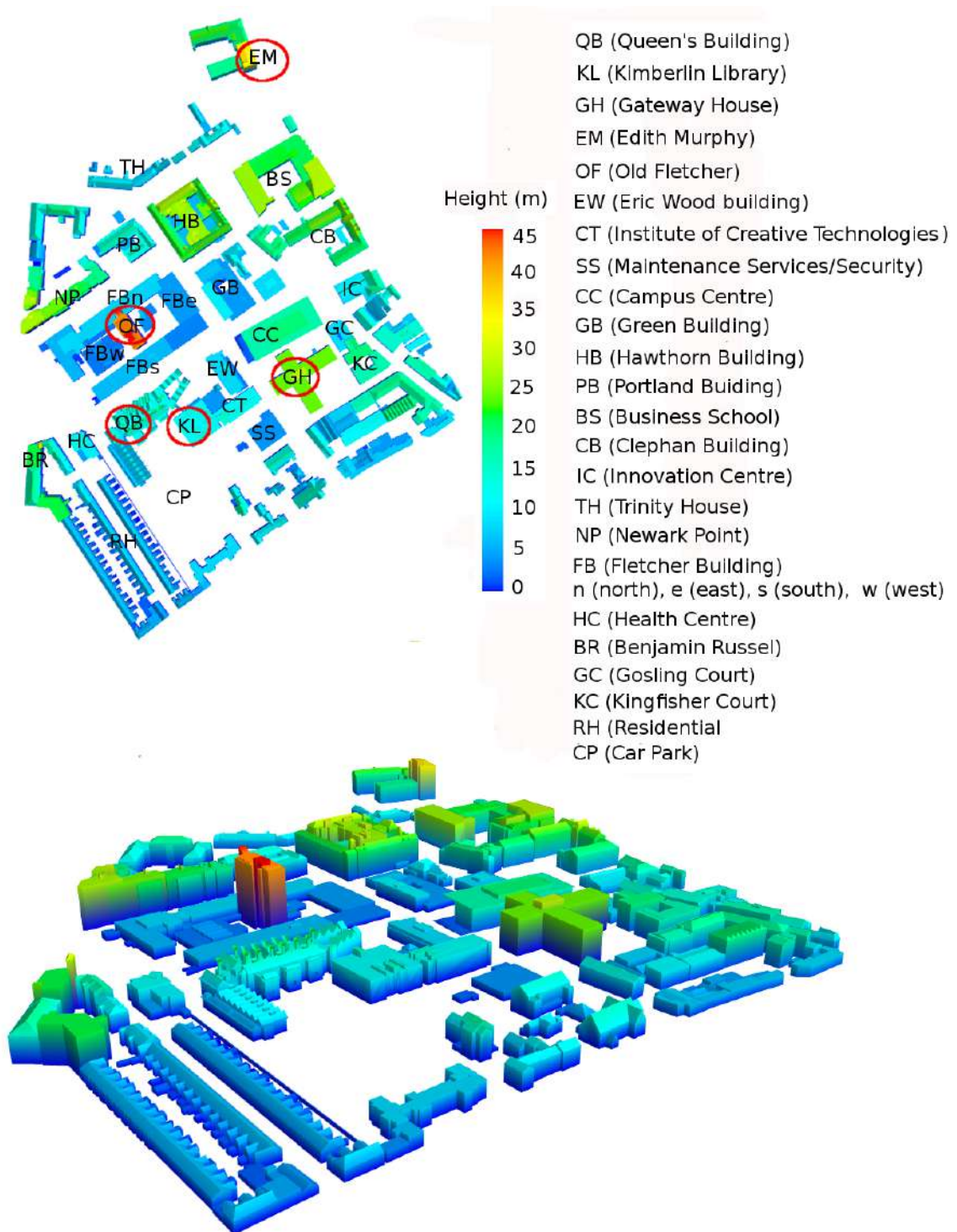


Figure 4.4: De Montfort university campus indicating the abbreviated building names and the average building heights.

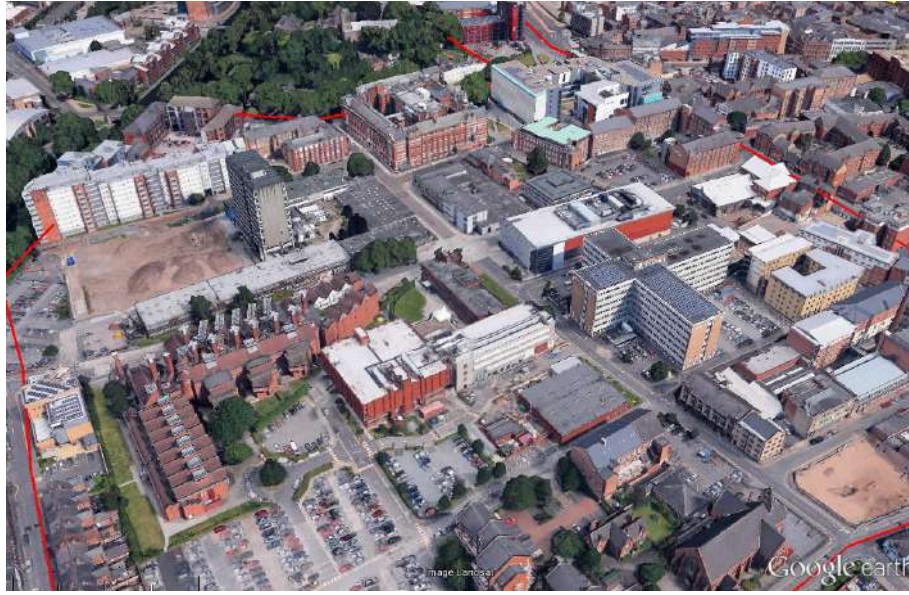


The university campus has been modelled in significant detail, including the exact geometry of building footprints, the roofs, the wind-catchers (Queens building) etc (Figure 4.5), while the surrounding buildings are modelled in simpler form with flat roof surfaces (Figure 4.6) [Franke et al., 2011]. The relatively few trees or other vegetation have not been included in the model. Inside the campus there are a few high-rise buildings as indicated in Figure 4.4, however the highest building in the model is located outside the campus at the edge of the building area, which is 50.1 m high. In the immediate outer area, there is a variation in buildings type, ranging from 2 storey residential buildings to high-rise and medium-rise buildings (Figure 4.7), but further away the terrain is more homogeneous, including mostly cultivated areas with low crops and scattered areas of low residential houses of 1 or 2 storeys, light industrial buildings and clumps of forest as indicated in Figure 4.8.

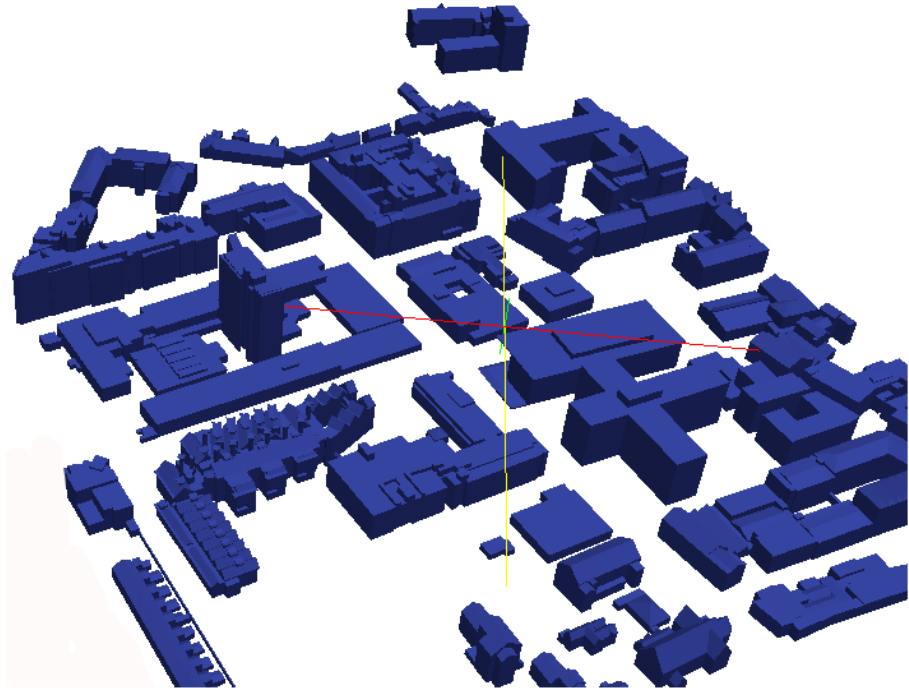
### 4.3 Full-scale measurements

Three ‘Windmaster Pro’ 3D ultrasonic anemometers (Gill instruments Ltd) were used for high resolution wind measurements at the university campus during the period January 2015 - March 2016:

- One was installed on the roof of the Edith Murphy (EM) building (Figures 4.9 and 4.10(a)), the second highest building on the university campus (30 m tall with 90 m above sea level), after Old Fletcher building of 45 m height (99 m above sea level), which, however, has no easy access to its roof (Figure 4.11). The anemometer was mounted on a 5.10 m mast which overhangs 2.35 m above the roof of the plant room and the total height of observation was 36.35 m from the ground.
- The second anemometer was mounted on top of a 5.10 m mast, positioned on the roof of the Kimberlin library (KL) building (14.60 m tall) (Figures 4.9



(a)



(b)

Figure 4.5: The geometry of De Montfort university campus in (a) reality and in (b) the model.

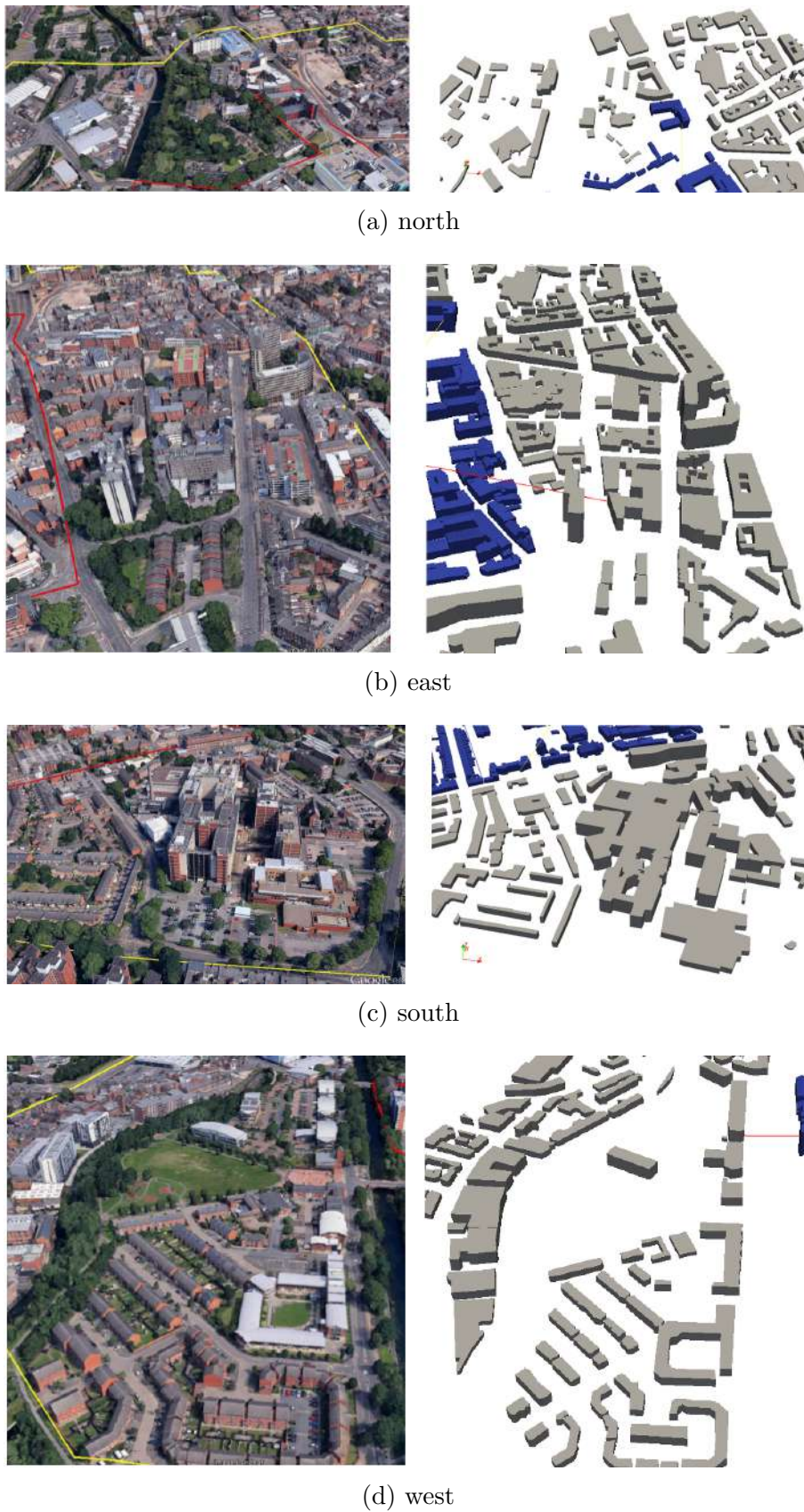


Figure 4.6: The geometry of the surroundings building in reality (left) and in the model (right).



(a) North direction



(b) East direction



(c) South direction



(d) West direction

Figure 4.7: Surroundings of the simulated area at each compass direction.

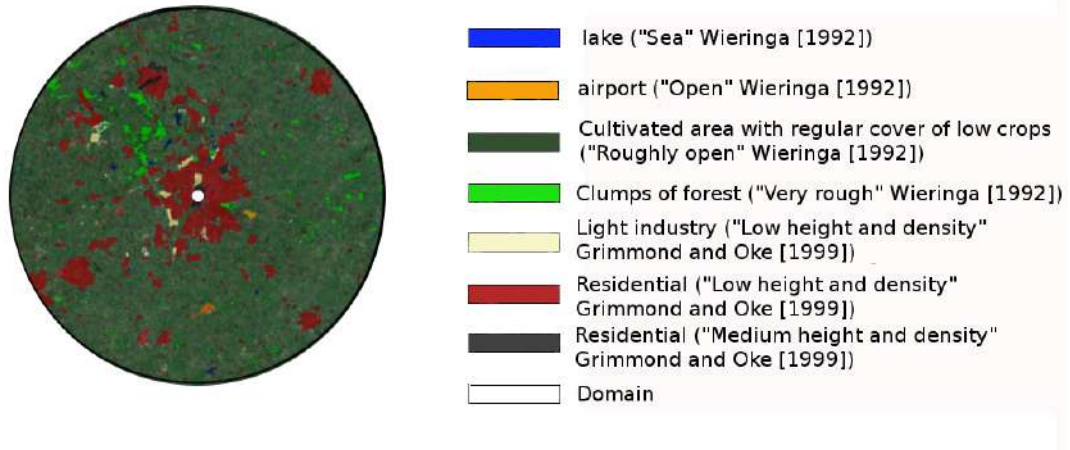


Figure 4.8: Plan view of the wider surroundings of the simulated area.

and 4.10(b)) and the total measurement height was 21 m from the ground. This position was chosen as it is partly in the shadow of the QB, as opposed to the previous well-exposed position and thus, the predictive capabilities of the DDES-SA model could be further evaluated.

- The third anemometer was used for short-term (2hours) measurements (SM), at the back of Queens Building (QB) (Figures 4.9 and 4.10(c)) and the observation heights range from 9.95 m to 11.35 m from the ground. Particularly 3 short-term measurements were made:
  - At 26/03/2015 from 14:00 to 16:00 (SM1),
  - At 28/03/2015 from 10.20 to 12:30 (SM2),
  - At 18/07/2015 from 14:50 to 16:30 (SM3).

They provide wind speed data in the range of 0 - 65 m/s with resolution of 0.01 m/s and accuracy of  $<1.5\%$  RMS and wind direction data with resolution of  $0.1^\circ$  and accuracy of  $2^\circ$ . Accuracy specifications apply for 12 m/s wind speed, and for wind incidence up to  $\pm 30^\circ$  from the horizontal [User Manual, 2016].

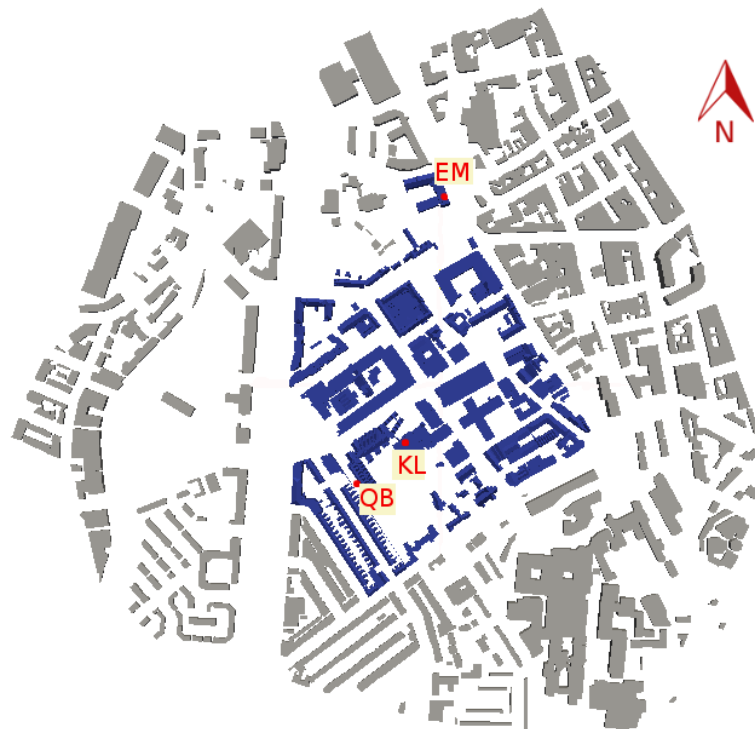
Data were sampled at 20 Hz and averaged (data-logger, Figure 4.10(d)) over periods of 1 sec, 1 min and 10 min, only if the sampled data were complete over the corresponding time intervals. To control the anemometers and adjust the data samples, a Windows-based computer program provided by the data logger manufacturer was used, while, for the data retrieval and analysis it was used the SSH File Transfer Protocol on Unix-like operating systems.

## 4.4 Computational domain and mesh

The computational domain is firstly defined by CAD data representing  $1100 \times 1100 \text{ m}^2$  of the De Montfort university campus and the surrounding buildings, which has been developed by Infoterra Ltd, a provider of geospatial products and services. The campus itself is about  $500 \times 500 \text{ m}^2$  and the city blocks extend in a radius of about 300 m around the campus (Figure 4.12). This building geometric data extends at least for two blocks beyond the central region containing the measurement points, satisfying the minimum requirements for one block extension according to the AIJ guidance [Yoshie et al., 2007a]. The dimensions of the complete domain (Figure 4.13) are (Length) $\times$ (Width) $\times$ (Height) =  $2200 \times 1300 \times 300 \text{ m}^3$  with a maximum blockage ratio of 2% (less than 3% as suggested by [Tominaga et al., 2008b]). It accommodates an upstream length of 5H (with H being the height of the highest building: 50m), a downstream subdomain length of 15H and a height of 6H. The lateral boundaries have been placed 2H from region of interest in accordance with best practice guidelines [Franke et al., 2007; Tominaga et al., 2008b].



(a)



(b)

Figure 4.9: Position of wind measurements at De Montfort university campus.



(a) Edith Murphy



(b) Library



(c) Queens building



(d) Data logger

Figure 4.10: 3D ultrasonic anemometers at De Montfort university campus.





Figure 4.11: Roof of the highest building (Old Fletcher) at De Montfort university.

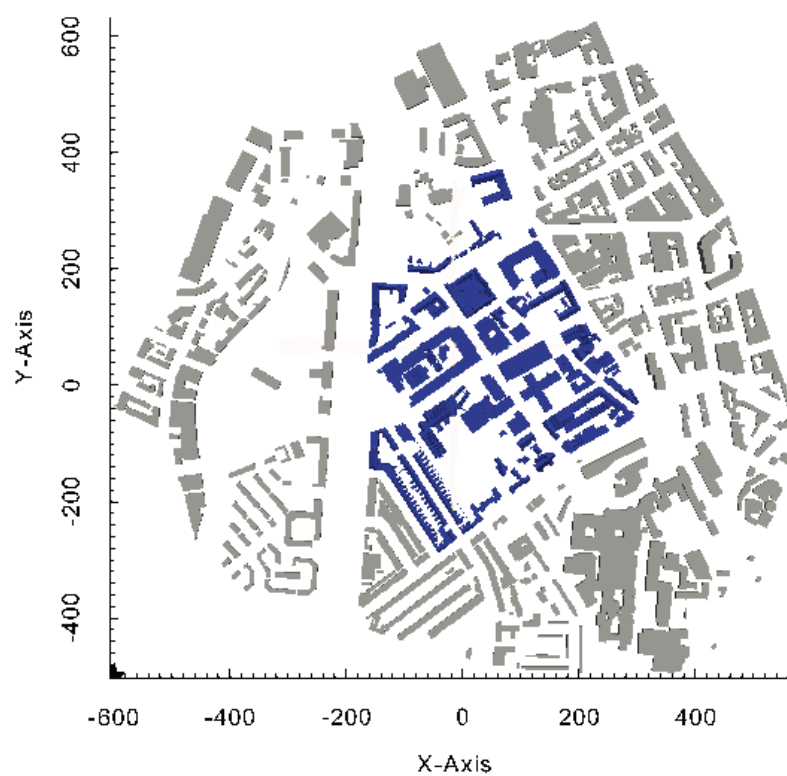


Figure 4.12: CAD data of De Montfort university and the surrounding buildings.

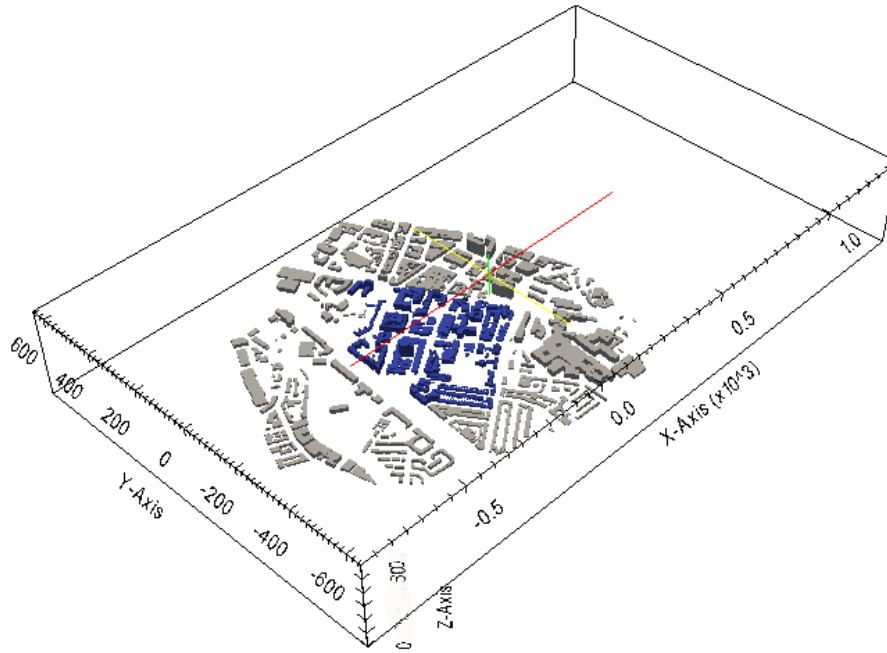
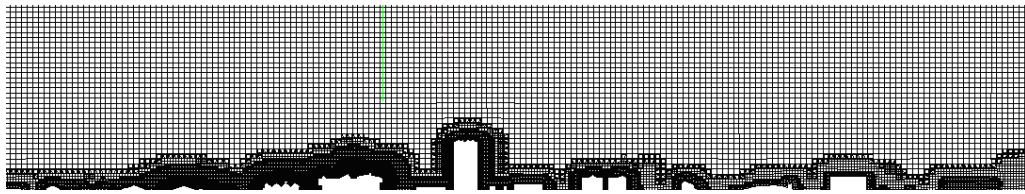


Figure 4.13: Computational domain.

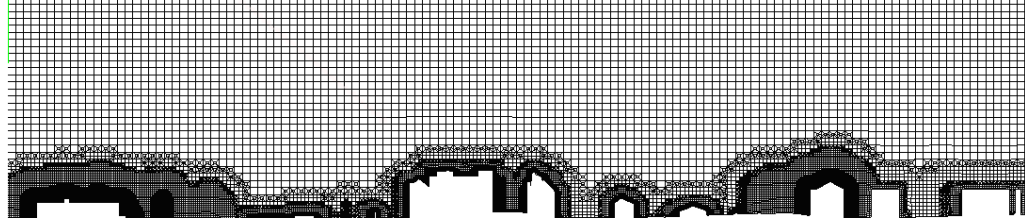
This case is representative of a complex urban environment of practical interest and as for the Shinjuku area in Tokyo it was used the OpenFOAM `snappyHexMesh` tool to mesh the case with a high degree of automation and good parallel efficiency. Again, the regions around the buildings were refined as indicated in Figure 4.14. The total number of cells for the whole domain was approximately 24 million for the west wind direction and similar results were obtained by simply rotating the background mesh to obtain meshes for the other wind directions resulting in meshes with comparable numbers of cells.

## 4.5 Turbulence model

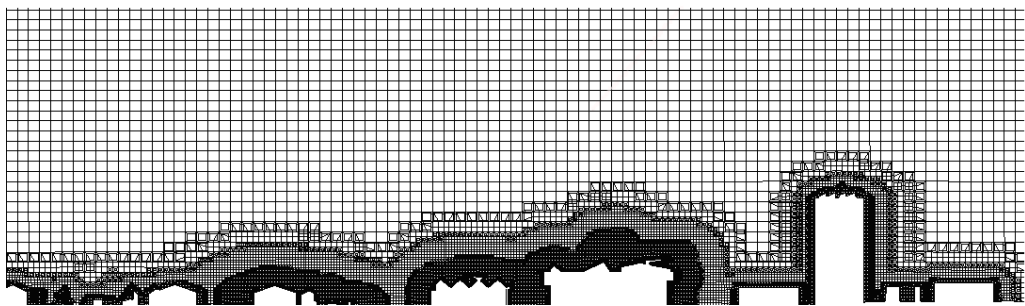
Analogous to test case B (Shinjuku area in Tokyo), the DDES-SA model was used with the `pimpleFoam` transient solver. The simulation time during which the data were averaged, was  $T = 2 \cdot T_0$ , where  $T_0$  is the time required for a cross-flow, preceded with a model spin-up time over  $T = 4.5 \cdot T_0$ . The solvers (`fvSolution` dictionary)



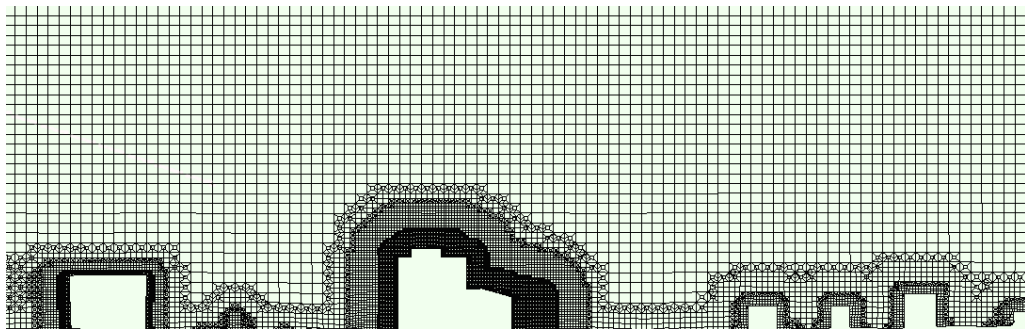
(a)



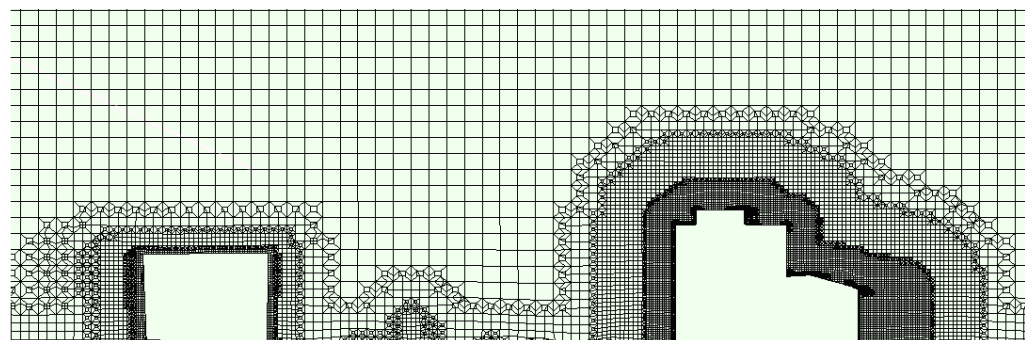
(b)



(c)



(d)



(e)

Figure 4.14: Refinement regions around the buildings.

and the numerical schemes (`fvSchemes` dictionary) for the DES calculations are presented in Appendix C.3.

## 4.6 Boundary conditions

At the inflow, the vertical velocity profile was given by the power law (Equation 2.27), since the implementation of the log-law (Equation 2.28) assumes a constant shear stress with height and hence the computational domain should be much lower than the atmospheric boundary layer [Tominaga et al., 2008b].

The Reynolds number (Re) based on the mean free stream velocity and the mean height of the buildings was approximately  $4.5 \cdot 10^6$  and the flow is considered Reynolds number independent. At high Re ( $\text{Re} > 11,000$ ), the separation of the flow over bluff bodies is forced by their shape, regardless of the nature of the boundary layer [White, 2003]. In aerodynamics and bluff body flows, the boundary layer is small and the flows are dominated by large length scales and separation induced vortices, and are insensitive to the Reynolds number [Hall et al., 2012]. The other boundary conditions were treated in a similar manner to Test Case B (for the DES calculations) (Section 2.4.3.3) and are shown in Table 4.1.

No turbulence fluctuations were imposed at the inlet. Turbulence produced by cuboid-shape bodies with sharp edges e.g. buildings, is building-block-scale dominated [Xie and Castro, 2009]. Hence, the upstream buildings generate turbulence in the model that it is dominant in determining conditions in the main region of interest rather than inlet conditions. Braun et al. [2012] demonstrated that LES produce turbulence fluctuations when an obstacle is placed in the flow field, however, when turbulence generation was employed at the inlet the flow configuration around the model was modified. Nevertheless, Braun et al. [2012] studied the flow field around a single building; when simulating an urban-type environment, the flow details above

---

Inflow	Power law velocity profile, $U(z) = U_s \left(\frac{z}{z_s}\right)^a$ , $a=0.24$ [Choi, 2009].
Outflow	Zero gradient condition.
Lateral and upper surfaces of the domain	Symmetry conditions.
Building and ground surfaces	Spalding's wall function.

---

Table 4.1: Boundary conditions.

the canopy layer are greatly dependent on the configuration of the local individual blocks upstream (below the mean building height the accurate specification of turbulence fluctuations is not crucial) [Xie and Castro, 2009].

## 4.7 CFD simulations and validation

To validate the CFD model, the long term measurements at the two fixed positions (EM and KL, Section 4.3) were used (Section 4.3). The mobile measurements at QB were made only for a few hours and they cannot serve validation purposes alone [Schatzmann and Leitl, 2011; Schatzmann et al., 1997], but they can give confidence to the CFD model when long term measurements exist. The short-term data SM1 and SM3 were only used as the SM2 were not uniform and could not be used for comparison purposes. Although the anemometer at EM building failed on August, 2015 due to a fault on one transducer pair, 6 months of measurements (February 2015 - July 2015) are considered sufficiently long period to be used as validation data [Blocken et al., 2012].

The data were sampled at 20 Hz and were averaged over 10 minute periods to give

the values of mean wind speed and wind direction. The measurements were clustered in wind direction intervals of 10, 45 and 90 degrees in order to investigate the influence of the wind sector ‘width’ on the results. Then, the wind speed ratios were calculated by dividing the wind speed values at the locations of the anemometers ( $U_{KL}$ ,  $U_{SM1}$ ,  $U_{SM2}$ ) by the reference wind speed. The Edith Murphy building was used as the reference wind speed ( $U_{EM,ref}$ ) for the Kimberlin Library and the Kimberlin Library was used as the reference wind speed for the short-term measurements (SM) ( $U_{KL,ref}$ ).

As shown in Table 4.2 the wind speed ratios for 10, 45 and 90 degrees wind direction intervals are similar for North and South wind directions. For the West direction there is a deviation of around 23% between 10 or 45 degree intervals and 90 degrees. As the wind aligns to the west the Library is located in the wake region of the Queens building and the wind speed reduces. On the other hand, the west direction benefits the anemometer on the Edith Murphy building, where the wind speed increases and hence the wind ratio  $U_{KL}/U_{EM}$  decreases. However, the impact of the wind direction on the wind speed in absolute values is small. Specifically, the mean wind speed at EM increases from 4.12 m/s to 4.50 m/s as the wind interval decreases from 90 degrees to 45 degrees and the wind speed at KL decreases from 2.87 m/s to 2.47 m/s respectively. Hence, although the reduction of the wind speed ratio is quite large (around 23%) the wind speed difference is only 0.3-0.4 m/s at each measurements point. This is attributed to the fact that the wind speeds are small and little increase or decrease of them results in high percentage error. In the East direction there is also a quite high percentage error of around 20% between the 10 or 45 degree intervals and 90 degrees. However, the absolute difference in wind speeds is 0.06 m/s at EM (from 3.67 m/s to 3.73 m/s) when the wind direction interval reduces from 90 degrees to 10 degrees and 0.24 m/s at KL (from 2.11 m/s to 1.87 m/s).

	Wind speed ratios ( $U_{KL}/U_{EM}$ )			
	Measurements clustered in:			
	10°	45°	90 °	CFD
N	0.70	0.72	0.67	0.68
E	0.49	0.47	0.59	0.46
S	0.79	0.78	0.81	0.81
W	0.57	0.57	0.70	0.57

Table 4.2: Wind speed ratios as calculated from the wind measurements clustered into 10 degrees, 45 degrees, 90 degrees and as calculated from CFD for four wind directions.

Generally, the smaller the wind direction intervals, the more accurate the results. However, it is impractical to do calculations for each wind direction and the measurements should be clustered in wind direction intervals. Intervals of 45 to 10 degrees i.e. 8 to 36 wind directions, have been used, based on how much the change in wind direction affects the wind speed ratio [Bechmann, 2012; Irshad, 2012; Kalmikov et al., 2010].

In this work, the wind flow was calculated for four wind directions, since the wind speed ratios were not significantly influenced by the wind direction, based on the wind measurements at the locations the anemometers were installed.

Table 4.2 also presents the wind speed ratios as calculated from the CFD simulations using the statistically averaged flows from the DES calculations (Section 4.5) and Figure 4.15 compares them with the measurements. As shown, there is a good agreement with a deviation of less than 10% apart from the North direction of SM1 where a discrepancy of 15% was found. In this position, only two hours measurements were carried out and hence, there are not enough data to rely on. Also, noticeable speed gradients exist (Figure 4.16) and hence, some shift in measurement position can influence the simulation results.

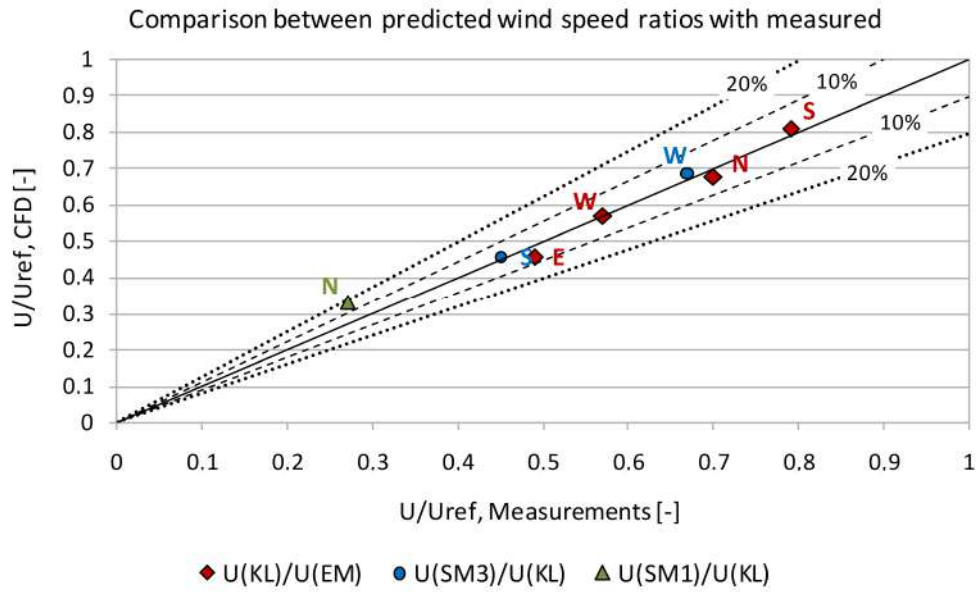


Figure 4.15: Comparison between numerical and experimental (10 degree interval) wind speed ratios ( $U/U_{ref}$ ) in the locations of anemometers for four wind directions -North (N), East (E), South (S), West (W).

Figure 4.17 shows the difference in wind direction between the locations of anemometers and the reference wind as calculated for the field measurements and the CFD results. A good agreement between measurements and CFD results is found for the angle deviation of the wind direction between the KL and the reference wind at EM ( $\Delta\phi = \phi - \phi_{ref}$ ). Although the deviation exceeds 20% in 3 of the 4 measurements (West, North and East direction) and at first sight the discrepancy might seem to be quite large, the actual difference between measured and simulated values are less than 3 degrees. This is explained by the fact that the  $\Delta\phi$  is very small ( $<10$ ), and little difference in the angle deviation, of the order of 2 to 3 degrees, gives a high deviation. Figure 4.18 illustrates the situation, presenting the values of the angle deviation indicating a rather good agreement.

The results for the short-term measurements (SM) are less good in terms of  $\Delta\phi$  (50% to 70% deviation). This might be attributed to the fact that the anemometer was not aligned correctly to the North direction, as for the short-term measurements



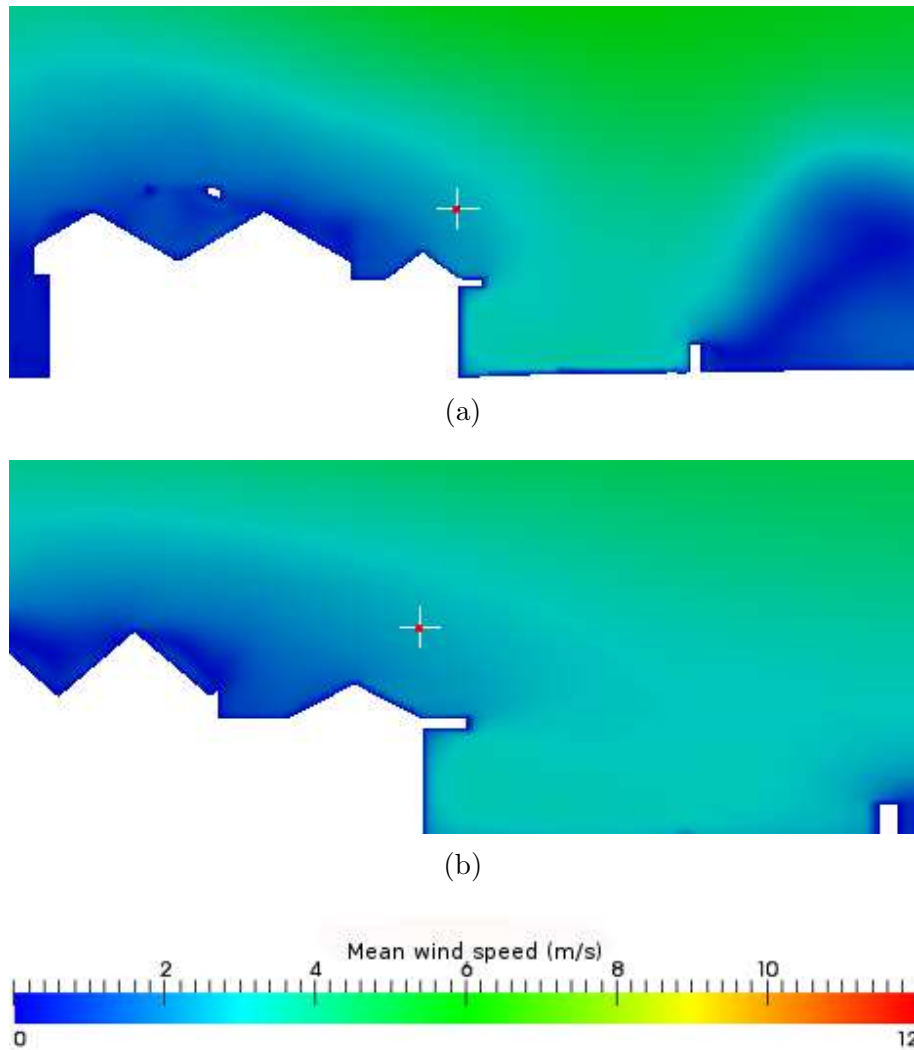


Figure 4.16: Wind speed mean in the position (red point) of SM1 for North wind direction at (a) xz plane and (b) at yz plane.

the alignment was based on eye observations and hence the error increases.

Summarising, the overall agreement is quite good, and the discrepancies at some points can be attributed to the difficulty to extract the exact coordinates of the points of measurements and the failure to calibrate the anemometer to read the North direction.

As regards the number of the wind directions simulated, they should be chosen based on how much the wind direction affects the wind speed ratios. In this work, the measurements indicate that there is small effect. However, if one wants to investigate

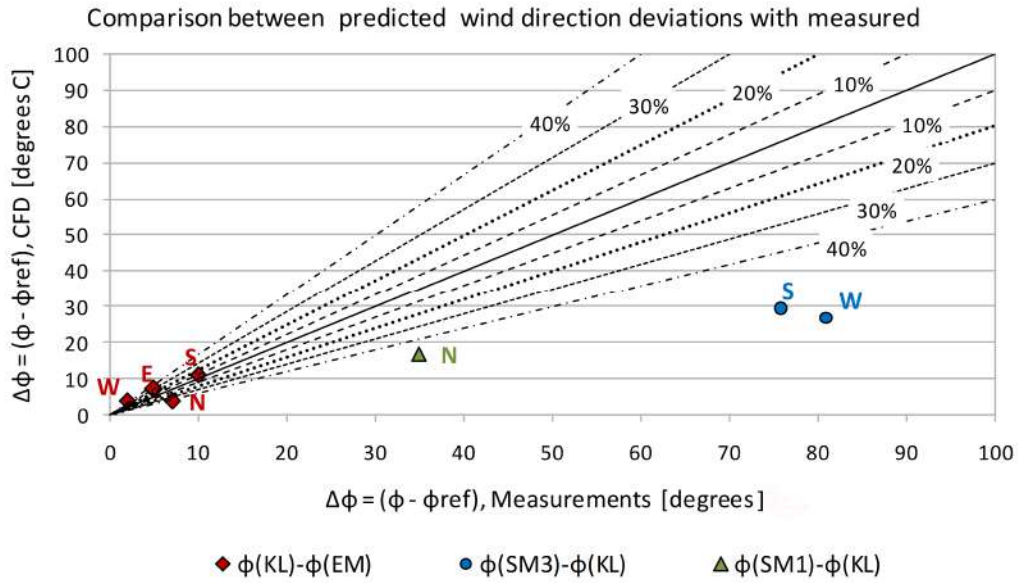


Figure 4.17: Comparison between numerical and experimental (10 degree interval) angle deviation between the locations of anemometers and the reference wind ( $\Delta\phi = \phi - \phi_{ref}$ ) for four wind directions -North (N), East (E), South (S), West (W).

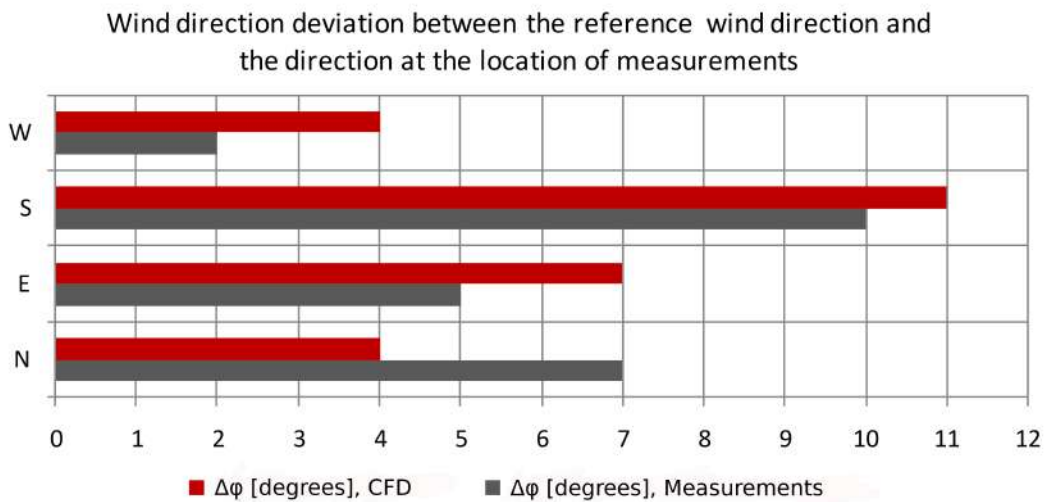


Figure 4.18: Comparison between numerical and experimental (10 degree interval) angle deviation of wind direction between the location of anemometers at KL and the reference wind at EM ( $\Delta\phi = \phi - \phi_{ref}$ ) for four wind directions -North (N), East (E), South (S), West (W).

further the response of this model to the wind direction, wind simulations of smaller wind intervals should be done and found the impact of the wind direction on wind speed ratio at various places.

## 4.8 Conclusions

In this Chapter the predictive capabilities of the DDES-SA model using the OpenFOAM CFD library were further investigated. The DDES-SA approach was applied at the DMU campus and the results compared with high frequency anemometer data. The mean velocity predictions above rooftop at a well exposed building and at a partly sheltered building were examined and found to be in good agreement with the anemometer data. Very limited CFD studies of complex urban areas have been validated using field measurements in this way.

The results obtained with the DDES-SA model in this study as well as the study of the two test cases developed by AIJ (Chapter 3) have offered robustness and accuracy over a range of wind conditions. However, this benefit came at some cost in terms of the computational resources required and time. Three super computers were engaged to perform the simulations (one at the DMU, one at Loughborough university and one at the university of Leeds) and it took almost a year to obtain the results. Nevertheless, during this time a lot more cases were tested before setting-up the final configuration of the models.

In the further study (Chapter 6) of wind resource at the De Montfort university campus, the wind behaviour will be described in terms of the reduction factors (Section 6.3) i.e. wind speeds normalised by the reference wind speed (8 m/s at 60 m). As the simulations have very high Reynolds number, the wind behaviour is the same at any reasonable reference wind speed [Heath et al., 2007].

In a highly turbulent environment, such as the urban areas, turbulence intensity can affect substantially turbine performance and hence, further studies of turbulence predictions above the roof are required. This issue will be examined later in Section 7.2.2.

# Chapter 5

## Meteorological data collection and analysis

### 5.1 Introduction

The use of reliable meteorological data is of major importance in wind turbines installation planning. However, it is not usually economic or practical to make long-term measurements in any potential urban development site for installation and therefore, the use of existing data is imperative. Consequently, for a methodology to be generalized to a wide range of sites, it is desirable to be able to translate data available from public weather stations to the target location.

Here, a method of estimating the hourly annual wind speed of a selected site using one year's recorded wind data at a remote site, such as airport weather stations, is presented. This process utilizes one year measured wind data of one site to extrapolate the annual wind speed at a new site, using the Wind Atlas Methodology [Landberg et al., 2003] as it is illustrated by Millward-Hopkins et al. [2013b]. In particular, this method scales wind speeds from the remote weather station up to the top of the urban boundary layer, the height at which the frictional effect of

the surface is assumed to be absent (Section 2.2.2.3), and then scales them down to a reference height, where the flow is assumed to be horizontally homogeneous [Grimmond and Oke, 1999].

In this work, hourly concurrent measurements from East Midlands airport weather station and anemometers at De Montfort university are used. Statistical analysis has been used to investigate the proper cross-correlation of the wind speed between the sites. Then, wind data from the East Midlands airport weather station was transferred at the De Montfort university campus and the predictions compared with the field measurements in order to test the validity of the methodology.

## 5.2 Meteorological data

### 5.2.1 East Midlands airport weather station

The measuring weather station with long-term wind data nearest to Leicester is located at East Midlands airport, U.K. (Figure 5.1). The data was accessed through MIDAS (Met Office Integrated Data Archive System) which is freely available for online access to UK academics through the British Atmospheric Data Centre (BADC) [BADC]. The data contain meteorological values of wind speed and direction measured on an hourly time scale, during the hour ending at the stated date and time (Table 5.1), and spans from 1875 to present. The dataset of 2015 is used in this study.

Generally, the data should cover a period of 30 years to be considered representative for the building site, but also one year of wind data can be sufficient to predict long-term mean wind speeds for wind turbines' site selection instalment [Spera, 1994] (Section 2.2.1). The wind data at East Midlands weather station will be used to extrapolate the annual wind speed at DMU, where wind measurements have been

made for validation purposes.



Figure 5.1: East Midlands weather station and target area.

Meteorological measurement	Data interval	Time interval
Wind speed	1 knot	10-minute average
Wind direction	10 degrees	10-minute average

Table 5.1: Weather data at East Midlands airport [Met Office].

### 5.2.2 De Montfort university campus measurements

As described in detail in Section 4.3, two 3d ultrasonic anemometers were installed at DMU university campus, one on the roof of the Edith Murphy building and one at the Kimberlin Library. High resolution (20 Hz) wind data were collected from February 2015 till July 2015 at EM and from February 2015 till January 2016 at KL.

### 5.2.3 Correlation between the wind speed data at two remote meteorological stations

To investigate the strength of the association between the two variables —wind speed at EMA and DMU measurements— the Pearson product-moment correlation coefficient ( $r$ ) [Pearson, 1929, 1931] was used. This correlation test is given by Equation 5.1 and is widely used as a measure of the degree of linear dependence between two sets of variables giving a value between +1 and -1 inclusive, where +1 denotes a perfect positive correlation, 0 no correlation, and -1 means perfect negative correlation. According to Nangolo and Musingwini [2011] you will very rarely find 0, -1 or 1, but a number somewhere in between those values and the Table 5.2 gives guidelines regarding the strength of the linear relationship corresponding to the correlation coefficient value.

$$r = r_{xy} = \frac{\sum_{n=1}^n (x_i - \bar{x})(y_i - \bar{y})}{\sqrt{\sum_{n=1}^n (x_i - \bar{x})^2} \sqrt{\sum_{n=1}^n (y_i - \bar{y})^2}} \quad (5.1)$$

where:  $n$  is the number of values in each dataset,  $\{x_i \dots x_n\}$ ,  $\{y_i \dots y_n\}$  the two datasets and  $\bar{x}$ ,  $\bar{y}$  the sample means.

Correlation Coefficient value	Strength of linear relationship
0.8 - 1	Very strong
0.6 - 0.8	Moderately strong
0.4 - 0.6	Moderate
0.2 - 0.4	Weak

Table 5.2: The Strength of relationship based on the value of  $r$ .

The results in Tables 5.3 and 5.4 indicate strong correlation between East Midlands airport and De Montfort university stations (both Edith Murphy and Kimberlin Library measurements) with slightly better results for Edith Murphy mea-

surements.

	Wind direction				
	all	N	E	S	W
r	0.79	0.74	0.83	0.81	0.81
r ( $v > 2\text{m/s}$ )	0.77	0.70	0.81	0.80	0.81

Table 5.3: Pearson product-moment correlation coefficient ( $r$ ) between East Midlands airport wind data and Edith Murphy wind measurements.

	Wind direction				
	all	N	E	S	W
r	0.73	0.75	0.68	0.88	0.75
r ( $v > 2\text{m/s}$ )	0.72	0.73	0.67	0.88	0.74

Table 5.4: Pearson product-moment correlation coefficient ( $r$ ) between East Midlands airport wind data and Kimberlin Library wind measurements.

As illustrated in Figure 5.2, all Pearson’s coefficients are higher than 0.60 i.e moderately strong correlation. Particularly, in 3 of the total of 4 wind directions the correlation coefficients between East Midlands and Edith Murphy are higher than 0.80, denoting a very strong correlation and one is in ‘moderately strong’ correlation range i.e higher than 0.70. The coefficients between East Midlands and Library stations fall in ‘very strong’ range in 1 out of a total of 4 wind directions and the rest suggest ‘moderately strong’ correlation with 2 being higher than 0.70 and one higher than 0.60.

In an attempt to ignore potential local thermal effects, the Pearson coefficients were also estimated for measurements of wind speed larger than 2 m/s. Since these measurements will be used for validation purposes of CFD simulations and CFD are implemented for neutral conditions (there is no heat transfer between the air and the ground, and buoyancy effects are absent, Section 2.2.2.1), it was important



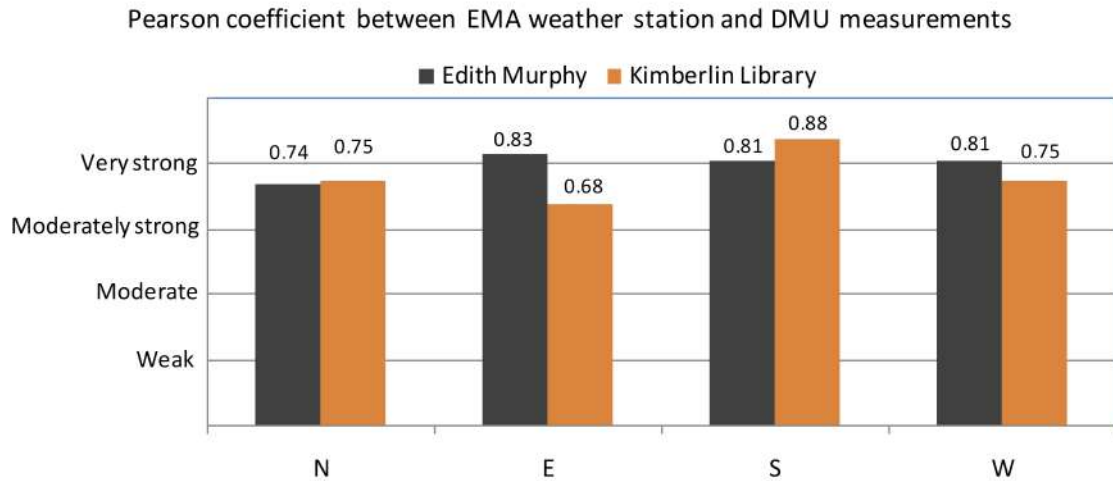


Figure 5.2: Pearson correlation coefficient ( $r$ ) between EMA wind data and wind measurements at DMU campus.

to investigate the degree of the thermal effects on the datasets. In addition, the cut-in wind speed at which the turbine starts to operate is usually about 2 – 4 m/s (Section 2.6.2) for the majority of wind turbines and lower speed values do not add to the energy yield. However, no thermal effects seemed to be included in the datasets and the Pearson coefficients ( $r$ ) for the wind measurements for  $v > 2$  m/s were very similar to the initial values, deviating only  $\pm 0.02$  as indicated in Tables 5.3 and 5.4 ( $r$  for  $v > 2$  m/s).

### 5.3 Extrapolation of meteorological data

The meteorological data from the East Midlands airport weather station (EMA) was transferred to the building site (‘Target area’) (Figure 5.1).

The ratio of the wind speed at the location of interest ( $U$ ) to the wind speed at meteorological station ( $U_{\text{MET}}$ ) (Figure 5.3) is given by the amplification factor  $\gamma$  (Equation 5.2), which can be decomposed to the ratio  $U_{\text{ref}}/U_{\text{MET}}$  and  $U/U_{\text{ref}}$ . The first ratio ( $U_{\text{ref}}/U_{\text{MET}}$ : terrain related contributions [Blocken and Persoon, 2009]) corresponds to the change in wind data from the meteorological site to a reference

location near the building site and it can be obtained by an analytical procedure, reported in Section 5.3.1. The second ratio ( $U/U_{ref}$ : design related contributions [Blocken and Persoon, 2009]) indicates the change in wind data due to the local urban design, i.e. the building configurations, and can be obtained by Computational Fluid Dynamics (CFD).

$$\gamma = \frac{U}{U_{MET}} = \frac{U_{ref}}{U_{MET}} \frac{U}{U_{ref}} \quad (5.2)$$

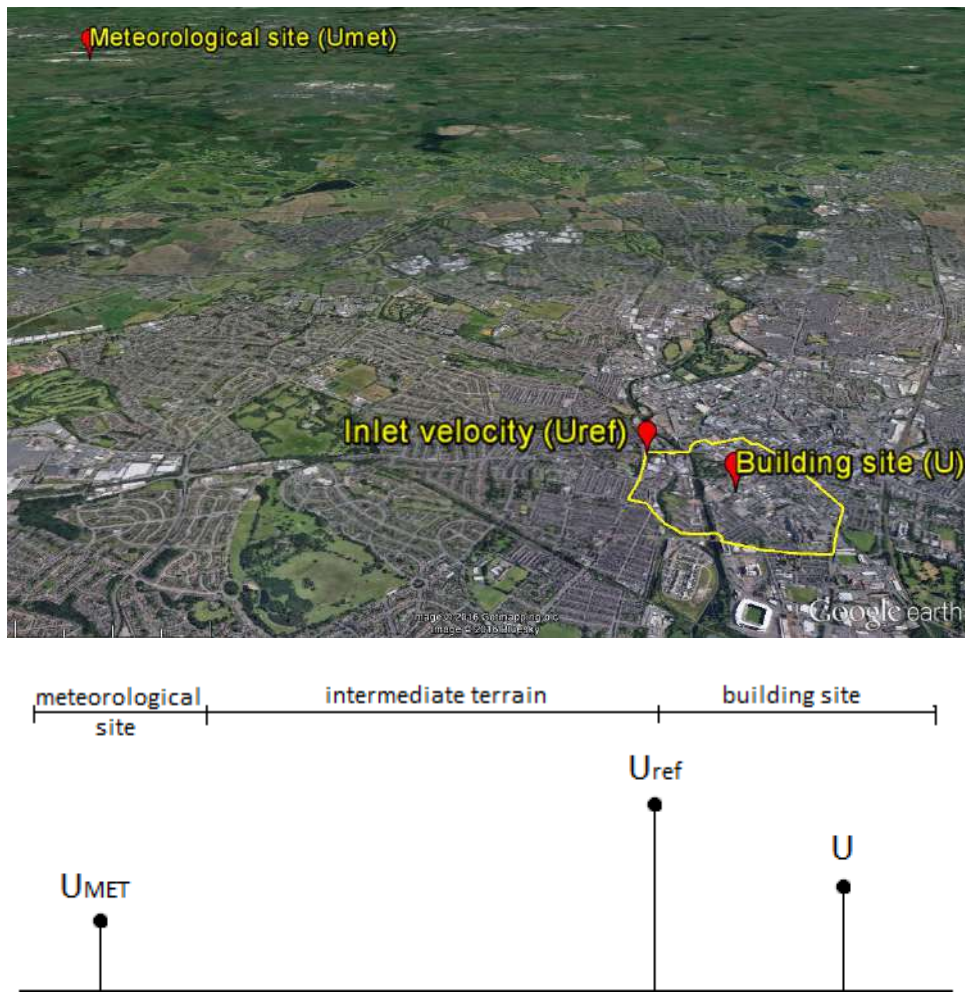


Figure 5.3: Graphical representation of the wind speed at the meteorological station ( $U_{MET}$ ), the wind speed at the inlet of the building site ( $U_{ref}$ ) and the wind speed at the target area ( $U$ ).

The methodology applied to the concurrent wind measurements for the year 2015 between East Midlands airport weather station and the anemometers at Edith Murphy and Kimberlin Library. Figures 5.4 and 5.5 present the wind data (wind speed and wind direction) for this period of time.

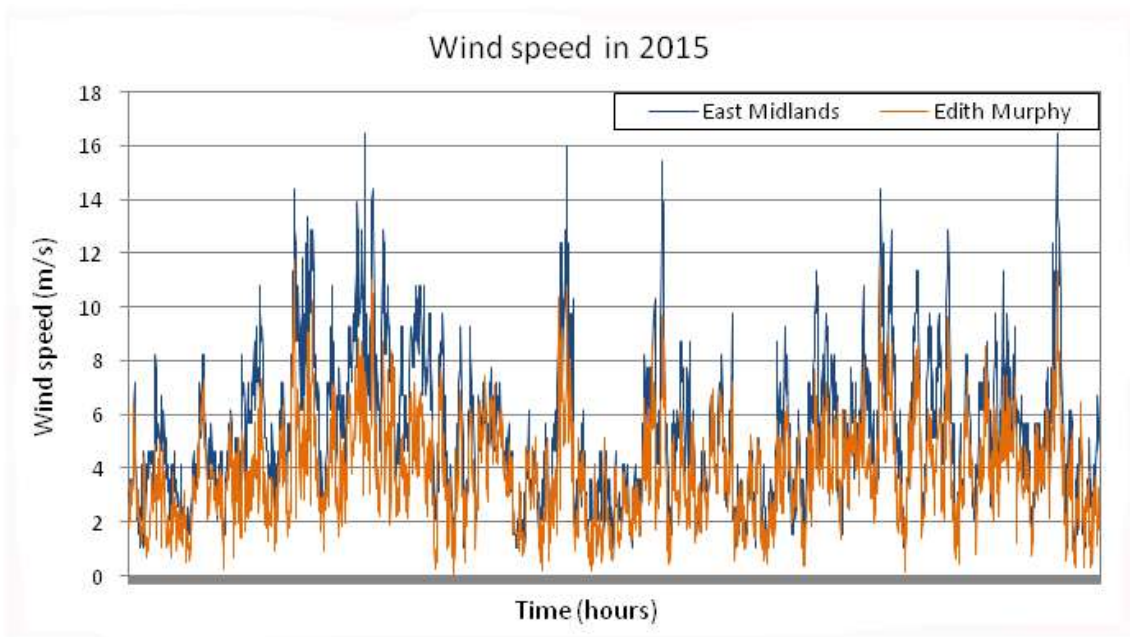
From a first reading of the raw wind speed data (Figure 5.4), the wind measurements at the building site (DMU) are lower than the measurements at the open, exposed terrain (EMA), as expected [Emejeamara and Tomlin, 2015], maintaining though the main trends. Particularly, the wind speed at Kimberlin Library (Figure 5.4(b)) is noticeably lower than the wind speed at EMA, while the wind data at EM (Figure 5.4(a)) are certainly closer to the airport measurements. This is due to the fact that the Library is partially sheltered by the Queens Building and the location of measurements is lower (21 m from the ground) than the one at EM's building (36.35 m).

Regarding the wind direction (Figure 5.5), the measurements at both sites show good agreement with the measurements at the meteorological station in East Midland airport, indicating the SW to be the prevailing wind direction.

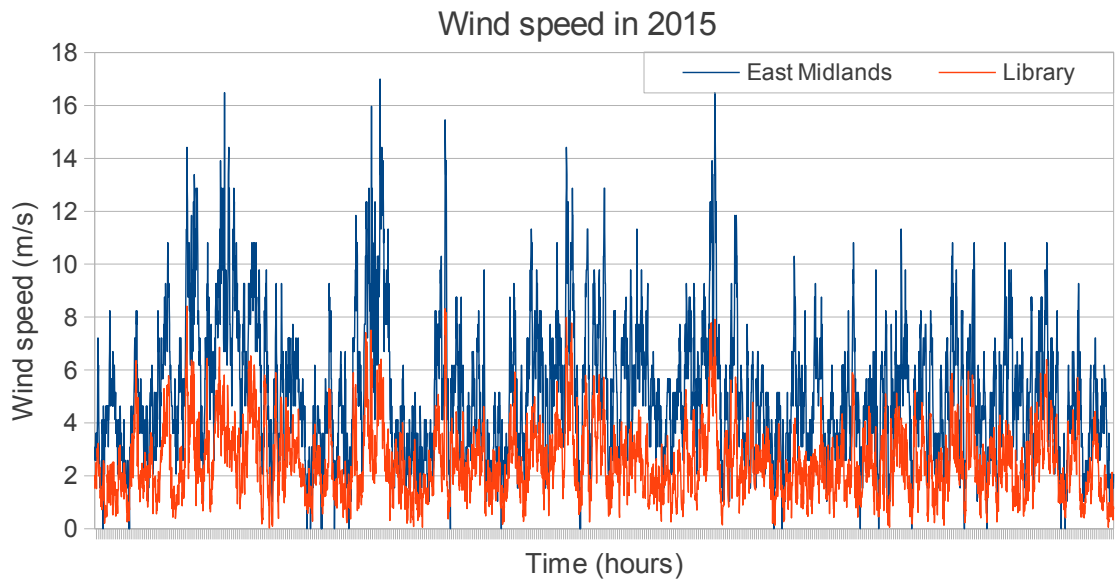
The amplification factors as calculated using the wind measurements for the year 2015 between East Midlands airport weather station and the anemometers at DMU campus ( $\gamma = U_{\text{DMU}} / U_{\text{MET}}$ ) are shown in Table 5.5.

		Wind direction			
		N	E	S	W
$\gamma$	EM	0.98	0.90	0.79	0.65
	KL	0.67	0.44	0.63	0.36

Table 5.5: Amplification factors ( $\gamma$ ) between EMA and DMU wind measurements based on the field measurements.



(a)



(b)

Figure 5.4: Wind speed time series (a) at East Midlands airport meteorological station and on the roof of the Edith Murphy building at De Montfort university for the year 2015 and (b) at East Midlands airport meteorological station and on the roof of the Library at De Montfort university for the year 2015.

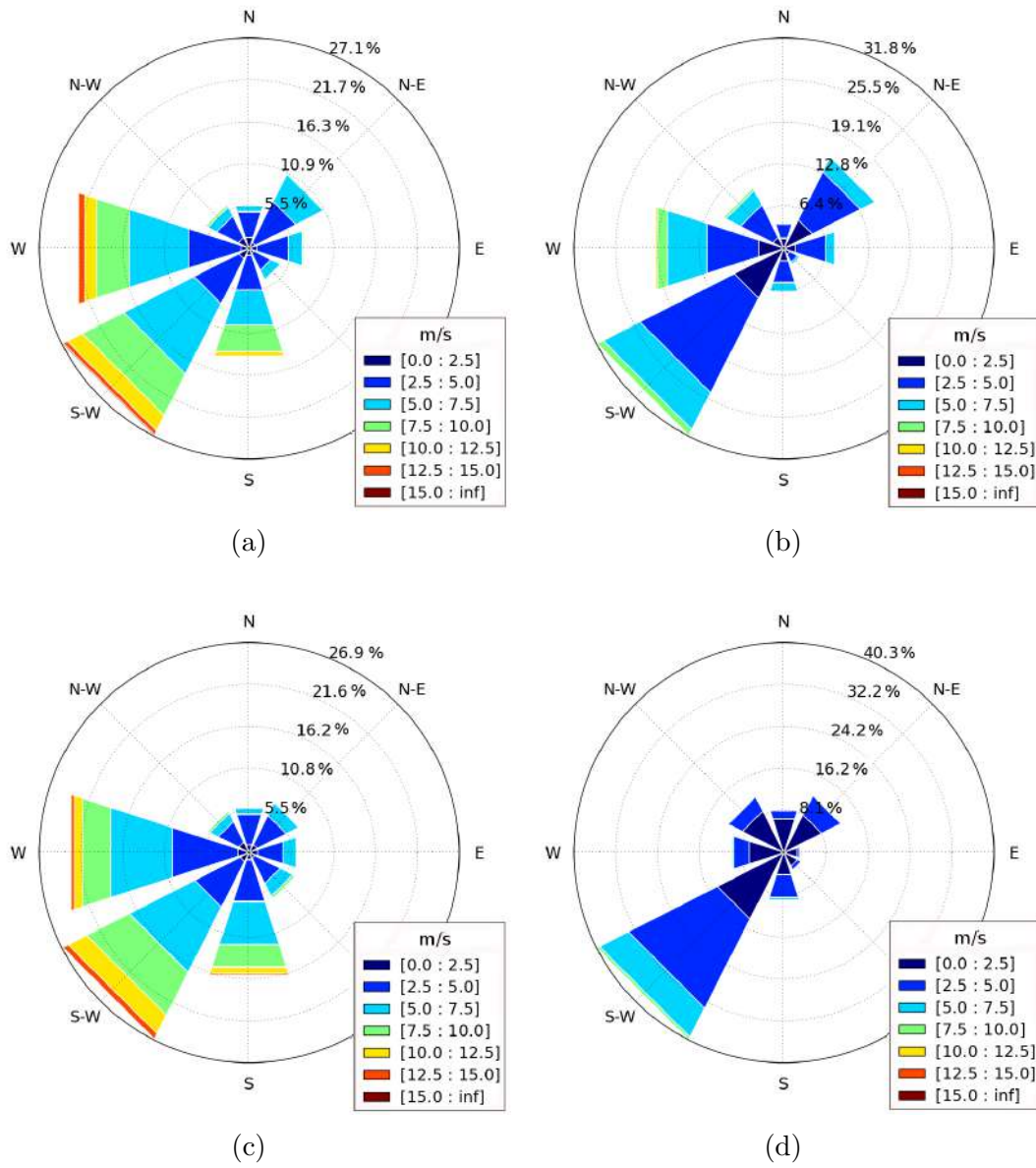


Figure 5.5: Wind roses for (a) East Midlands airport wind data during the wind measurements in Edith Murphy building (b) Edith Murphy data (c) East Midlands airport data during the wind measurements in Kimberlin Library and (d) Kimberlin Library wind data.

### 5.3.1 Terrain related contributions

To transfer the meteorological data from the airport weather station to the edge of the target area a procedure based on the Wind Atlas Methodology [Landberg et al., 2003] is used. The process involves two steps and is illustrated in Figure 5.6:

- scaling the wind speed measurements at the meteorological station ( $U_{MET}$ ) up to the top of the urban boundary layer ( $z_{UBL}$ ), where there is no influence of the urban surface, and then
- scaling down to the reference height  $z_{ref}$ , where the flow is considered to be horizontally homogeneous, upstream of the target area.

Specifically, in this study the wind speed at 10 m above the ground from the East Midlands airport meteorological station ( $U_{MET}$ ) is scaled-up to 500 m ( $z_{UBL}$ ). Applying the standard logarithmic wind profile Equation (2.4), the wind speed is given by:

$$U_{UBL} = U_{MET} \frac{\ln(z_{UBL}/z_{0-MET})}{\ln(z_{MET}/z_{0-MET})} \quad (5.3)$$

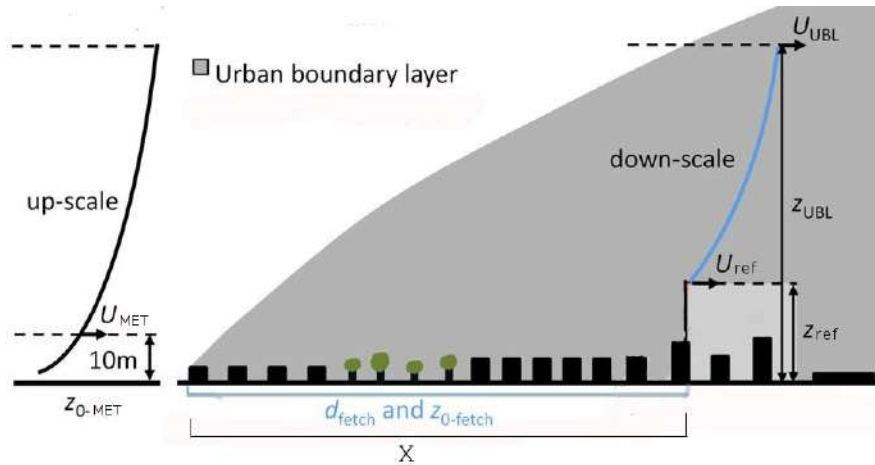


Figure 5.6: Schematic diagrams of the wind atlas methodology implemented in the current work, Millward-Hopkins et al. [2013b] (modified).

with  $z_{0\text{-MET}} = 0.03\text{m}$ , the roughness length for the runway area of airports based on the updated Davenport roughness classification by [Wieringa \[1992\]](#).

The height of the UBL is estimated using the Elliot formula [[Elliott, 1958](#)] (Equation 5.4), which accounts for the boundary layer depth ( $X$ ), and a value of 500 m is used as a rational maximum depth [[Millward-Hopkins et al., 2013b](#); [Raupach et al., 1991](#)].

$$z_{UBL} = \min\left\{ z_{0\text{-fetch}} \left[ 0.65 - 0.03 \ln(z_{0\text{-fetch}}/z_{0\text{-MET}}) \right] \left[ \frac{X}{z_{0\text{-fetch}}} \right]^{0.8}, 500 \right\} \quad (5.4)$$

where:  $X$  is the distance to the upwind edge of the building area and  $z_{0\text{-fetch}}$  the roughness length for the land area upstream.

In practice, the precise determination of the  $X$  is not feasible, but the estimated wind speeds ( $z_{UBL}$ ) are not sensitive to this variable for distances over a few hundred metres from the edge of the city. The roughness length are calculated by considering the roughness values of the various land covers for this 25 km fetch (Figure 5.7), based on the updated roughness classification by [Wieringa \[1992\]](#) and [Grimmond and Oke \[1999\]](#) (Table 2.1). Residential, low-height and density surface form was applied to the four directional sectors i.e  $z_{0\text{-fetch}} = 0.8$  m and  $d_{\text{fetch}} = 4.0$  m.

Then, the  $U_{UBL}$  is scaled down to 60 m height ( $z_{\text{ref}}$ ), accounting for the effect of the aerodynamic parameters (roughness length ( $z_{0\text{-fetch}}$ ) and displacement height ( $d_{\text{fetch}}$ )) of the surface upstream the target area. Applying again the standard logarithmic wind profile (Equation (2.4)), the wind speed is given by 5.5, and the terrain related contributions (ratio:  $U_{\text{ref}}/U_{\text{MET}}$ ) for the four wind directions are calculated to be 1.10.

$$U_{\text{ref}} = U_{UBL} \frac{\ln((z_{\text{ref}} - d_{\text{fetch}})/z_{0\text{-fetch}})}{\ln((z_{UBL} - d_{\text{fetch}})/z_{0\text{-fetch}})} \quad (5.5)$$

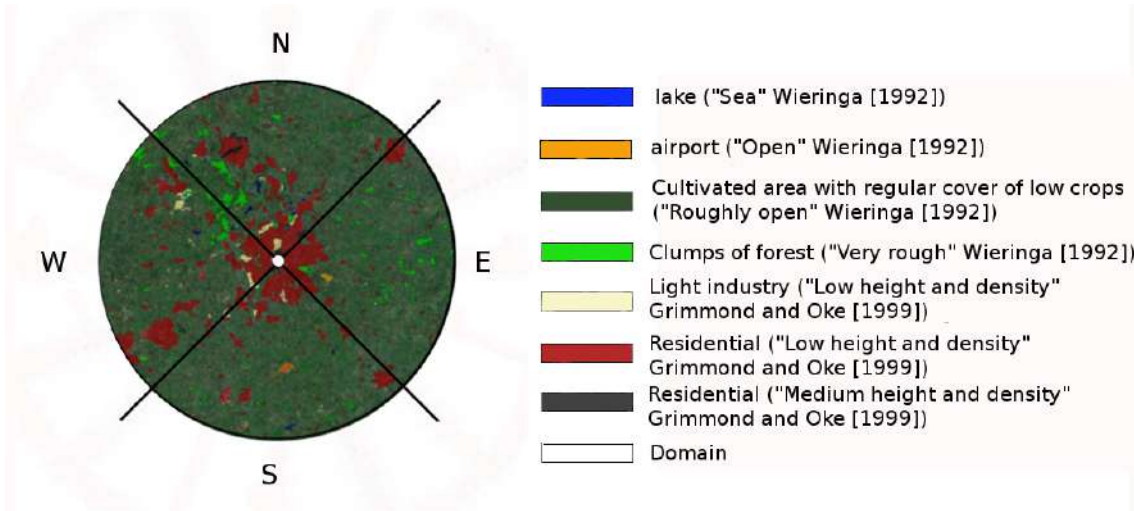


Figure 5.7: Terrain surrounding the target area with a radius of 25km for estimating aerodynamic roughness lengths  $y_0$ . The white area in the middle represents the building area used in this study.

### 5.3.2 CFD contributions

CFD simulations were carried out for four wind directions with a reference velocity ( $U_{\text{ref}}$ ) of 8 m/s at 60 m height and Table 5.6 shows the predicted ratios of  $U_i/U_{\text{ref}}$  (design-related contributions) for the two sites (Edith Murphy building and Kimberlin Library) of wind measurements at DMU.

	Wind direction			
	N	E	S	W
$U_{\text{EM}}/U_{\text{ref}}$	0.88	0.85	0.75	0.57
$U_{\text{KL}}/U_{\text{ref}}$	0.60	0.39	0.61	0.32

Table 5.6: Design related contributions based on CFD results.

### 5.3.3 Predicted vs calculated amplification factors

According to Equation 5.2, the amplification factor  $\gamma$  can be decomposed to the ratios  $U_{\text{ref}}/U_{\text{MET}}$  (terrain-related contributions) and  $U/U_{\text{ref}}$  (building (CFD) con-



tributions). Hence, using the results in Sections 5.3.1 and 5.3.2 ( $U_{\text{ref}}/U_{\text{MET}}=1.10$  and Table 5.6) the predicted amplification factors ( $\gamma'$ ) for each wind direction were estimated and compared to the amplification factors ( $\gamma$ ) as calculated using the field measurements (Table 5.5). The results are presented in Tables 5.7 and 5.8 and compared in Figures 5.8 and 5.9.

Overall, there is good agreement between the predicted and calculated values for both sites, with a deviation of less than 6%.

	Wind direction			
	N	E	S	W
Predicted $\gamma'$	0.97	0.93	0.82	0.63
Calculated $\gamma$	0.98	0.90	0.79	0.65

Table 5.7: Predicted ( $\gamma'$ ) and calculated ( $\gamma$ ) amplification factors between East Midlands airport and Edith Murphy building at DMU campus.

	Wind direction			
	N	E	S	W
Predicted $\gamma'$	0.66	0.43	0.67	0.35
Calculated $\gamma$	0.67	0.44	0.63	0.36

Table 5.8: Predicted ( $\gamma'$ ) and calculated ( $\gamma$ ) amplification factors between East Midlands airport and Kimberlin building at DMU campus.

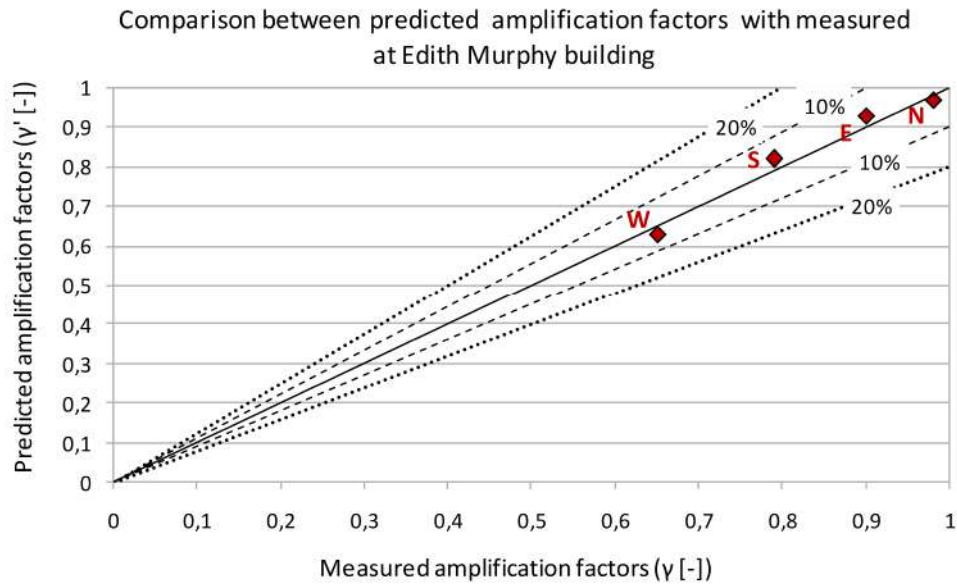


Figure 5.8: Comparison between calculated ( $\gamma$ ) and predicted ( $\gamma'$ ) amplification factors between the EMA weather station and the location of the anemometers at EM for four wind directions -North (N), East (E), South (S), West (W).

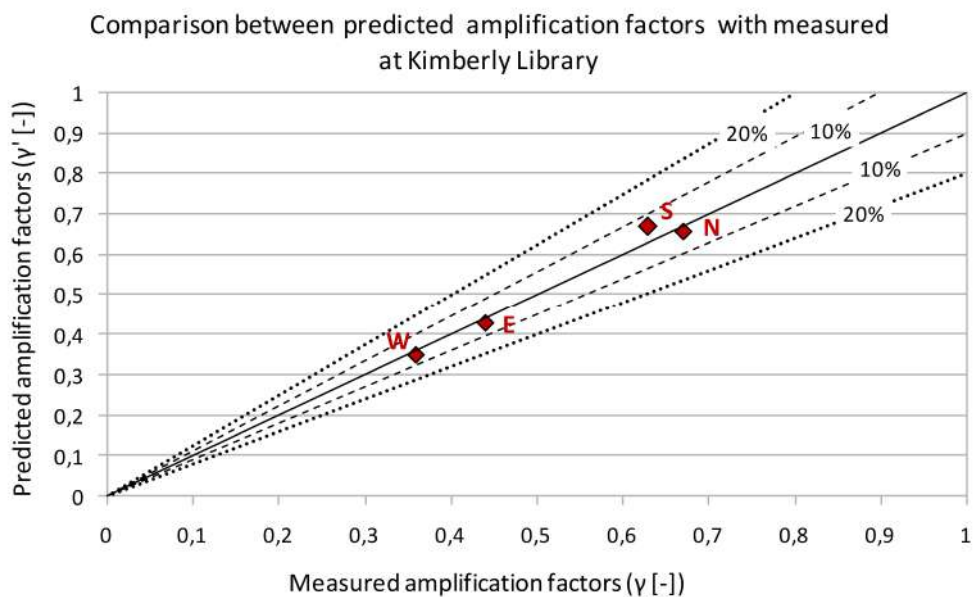


Figure 5.9: Comparison between calculated ( $\gamma$ ) and predicted ( $\gamma'$ ) amplification factors between the EMA weather station and the location of the anemometer at KL for four wind directions —North (N), East (E), South (S), West (W).

### 5.3.4 Discussion

The range of the  $\gamma$  values is 0.35 to 0.66 for the anemometer at KL and 0.62 to 0.95 for the anemometer located in EM. As expected at the built environment the mean wind speed decreases. Generally, the lower the measurement point, the lower the expected amplification factors. EM is the second highest building at DMU (measurements at 36.35 m above the ground). Thus, the amplification factors are higher than the corresponding values for KL (measurements at 21 m above the ground). However, looking closer at the measurement points, the building topography (Figure 5.10) has a significant impact on the measurements and some shift of the anemometers on the vertical or horizontal direction can influence significantly the results (Figures 5.11 and 5.12).

For example, when the wind flows from North and East, the anemometer at EM is located 1.5 m above the zone influenced by the separation of the flow at the leading edge of windward roof, where the wind speed falls rapidly. Noticeable speed gradients exist (Figure 5.11(a)-right) in the vertical direction and hence, some shift in the height of anemometer can influence considerably the results.

When the wind flows from North the anemometer on the roof of the Library is influenced by the separation of the flow at the leading edge of windward roof. Speed gradients exist in the horizontal direction and some shift in the location of the anemometer can influence the results. When the wind flows from South, speed gradients exist in the vertical direction and the height of the anemometer plays a significant role on the wind power available.

When the wind flows from East and West, the Library is in the wake of Gateway House and the Queens building respectively and the wind speed is significantly reduced. With the design related contributions ( $U_{KL}/U_{ref}$ ) equal to 0.39 and 0.32 and  $U_{ref} = 8$ , the mean wind speed at KL is 3.12 m/s and 2.56 m/s, while at this

height (21 m) the  $U_{ref,21}$  is around 5.8 m/s.

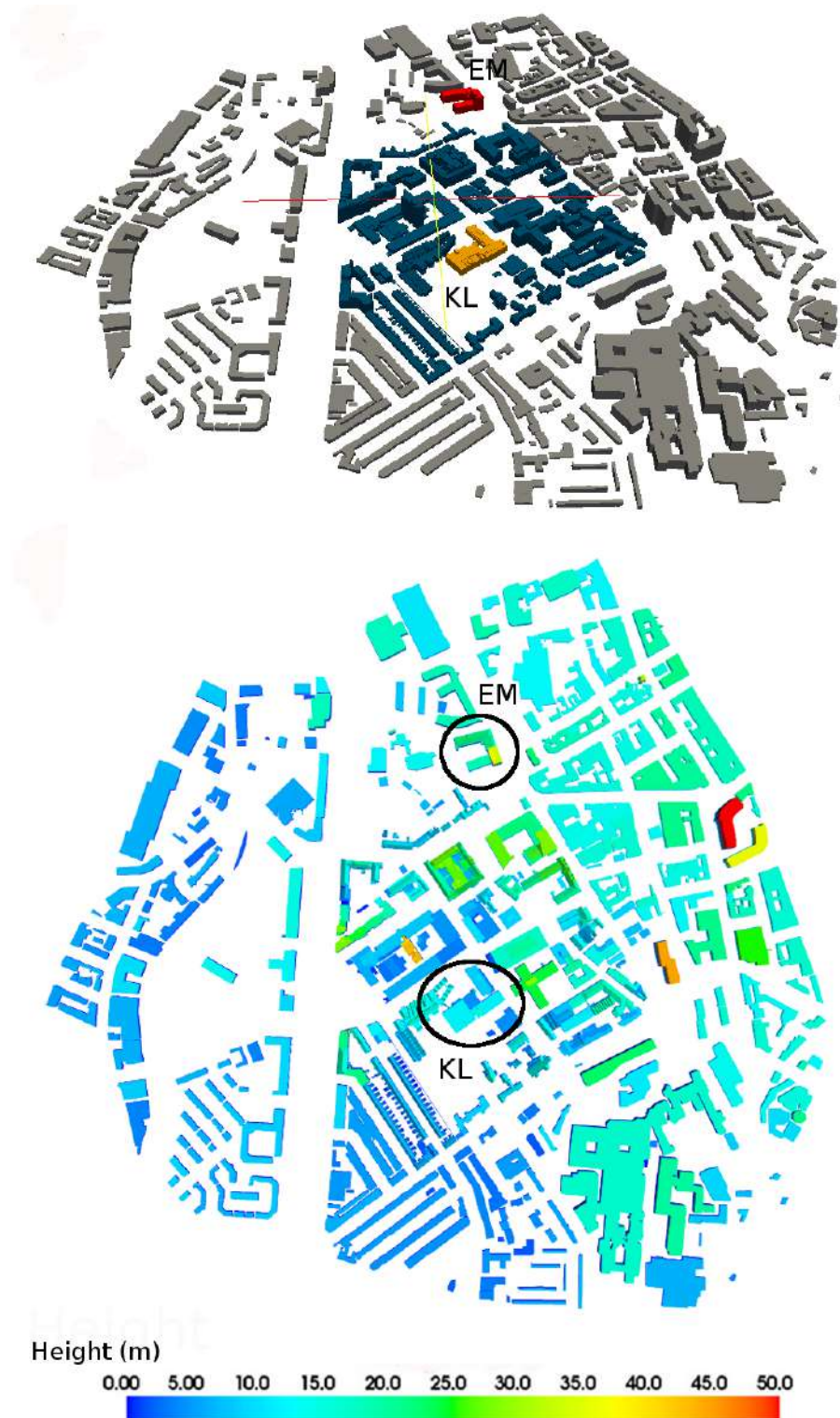


Figure 5.10: De Montfort university campus indicating (a) the position and (b) the height of Edith Murphy (EM) and Kimberlin Library (KL) buildings where the anemometers are located.

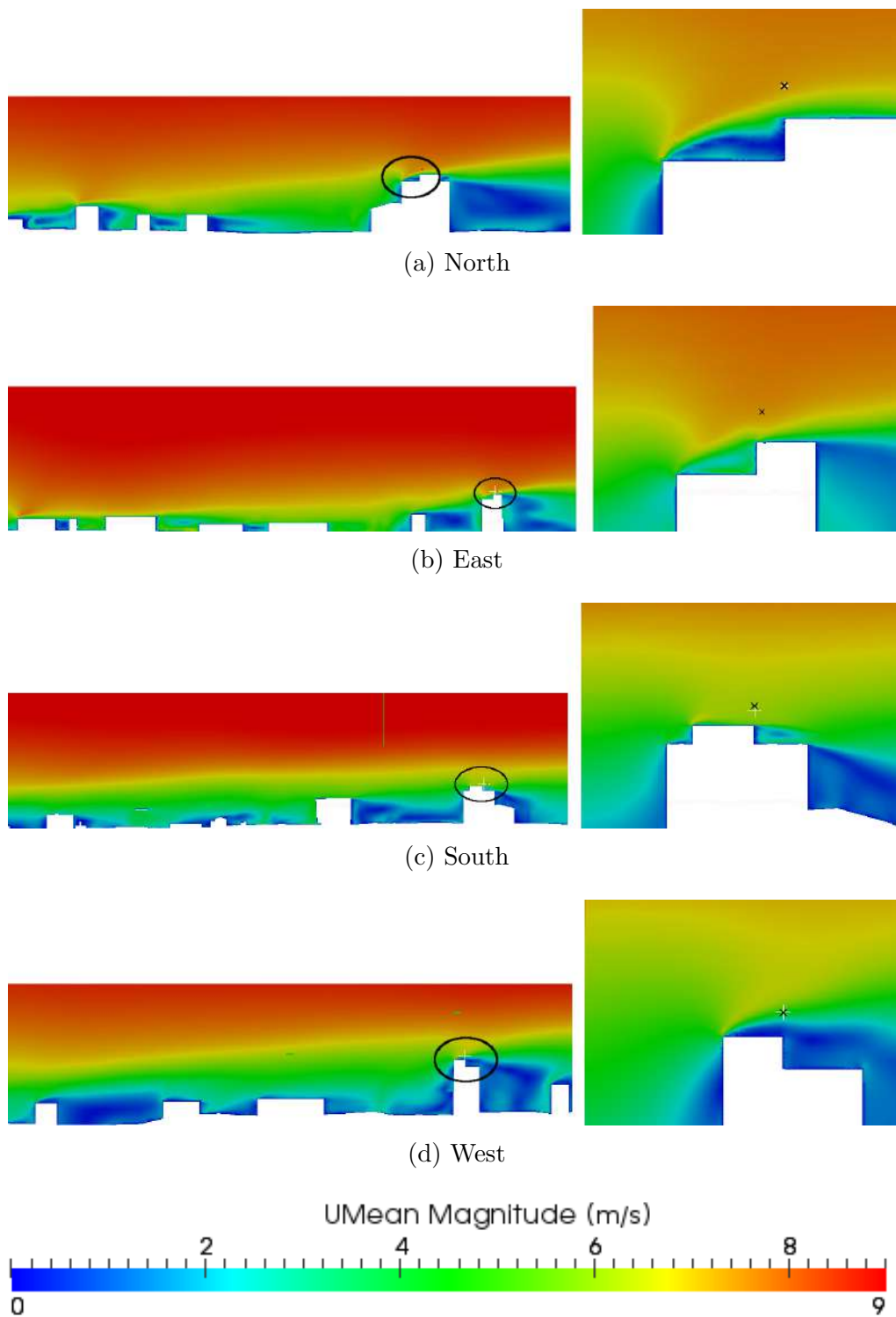


Figure 5.11: Wind flow at Edith Murphy (EM) for four directions. The right images zoom in the area captured by the black circle as indicated at the left image and the black symbol 'x' specifies the location where the measurements carried out.

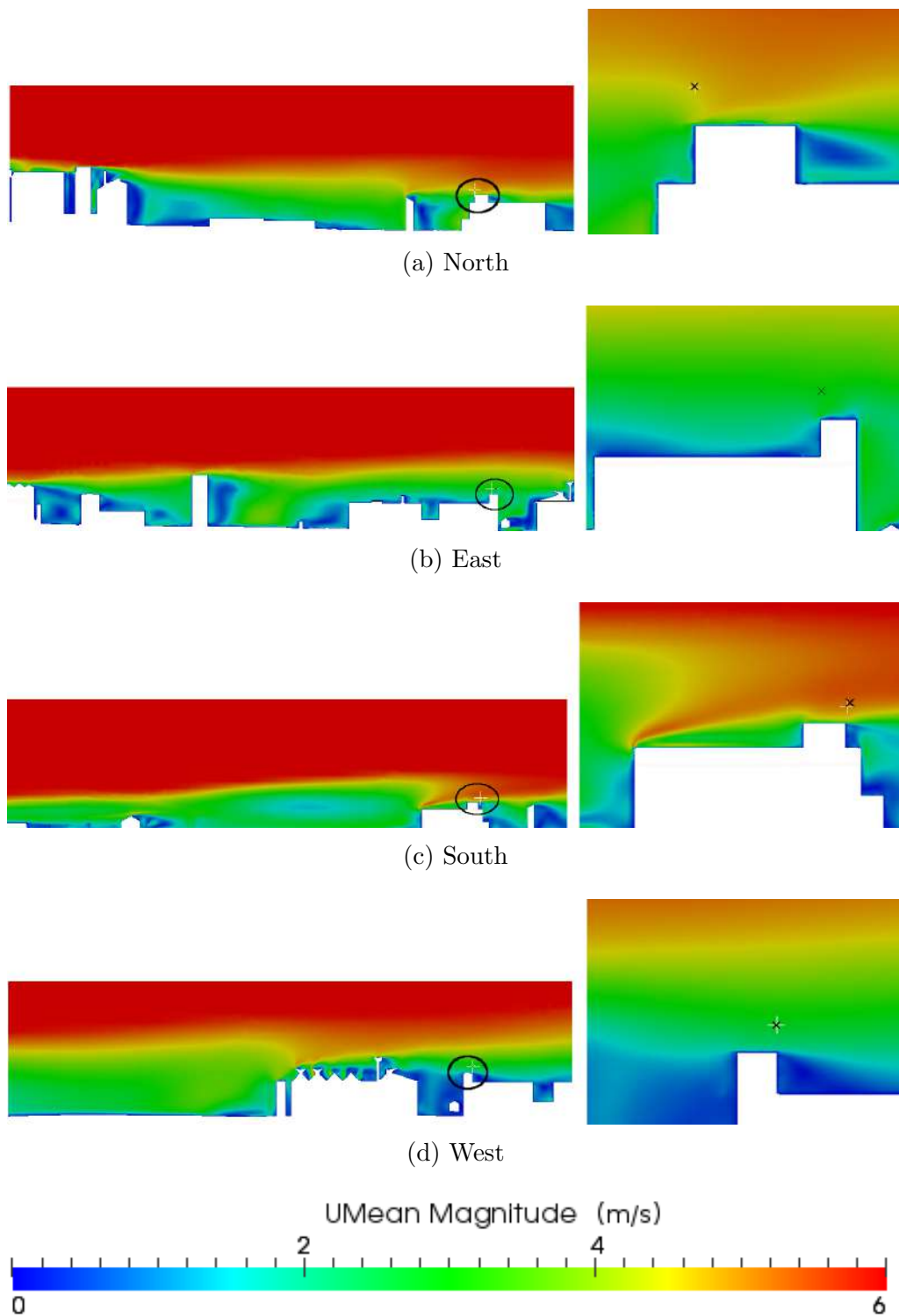


Figure 5.12: Wind flow at Kimberlin Library (KL) for four directions. The right images zoom in the area captured by the black circle as indicated at the left image and the black symbol 'x' specifies the location where the measurements were carried out.

## 5.4 Conclusions

Summarising, the overall agreement in  $\gamma$  values is very good. The discrepancies at some points are small and can be attributed to the approximations involved in the procedure (terrain related contributions and design related contributions) and the difficulty to extract the exact coordinates of the points of measurements. Noticeable speed gradients exist in the vertical direction and hence, even small shifts in the height of anemometers can influence considerably the results.

Although the ‘Wind Atlas Methodology’ [?] cannot handle well complex terrain [Veronesi et al., 2016] (the wind potential is often overestimated [Simoes and Estanqueiro, 2016]), it serves very well the purpose to transfer the meteorological data from the weather station to the height where the flow is considered to be horizontally homogeneous. Then, the CFD model can be used to account for the influence of individual obstacles on the wind flow, making corrections for local shadowing effects. It is indicative, that the predicted wind speed at KL (which is partially shadowed by QB) based on CFD calculations is 2.6 m/s (for the West wind flow), while the Wind Atlas Methodology calculates 5.3 m/s.

So, using this approach, the meteorological data is transferred from the East Midlands airport weather station to the edge of the DMU campus (terrain related contributions) to estimate the hourly annual wind speed for 2015 upstream of the site of interest. This data can be then combined with the results of the corrections indicated by the CFD model to make an annual assessment of the mean wind speed (Section 6.6.3) and the energy production (Section 6.6.4).

Regarding the type of weather data, it has been broadly accepted [Hong et al., 2013; Kneifel and O’Rear, 2014] that the typical meteorological year (TMY) files [Wilcox and Marion, 2008] are usually not representative of the ‘typical’ weather conditions for an area. According to Manwell et al. [2010], it takes five years data to arrive at

a reliable average annual wind speed at a given location, while the [EWEA \[2009\]](#) suggests that using a three-year rolling average of data, the deviation of the mean wind speed from long-term averages, is reduced from 10% for a single year to 3%. However, it only considered the variation in annual mean wind speed and has largely ignored the annual variability in wind speed frequency distribution, which is also important in assessing the uncertainty in the annual energy production. [Aspliden and Elliot \[1986\]](#) noted that one year of data is generally sufficient to predict long-term seasonal mean wind speeds within an accuracy of 10% with a confidence level of 90% and according to [Doggett](#) the use of a single contiguous year is favoured when examining a typical year.





# Chapter 6

## Micrositing

### 6.1 Introduction - Chapter overview

Micrositing is the procedure to identify the optimum location for wind turbine application. Usually, when CFD methods are used, it is based on simulations of the mean wind speed of the prevailing wind direction [Yang et al., 2016]. However, wind is not constant in terms of magnitude and direction during the course of a year. Thus, in this work, the whole annual hourly data was considered to estimate the average annual wind speed and the annual energy production (AEP) at each point of the domain and each direction (3D wind maps). Essentially, these 3d maps will enable identification of the effects of the complex urban topography on the wind flow, and the potential locations for micro wind turbines installation.

The procedure makes use of a combination of the climate data at the region of interest with the CFD results to calculate the mean wind speed and then, considering the power characteristics of the micro wind turbines estimates the energy yield.

In the next sections, processing and analysis of the climate data, the CFD results and the power characteristics of a wind turbine in order to develop the 3d wind maps are described.

## 6.2 Processing the regional climate data

In Chapter 5 a method to transfer the wind data from a remote meteorological station (usually from the nearest airport) to the urban site of interest was described. These data contain the hourly wind speed and direction values at a reference point at 60 m height, where the flow is considered not to be affected by the individual obstacles.

In order to use the climate data in combination with the CFD results for wind resource assessment, they are divided into bins in terms of 4 wind directions (N, E, S, W), equivalent to those used in the CFD simulations. Then the wind speed values ( $u_i$ ) are summed up for each direction (d) and the sums are divided with the number of the total wind records (n) (n = 8760 if the annual hourly climate data is complete) to calculate the  $F_d$  values ( $F_d = \sum u_{i,d}/n$ ) (Table 6.1). These are the weighted average wind speed values for each direction that will be used later (see Section 6.3) to calculate the mean wind speed and develop the 3d wind speed map of DMU campus. A Python script has been developed to automate the procedure.

Wind direction	F values
N	$\sum u_{i,N} / n = F_N$
E	$\sum u_{i,E} / n = F_E$
S	$\sum u_{i,S} / n = F_S$
W	$\sum u_{i,W} / n = F_W$

Table 6.1: Calculation procedure of F values.

To estimate the annual energy yield (see Section 6.5) the climate data is divided in bins in terms of wind speed as well as wind direction. Table 6.2 clarifies the process, where  $f$  values represent the number of occurrences of the data divided

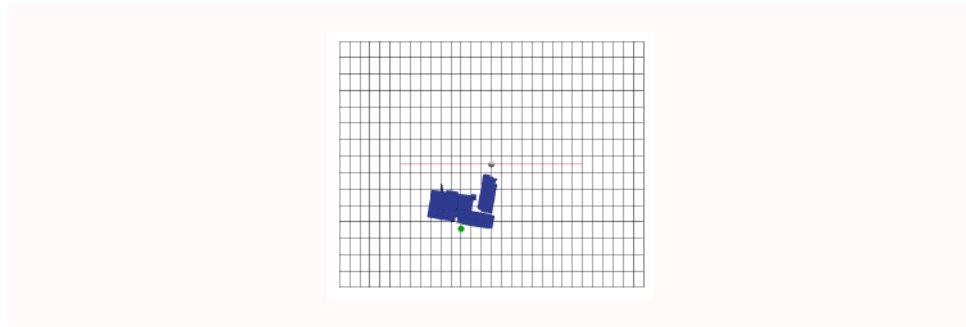
by wind speed bins for each direction. Short-range bins are used, to minimise the error of rounding the wind speeds to the mean value of the bin and the number of the wind speed bins depends on the range of the wind data as will be described in Section 6.6.4, where the method is applied at DMU campus. Section 6.5 describes then how the  $f$  values are used during the process to estimate the annual energy production at every point of the domain.

Wind direction	Wind speed					
	bin 1	bin 2	bin 3	bin 4	...	...
N	$f_{1,N}$	$f_{2,N}$	$f_{3,N}$	$f_{4,N}$	...	...
E	$f_{1,E}$	$f_{2,E}$	$f_{3,E}$	$f_{4,E}$	...	...
S	$f_{1,S}$	$f_{2,S}$	$f_{3,S}$	$f_{4,S}$	...	...
W	$f_{1,W}$	$f_{2,W}$	$f_{3,W}$	$f_{4,W}$	...	...

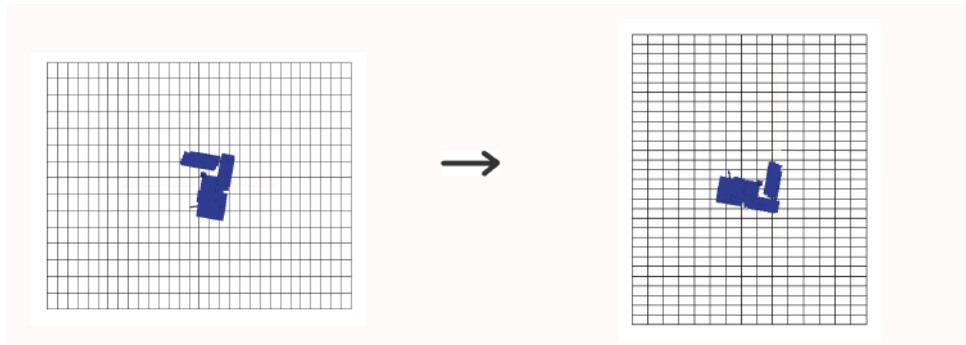
Table 6.2: Climate data divided in bins in terms of wind direction as well as wind speed;  $f$  represents the number of occurrences the data are into the range of a wind speed bin for each direction.

### 6.3 Processing the CFD results

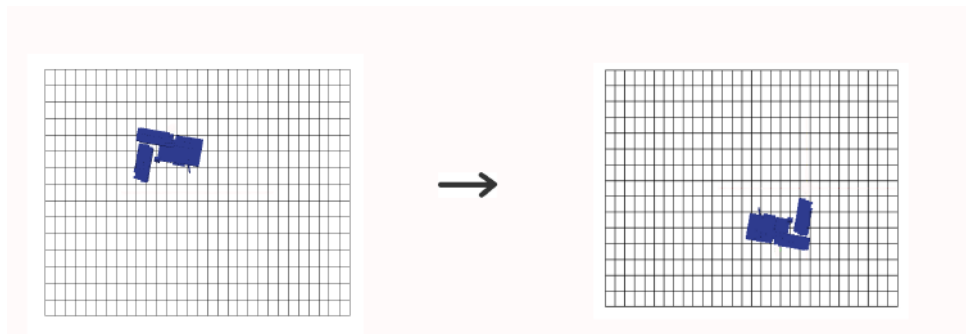
Having run the CFD model for each direction, the development of a single model which contains information from all the directions requires the use of the same mesh coordinates. For this purpose, the `rotateMesh` OpenFOAM application, which rotates both the mesh and fields from one direction to another, so as the corresponding points of each case (direction) have the same coordinates, was used. Figure 6.1 demonstrates the process of rotating the mesh for four wind directions, however, it can be applied to as many wind directions as required.



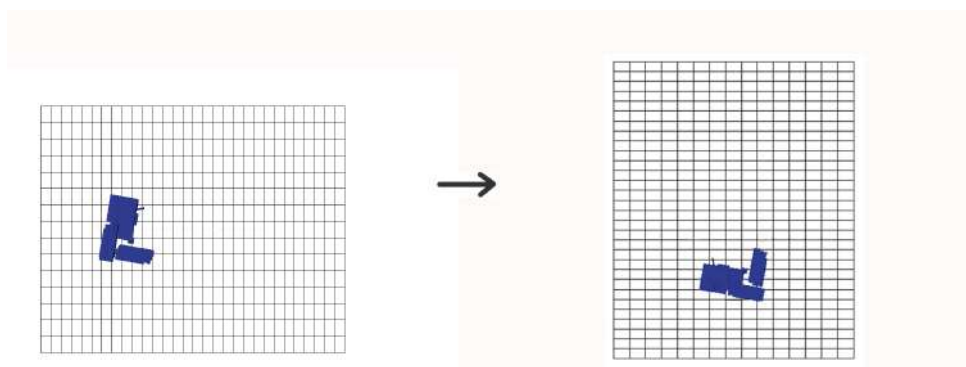
(a) West



(b) North to West



(c) East to West

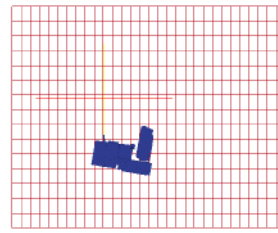


(d) South to West

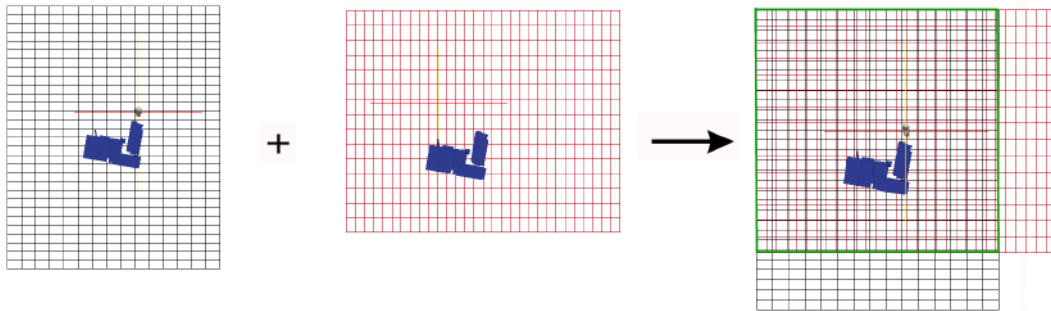
Figure 6.1: Rotation of the mesh of each case (directions North, East and South) to the same direction (West) in order to be comparable and the corresponding points have the same coordinates.

Then, the `mapFields` utility maps the fields related to the mesh of each case onto the corresponding fields associated to the mesh for the direction they were all rotated to (Figure 6.2). In this way, the meshes of all models are analogous and hence the fields can be compared and processed with each other.

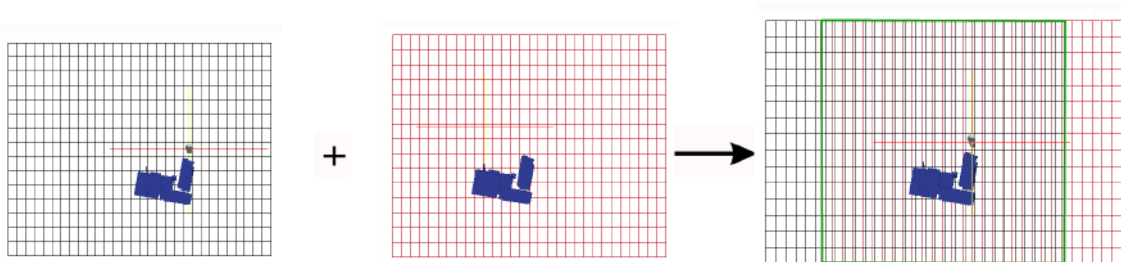
However, the fields for each case are related to a particular inlet velocity profile. To create scalar fields associated to each wind direction, known as reduction factors (RF), the velocity fields should be divided by the reference velocity (velocity at 60 m height in this work,  $RF_i = U_i/U_{ref60}$ ). For this purpose, the `reductionFactors` OpenFOAM utility was developed to automate the process. When these values are multiplied by any reference velocity in the given direction, they will produce the corresponding wind speed values for the whole domain (Figure 6.3) and hence they can be used in combination with the climate data for wind resource assessment purposes.



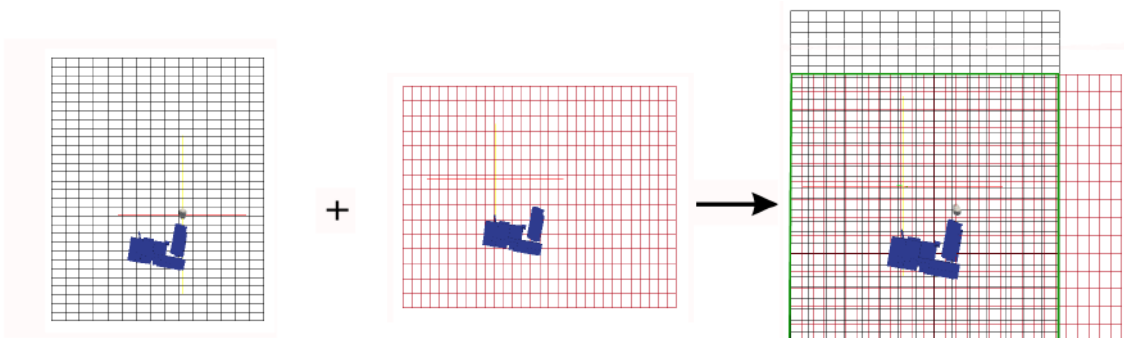
(a) West



(b) Mapfield North fields to the mesh of West direction



(c) Mapfield East fields to the mesh of West direction



(d) Mapfield South fields to the mesh of West direction

Figure 6.2: `MapField` utility maps the fields related to the mesh of each case (directions North, East and South) onto the corresponding fields associated to the mesh for the direction they were all rotated to (West direction).

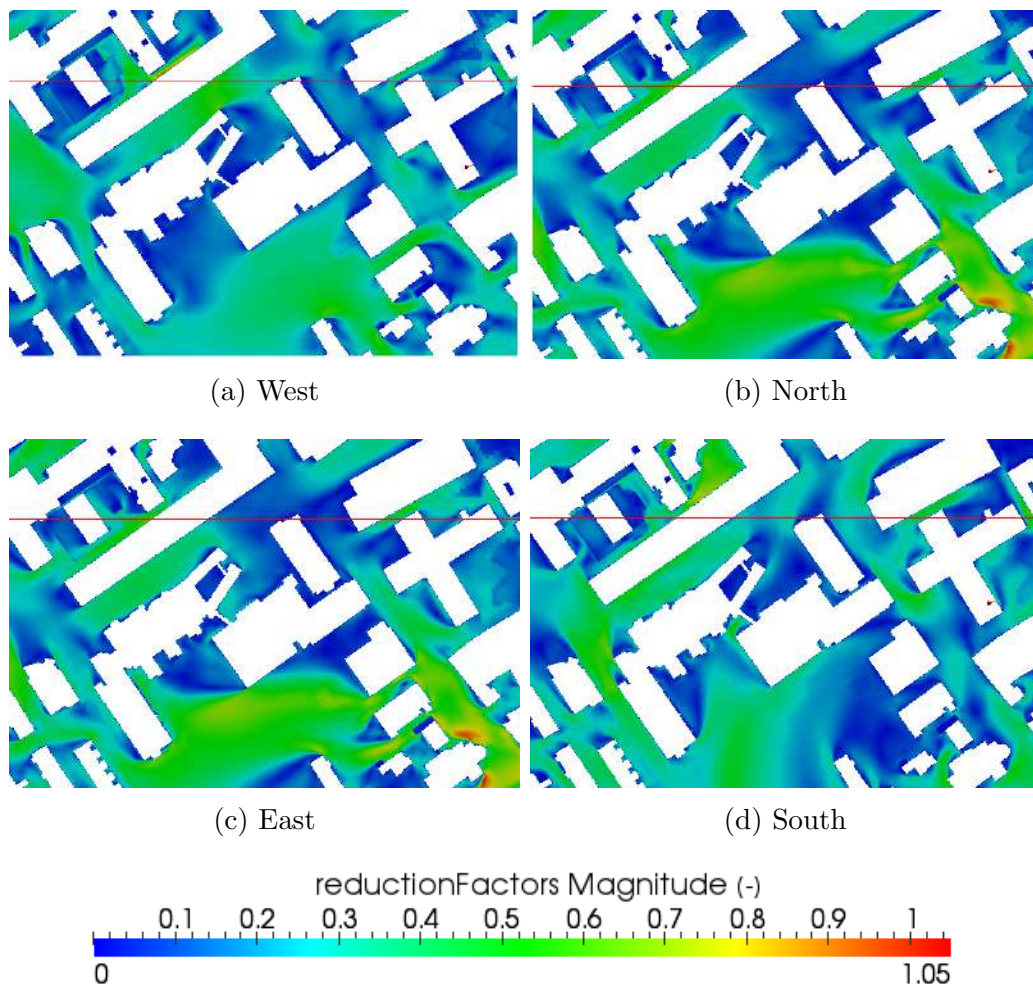


Figure 6.3: Reduction factors for each direction.

## 6.4 Mean annual wind speed - 3d map

To assess the wind energy resource at a site, the first step is to develop a 3D wind speed map, i.e. a 3D data set of the average annual wind speed, combining the annual hourly climate data with the CFD results.

Figure 6.4 illustrates the procedure. Specifically, to calculate the mean annual wind speed at each point of the domain, the  $F$  values (see Section 6.2) for each direction are multiplied with the corresponding (in terms of wind direction) reduction factors (RF) (see Section 6.3) and the products are summed.



		Regional wind direction				Applications
		N	E	S	W	
1	<u>Processing the regional climate data (section 6.2)</u> $U_{i,d} + U_{i,d} + U_{i,d} + \dots + \dots = \Sigma U_{i,d} / n = F_d$					<b>Developed:</b> cdata.py
	F <sub>N</sub>		F <sub>E</sub>	F <sub>S</sub>	F <sub>W</sub>	
2	<u>Processing the CFD results (section 6.3)</u>					<b>Existing:</b> rotateMesh (OF)  MapFields (OF)  <b>Developed:</b> reductionFactors (OF)
	A)					
	B)					
C)		$U / U_{ref} = RF$				
RF <sub>N</sub>		RF <sub>E</sub>	RF <sub>S</sub>	RF <sub>W</sub>		
3	<u>Mean annual wind speed (section 6.4)</u> $\Sigma F_d \times RF_d$					<b>Developed:</b> windMap (OF)
	F <sub>N</sub> x RF <sub>N</sub>		F <sub>E</sub> x RF <sub>E</sub>	F <sub>S</sub> x RF <sub>S</sub>	F <sub>W</sub> x RF <sub>W</sub>	
4	<u>Visualization</u>					<b>Existing:</b> foamToVTK (OF)

Figure 6.4: Illustration of the methodology to calculate the annual mean wind speed at each point of the domain (3d map). The applications used at each step are mentioned at the right side of each step.

Since the aim is to produce a 3D view of the whole domain, dealing with a data set containing vast amounts of records, the process again is automated. An OpenFOAM utility, entitled `windMap`, was created to multiply the F values with the corresponding fields of RF values. The `foamCalc` utility was used to calculate the magnitude of the wind velocity and using the `foamTimeSum`—a modification of `foamTimeAverage` utility developed by Eelco van Vliet [Vliet]— to calculate the arithmetic averages over the whole year to find the spatially varying annual mean wind speeds.

Although vertical axis wind turbines, which operate for every wind direction, are mostly suggested for installation in urban areas by many recent works [Abraham et al., 2012; Ayhan and afak Salam, 2012; Bhutta et al., 2012] speeds calculated only in the horizontal plane have been derived for investigation of horizontal axis wind turbine applications. This calculation was made using a similar method to `windMap` utility (`windMapXY`), which excludes the wind speed values in the z direction.

To visualise the results and produce the 3D wind speed map, the datasets were first converted to `.vtk` format files using the `foamToVTK` utility. Then, the ‘ParaView’, an open-source multi-platform visualization application, was used to open these files, as it supports distributed computational models to process large data sets [ParaView].

In Section 6.6.3 the 3d wind speed map of DMU campus is produced and the procedure is explicitly demonstrated.

## 6.5 Annual energy production (AEP) - 3d map

To predict the annual energy yield the CFD results are combined with the hourly climate data and the power curve of the potential micro wind turbine. Generally, multiplying the regional wind speed data with the corresponding (in terms of the wind direction) reduction factors, the hourly wind speed for any location in the

domain is obtained. Then, the power curve of a micro-wind turbine is combined with the wind speed to calculate the annual energy yield. This is the estimate of the energy production if the particular turbine were located at that point.

The procedure is described in detail in Figure 6.5 and the steps are outlined as follows.

1. To obtain the velocity field at each point of the domain for every regional wind velocity, the mean wind speed of the bins (Table 6.2) is multiplied with the reduction factors in each direction.
2. Then, the wind speed in horizontal plane ( $xy$ ) is calculated, for assessment of the horizontal axis wind turbines (HAWTs), and in 3d space ( $xyz$ ) for assessment of vertical axis wind turbines (VAWTs) installations.
3. For each wind speed in the domain, the power output is estimated, interpolating the power values of a known power curve to find the power field for every regional mean wind speed.
4. To calculate the annual energy yield, the power values are multiplied by the  $f$  values (Table 6.2) —the number of occurrences the data are into the range of a wind speed bin for each direction— and the fields for every mean wind speed and every direction are summated.

The methodology includes the synthesis and manipulation of a huge amount of data, thus, applications in Python programming language and OpenFoam utilities were developed to automate the process and they are noted in Figure 6.5 at the right side of each step. The procedure is further illustrated in Section 6.6 where it is used to assess the wind resource at the DMU campus.

Regional wind direction					Applications				
					N	E	S	W	
1					<b>Developed:</b> vRF (OF)				
	Vel1,N Vel2,N ...		Vel1,E Vel2,E ...		Vel1,S Vel2,S ...		Vel1,W Vel2,W ...		
2					<b>Developed:</b> vRF_xy (OF) magvRF_xy (OF)				
	mag1,N (xy-xyz) mag2,N (xy-xyz) ...		mag1,E (xy-xyz) mag2,E (xy-xyz) ...		mag1,S (xy-xyz) mag2,S (xy-xyz) ...		mag1,W (xy-xyz) mag2,W (xy-xyz) ...		<b>Existing:</b> foamCalc (OF)
3					<b>Developed:</b> interpolate.py				
	P1,N (xy-xyz) P2,N (xy-xyz) ...		P1,E (xy-xyz) P2,E (xy-xyz) ...		P1,S (xy-xyz) P2,S (xy-xyz) ...		P1,W (xy-xyz) P2,W(xy-xyz) ...		
4	$P_{i,d} (xy-xyz) \times f = E_{i,d}$				<b>Developed:</b> energy (OF) energyTotal (OF) energyD (OF)				
	E1,N (xy-xyz) E2,N (xy-xyz) ...		E1,E (xy-xyz) E2,E (xy-xyz) ...		E1,S (xy-xyz) E2,S (xy-xyz) ...		E1,W (xy-xyz) E2,W(xy-xyz) ...		$E_{total} = \sum E_{i,d}$

Figure 6.5: Illustration of the methodology to calculate the annual energy production at each point of the domain (3d map) as it is explained step by step in Section 6.5. The applications used at each step are also mentioned.

## 6.6 Case study: DMU campus

The procedure detailed above has been applied to the DMU campus to assess the wind resource and identify the optimum locations for micro wind turbines installation. To calculate the annual mean wind speed, the East Midlands airport climate data for the year of 2015 was used (Chapter 5) and the CFD model of the DMU campus, which described in Chapter 4. Then, the power data of a 5 kW horizontal axis small wind turbine is used to estimate the annual energy production. The procedure is presented in detail in the following sections.

### 6.6.1 Processing the regional climate data

As reported in Chapter 5, using the Wind Atlas Methodology [Landberg et al., 2003], the meteorological data from East Midlands airport weather station were transferred to the edge of DMU campus at 60 m height and the hourly annual wind data for the year 2015 were obtained. Figures 6.6 and 6.7 present the extrapolated wind data (wind speed and direction respectively) for this period of time.

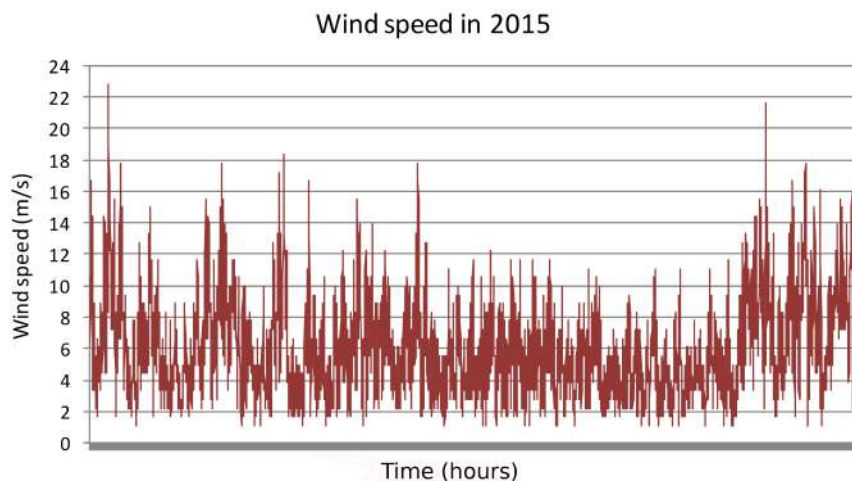
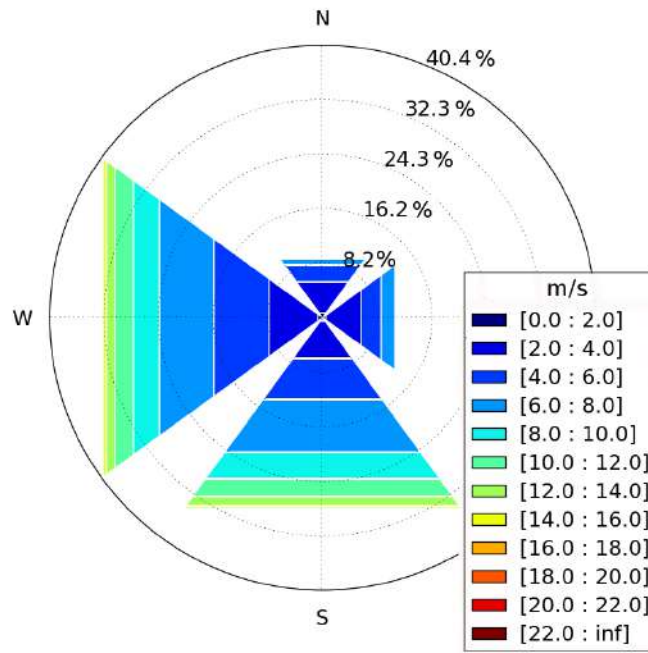
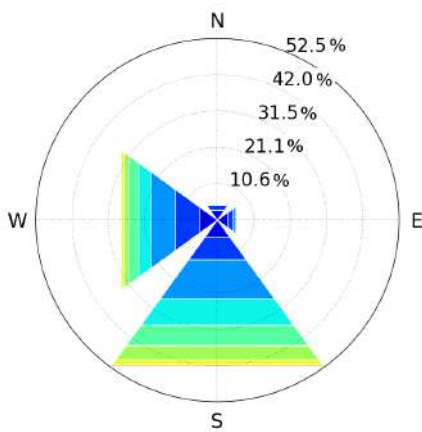


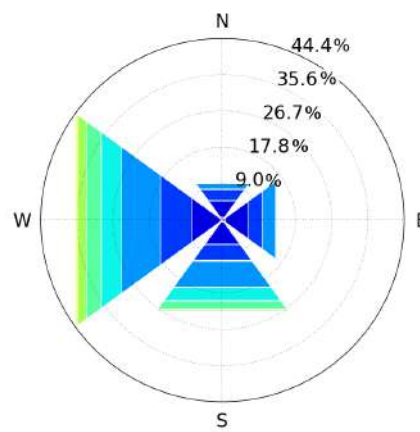
Figure 6.6: Wind speed hourly data in the DMU region for the year 2015, transferred from the East Midlands airport weather station.



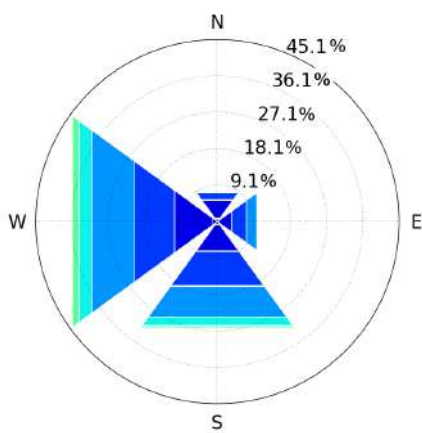
(a) all year



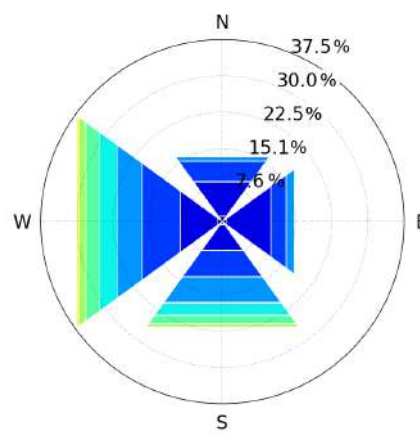
(b) Dec-Feb



(c) Mar-May



(d) Jun-Aug



(e) Sep-Nov

Figure 6.7: Wind roses for DMU wind data for the year 2015.

There are 8166 data records instead of 8760 of a complete year (i.e. 93.2 %), since the MIDAS database, where the climate data retrieved from, was not complete. The annual average wind speed is around 6 m/s with a maximum of 22.8 m/s during January (Figure 6.6). Figure 6.8 shows the average wind speeds for each season of the year. During winter (Dec-Feb) the wind speed increases to an average of 7.2 m/s, in spring (Mar-May) it is in the average range (6 m/s), while during summer and autumn it slightly reduces to 5.3 m/s.

The prevailing wind directions are the west, with the 40% of the data falling in this directional sector and the south (35% of the data). This is followed by the East wind direction with only 14% of the data into this range and the North (11% of the data). Figure 6.7 shows the prevailing wind directions at each period of the year. The West direction is the dominant, except for the winter period (Dec-Feb), when the wind blows mostly from the South.

To develop the 3d wind speed map, the climate data are divided into bins in terms of 4 wind directions, the same as for the CFD simulations i.e. North, East, South and West. Then, the wind speed values of each direction were summed and divided by the number of the wind records (i.e. 8166) to calculate the weighted average wind speed values,  $F_d$ , as described in Section 6.2. In accordance with Table 6.1, Table 6.3

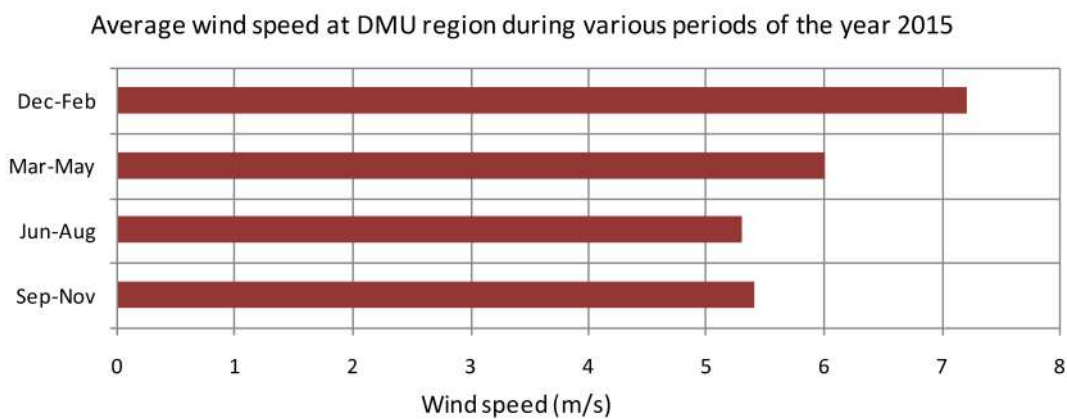


Figure 6.8: Average wind speed at DMU region for various periods of the year 2015.

shows the F values as calculated for the climate data for the DMU region for 2015. Moreover, the number of the data records and the average wind speed of each wind direction were calculated. The west is the prevailing wind direction and it gives the highest F value (2.61), followed by the F value for the South direction (2.38), and then the East and North directions with F values of 0.58 and 0.44 respectively. It means that the wind flows predicted by the CFD simulations for the West and South direction will have the dominant impact on the calculated mean wind speed field (Section 6.6.3).

For energy yield estimations the climate data is divided in bins in terms of wind directions as well as wind speed (Table 6.4, Figure 6.9). Short-range bins of 1 m/s (from 2 m/s to 23 m/s) were chosen in order to minimise the error in rounding the wind speeds to the mean value of the bin range. The importance of the error for larger wind bins of 2 m/s (Table 6.5, Figure 6.10) is investigated in Section 6.6.4. The first bin (0-2 m/s) was not divided into smaller ranges as most of wind turbines are not operated for such small wind speeds (cut-in wind speed  $>2$  m/s). The number of the wind bins is controlled by the maximum wind speed, so all the records are accommodated.

Wind direction	F values	Number of records	Average wind speed
N	3560 / 8166 = 0.44	895 (11%)	4.0 m/s
E	4741 / 8166 = 0.58	1099 (14%)	4.3 m/s
S	19440 / 8166 = 2.38	2875 (35%)	6.8 m/s
W	21295 / 8166 = 2.61	3297 (40%)	6.5 m/s

Table 6.3: F values for each wind direction as calculated for the climate data at DMU region for 2015.



Wind speed bins (m/s)	Wind direction			
	N	E	S	W
0-2	69	49	49	72
2-3	223	250	236	290
3-4	241	274	325	437
4-5	104	103	205	265
5-6	157	196	411	558
6-7	55	146	451	459
7-8	25	63	331	353
8-9	13	17	293	273
9-10	1	0	105	113
10-11	5	0	158	170
11-12	1	1	107	107
12-13	0	0	87	80
13-14	1	0	53	49
14-15	0	0	19	23
15-16	0	0	27	27
16-17	0	0	12	7
17-18	0	0	6	6
18-19	0	0	0	2
19-20	0	0	0	1
20-21	0	0	0	2
21-22	0	0	0	2
22-23	0	0	0	1

Table 6.4: Climate data at DMU region for 2015 divided in bins of 1 m/s in terms of four wind directions (North, East, South and West) as well as wind speed.

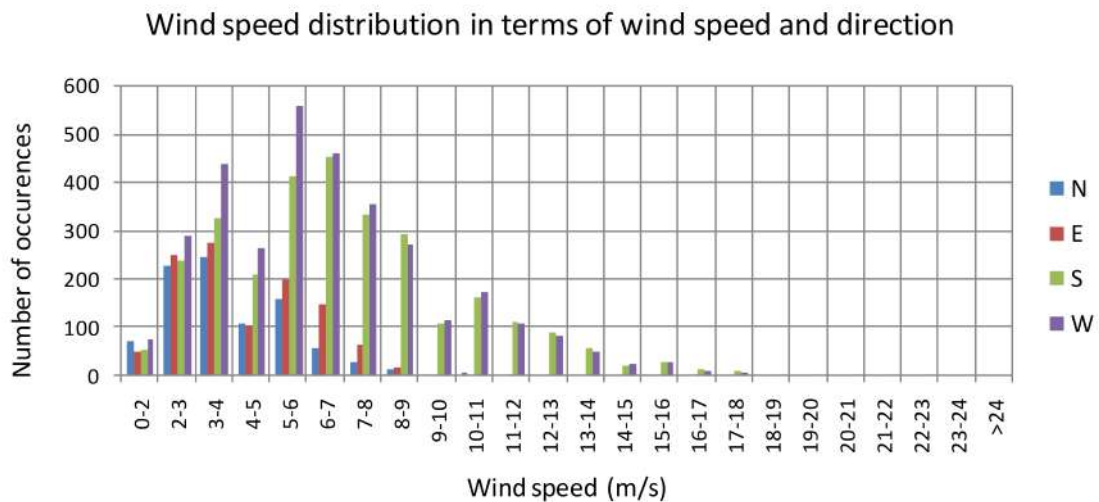


Figure 6.9: Wind speed distribution in terms of wind speed (bins of 1m/s) and direction (four wind directions: N, E, S and W) for the year 2015

Wind speed bins (m/s)	Wind direction			
	N	E	S	W
0-2	69	49	49	72
2-4	464	524	561	727
4-6	261	299	616	823
6-8	80	209	782	812
8-10	14	17	398	386
10-12	6	1	265	277
12-14	1	0	140	129
14-16	0	0	46	50
16-18	0	0	18	13
18-20	0	0	0	3
20-22	0	0	0	4
22-24	0	0	0	1

Table 6.5: Climate data at DMU region for 2015 divided in bins of 2 m/s in terms of four wind directions (North, East, South and West) as well as wind speed.

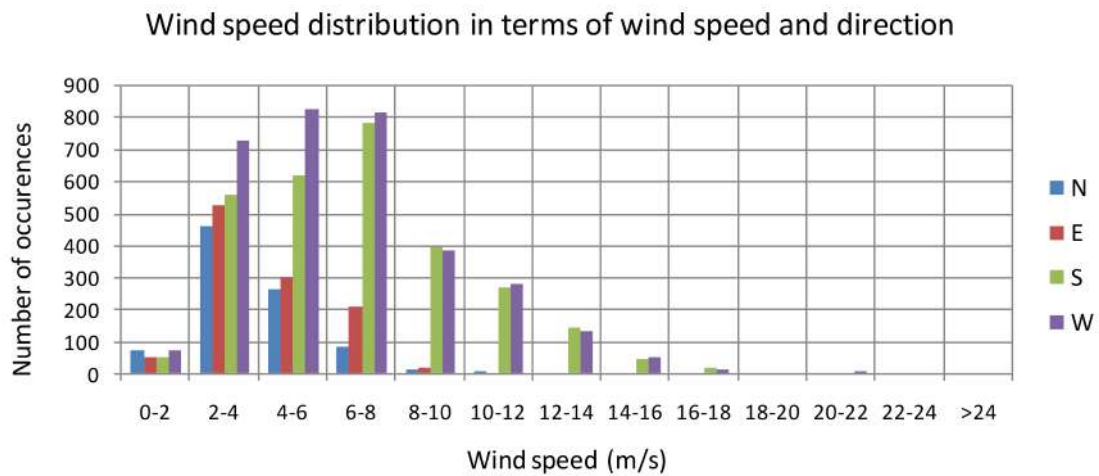


Figure 6.10: Wind speed distribution in terms of wind speed (bins of 2m/s) and direction (four wind directions: N, E, S and W) for the year 2015

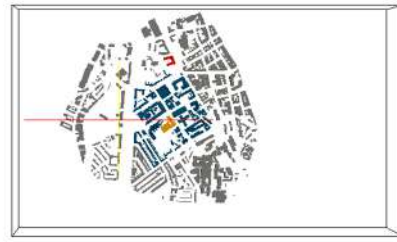
### 6.6.2 Processing the CFD results

To develop a single CFD model, which combines the velocity fields as calculated for each wind direction simulated, all the fields should refer to the same meshes.

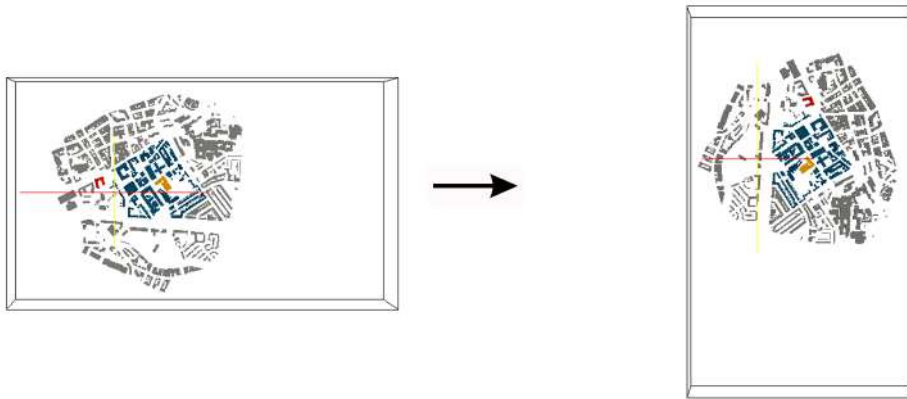
Therefore, first the meshes and the corresponding fields are rotated from the direction the simulations are performed to a reference direction using the `rotateMesh` OpenFOAM application as explained in Section 6.3. In this work, simulations have implemented for the four cardinal directions (North, East, West and South) and used the West wind direction as the reference that all the other models will be rotated to, as shown in Figure 6.11.

Then, the rotated fields, which relates to the mesh developed for each direction are mapped onto the reference mesh i.e. onto the mesh for the CFD model associated to West wind direction (Figure 6.12). The green square denotes the common area of the CFD models, which surrounds the area of interest.

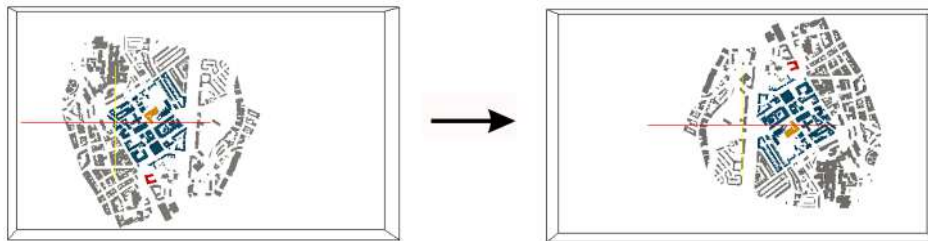
Finally, in order to create generic fields (reduction factors), which are independent of the inlet velocity and can be extrapolated to any velocity, they are divided by the reference velocity at 60 m from the ground (8 m/s in our study). Then, when these generic fields are multiplied by any reference velocity, the wind speed at any location in the domain can be predicted. Figure 6.13 illustrates the analogy between the two fields; the initial velocity field was scaled down 8 times (8 m/s the reference velocity) and the scale range adjusted from 0-11.51 to 0-1.43.



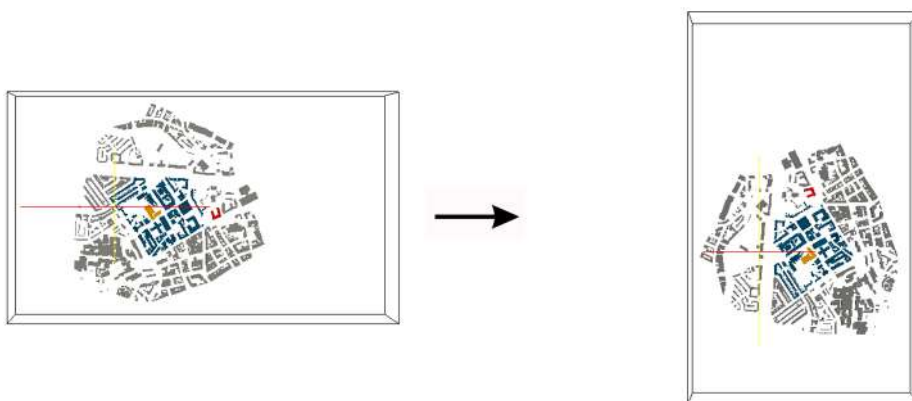
(a) West



(b) North to West



(c) East to West



(d) South to West

Figure 6.11: Rotation of the mesh of each case (directions North, East and South) to the same direction (West) in order to be comparable and the corresponding points have the same coordinates.

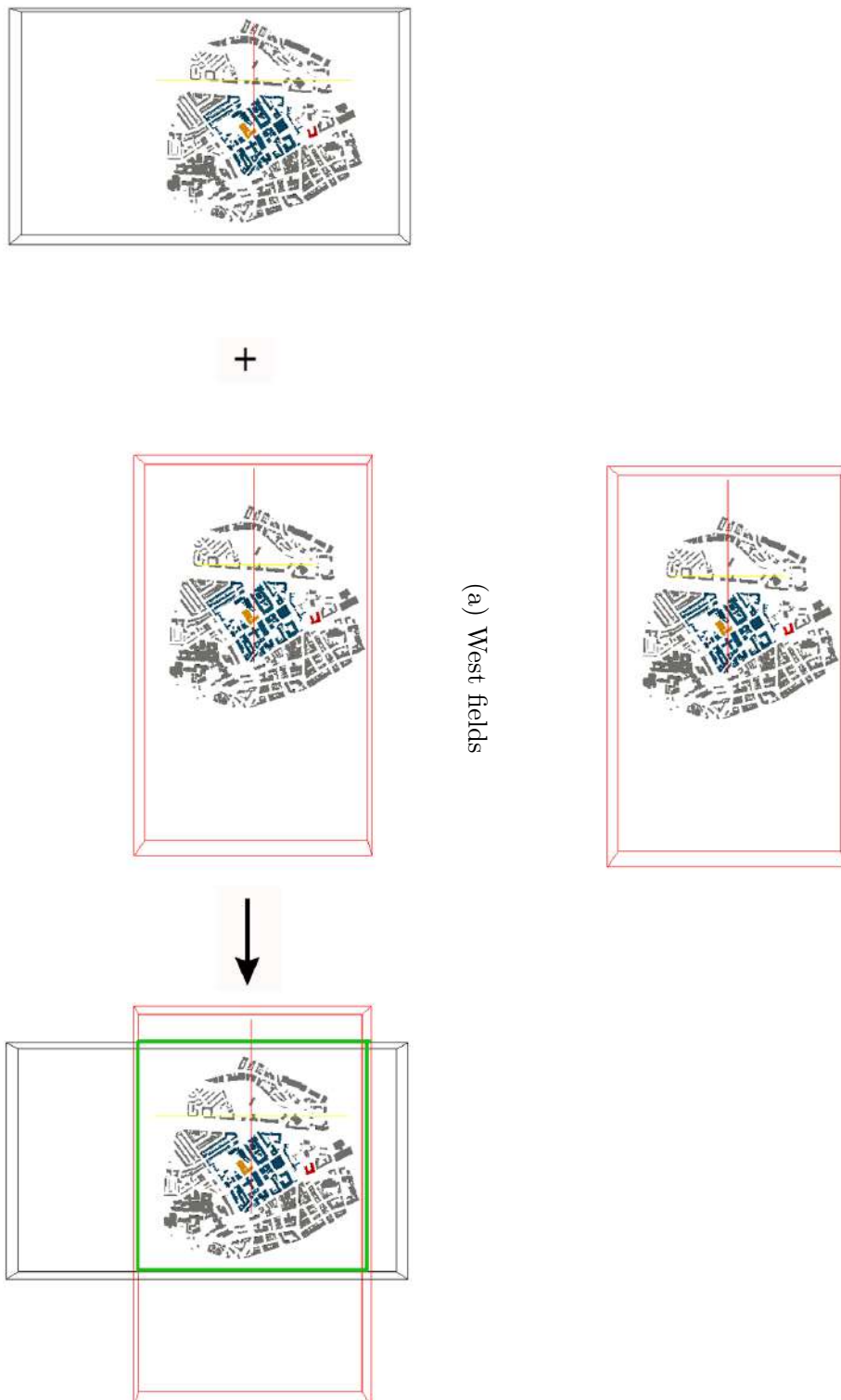
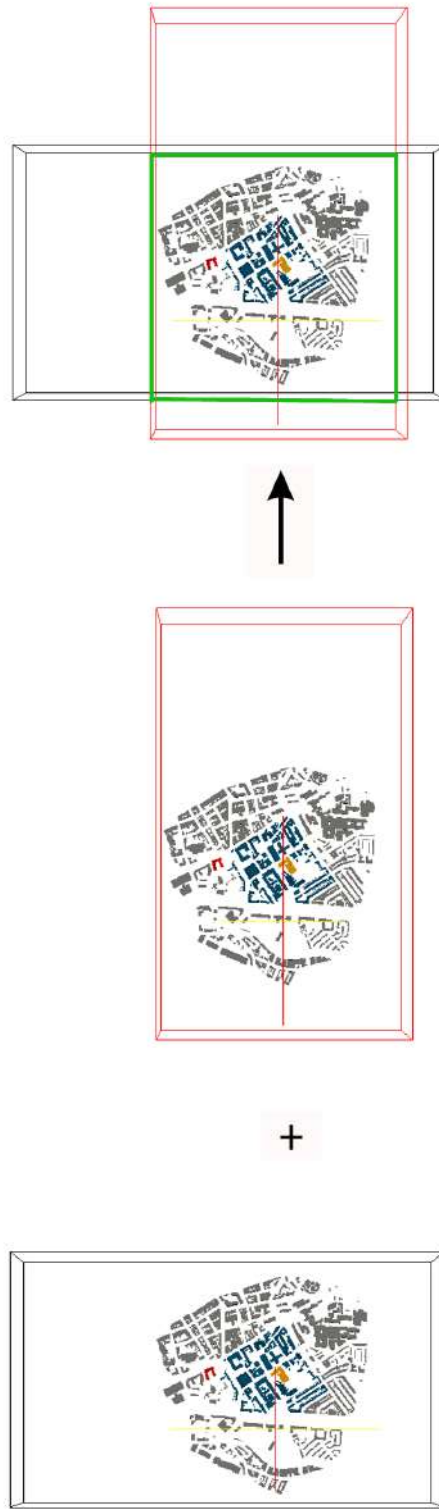


Figure 6.12: **MapField** utility maps the fields related to the mesh for the direction they were all rotated to (West direction) onto the corresponding fields associated to the mesh for the direction they were all rotated to (West direction).

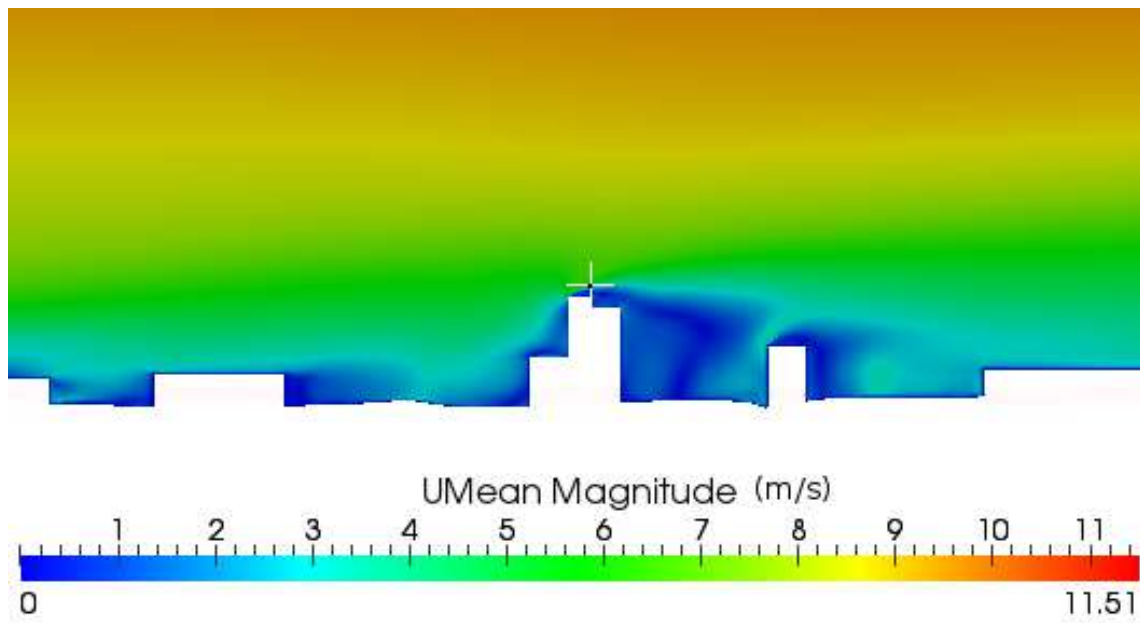


(c) Mapfield East fields to the mesh of West direction

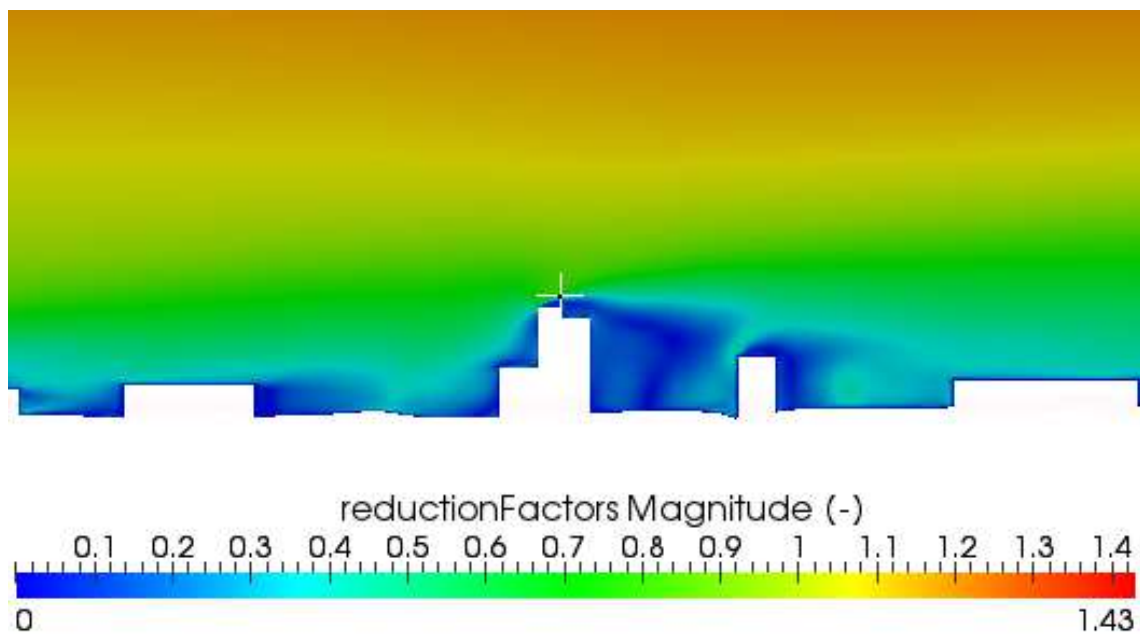


(d) Mapfield South fields to the mesh of West direction

Figure 6.12: MapField utility maps the fields related to the mesh of each case (directions North, East and South) onto the corresponding fields associated to the mesh for the direction they were all rotated to (West direction).



(a) UMean



(b) Reduction factors

Figure 6.13: Maps of the velocity field and the corresponding reduction factor field for the West wind direction CFD model.

### 6.6.3 Mean annual wind speed - 3d map

Using the reduction factors and the annual hourly climate data, the wind speed distribution at any location in the domain can be estimated.

Figure 6.14 shows the wind speed distribution at EM and KL; the corresponding reduction factors for each direction are shown in Figure 6.15. As expected, the reduction factors at KL are lower than they are at EM, which is one of the highest buildings at DMU campus as well as the location of the anemometer is high enough not to be into the separation zone of reduced speed on the roof, as explained in Section 5.3.4 and illustrated in Figure 5.11. Hence, the wind speeds at EM are higher than they are at KL.

As regards the most favourable wind directions, East and North are the most unobstructed winds for the EM building with high reduction factors (around 0.9). It follows the South wind direction with 0.75 reduction factor and last is the west direction (the prevailing wind direction), where the wind speed is almost halved of the reference wind speed (0.57 RF).

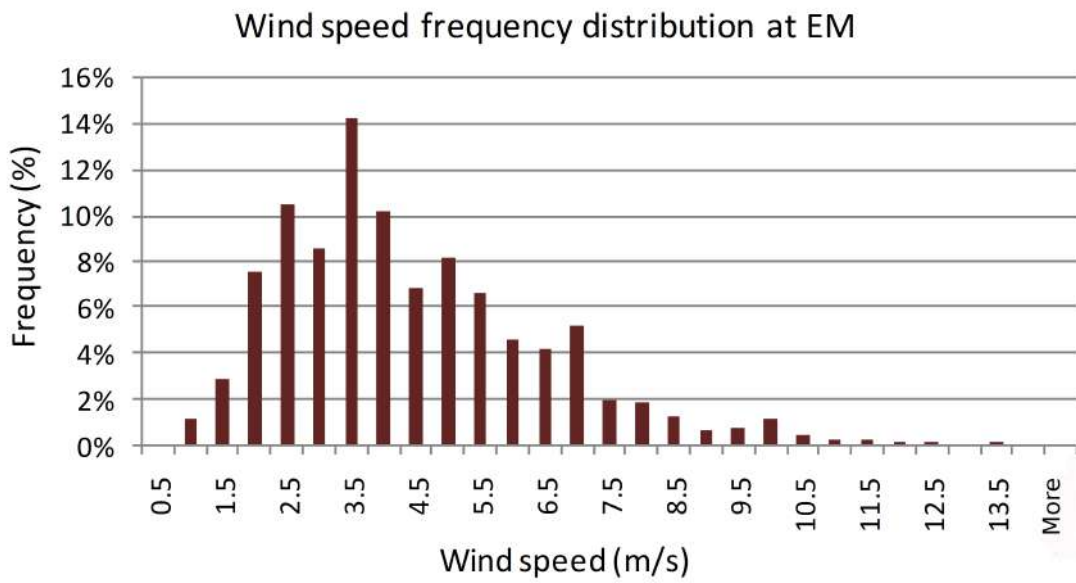
At KL, South and North are the most beneficial wind direction (RF of around 0.6) and follow the East and West direction with 0.39 and 0.32 RF respectively.

To calculate the mean annual wind speed field, the reduction factors should be multiplied with the corresponding F values (Table 6.3) and sum up the results.

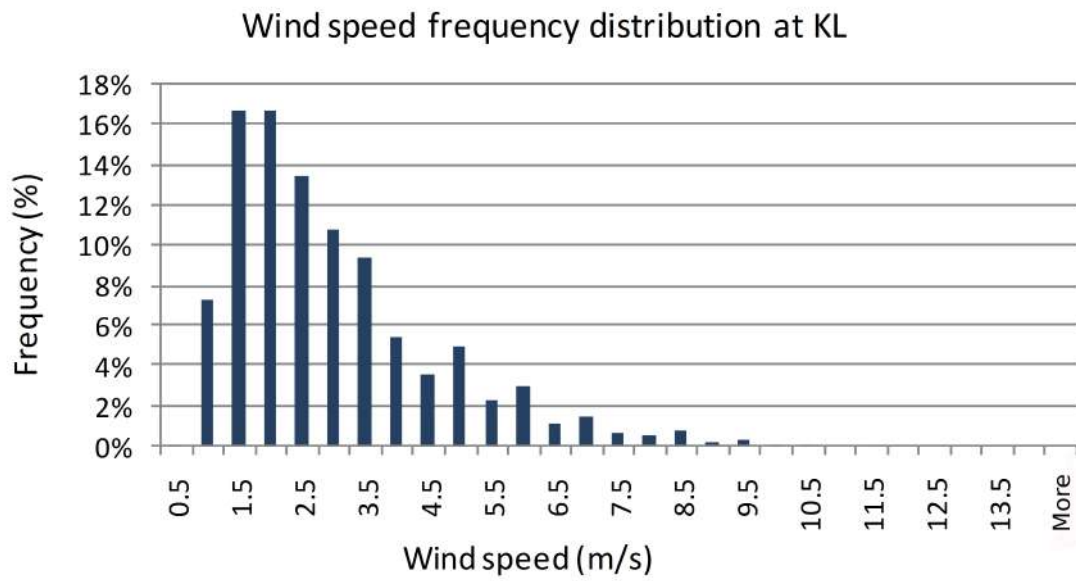
The F values represent the weighted mean for the wind speed datasets of each direction; i.e. they express the contribution of each dataset to the final mean. Since the wind blows mainly from West and South the corresponding F values are higher than the values for the East and North direction.

Thereupon, a single CFD model is produced, which combines the velocity fields for each direction with the climate data of the area of interest. As an example,





(a) EM



(b) KL

Figure 6.14: Wind speed distribution at (a) EM and (b) KL.

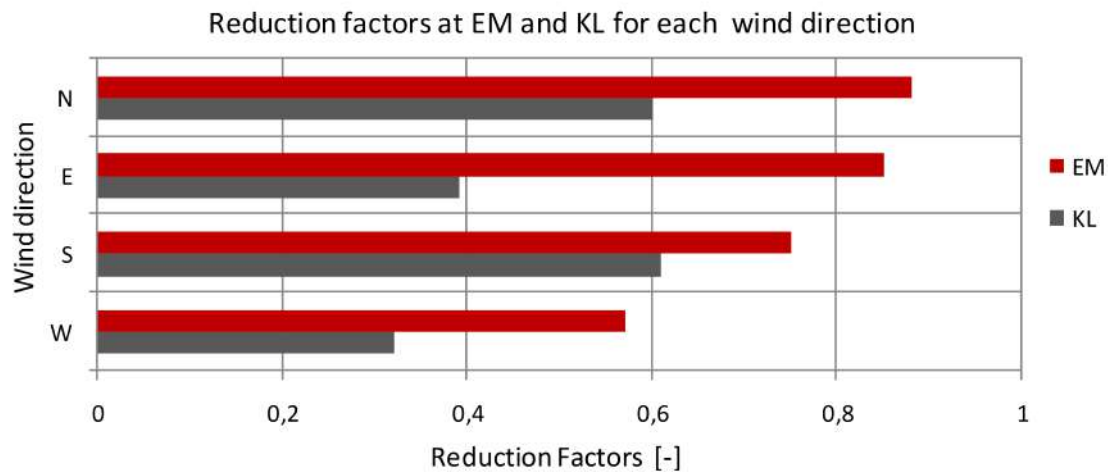


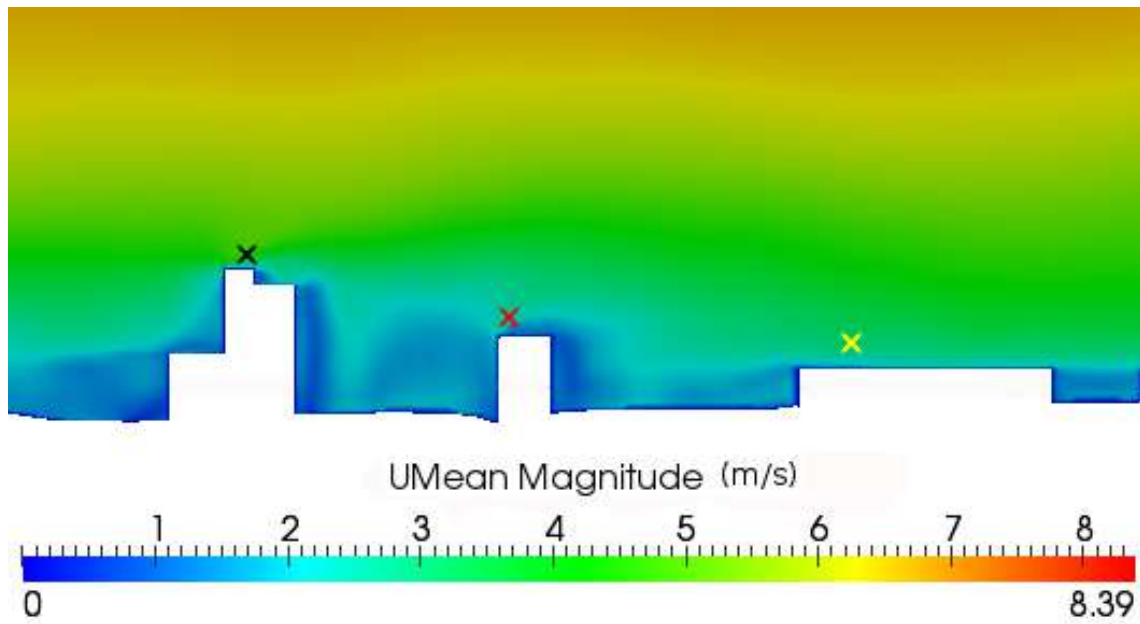
Figure 6.15: Reduction factors at EM and KL for each wind direction

Figure 6.16 shows the mean annual wind speed at EM and KL (4.2 m/s and 2.8 m/s respectively).

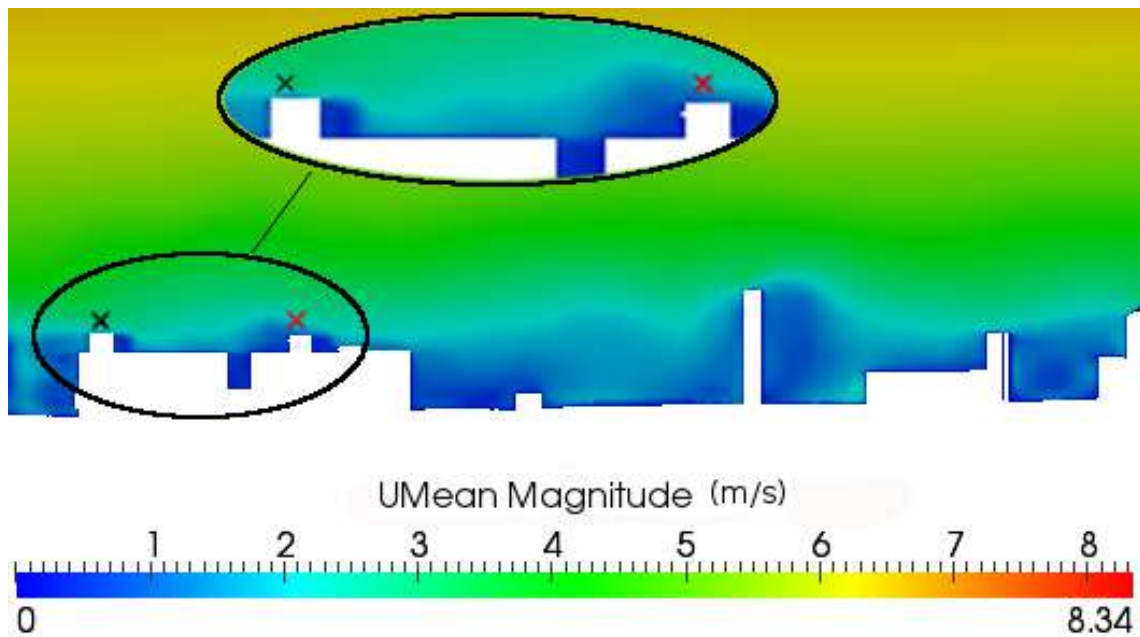
It is of interest that the wind flow and speed on the roofs of the same height and close each other may differ substantially. Figures 6.16(b) and 6.17(b) compare the wind speed at KL (2.8 m/s, black 'x'), where the anemometer has been placed, with the wind speed (1.5 m/s, red 'x') at another location of the same height and on the same building.

It is even noteworthy that lower buildings can have higher potential for micro wind turbines installation than taller, depending on the surrounding buildings and their effect on the wind flow. Figures 6.16(a) and 6.17(a) illustrate a situation where very low buildings (15 m, yellow 'x') seem more promising (mean annual wind speed 2.5 m/s) than higher (25 m, red 'x', mean wind speed of 1.5 m/s).

However, overall the annual mean wind speeds are quite low, with a maximum of 5.6 m/s above the roof of Old Fletcher building (45 m), which has no easy access to its roof (Figure 4.11), and 5.5 m/s above the roof of the highest building (50.1 m) (Figures 6.18 and 6.19).

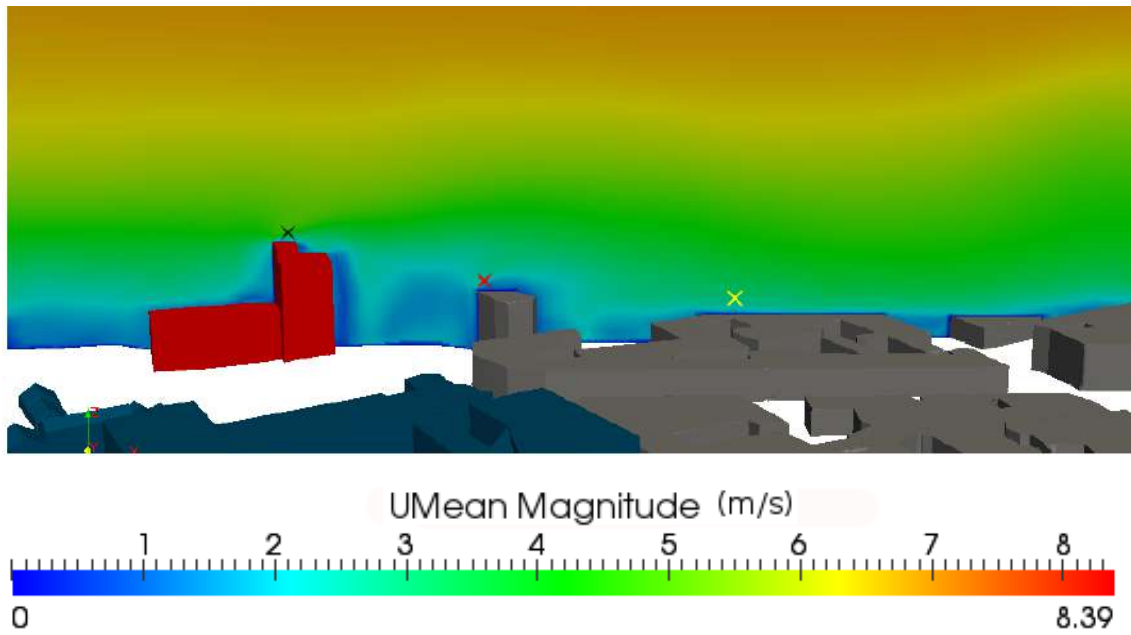


(a) EM

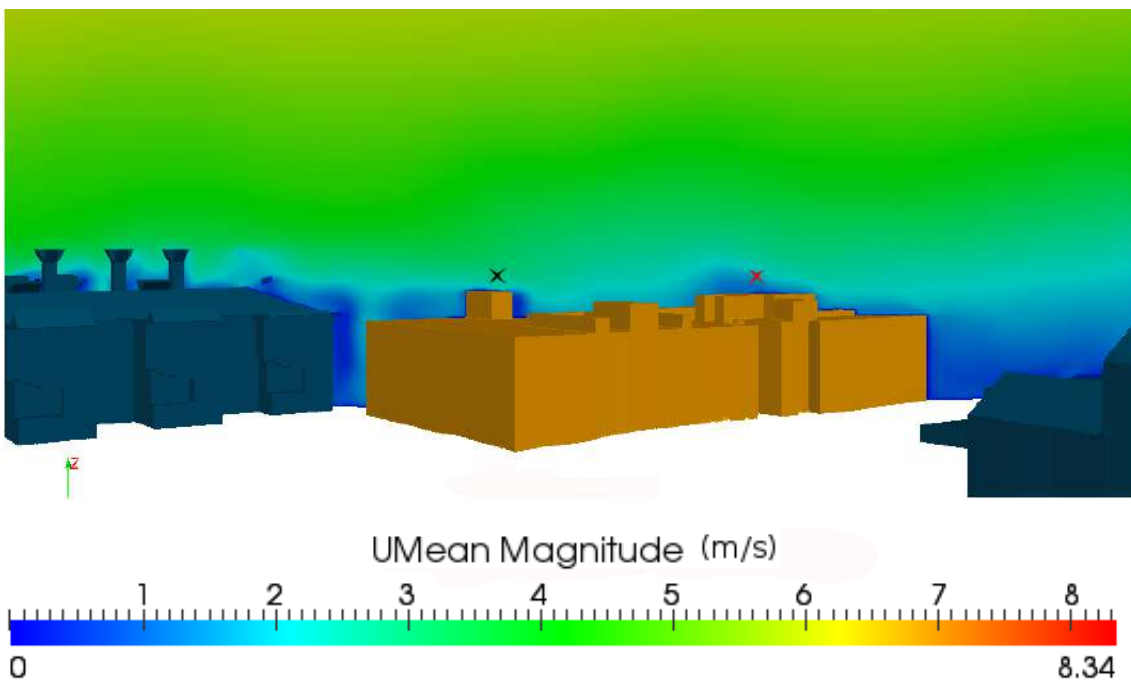


(b) KL

Figure 6.16: Annual mean wind speed at the DMU campus; (a) at EM (black 'x' symbol) and the nearby buildings in a xz plane (red and yellow 'x' symbols) and (b) at KL (black 'x' symbol) and the nearby buildings in a xz plane (red 'x' symbol).

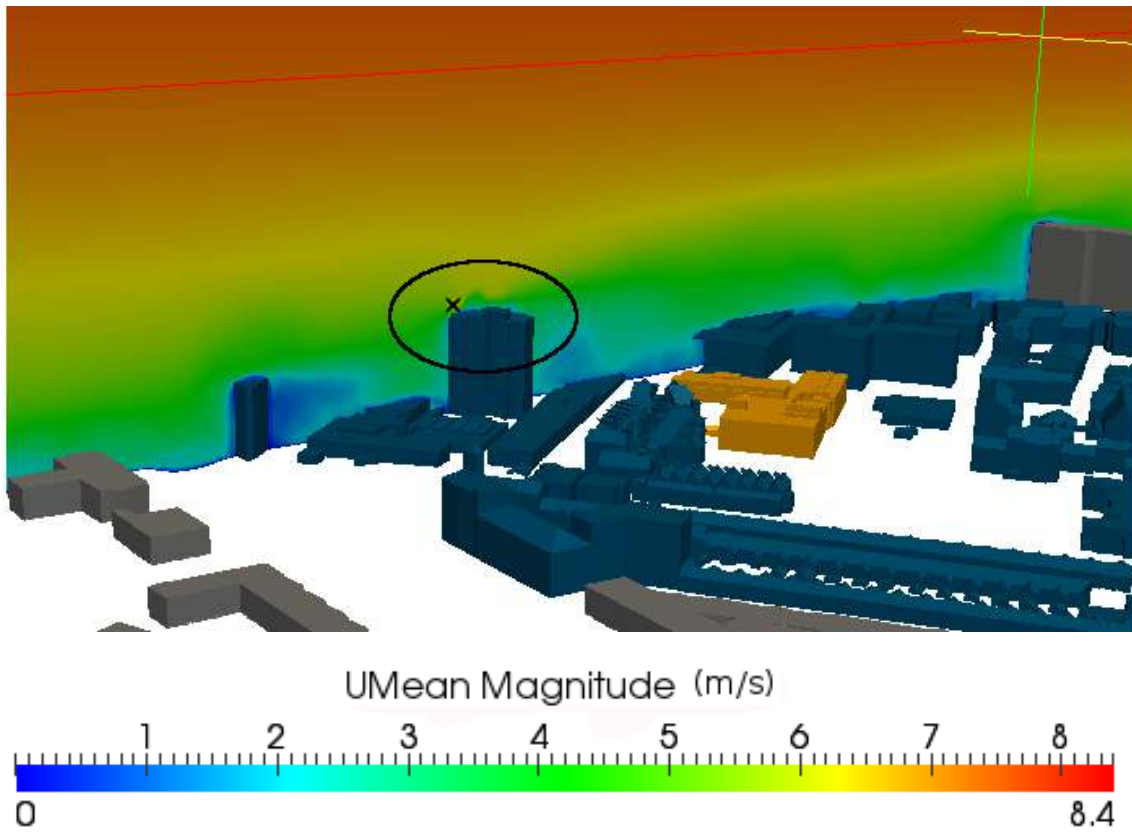


(a) EM

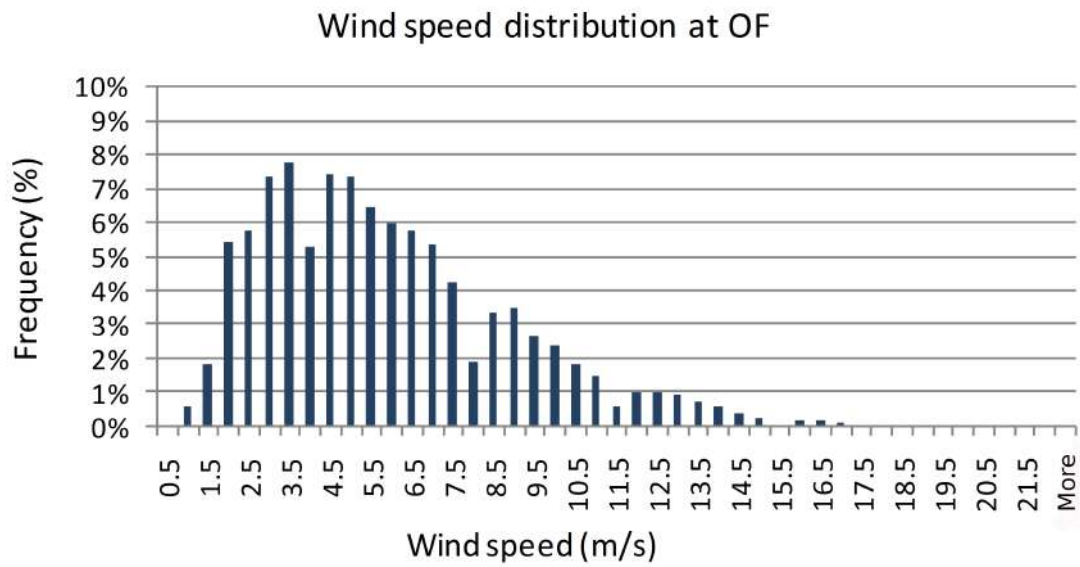


(b) KL

Figure 6.17: Annual mean wind speed at the DMU campus; (a) at EM (black 'x' symbol) and the nearby buildings in a xz plane (red and yellow 'x' symbols) and (b) at KL (black 'x' symbol) and the nearby buildings in a xz plane (red 'x' symbol).

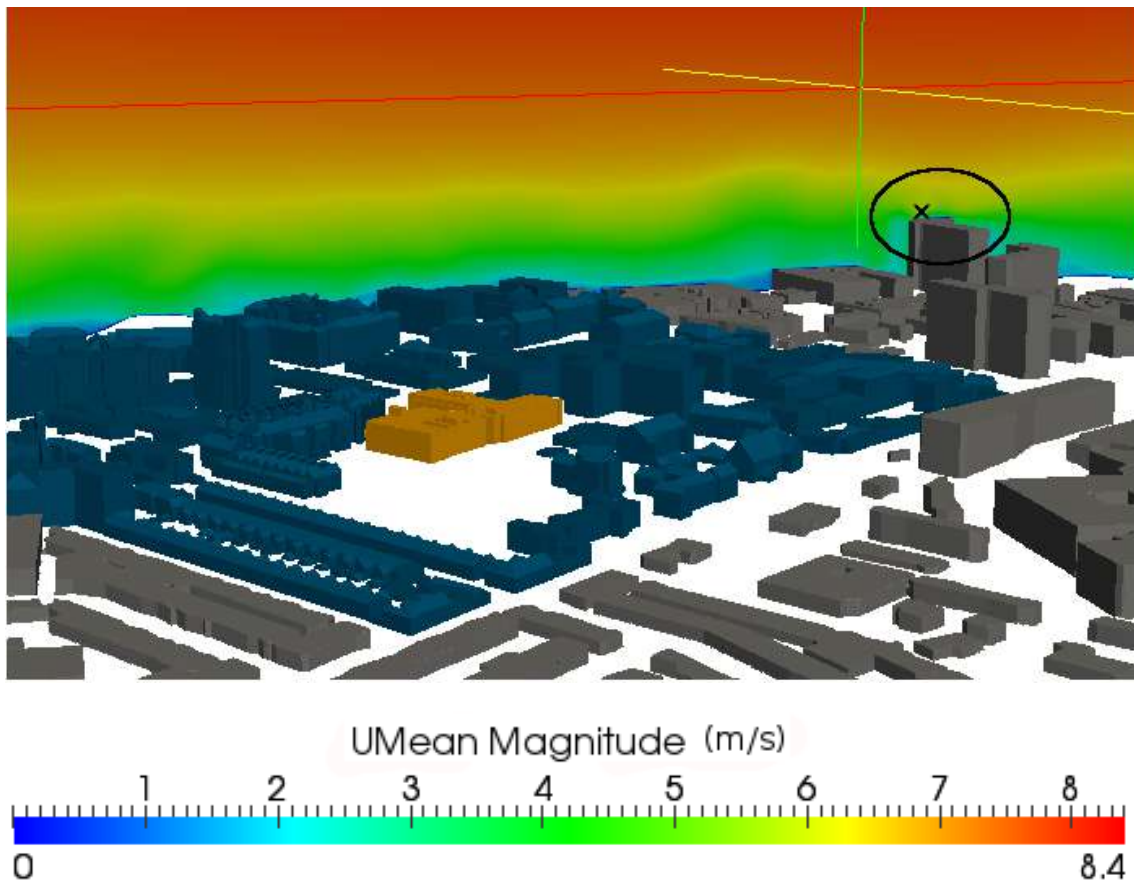


(a)

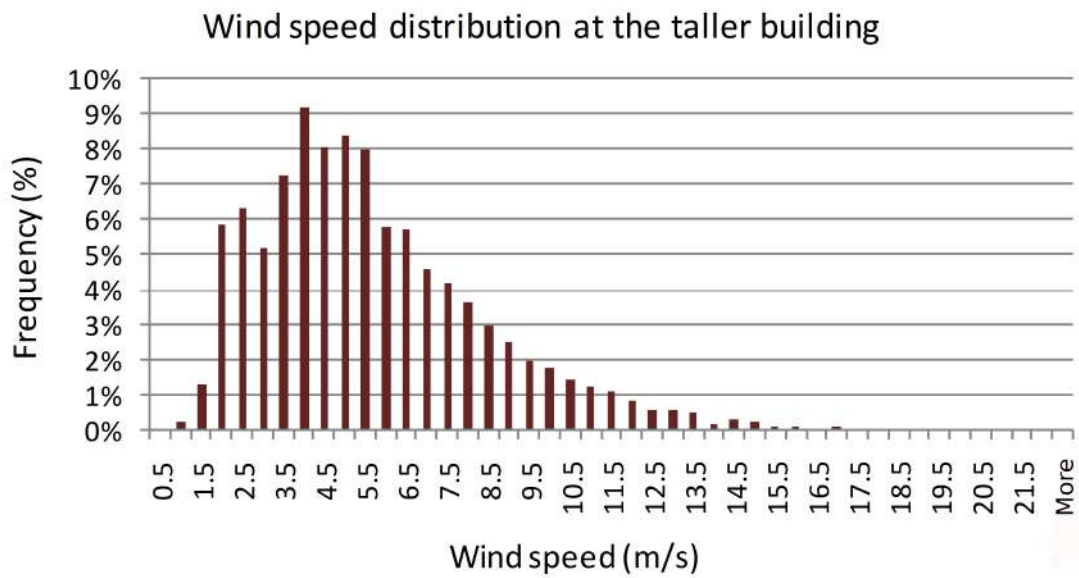


(b)

Figure 6.18: (a) Mean annual wind speed at Old Fletcher building and (b) the wind speed distribution.



(a)



(b)

Figure 6.19: (a) Mean annual wind speed at the taller building (office building (OB) in city center) and (b) the wind speed distribution.

### 6.6.4 Annual energy production - 3d map

To calculate the annual energy yield, the four steps described in Section 6.5 are followed.

1. First, the reduction factors for each direction are multiplied with the mean wind speed of the bins, in which the climate data were divided in Section 6.6.1, using the application `vRF`, built specifically for OpenFOAM. In order to investigate the effect of the range of the bins on the final output, the data are divided in bins of 1 m/s as well as 2 m/s (Tables 6.4 and 6.5).
2. Then, the wind speed in horizontal plane is calculated, since the power data of a 5 kW HAWT [Vermeir and Runacres, 2015] is used to estimate the annual energy production. It was achieved by using the `foamCalc` OpenFOAM application and two more applications (`vRF_xy`, `magvRF_xy`), developed for this purpose.
3. Figure 6.20 shows the power curve of the turbine. Interpolating the power data of the power curve, the power output for the wind speed estimated in the previous step is found. As it requires millions of interpolations, the python script ‘`interpolate.py`’ undertook the job.
4. Finally, the power outputs are multiplied with the corresponding `f` values of the Tables 6.4 and 6.5 (`energy` OpenFOAM application) and the predicted fields for each mean wind speed and direction were summed up (`energyTotal` and `energy4D` applications) to calculate the annual energy yield.

Figure 6.21 shows the AEP at EM (3261 kWh). Noticeable gradients exist in both horizontal and vertical directions and small shift in turbines position can change the output substantially. Moving the turbine 4 meters to the left side the energy yield increases by 1000 kWh (4260 kWh), while for only one meter higher, the energy production increases by 1200 kWh (4463 kWh).

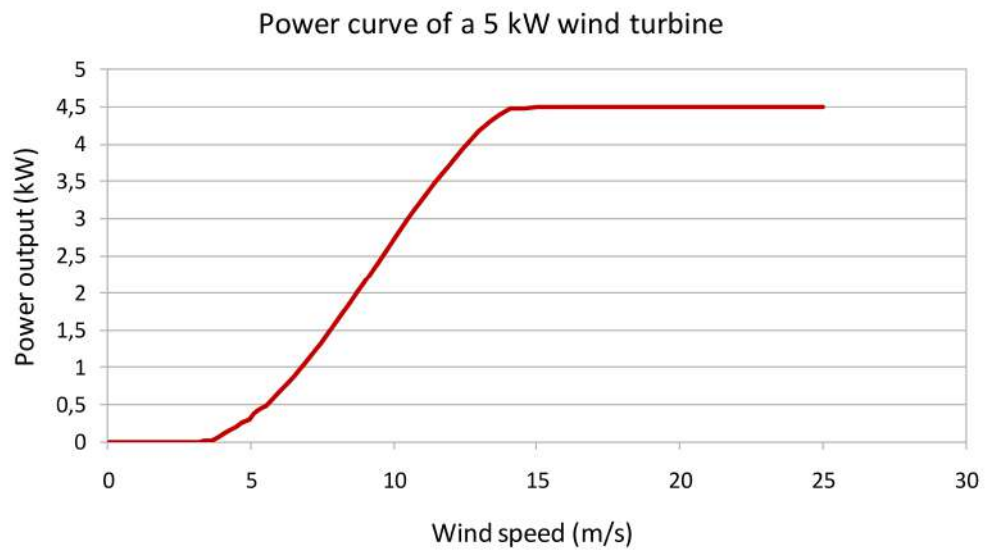


Figure 6.20: Power curve of a 5 kW HAWT [Vermeir and Runacres, 2015].

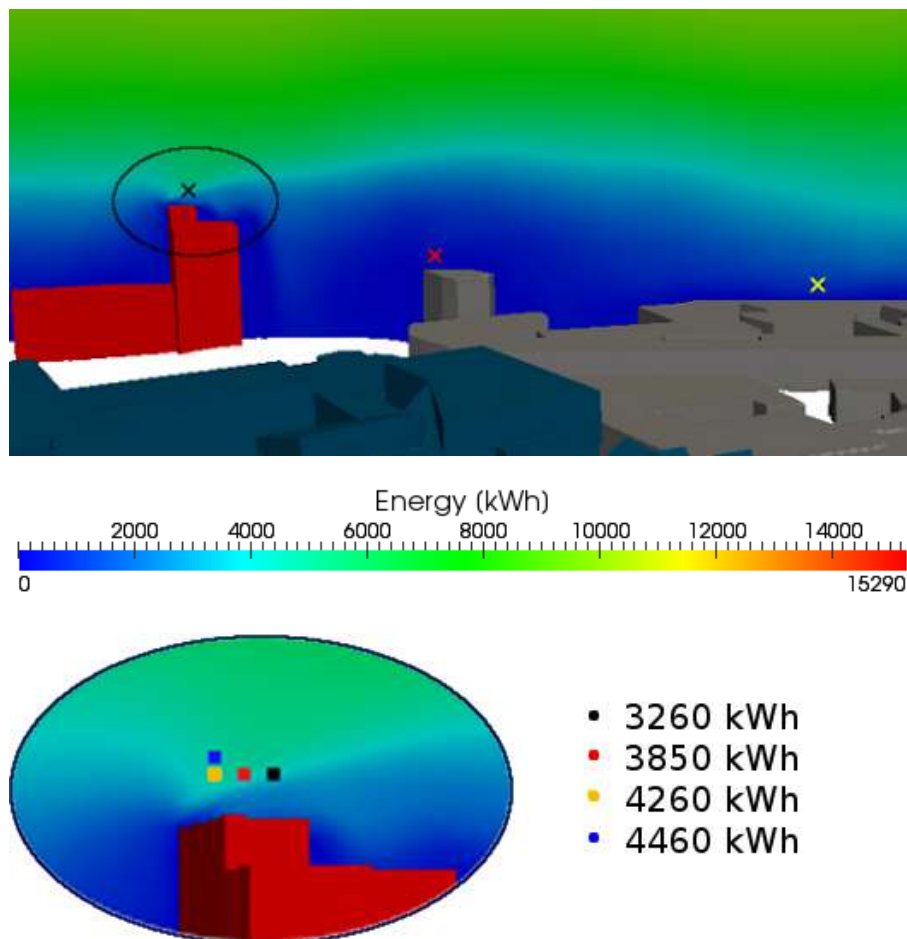


Figure 6.21: Energy yield at EM.



In accordance with the annual mean wind speed outputs, the potential energy production on the roof of the 15 m height building (1050 kWh, yellow 'x') is notably higher than the AEP at a 25 m height building (210 kWh, red 'x') (Figure 6.21).

As expected, at KL (Figure 6.22) the AEP is noticeably lower. The AEP at almost any position of the roof is less than 600 kWh and only at the location of the anemometer, the most favourable position, the AEP goes up to 1230 kWh.

As indicated from the mean annual wind speed the most promising places for micro wind turbines installation are the roof of the two tallest buildings, the Old Fletcher (Figure 6.23(a)) at the DMU campus and an office building (OB) in the city center (Figure 6.23(b)). The AEP climbs to 6964 kWh and 6320 kWh respectively.

However, using wind speed bins of 2 m/s the results are noticeably different (Figure 6.24). The energy yield is overestimated at EM and underestimated at the Old Fletcher and the office building. The wind speed distributions (Figures 6.14, 6.18

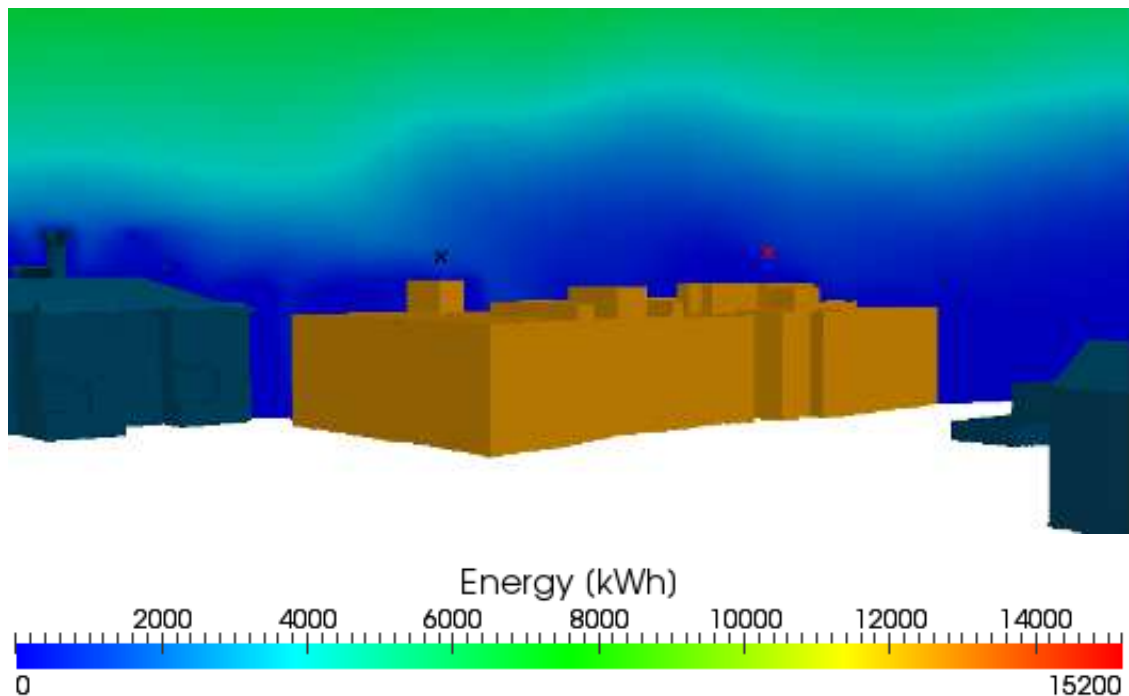
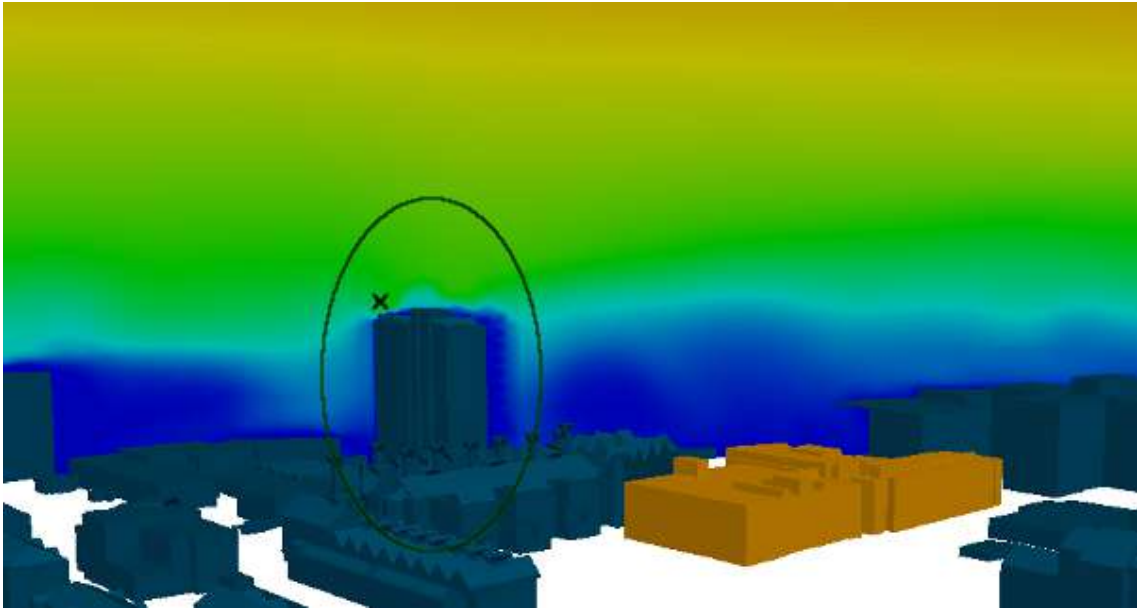
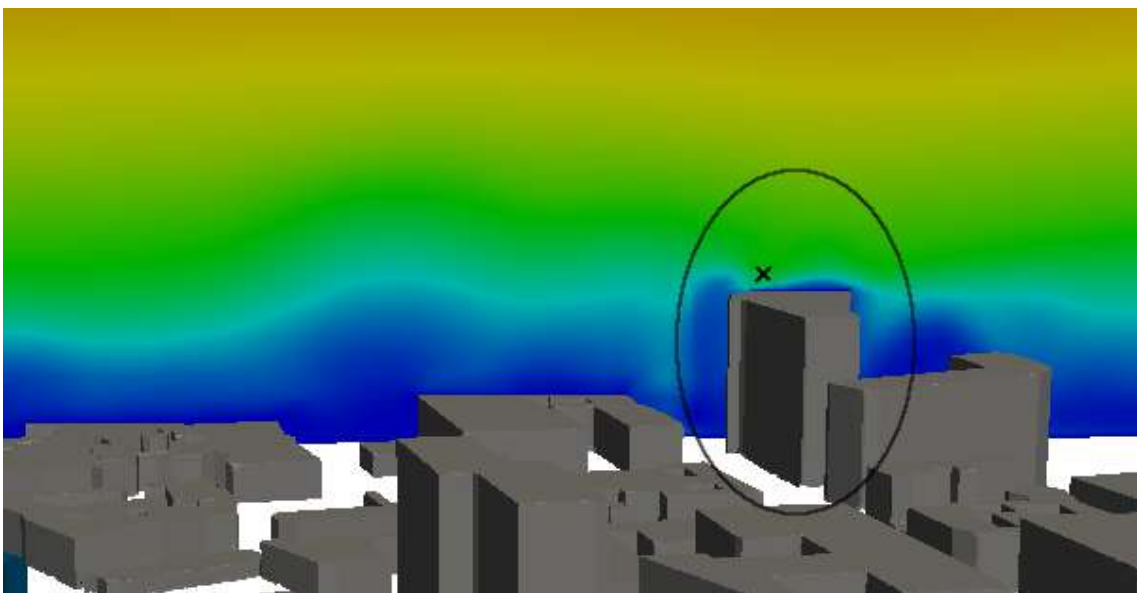


Figure 6.22: Energy production at KL.



(a) Old Fletcher building



(b) Office building

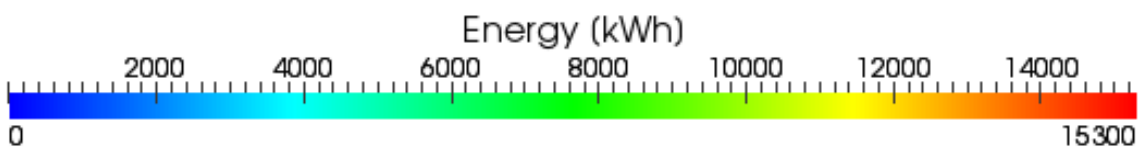


Figure 6.23: Energy production at (a) OF at the DMU campus and (b) at OB in the city center.

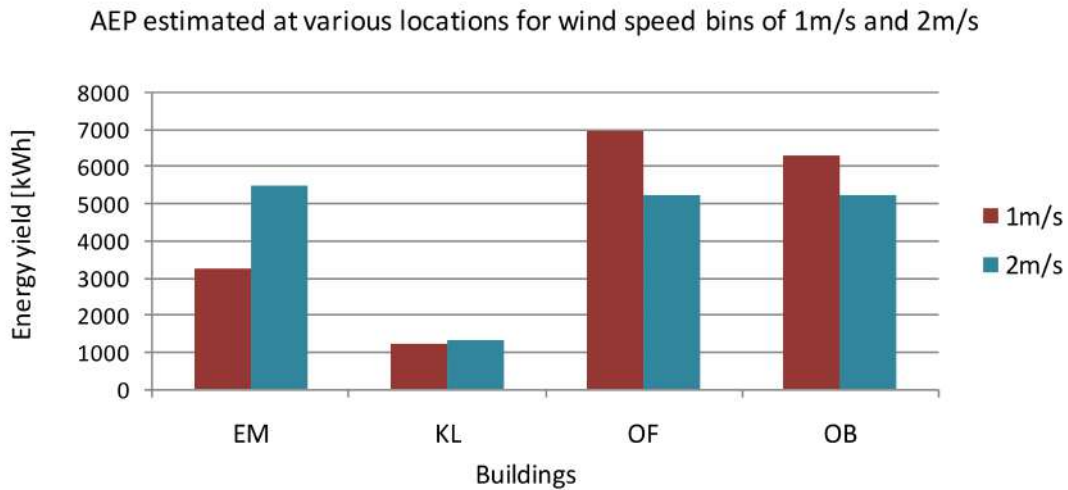


Figure 6.24: AEP estimated at various locations for wind speed bins of 1 m/s and 2 m/s.

and 6.19) indicate that at EM and KL the wind speeds are near the cut-in wind speed and there are no wind speeds near the rated wind speed range, while the wind histograms of the tall buildings have moved to the right. Therefore, the results imply that using wider wind speed bins, wind speeds lower than the cut-in wind speed are averaged to a higher wind speed and the turbine seems to produce energy, while wind speeds higher than the rated wind speed (and lower than the cut-off wind speed) are averaged to a lower wind speed. Hence, at wind speeds near the rated speed, larger wind speed bins appear to decrease power output, while at low wind speeds, near the cut-in wind speed, increased bins results in increased energy production.

## 6.7 Discussion - Conclusions

The primary obstacle for BWT deployment in the complex urban environment is the lack of accurate estimations for the mean wind speed and the energy yield at the potential mounting locations [Yang et al., 2016].

This chapter has shown how hourly climate data and computational fluid dynamics can be used to derive spatially varying estimates of the wind speed and the energy yield for micro-scale wind turbines. Different mounting positions are better suited to different prevailing wind situations (Figures 5.11 and 5.12). In areas with a strongly prevailing wind direction, the optimum mounting position is likely to be the windward corners of the roof as illustrated in Figures 5.11, 5.12 and 6.13, while for a wind rose where the probability of wind blowing is distributed to various directions, optimum mounting location can vary as shown for example in Figure 6.16. The geometry and the height of the target building as well as the surrounding buildings will specify the optimal location for installing BWTs. The impact of individual buildings on the wind flow and the sensitivity of output to relatively small differences in position, was illustrated. Due to the roof shape and the separation of the flow, noticeable speed gradients exist and small variations in horizontal or vertical direction can change the predicted energy yield significantly. This also suggests that the geometry of the buildings of interest should be represented in detail.

Recent work has shown that turbulence intensity (TI) is another important factor to consider in the determination of the mounting location, since it has a major impact on the power performance of the turbines. The next chapter (Section 7.2.2) investigates how the energy production is influenced by turbulence intensity (TI), presents methods to analyse the turbulence data and identifies areas for future research.



# Chapter 7

## Site specific power curves and corrected AEP

### 7.1 Introduction - Chapter overview

This chapter investigates the validity of micro turbine power curves in urban environments, the accuracy of the annual energy production (AEP) estimation techniques and develops guidelines on the calculations.

In the previous chapter it was shown how the CFD results can be successfully combined with the hourly climate data and the power curve of the potential micro wind turbine. Multiplying the regional wind speed with the corresponding (according to the wind direction) reduction factors, can be used to obtain the annual hourly wind speed for any potential location for micro wind turbines installation. Then, interpolating the values of the power curve at the hourly wind speeds and integrating the results the annual energy yield is calculated.

However, the default power curves available are valid for standard values of air density and turbulence intensity, which may differ from the site measurements. There-

fore this chapter aims:

- to adjust the micro wind turbines' power curves to the site air density and turbulence intensity parameters,
- to evaluate the effects of the site-specific values of air density and turbulence intensity on the annual energy production and
- to provide guidance on the calculations of AEP.

## 7.2 Site specific power curves

Typically, a particular wind turbine's power performance is indicated by the theoretical power curves provided by the manufacturer. They are valid for a reference air density and turbulence intensity, which may differ from the site specific measurements and conditions.

To account for the air density differences and investigate their effect on AEP, a modification of the IEC 61400-12 standard [Svenningsen, 2010b] is proposed that can be used to correct a power curve given at a reference air density to higher or lower site specific air densities as described in the next section.

In addition, the energy production is influenced by the turbulence intensity, but it has different effects at different wind speeds. At wind speeds near the rated speed, increased turbulence has been found to decrease power output, while at low wind speeds, near the cut-in wind speed, increased turbulence results in increased energy production [Lubitz, 2014]. To account for the differences in power output and investigate their effect on AEP, a technique by Albers [2009b] is proposed for inclusion in the assessment methodology to correct the power curve given for a reference turbulence intensity to a site specific turbulence intensity. This is explained in detail in Section 7.2.2).

## 7.2.1 Air-density correction

### 7.2.1.1 Methodology

The IEC 61400-12 standard includes a method to correct the standard power curve from the default air density to site-specific air densities. Since, the temperature and air density are associated (Equation 2.3) this method also implicitly introduces temperature correction [Wagenaar and Eecen, 2011]. It is a two step procedure. First the wind speed is scaled to the new air-density according to Equation 7.1. The new power curve is sampled at the new wind speed values  $(u_{site}, P_{std})$  and then using interpolation the power is calculated for the initial wind speeds  $(u_{std}, P_{site})$  [Svenningsen, 2010b].

$$u_{site} = u_{std} \left( \frac{\rho_{std}}{\rho_{site}} \right)^{1/3} \quad (7.1)$$

This method is based on the assumption that the efficiency of the wind turbine is fixed at all wind speeds, which is not fully accomplished as indicated from the power coefficient ( $C_p$ ) curves. Close to rated power the power output is not proportional to  $u^3$ , but  $u$  at some lower exponent [Svenningsen, 2010b]. As a result, the calculated power output will be over-predicted for very low air densities for wind speeds near the rated power (where the power output is proportional to wind speed at a lower exponent than three) and under-predicted for higher air densities.

To overcome the shortcomings of the IEC 61400-12 standard a new approach has been introduced which is identical to the two step procedure of the IEC 61400-12 standard, but it uses an exponent as a function of wind speed instead of a constant value. For wind speeds lower than 7–8 m/s the exponent is 1/3 as for the IEC method, between 7–8 m/s and 12–13 m/s, the exponent is smoothly stepped from 1/3 up to 2/3 and above 12–13 m/s the exponent is constant at 2/3. The exact



values of the exponent have been calibrated against a large pool of density specific power curves [Svenningsen, 2010b]. The advantage of this approach over the IEC 61400-12 standard is illustrated in Figure 7.1, which presents the power curves at standard air density and the corrected power curves at  $1.0 \text{ kg/m}^3$  using the IEC 61400-12 standard and the approach developed by Svenningsen [2010a]. It also presents the true power curve at  $1.0 \text{ kg/m}^3$  based on field measurements. It can be seen that the new approach predicts with high accuracy the true power performance of the wind turbine.

Accordingly, using the approach by Svenningsen [2010a] and the power curve of a 5kW wind turbine [Vermeir and Runacres, 2015], developed according to the IEC 61400-12-1 standard at a site with 13% turbulence intensity, the corrected power curves at  $1.0 \text{ kg/m}^3$ ,  $1.1 \text{ kg/m}^3$  and  $1.3 \text{ kg/m}^3$  air densities have been calculated. Figure 7.2 illustrates the results and demonstrates the effect of the air density on

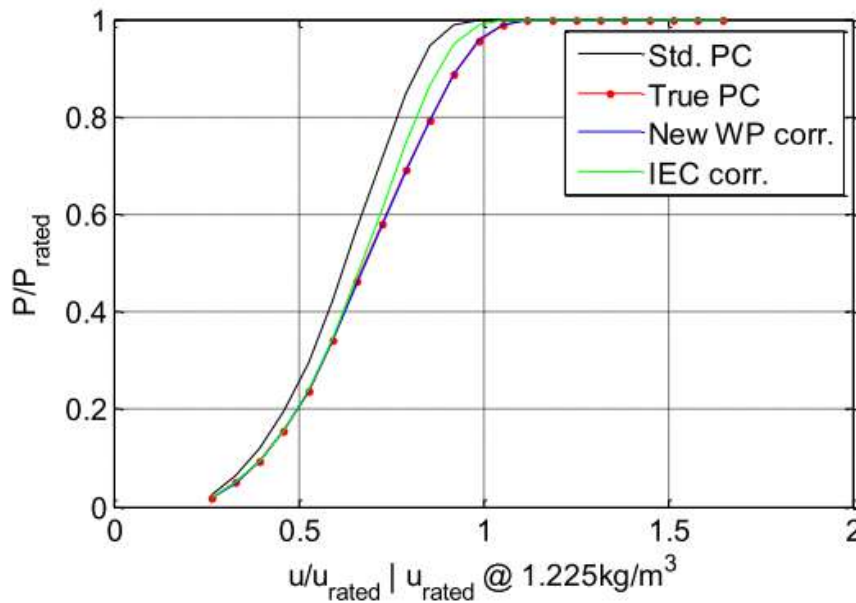


Figure 7.1: Illustration of the standard power curve at  $1.225 \text{ kg/m}^3$  air density (black line) and the corrected power curves for  $1.0 \text{ kg/m}^3$  air density using the IEC 61400-12 standard (green line) and the new approach by Svenningsen [2010a] (blue line). It also represents the true power curve based on field measurements (red dots) [Svenningsen, 2010b].

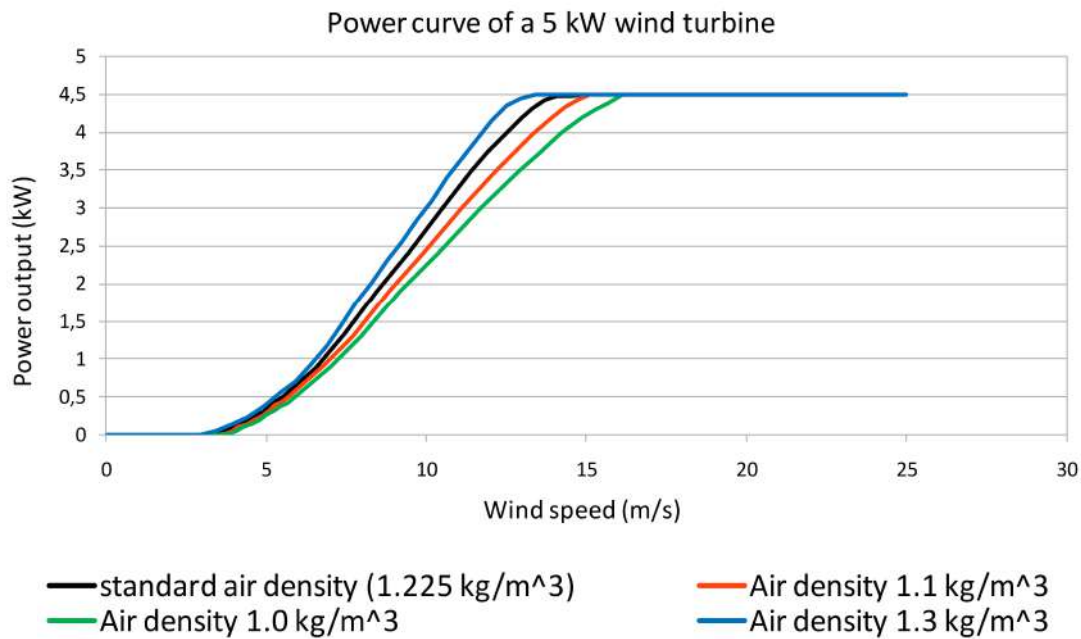


Figure 7.2: Standard power curve at the reference air density (1.225 kg/m<sup>3</sup>) and the corrected power curves at 1.0 kg/m<sup>3</sup>, 1.1 kg/m<sup>3</sup> and 1.3 kg/m<sup>3</sup> air densities.

the wind turbine's power performance. The effect is more pronounced at wind speeds above 8 m/s, where the exponent in Equation 7.1 is smoothly stepped from 1/3 up to 2/3 [Wagenaar and Eecen, 2011]. This example is an extreme case and usually the differences between the power curves are not as large. The next section explains the evaluation of the effect of the difference between the default air density and the site specific air density on the annual energy production at DMU campus, using the field measurements at Kimberlin Library and Edith Murphy building (see Section 4.3).

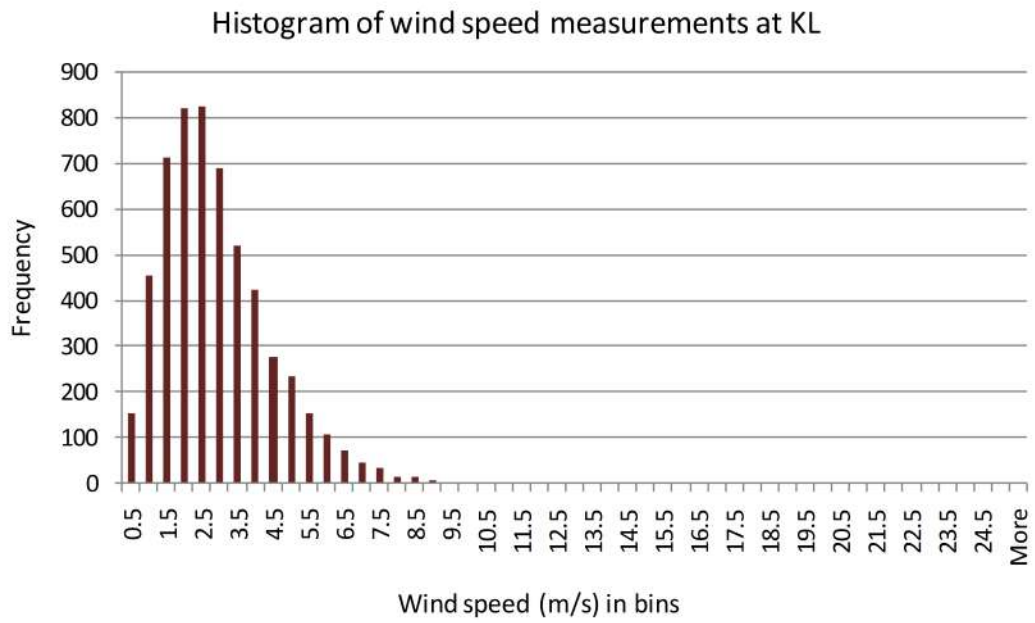
### 7.2.1.2 Case study of the DMU campus

To investigate the impact of the air density differences between the standard air density and the site-specific air density on the energy production, the field measurements at Kimberlin Library for the period of February 2015 till January 2016 and Edith Murphy building from February 2015 till June 2015 were used. The mea-

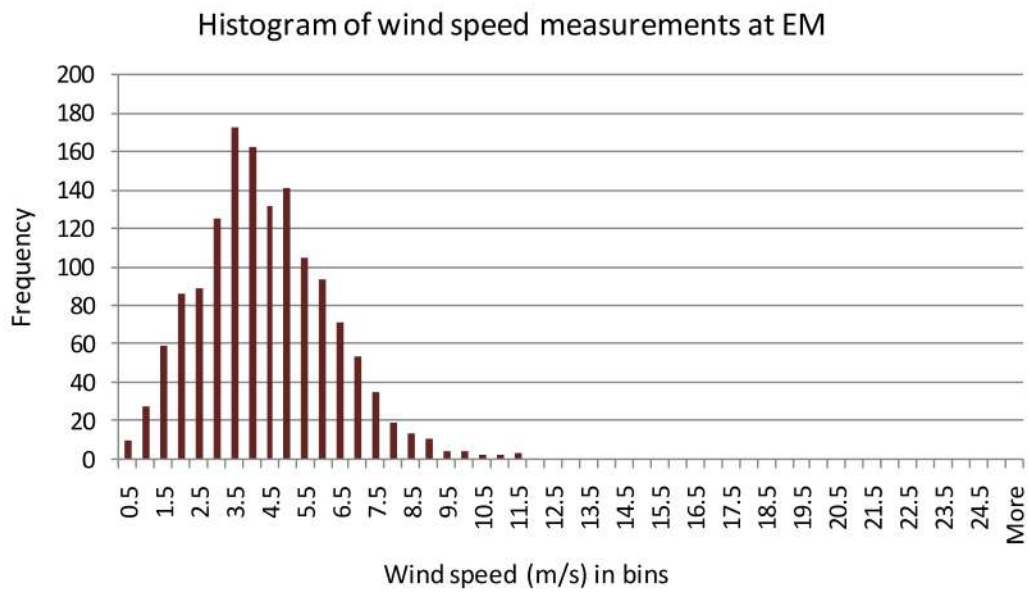
measurements of temperature and atmospheric pressure on the Edith Murphy building required for the calculation of air density were not complete and the final number of hours with reliable data were 5534 for the Kimberlin Library (i.e. around 7.7 months) and 1428 for the Edith Murphy building (i.e. about 2 months).

Figure 7.3 shows the histograms of the wind speed data for the two sites. The 90% of the data lie between 0.96 m/s and 4.72 m/s for the KL data with an average value of 2.6 m/s and between 1.8 m/s and 6.6 m/s for EM data with 4.1 m/s the mean wind speed. At KL the wind speeds are gathered around the mean value ( $\sigma_{KL}=1.5$ ), while at EM they are distributed a little more ( $\sigma_{EM}=1.9$ ).

In Figures 7.4 and 7.5, the relationship between air density, air temperature and barometric pressure is examined. The average site air-density was 1.224 kg/m<sup>3</sup> during the period of KL measurements and 1.233 kg/m<sup>3</sup> during the period of EM measurements (the median values were 1.223 kg/m<sup>3</sup> and 1.23 kg/m<sup>3</sup> respectively) with a maximum of 1.302 kg/m<sup>3</sup> for both sites and minimum 1.132 kg/m<sup>3</sup> and 1.173 kg/m<sup>3</sup> respectively (Figures 7.4 and 7.5(a)). Specifically, during winter, the air density is higher, as the temperature decreases (Figures 7.4 and 7.5(a)) and the barometric pressure seems to slightly increase (Figures 7.4 and 7.5(b)). According to the ideal gas law (Equation 2.3:  $\rho=p/(RT)$ ), which demonstrates the relationship between the air density ( $\rho$ ), the air temperature (T) and the barometric pressure (p) and reported in Section 2.2.3.1, the higher the air temperature, the lower the air density and the higher the air pressure, the higher the air density. Regarding the relationship between the air temperature and barometric pressure (Figures 7.4 and 7.5(c)) there is not a clear tendency, despite the fact it is observed a small decrease of air pressure during summer.



(a)



(b)

Figure 7.3: Histograms for the wind speed data at (a) Kimberlin Library and (b) Edith Murphy.

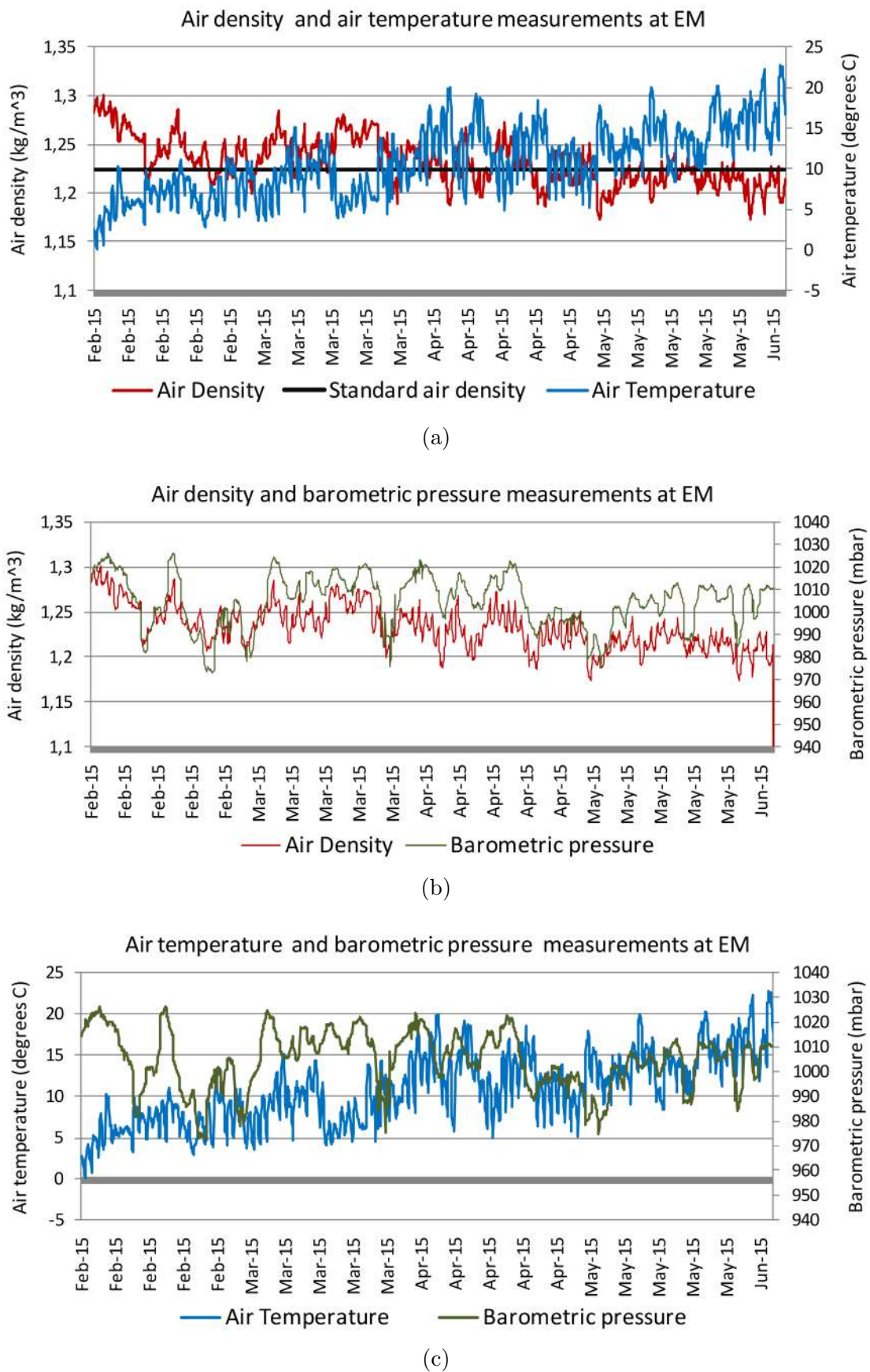


Figure 7.4: Time-series (hourly data) of air-density, air temperature and barometric pressure at DMU for the time period we have wind measurements at Edith Murphy.

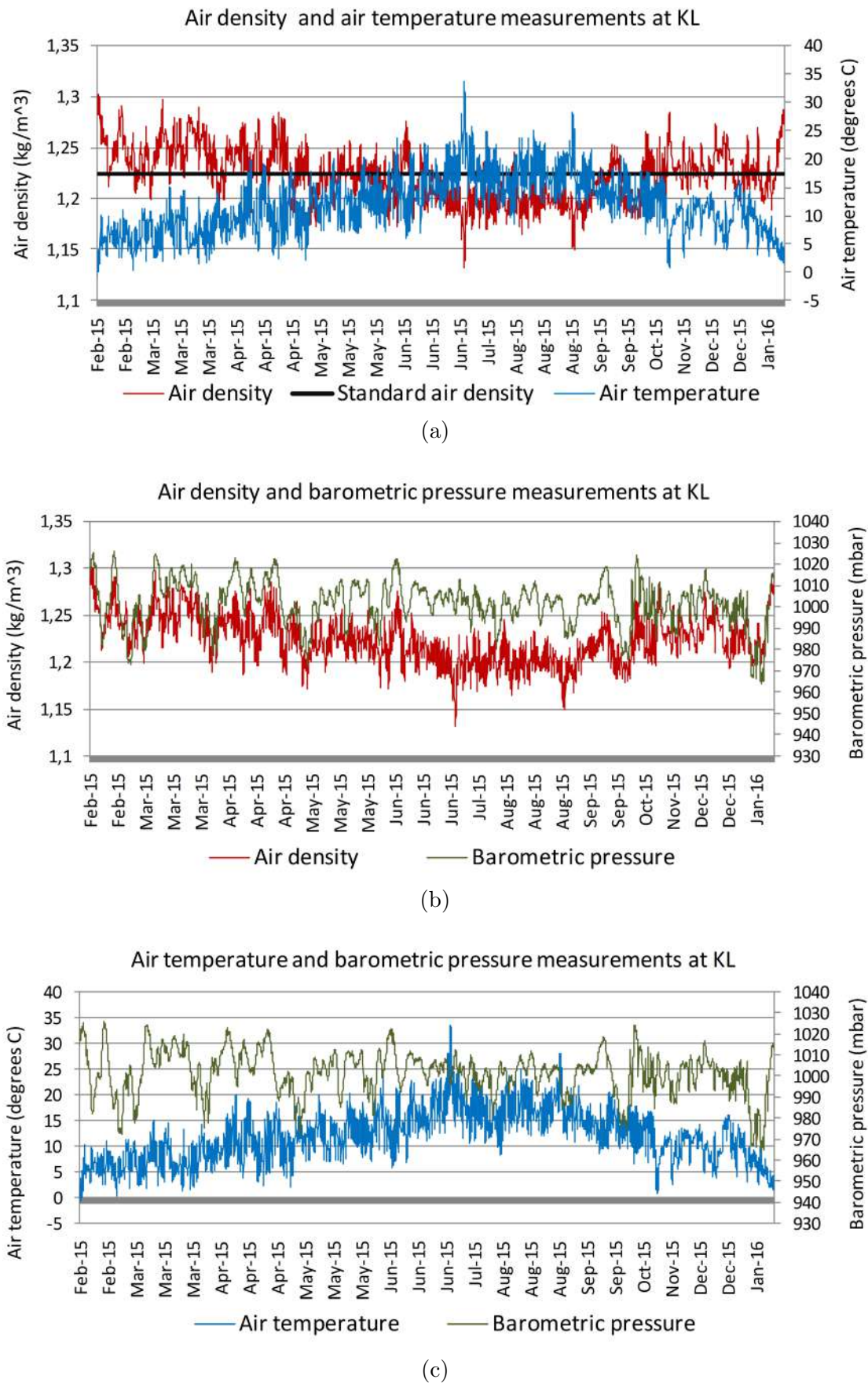


Figure 7.5: Time-series (hourly data) of air-density, air temperature and barometric pressure at DMU for the time period we have wind measurements at Kimberlin Library.

To examine the impact of the differences between the standard air density and the site-specific air density on energy calculations, firstly the energy yield at the reference air density ( $1.225 \text{ kg/m}^3$ ) is calculated using the power curve given by the manufacturer. Secondly, the energy production was estimated for the site-specific air density calculated using the hourly measurements of temperature and pressure (Equation 2.3) and the corrected power curves based on the technique described above.

Since the process involved the adjustment of the initial power curve a thousand times (as many as the hourly measurements) and the equivalent interpolation of the wind speed measurements, it was automated using the Python programming language.

The results are shown in Table 7.1. There is a negligible difference of 1% for the Kimberlin library measurements and practically no difference for the Edith Murphy calculations. This can be explained by the fact that the mean air density is close to the standard air density and the power output differences at the higher and lower densities were cancelled out.

However, if the air density was constant at  $1.1 \text{ kg/m}^3$  and  $1.3 \text{ kg/m}^3$  the corresponding power outputs would be 486.3 kWh and 589.4 kWh at KL and 441.4 kWh and 530.6 at EM respectively (Table 7.2). Then, the error would be around -11.4% at  $1.1 \text{ kg/m}^3$  air density and +6.8% at  $1.3 \text{ kg/m}^3$  air density, which should not be ignored.

	KL	EM
Standard air density	550.7 kWh	497.9 kWh
Site specific air density	545.5 kWh	497.8 kWh
Error	1%	0%

Table 7.1: Estimation of the energy yield (kWh) from a 5 kW wind turbine placed on Kimberlin Library (KL) and Edith Murphy (EM) buildings at standard air density ( $1.225 \text{ kg/m}^3$ ) and site specific air density for a period of 7.7 months and 2 months respectively.

	KL	EM
Standard air density	550.7 kWh	497.9 kWh
1.1 kg/m <sup>3</sup> air density	486.3 kWh (-11.7%)	441.4 kWh (-11.3%)
1.3 kg/m <sup>3</sup> air density	589.4 kWh (+7.0%)	530.6 kWh (+6.6%)

Table 7.2: Estimation of the energy yield (kWh) from a 5 kW wind turbine placed on Kimberlin Library (KL) and Edith Murphy (EM) buildings at standard air density (1.225 kg/m<sup>3</sup>) and at 1.1 kg/m<sup>3</sup> and 1.3 kg/m<sup>3</sup> air density.

If there are no available field measurements of air temperature and pressure, one can estimate the mean air density of dry air at the site of interest as a function of altitude, as follows:

- In the troposphere, the temperature is linked to the geopotential altitude by:

$$T = T_0 + LH \quad (7.2)$$

where:

- T<sub>0</sub>: the standard temperature at sea level, 288.15 K,
- L: the temperature lapse rate, 0.0065 K/m,
- H: the geopotential height.

For altitude less than 500 m the difference between the geometrical and geopotential height is negligible (<1%) and hence, we can use the geometric height (h).

- The pressure at altitude h is given by:

$$p = p_0 \left(1 - \frac{Lh}{T_0}\right)^{\frac{gM}{RL}} \quad (7.3)$$

where:



- $p_0$ : the standard atmospheric pressure at sea level, 101.325 kPa
- $g$ : the gravitational acceleration at earth surface, 9.80665 m/s<sup>2</sup>
- $M$ : the molar mass of dry air, 0.0289644 kg/mol
- $R$ : the universal gas constant, 8.31447 J/(molK)
- Then, the air density can be expressed from the ideal gas law as:

$$\rho = \frac{pM}{RT} \quad (7.4)$$

In the absence of the field measurements and using this procedure, the estimated mean air density for the DMU campus would be 1.216 kg/m<sup>3</sup> instead of 1.224 kg/m<sup>3</sup> and 1.233 kg/m<sup>3</sup> calculated during the period of KL wind measurements and EM measurements respectively. Then, the predicted energy yield would be 545.7 kWh at KL and 493.7 kWh at EM, i.e. less than 1% difference from the corresponding energy predictions (Table 7.1) from the field measurements.

Although this technique for estimating the air density works well in this case, the air density for moist air (moist air is less dense than dry air) is calculated as a mixture of water vapour molecules and dry air molecules (Equation 7.5) and field measurements of relative humidity (RH) or dew point ( $T_{\text{dew}}$ ) are required.

$$\rho = \frac{p_d}{R_d T} + \frac{p_v}{R_v T} \quad (7.5)$$

where:

- $p_d$ : the partial pressure of dry air [Pa],
- $p_v$ : the partial pressure of water vapour [Pa],
- $R_d$ : the specific gas constant of dry air, 287.05 [J/(kgK)]
- $R_v$ : the specific gas constant of water vapour, 461.495 [J/(kgK)]

Specifically, to calculate the moist-air density, one should know the water vapour pressure ( $p_v$ ), which can be determined by either the dew point ( $T_{dew}$ ) (Equation 7.6) or the relative humidity (RH) (Equation 7.7).

$$p_v = E_s(T_{dew}) \quad (7.6)$$

$$p_v = RH \cdot E_s(T) \quad (7.7)$$

where  $E_s$  is the saturated vapour pressure and can be approximated by a polynomial suggested by Herman Wobus [Thogersen, 2000].

However, the relative difference between dry air density and moist air density is below 0.7 % (for the first 5000 m above sea level) (Figure 7.6) and hence, the moisture content can be ignored [Thogersen, 2000].

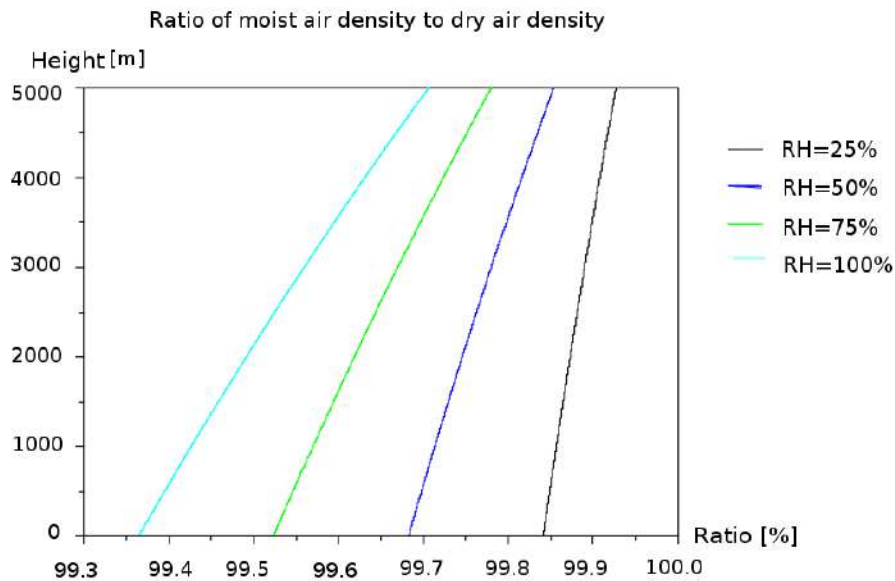


Figure 7.6: Ratio of moist air to dry air [Thogersen, 2000].

Finally, it is noticeable that the energy production at EM (497.9 kWh) as calculated for only 2 months is close to the output at KL (550.7 kWh), which refers to a period of 7.7 months. This is because the average wind speed at EM was 4.1 m/s and at

KL only 2.6 m/s, less than the cut-in wind speed (3.0 m/s), as this place is partially sheltered by the Queens building. The corresponding hourly outputs for the EM and KL were 0.35 kWh and 0.10 kWh respectively.

## 7.2.2 Turbulence intensity correction

### 7.2.2.1 Methodology

For the purpose of wind resource assessment, the draft of the second edition of the standard IEC 61400-12-1 [Albers and Windguard, 2014], which is planned to be published on January 2017, includes an approach for adjusting a power curve given for a standard (reference) turbulence intensity to a site specific turbulence intensity.

The normalised power is given by:

$$P_{corrected} = P_{givenPC,I-ref}(v) - P_{simulated,I-ref}(v) + P_{simulated,I-meas}(v) \quad (7.8)$$

where:

- $P_{corrected}$ : the normalised power output,
- $P_{givenPC,I-ref}$ : given power output for reference turbulence,
- $P_{simulated,I-ref}$ : simulated power output at reference turbulence,
- $P_{simulated,I-meas}$ : simulated power output at site turbulence.

In fact, the normalised power curve is calculated by applying a correction to the standard power curve ( $P_{simulated,I-meas} - P_{simulated,I-ref}$ ). In other words, correction is defined as the power difference between the simulated power at site turbulence and the simulated power at reference turbulence. As it can be seen, the simulated power at the site turbulence is not used directly, since the simulated power is reliable

to determine a correction (from one turbulence to another), but it is not reliable to specify the absolute value at given turbulence [Power Curve Working Group, 2014]. Computing the formula 7.8 for the wind speeds given for a reference power curve, the normalised power curve is obtained.

The simulation method to calculate the power at any required turbulence intensity is based on two assumptions:

1. The wind turbine follows at each instant a certain power curve, which corresponds to zero turbulence intensity, and hence is defined as zero turbulence power curve.
2. The wind speed within an observation period is Gaussian distributed and hence can be fully determined by the average wind speed and the turbulence intensity.

Then the simulated power at any required turbulence intensity is given by:

$$P_{simulated} = \int_{v=0}^{\infty} P_{I=0}(v) f(v) dv \quad (7.9)$$

where:

- $P_{simulated}$ : simulated power output at any turbulence.
- $v$ : wind speeds given for the reference power curve,
- $f(v)$ : Gaussian distribution determined by wind speed ( $v$ ) and standard deviation  $\sigma(v) = TI \cdot v$ ,
- $P_{I=0}$ : the zero turbulence power which is determined from given power curve under consideration of reference turbulence intensity (later in this section it is explained how to derive it).

Figure 7.7 illustrates the method. First, for every wind speed in the probability distribution (0 to 100 m/s in 0.1 m/s steps) one should interpolate the zero turbulence

power curve and then compute the sum product of the interpolated zero turbulence power values and the corresponding probability density to find the simulated power.

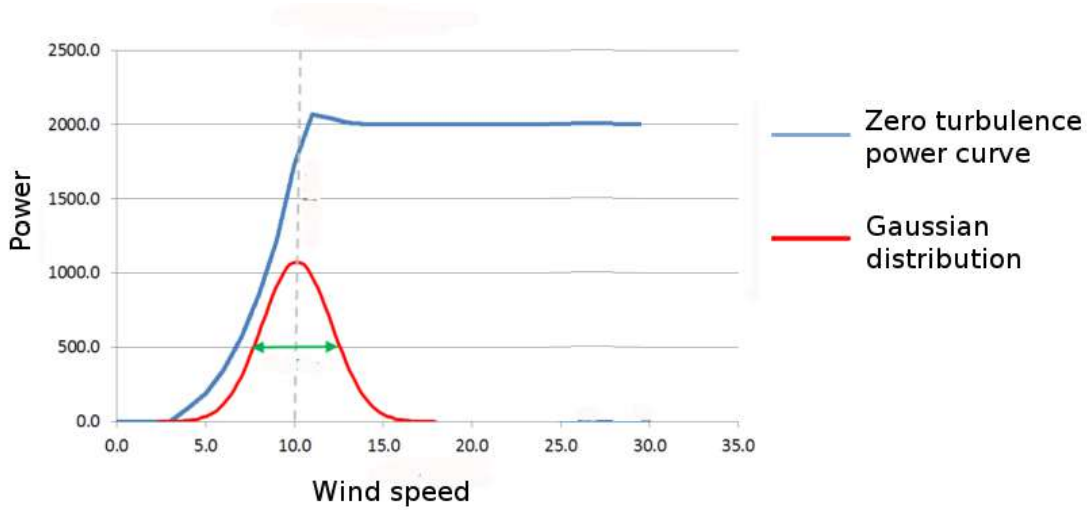


Figure 7.7: Computation method of the simulated power output [Power Curve Working Group, 2014].

The zero turbulence power curve is determined based on the following criteria [Albers, 2009b] (Table 7.3):

1. The simulated power rate at the reference turbulence intensity fits the maximum power of the standard (given) power curve ( $| P_{\text{rated}} - P_{\text{rated,sim}} | < 0.1\% \cdot P_{\text{rated}}$ ).
2. The simulated cut-in wind speed at the reference turbulence intensity fits the cut-in wind speed of the standard (given) power curve ( $| v_{\text{cut-in}} - v_{\text{cut-in,sim}} | < 0.5 \text{ m/s}$ ).
3. The power coefficient of the simulated power curve at reference turbulence intensity fits the power coefficient of the standard power curve ( $| C_{\text{pmax}} - C_{\text{pmax,sim}} | < 0.01$ ).

As a first approach the initial zero turbulence power curve is created based on the

following assumptions:

1. The rated power of the zero turbulence power curve fits the rated power of the standard power curve ( $P_{rated,zero} = P_{rated,ref}$ ).
2. The cut-in wind speed is set to cut-in wind speed of the standard power curve ( $v_{cut-in,zero} = v_{cut-in,ref}$ ).
3. The power coefficient ( $C_p$ ) shall be set to the maximum power coefficient of the standard power curve and it is constant between cut-in wind speed and rated wind speed ( $C_p = \max C_{p,ref}$ ).
4. The rated wind speed is calculated from the standard rated power, the rotor swept area ( $A$ ), the  $C_{pmax}$  and air density ( $\rho$ ) by:  $v_{rated} = (2 \cdot P_{rated} / (\rho \cdot C_{pmax} \cdot A))^{1/3}$ .

Then the rated power, the cut-in wind speed and the maximum power coefficient of the initial zero turbulence power curve are adjusted in the given order until the three parameters converge (Table 7.3). Sufficient convergence is usually reached after the first or second iteration.

$  P_{rated} - P_{rated,sim}   < 0.1\% \cdot P_{rated}$
$  v_{cut-in} - v_{cut-in,sim}   < 0.5\text{m/s}$
$  C_{pmax} - C_{pmax,sim}   < 0.01$

Table 7.3: Convergence criteria

Then, the initial zero turbulence curve is further refined using the Equation 7.8 as follows:

$$P_{zero} = P_{givenPC,I-ref}(v) - P_{simulated,I-ref}(v) + P_{simulated,I=0}(v) \quad (7.10)$$

Although this final adjustment can result in power outputs higher than the rated power (which is not a physical result), the accuracy of the final application is improved [Power Curve Working Group, 2014]. Hence, the zero turbulence power curve should be thought as the best correction to the standard curve rather than of being the true reflection of the instantaneous behaviour of the power curve.

### 7.2.2.2 Case study of the DMU campus

To investigate the impact of the turbulence intensity on the energy production, the power curve of the 5 kW wind turbine [Vermeir and Runacres, 2015] is used, which has been developed at a site with 13% turbulence intensity, and the field measurements at Kimberlin Library and Edith Murphy building, i.e. 5534 hours of measurements for the Kimberlin Library (i.e. around 7.7 months) and 1428 hours for the Edith Murphy building (i.e. about 2 months). 1 Hz samples were averaged over 10 min and the turbulence intensity (TI) is calculated using the time averaged wind speed and standard deviation:

$$TI = \frac{\sigma}{U_{mean}} \quad (7.11)$$

Elliott and Infield [2014] showed that the calculated turbulence intensity depends greatly on the averaging period and they recommend that it should be calculated in the conventional manner using 10 minute data, even if the power curve for small wind turbines is developed based on 1 minute averages.

Turbulent fluctuations occur in three dimensions: along-flow, across flow and vertically. Standard method to analyse the turbulence data [Carpman, 2011; IEC, 2006] is to rotate the horizontal wind vector ( $u_1(x), v_1(y)$ ) into a coordinate system that aligns with the mean wind direction during every 10 min averaging period. The mean wind direction is given by Equation 7.12 and the rotated components are

given by Equation 7.13.

$$\theta = \tan^{-1}\left(\frac{\overline{v_1}}{u_1}\right) \quad (7.12)$$

$$\begin{aligned} u &= u_1 \cos \theta + v_1 \sin \theta \\ v &= v_1 \cos \theta - u_1 \sin \theta \end{aligned} \quad (7.13)$$

where  $u$  describes the longitudinal wind velocity and  $v$  the lateral component.

Then, TI is determined by the standard deviation of longitudinal wind speed normalized with the mean wind speed (Equation 7.14).

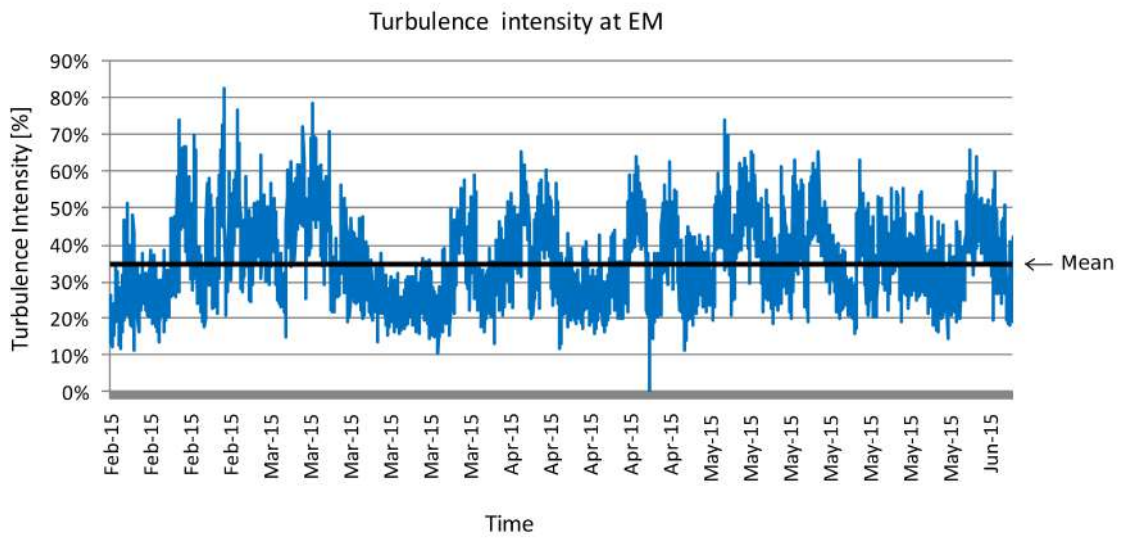
$$TI_u = \frac{\sigma_u}{\bar{u}} \quad (7.14)$$

The 10 min averaged  $TI_u$  calculated at EM and KL are shown in Figure 7.8. The TI values that corresponds to wind speeds lower than 3.5 m/s (cut-in wind speed) have been removed from the dataset. As shown in Figure 7.9, at low wind speeds the TI increases [Carpman, 2011], but they do not contribute to energy production.

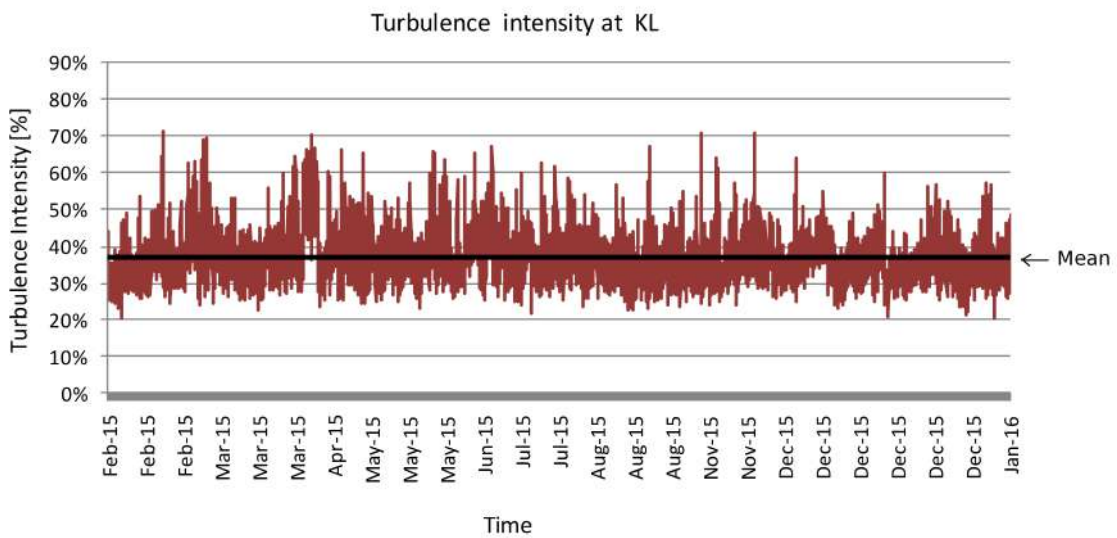
Both sites are characterised by high turbulence intensity (mean TI 35% and 37% at EM and KL respectively), thus the installation of small wind turbines should be interrogated; each wind turbine is designed to operate up to a specific magnitude of TI [IEC, 2006; Yang et al., 2016]. A large amount of turbulence generates a large amount of fatigue loadings on the construction, increasing the risk of breakdown [Carpman, 2011].

Assuming all the gust energy can be captured, the energy yield for the TI corrections was calculated and the energy production increased by 23.8% at Edith Murphy and 33.3% at Kimberlin Library. Figure 7.10 shows the corrected (in terms of turbulence intensity) power curves. Specifically the energy production is 607 kWh instead of 486



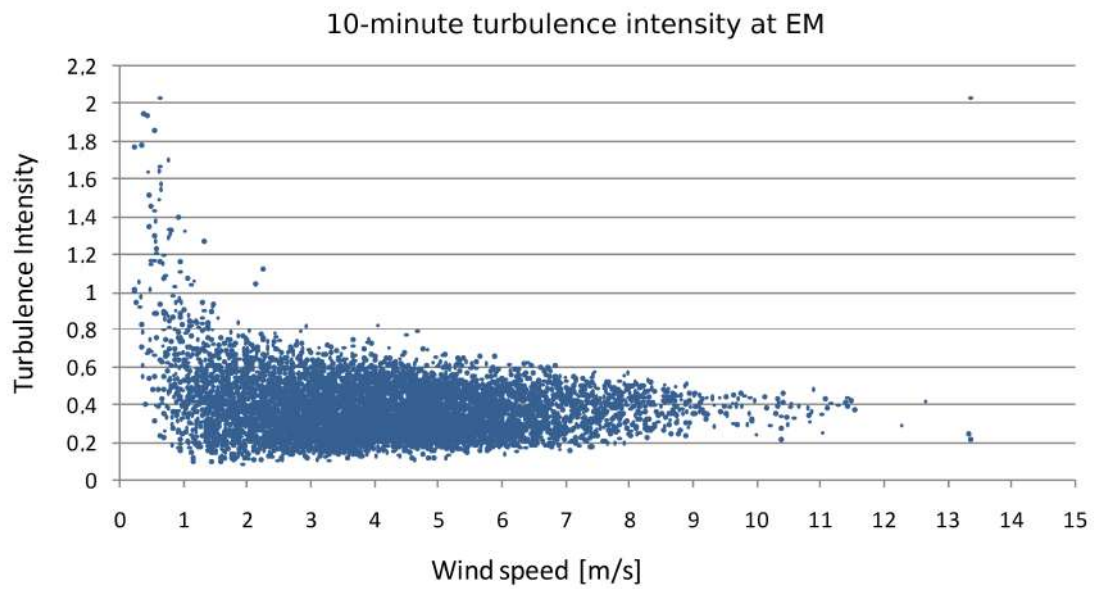


(a)

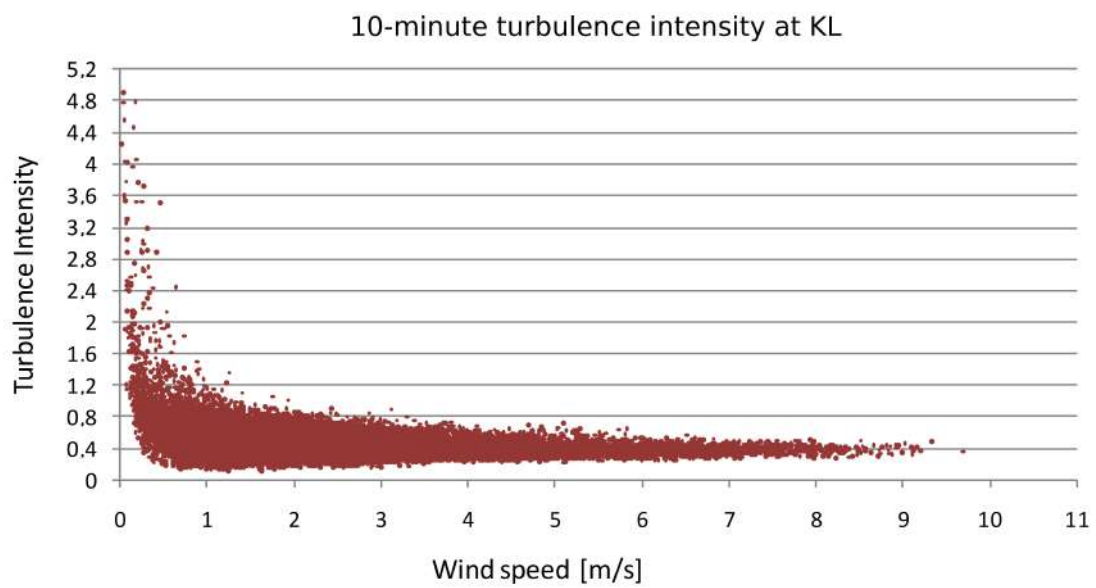


(b)

Figure 7.8: Turbulence intensity at a) EM and b) Kimberlin library as calculated from the 10 min averages, excluding the TI values which correspond to wind speeds lower than 3.5 m/s (cut-in wind speed).



(a)



(b)

Figure 7.9: Turbulence intensity as a function of wind speed at a) EM and b) KL.

kWh at Edith Murphy and 700 kWh instead of 525 kWh at Kimberlin Library.

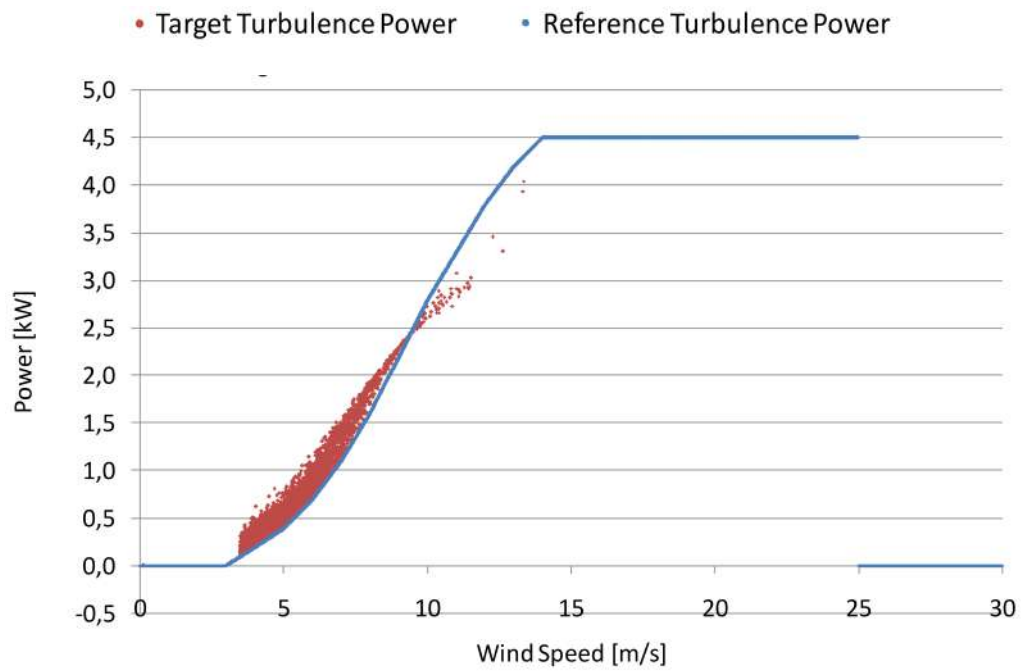
It should be noted that the calculated energy output (with no corrections) using the 10 minutes data is very similar to the energy estimations using the hourly data (Table 7.1), 486 kWh instead of 498 kWh and 525 kWh instead of 551 kWh. This has been even noted by Elliott and Infield [2014] who mentioned that there is little difference between the results obtained for 1 hour or 10 min averaging period and selection of smaller averaging period, such as one minute, affect the yield predictions by around 1 %. This difference is solely due to the different averaging time applied to calculate the frequency distribution.

Figure 7.10 illustrates the impact of TI at low wind speeds. The wind speed at both sites is much less than the rated wind speed and close to cut-in wind speed (4.1 m/s the mean wind speed at Edith Murphy and 2.6 m/s at Kimberlin Library) (Figure 7.3), then the power predictions increase for high TI levels.

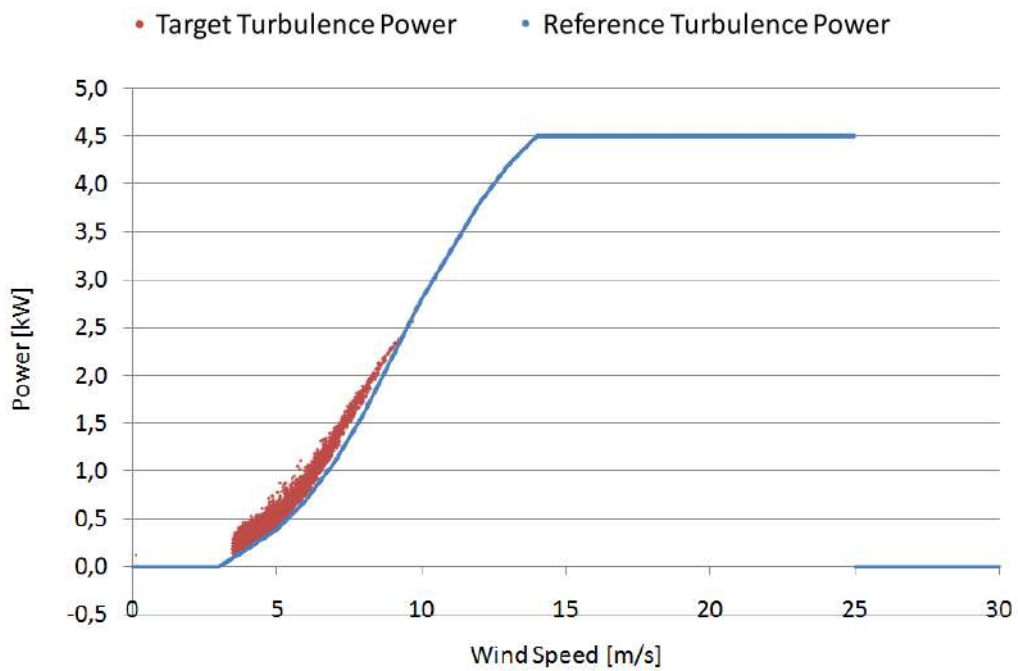
In practice these high turbulence levels do not allow the operation of most of the small wind turbines [Yang et al., 2016] and these rates of increase in energy production are not realistic.

For this reason, it was calculated the energy production assuming that the TI is constant at 18% (Figure 7.11a). Then, the predicted increase in energy output was 3.9% (505 kWh) at Edith Murphy and 4.8% (550 kWh) at Kimberlin Library. For lower turbulence intensity (5%) (Figure 7.11b) the predicted energy decreased by 3.5% (469 kWh) at Edith Murphy and 4.8% (500 kWh) at Kimberlin Library. Table 7.4 gathers the results.

It should be noted that the procedure for turbulence intensity correction was applied using the Excel application, which has been developed for this purpose by the power curve working group [Power Curve Working Group, 2014].

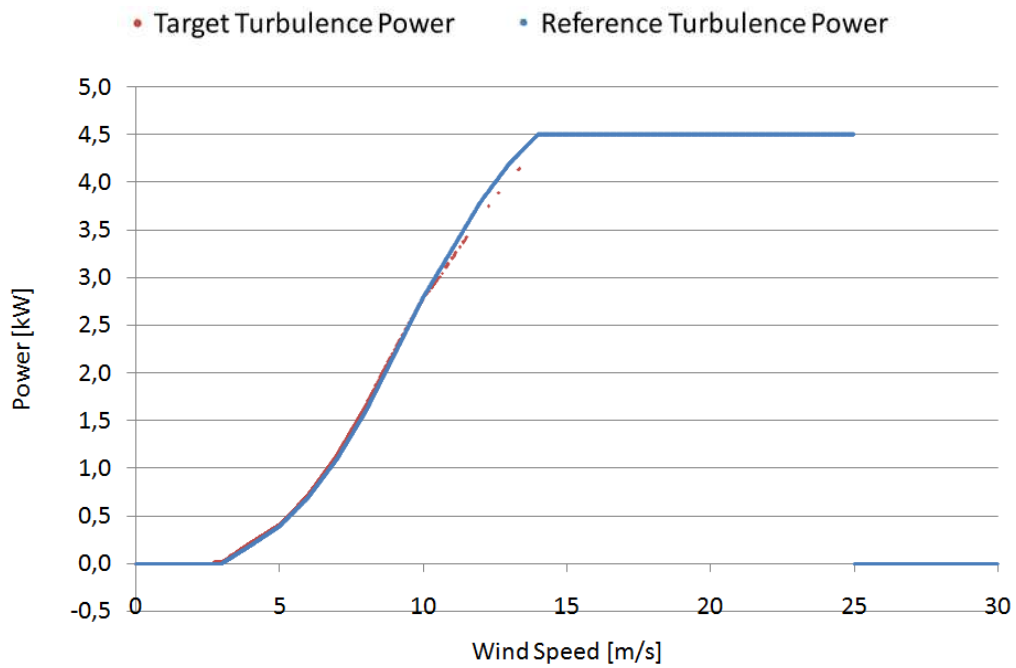


(a)

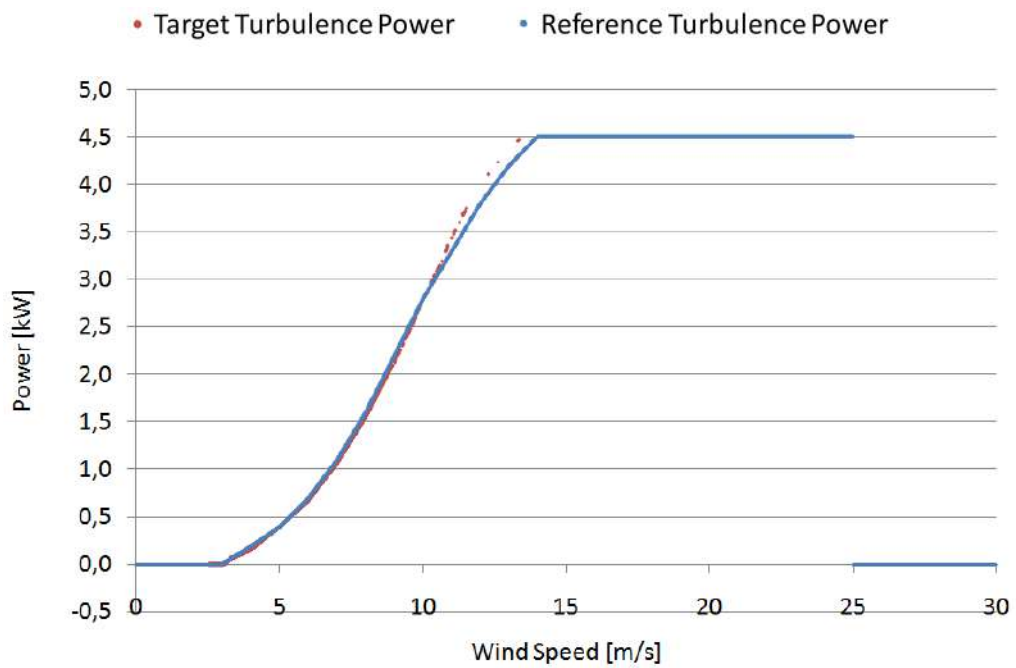


(b)

Figure 7.10: Corrected power curve for the 10 minute averaged wind speed and turbulence intensity at a) Edith Murphy b) Kimberlin library.



(a)



(b)

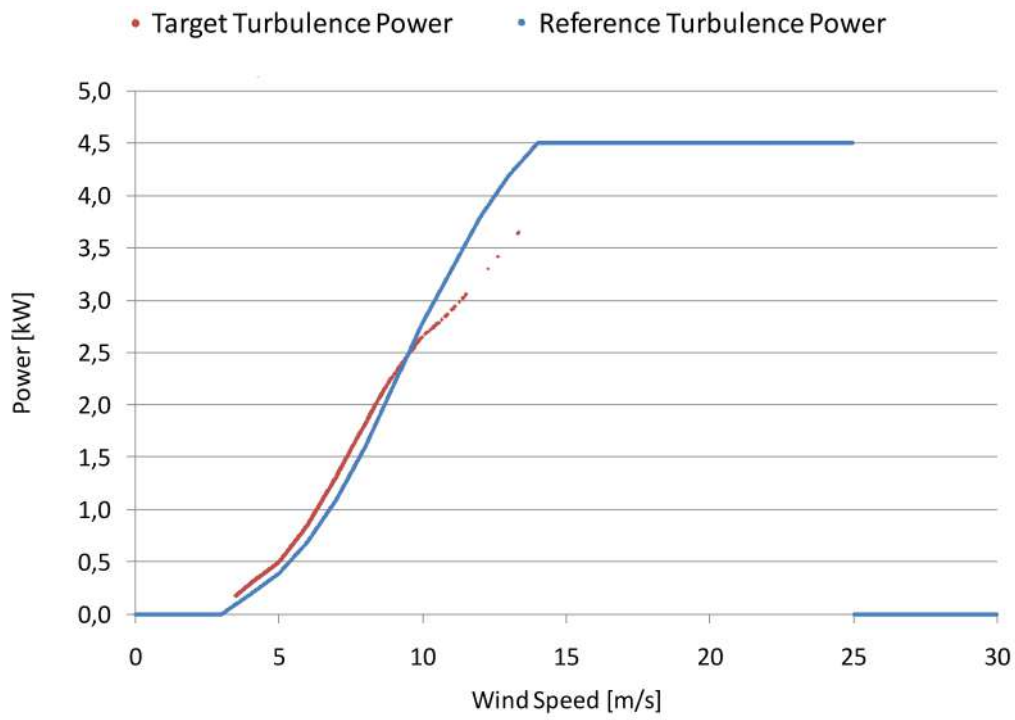
Figure 7.11: Corrected power curve for constant turbulence intensity at a) 18% and b) 5%.

TI	KL	EM
Reference	525 kWh	486 kWh
18%	550 kWh (+4.8%)	505 kWh (+3.9%)
5%	500 kWh (-4.8%)	469 kWh (-3.5%)

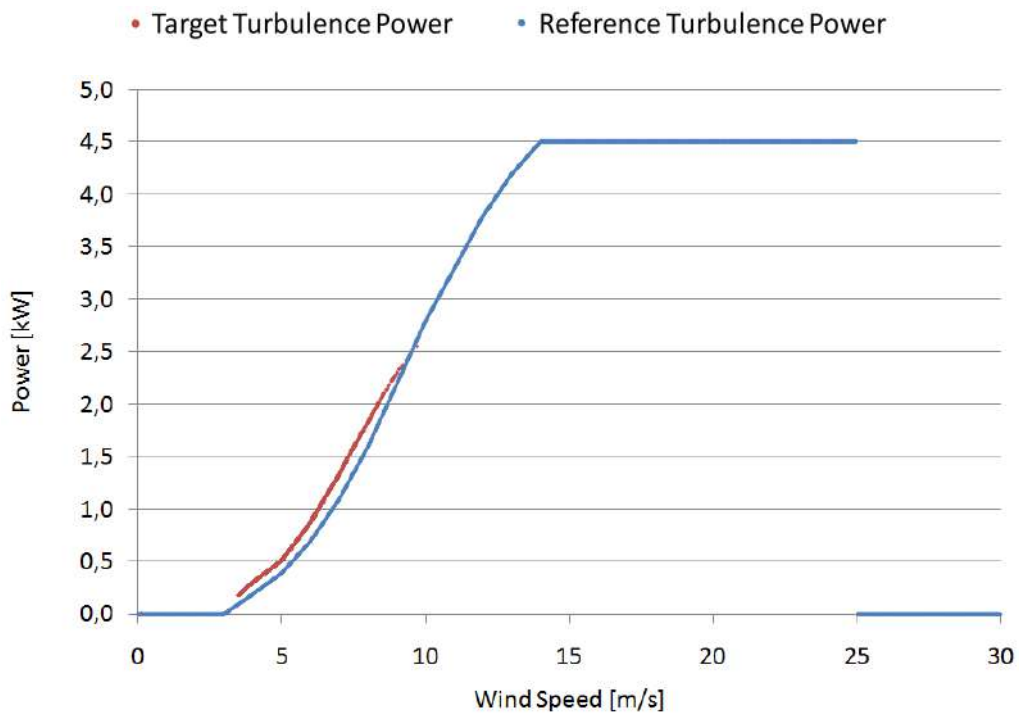
Table 7.4: Estimation of the energy yield (kWh) from a 5 kW wind turbine placed on Kimberlin Library (KL) and Edith Murphy (EM) buildings calculated at 10 min averages TI and at constant TI of 18% and 5%. In parenthesis, there is the rate of increase or decrease in power output in relation to the energy yield as calculated for the 10 min averages TI.

To incorporate the TI calculations in CFD methods, the mean TI should be used instead of the 10-min averages; at every time-step of the LES, velocity is calculated and can be used to obtain the values of TI according to the Equation (7.14). For this purpose, the impact of the difference between the mean TI and the 10-min averages on the power production was investigated. The corrected power curves for the mean TI at EM and KL were developed (Figure 7.12) and the calculated AEP were compared with the AEP as estimated using the 10-min TI averages. As shown in Figure 7.13, there is negligible difference in energy yields; 617 kWh at EM and 699 kWh at KL for the calculations using the mean TIs as opposed to 607 kWh and 700 kWh respectively for the calculations with the 10 min averages (error <2%), since the differences in energy yields for higher and lower turbulence intensities were cancelled out using the mean TI. However, this would not have happened if the TIs for the wind speeds lower than the cut-in wind speed had not been excluded from the calculations; as the TIs increase at low wind speeds (Figure 7.9) the mean TI would have been 38% at EM and 45% at KL instead of 35% and 37% respectively.

Consequently, the results imply that the TI could be included in CFD methods, however, special treatment is required at the region of cut-in wind speed and apparently at rated and cut-off wind speeds. I.e although the mean TI can be in the range of the turbine operation, turbines may not withstand the higher values that were used for the estimation of the mean TI and hence they should also be excluded from



(a)



(b)

Figure 7.12: Corrected power curve for the mean turbulence intensity at a) Edith Murphy b) Kimberlin library.

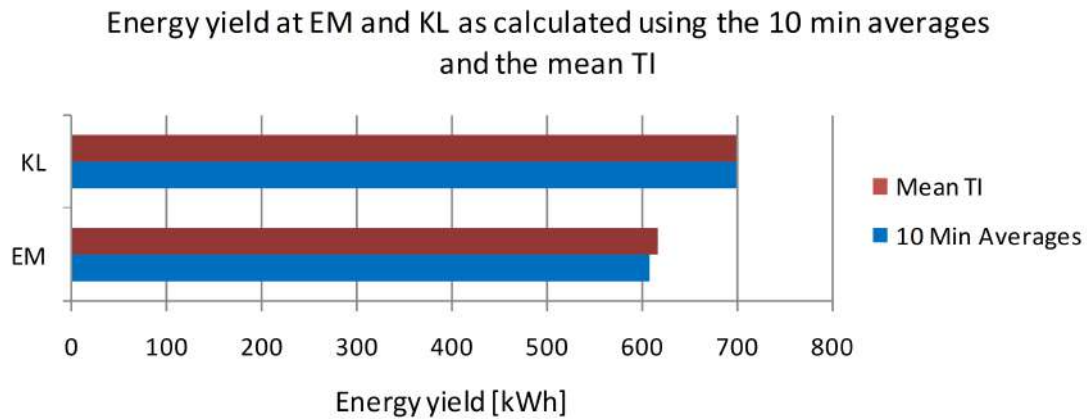


Figure 7.13: Energy yield calculated for the 10 min averages and the mean TI at EM and KL.

the calculations of energy yield. Since this study was focused on the calculations of mean wind speed and energy production, further studies of TI prediction above roof are required. Accurate prediction of the TI above roof is crucial for micro wind turbines application, because TI has a significant impact on the turbines' power performance and the fatigue of the machines.

[Carpman \[2011\]](#) measured with sonic anemometers the TI at an urban site, and found it 43% above rooftop, while the data contained a number of occasions with extreme values of standard deviation and TI. [Kalmikov et al. \[2010\]](#); [Yang et al. \[2016\]](#) have used the turbulence intensity in CFD calculations to identify suitable installation sites of micro-wind turbines. However, little information of the calculation process is provided. [Tabrizi et al. \[2014b\]](#) was planned to study the turbulence intensity prediction on the roof using TurbSim [[Jonkman, 2009](#)] simulator.

## 7.3 Discussion - Conclusions

Power curves provided by the manufacturers are valid for a reference air density and turbulence intensity, which may differ from the site-specific rates. In this chap-



ter, it was investigated the impact of the difference between the standard and the site-specific measurements on the energy production and provided guidance on the calculations.

### **Air-density correction**

Using the field measurements at DMU campus and an improved approach of the IEC 61400-12 standard to correct the power curve for the site specific air density, it was estimated the energy output assuming a 5 kWh wind turbine mounted at EM and KL.

It was found that for small differences between the default and the site specific mean  $\rho$  (of the order of  $10^{-3}$ ), there is negligible change in the energy production. However, for higher discrepancies of the order of  $10^{-2}$ , the power output can differ more than 10%, which should not be ignored.

If there are no available field measurements (air temperature and atmospheric pressure), one can estimate the site air density, as a function of altitude.

### **Turbulence intensity correction**

TI is important for wind resource analysis and wind energy applications, since it affects the turbine's power production. At low wind speeds the power output increases with increasing TI, while in the transition region to rated power the T.I. decreases the power output [Kaiser et al., 2007; Tindal et al., 2008; Wagner et al., 2009] (Figure 2.11).

However, wind turbines are designed to withstand specific external wind conditions, including turbulence. A large amount of turbulence generates a large amount of fatigue loadings on the construction, increasing the risk of breakdown [Carpman, 2011]. Hence, for built environment wind turbines, TI is an important issue as they

are located in the most turbulent area of the ABL.

High turbulence above rooftop was measured at EM and KL —the mean TI was 35% and 37% respectively— while the mean wind speeds were near the cut-in wind speed (4.1 m/s and 2.6 m/s at EM and KL respectively). These measurements are similar to [Carpman \[2011\]](#) at an urban site (43% above rooftop), while both datasets contained a number of occasions with extreme values of standard deviation and TI.

Assuming all the gust energy can be captured with a 5 kWh turbine, the energy yield for the 10-min averaged TI calculations would increase by 23.8% at EM and 33.3% at KL (at low wind speeds the power output increases with increasing TI). However, most micro-wind turbines cannot operate at such high turbulence and actually the high TI would have a mitigating impact on the power output. Assuming a constant TI of 18% (the common maximum TI the wind turbines withstand [[Yang et al., 2016](#)]) the energy yield would increase by 3.9% and 4.8% at EM and KL respectively, while for higher wind speeds, in the range of rated wind speed, this TI would decrease the power output.

Summarizing, it was shown that the impact of TI on the power output is not straightforward and highly depends on wind speed and the turbine's characteristics. Since, it can substantially influence the energy production, it should not be ignored and accurate predictions of TI and wind speed are required to quantify its effect.

The field measurements of TI at discrete points cannot be used for predictions at the rest of the domain, and CFD-based evaluating methods need to be established. Since CFD methods are based on the reduction factors assumption (at high Re numbers, the wind behaviour is the same at any reasonable reference wind speed), while TI has different impact on energy production at different wind speeds, the impact of the difference between the mean TI and the 10-min averages on the power production was investigated. It was found that, under specific circumstances, there is essentially

no difference in the energy yield predictions using the 10-min averages and the mean TI. In practice, using the mean TI, the differences in energy yields for higher and lower TIs are cancelled out, however, special treatment is required at the region of cut-in wind speed as TI measurements at these wind speed rates (TI increases at low wind speeds) should be excluded from the calculations. Correspondingly, the TI measurements above the cut-off wind speeds should also be excluded from the calculations, as they do not contribute to the energy production. However, in this work, there were not measurements of the range of rated and cut-out wind speeds and it was only studied the energy yield at low wind speeds. Hence, further studies of TI prediction above roof are required and CFD-based evaluating methods need to be established and described explicitly. Using LES the velocity field is calculated at every time-step and Equation (7.14) can be used to obtain the values of TI, while in steady-state RANS simulations this procedure cannot be implemented [Heath et al., 2007; Kono et al., 2016]. Micro-wind turbine mounted at urban areas could verify the calculations.

# Chapter 8

## Conclusions and Future work

### 8.1 Summary of achievements

One of the main obstacles for built environment wind turbines (BWT) deployment in complex urban environments is the lack of accurate and economic methods for estimating the mean wind speed and the energy yield at potential mounting locations [Yang et al., 2016].

This research offers a framework for wind resource assessment in the context of BWT applications in urban areas and it has sought to address the following issues:

- A) Analysis of wind flows at city scale using a fully transient CFD approach that offers improved robustness and accuracy over a range of conditions compared to quasi steady-state methods.
- B) Development of a novel CFD-based methodology to identify the optimum location for BWT application based on calculations of 3D data fields corresponding to the mean annual wind speed and the AEP.
- C) Refinement of AEP estimation according to density variations and turbulence intensity and guidance on the calculation and reliability of AEP estimation techniques.

## A) Wind flow analysis in urban areas

In this study, the analysis of wind flow in urban areas was based on CFD approaches. Analytical methods do not account for the impact of individual obstacles on the flow and hence cannot predict the variability of the wind speed in the vicinity to the buildings [Drew et al., 2013]. ‘Wind speeds at sheltered sites are difficult to predict accurately without site specific fluid dynamical modelling’, as reported by Millward-Hopkins et al. [2013a]. Statistical analysis (e.g. Weibull analysis) can contribute to macrositing studies, however, it cannot provide the precision required for micro-siting [Yang et al., 2016]. ‘A CFD simulation approach would be ideal to understand the actual flow patterns in these localities to decide the best locations for wind turbine installations’ [Karthikeya et al., 2016]. Analysis of on-site measurements is considered the most accurate approach, however they are costly and time-consuming and they can only capture the wind characteristics at discrete points [Gagliano et al., 2013]. Computational Fluid Dynamics (CFD) is a numerical analysis approach which has been confirmed as a promising technique to analyse the wind flow in complex urban environment for evaluating the potential for micro wind turbines installation [Yang et al., 2016].

Limited CFD studies of complex urban areas have been validated using field measurements [Kalmikov et al., 2010; Simoes and Estanqueiro, 2016; Tabrizi et al., 2014b; Yang et al., 2016] and none of them have used a DES model. In this work, the predicted capabilities of the unsteady CFD approach, known as DES, were examined. This approach offers improved prediction of flows in wake regions compared to RANS methods but is less computationally demanding than full LES approaches. Initially, two test cases, developed by AIJ, were modelled and the results were validated against benchmark data (wind tunnel data, as well as field measurements). It was found that the SA-DDES model offers improved robustness and accuracy over a range of conditions. Thus, in the further study of wind flows at the DMU campus,

the DES approach was applied and the results compared again very well with high frequency on site anemometer data.

## **B) Identification of the optimum mounting location for BWT application**

A new approach was developed to identify the potential mounting locations for BWTs. The methodology developed by [Simoes and Estanqueiro \[2016\]](#) smooths the city geometry to conduct mesoscale modeling and then applies correction factors to describe the urban wind flow more accurately. [Tabrizi et al. \[2014b\]](#) based his work on modeling the mean wind speed for eight wind directions and ignored the annual variability in wind speed frequency distributions, which is also important in assessing the AEP. Different mounting positions are better fitted to different prevailing wind situations and his work does not provide a rigorous methodology for identifying the optimum mounting locations. [Yang et al. \[2016\]](#) used the predictions for the prevailing wind direction and the mean wind speed to identify the optimum sites for micro wind turbines and he did not account for different wind situations. [Kalmikov et al. \[2010\]](#) considered the complex geometry of the Massachusetts Institute of Technology (MIT) campus in the USA to conduct CFD simulations to assess the wind energy potential. He created a three dimensional structure of wind resource by combining real measured wind data with CFD calculations. However, little information of the calculation process is provided.

This work provides a new, rigorous, step by step methodology for CFD-based evaluation of mounting micro wind turbines in a complex urban environment, based on the spatial variations in mean annual wind speed and the corresponding AEP. The ‘Wind Atlas Methodology’ is used first to transfer the meteorological data from the weather station to the height where the flow is considered to be horizontally homogeneous. Then, the CFD is applied for making corrections for local shadowing

effects. The corrections are described in terms of the reduction factors i.e. wind speeds normalised by the reference wind speed. This is justified given that at high Re numbers, the wind speed reduction (e.g. in wake regions) is linear at any reasonable reference wind speed. As opposed to most previous studies, this methodology accounts for the hourly fluctuations of the wind speed in magnitude and direction recorded in climate data sets and creates the three dimensional field of the average annual wind speed. Then, a real turbine's power curve was used and combined with the hourly wind data (wind speed and direction) to create the three dimensional field of the AEP. Since the power curves are not linear, this approach is favoured for predicting the actual energy output at the site, rather than using the wind power density, which indicates how much energy is available at the site [Dabbaghiyan et al., 2016]. As the power data of real machines is used, the results are also useful for evaluating the economic viability of particular small wind turbines.

### **C) Correction of the power curves and guidance on the calculation and reliability of AEP estimation techniques**

Another aspect investigated, was the accuracy of the power curves given possible variations in density and turbulence intensity at particular locations. The default power curves are valid for standard values of air density ( $\rho$ ) and turbulence intensity, which may differ from the site rates. Their impact on turbine's power performance has been examined.

It was found that for differences of the order of  $10^{-3}$  between the default and the site specific mean  $\rho$ , there is negligible change in the energy production. However, for higher discrepancies of the order of  $10^{-2}$  the power output can differ more than 10%, which should not be ignored. Techniques to estimate the site air density and correct the power curves are provided.

Turbulence affects the wind energy in two ways: through power performance impacts

and through effects on turbine loads and fatigue. In the operational range of each turbine, TI increases the output at low wind speeds, while in the transition region to rated power it decreases the power output. Assuming all the gust energy can be captured with a 5 kW wind turbine (its power curve measured at a site with 13% TI), the TI at DMU (35% mean TI and 4.1 m/s mean wind speed), increased the AEP by 24%, but limiting the TI to 18% the increase was only 4%. In any case turbulence has a measurable effect on turbine's power production and on the loads that cause wind turbine component fatigue, and hence, accurate predictions are crucial for accurate power production estimates.

In order to investigate the suitability of the CFD approach to predict TI, the impact of the mean TI on the power output was examined. It was found that, under specific circumstances, there is essentially no difference in the energy production between the 10 min averaged and the mean TI. Hence, the CFD model, which is based on the assumption that the velocity ratios are independent of the reference velocity, could include TI calculations, although TI varies with wind speed.

### **Case study - DMU campus**

The methodology was applied at DMU campus to identify the optimum mounting locations and predict the AEP, and some very interesting observations were distinguished.

- Considering only the mean wind speed field for the prevailing wind can be misleading. Different mounting positions are better fitted to different prevailing wind situations.
- High speed gradients exist in both horizontal and vertical direction, and small shifts of the location of the turbine can change considerably the output. At rooftop height the wind shear is strong and the height of the turbine is very important.



- However, the effect of the urban topography on the wind potential is not always apparent. Lower building can have higher potential for micro wind turbines installation than taller in close proximity and roofs of the same height and close each other may differ substantially in their predicted energy output.

## 8.2 Recommendations for future work

This method could be used to model a whole city and develop an interactive wind energy map (similar to New York solar map [[NY Solar Map](#)]), which will provide the potential that a rooftop possesses for wind energy and the economic viability of particular small wind turbines. This map could be a tool that all people can use and learn about the wind energy potential; it could be of use to planners, consultants and architects and those interested in new or retrofit applications.

However, as the built environment is highly turbulent and can affect substantially turbine performance, further studies of TI prediction above roofs are required and rigorous CFD-based evaluating methods need to be established.

Field measurements are of high value for validation purposes. In this study, only measurements of high TI at low wind speeds were examined. Special treatment was required at the region of cut-in wind speed and TI predictions could be included in CFD evaluation methods. Accordingly the influence of the TI on the power output for wind speeds at the rated and cut-off ranges should be found. Hence, longer monitoring periods and variation in wind conditions should be investigated in order to establish rigorous methods applied in various circumstances.

An important issue to be addressed is how the TI can be predicted by the CFD approach. The standard method to analyse turbulence uses the longitudinal TI which differs from the a-axis (x, y or z) of the CFD domain, the standard deviation is usually calculated for. Moreover, turbulent fluctuations occur in three dimensions

and the standard turbulence analysis method ignores the lateral and vertical contribution of turbulence, that can be very strong. Studies of micro-wind turbines mounted at urban areas would be useful for investigating the directional impact of turbulence on the power output and for validation purposes.



# References

- Abohela, I., Hamza, N., and Dudek, S. 2011. Assessment of wind flow within the built environment. *Built and Natural Environment Research Papers*, 4:81–94.
- Abohela, I., Hamza, N., and Dudek, S. 2013. Effect of roof shape, wind direction, building height and urban configuration on the energy yield and positioning of roof mounted wind turbines. *Renewable Energy*, 50:1106 – 1118.
- Abraham, J. P., Plourde, B. D., Mowry, G. S., Minkowycz, W. J., and Sparrow, E. M. 2012. Summary of savonius wind turbine development and future applications for small-scale power generation. *Journal of Renewable and Sustainable Energy*, 4(4).
- Acheson, D. 1990. *Elementary Fluid Dynamics*. Oxford Applied Mathematics and Computing Science Series. Clarendon Press.
- AIJ 2009. Guidebook for practical applications of CFD to pedestrian wind environment around buildings. <http://www.aij.or.jp/jpn/publish/cfdguide>. [Online; accessed 12/5/15].
- Albers, A. 2009a. Turbulence and Shear Normalisation of Wind Turbine Power Curve. *Deutsche WindGuard Consulting GmbH*.
- Albers, A. 2009b. Turbulence Normalisation of Wind Turbine Power Curve Measurements. *Deutsche WindGuard Consulting GmbH*.

- Albers, A. and Windguard, D. 2014. Power Curve Turbulence Normalisation for Wind Resource Assessments. In *EWEA, Real World Power Curves*, Barcelona, Spain.
- Aly, A. M. 2013. Pressure integration technique for predicting wind-induced response in high-rise buildings. *Alexandria Engineering Journal*, 52(4):717 – 731.
- Anjum, L. 2014. Wind resource estimation techniques-an overview. *International Journal of wind and Renewable Energy*, 3(2):26–38.
- Aral, M. M. and Mustafa, M. 2010. Environmental modeling and health risk analysis (acts/risk).
- Armenio, V., Geurts, B., and Fröhlich, J. 2010. *Direct and Large-Eddy Simulation VII: Proceedings of the Seventh International ERCOFTAC Workshop on Direct and Large-Eddy Simulation, held at the University of Trieste, September 8-10, 2008*. ERCOFTAC Series. Springer Netherlands.
- Aspliden, C. I. and Elliot, D. L. and Wendell, L. L. 1986. Resource Assessment Methods, Siting, and Performance Evaluation. In *Physical Climatology for Solar and Wind Energy*, World Scientific, New Jersey.
- Ayhan, D. and afak Salam 2012. A technical review of building-mounted wind power systems and a sample simulation model. *Renewable and Sustainable Energy Reviews*, 16(1):1040 – 1049.
- BADC. The british atmospheric data centre. <http://badc.nerc.ac.uk/home/>. [Online; accessed 2016-03-22].
- Bahlouli, A. E. L. and Bange, J. 2015. An experimental and numerical study of the airflow around university buildings in Tübingen. In *WINERCOST Workshop ‘Trends and Challenges for Wind Energy Harvesting’*, pages 79–85, Coimbra, Portugal.

- Balduzzi, F., Bianchini, A., and Ferrari, L. 2012. Microeolic turbines in the built environment: Influence of the installation site on the potential energy yield. *Renewable Energy*, 45:163 – 174.
- Balogh, M., Parente, A., and Benocci, C. 2012. RANS simulation of ABL flow over complex terrains applying an enhanced k- $\epsilon$  model and wall function formulation: Implementation and comparison for fluent and OpenFOAM. *Journal of Wind Engineering and Industrial Aerodynamics*, 104-106:360 – 368. 13th International Conference on Wind Engineering.
- Barlow, J. F. 2014. Progress in observing and modelling the urban boundary layer. *Urban Climate*, 10, Part 2:216 – 240. ICUC8: The 8th International Conference on Urban Climate and the 10th Symposium on the Urban Environment.
- Barry, R. and Chorley, R. 1987. *Atmosphere, Weather, and Climate*. University paperbacks. Methuen.
- Battan, L. 1979. *Fundamentals of Meteorology*. Prentice-Hall.
- Bechmann, B. A. 2012. WAsP CFD A new beginning in wind resource assessment. Technical report, Riso National Laboratory, Denmark.
- Betz, A. 1966. *Introduction to the theory of flow machines*. Pergamon Press.
- Bhutta, M. M. A., Hayat, N., Farooq, A. U., Ali, Z., Jamil, S. R., and Hussain, Z. 2012. Vertical axis wind turbine a review of various configurations and design techniques. *Renewable and Sustainable Energy Reviews*, 16(4):1926 – 1939.
- Bianchi, S., Bianchini, A., Ferrara, G., and Ferrari, L. 2013. Small Wind Turbines in the Built Environment: Influence of Flow Inclination on the Potential Energy Yield. *Journal of Turbomachinery*, 136(4):041013.
- Blocken, B., Janssen, W. D., and Hooff, T. V. 2012. CFD simulation for pedestrian

- wind comfort and wind safety in urban areas : General decision framework and case study for the Eindhoven University campus. 31(0):15–34.
- Blocken, B. and Persoon, J. 2009. Pedestrian wind comfort around a large football stadium in an urban environment: CFD simulation, validation and application of the new Dutch wind nuisance standard. *Journal of Wind Engineering and Industrial Aerodynamics*, 97(5-6):255–270.
- Blocken, B., Stathopoulos, T., and Carmeliet, J. 2008. Wind Environmental Conditions in Passages between Two Long Narrow Perpendicular Buildings. *Journal of Aerospace Engineering*, 21(4):280–287.
- Boussinesq, J. 1877. *Essai sur la théorie des eaux courantes*. Mémoires présentées par divers savants à l’Académie des Sciences. Imprimerie Nationale.
- Braun, A. L., Madalozzo, D., Awruch, A. M., and Wind, C. 2012. Numerical investigation on the influence of turbulence fluctuations over wind engineering problems using large eddy simulation and a synthetic inflow turbulence generator. XXXI:13–16.
- Breuer, M., Jovii, N., and Mazaev, K. 2003. Comparison of des, rans and les for the separated flow around a flat plate at high incidence. *International Journal for Numerical Methods in Fluids*, 41(4):357–388.
- Brown, O. W. and Hugenholtz, C. H. 2012. Estimating aerodynamic roughness (zo) in mixed grassland prairie with airborne lidar. *Canadian Journal of Remote Sensing*, 37(4):422–428.
- Bussel, G. and Mertens, S. M. 2005. Small wind turbines for the built environment. In *The Fourth European & African Conference on Wind Engineering*, Prague.
- Calautit, J. K. and Hughes, B. R. 2014. Wind tunnel and CFD study of the natural

- ventilation performance of a commercial multi-directional wind tower. *Building and Environment*, 80:71 – 83.
- Campbell Scientific Inc 2016. *CS106 Barometric Pressure Sensor Manual*.
- Campos-Arriaga, L. 2009a. *Wind energy in the built environment : a design analysis using CFD and wind tunnel modelling approach* . PhD thesis, University of Nottingham.
- Campos-Arriaga, L. 2009b. Wind energy in the built environment: a design analysis using CFD and wind tunnel modelling approach.
- Carpman, N. 2011. Turbulence Intensity in Complex Environments and its Influence on Small Wind Turbines. Master's thesis, Department of Earth Sciences, Uppsalla University, Uppsalla.
- Cebeci, T. and Bradshaw, P. 1977. *Momentum transfer in boundary layers*.
- Cheng, Y., Lien, F., Yee, E., and Sinclair, R. 2003. A comparison of Large Eddy simulations with a standard  $k-\epsilon$  Reynolds-averaged Navier-Stokes model for the prediction of a fully developed turbulent flow over a matrix of cubes. *Journal of Wind Engineering and Industrial Aerodynamics*, 91(11):1301–1328.
- Choi, E. C. C. 2009. Proposal for unified terrain categories exposures and velocity profiles. In *The 7<sup>th</sup> Asia-Pacific Conference on wind engineering*, Taipei, Taiwan.
- Christen, A., van Gorsel, E., and Vogt, R. 2007. Coherent structures in urban roughness sublayer turbulence. *International Journal of Climatology*, 27(14):1955–1968.
- Churchfield, M. J. and Moriarty, P. J. 2010. Wind Energy-Related Atmospheric Boundary Layer Large-Eddy Simulation Using OpenFOAM. In *19<sup>th</sup> Symposium on Boundary Layers and Turbulence*, Keystone, Colorado.



- Clifford, M., Everitt, P., Clarke, R., and Riffat, S. 1997. Using computational fluid dynamics as a design tool for naturally ventilated buildings. *Building and Environment*, 32(4):305 – 312.
- Coirier, W. J. and Kim, S. 2006. CFD modeling for urban area contaminant transport and dispersion: Model description and data requirements. In *6th Symposium on the Urban Environment, Atlanta, American Meteorological Society*, volume 11.
- COST. European cooperation in science and technology. <http://www.cost.eu>. [Online; accessed 2016-07-12].
- Cui, P.-Y., Li, Z., and Tao, W.-Q. 2016. Wind-tunnel measurements for thermal effects on the air flow and pollutant dispersion through different scale urban areas. *Building and Environment*, 97:137 – 151.
- Cushman-Roisin, B. 2001. *Physical oceanography of the Adriatic Sea: past, present, and future*. Kluwer Academic Publishers, Dordrecht ; Boston. xiv, 304 p.
- Dabbaghiyan, A., Fazelpour, F., Abnavi, M. D., and Rosen, M. a. 2016. Evaluation of wind energy potential in province of Bushehr, Iran. *Renewable and Sustainable Energy Reviews*, 55:455–466.
- Department of Energy and Climate Change 2011. UK Renewable Energy Roadmap.
- Department of Energy and Climate Change 2013. UK Renewable Energy Roadmap.
- Doggett, S. Climate data for building simulations. <https://builtenv.wordpress.com/2014/02/27/climate-data-for-building-simulations/>. [Online; accessed 2016-09-22].
- Drew, D., Barlow, J., and Cockerill, T. 2013. Estimating the potential yield of small wind turbines in urban areas: A case study for Greater London, UK. *Journal of Wind Engineering and Industrial Aerodynamics*, 115:104–111.

- Elliott, D. and Infield, D. 2014. An assessment of the impact of reduced averaging time on small wind turbine power curves, energy capture predictions and turbulence intensity measurements. *Wind Energy*, 17(2):337–342.
- Elliott, W. P. 1958. The growth of the atmospheric internal boundary layer. *Eos, Transactions American Geophysical Union*, 39(6):1048–1054.
- Emejamara, F. C. and Tomlin, A. S. 2015. A method for mapping the turbulence intensity and excess energy available to building mounted wind turbines over a UK City. *Wind Energy*.
- Encraft 2009. Warwick Wind Trial. Technical report.
- European Commission 2011. Impact Assessment. Technical report.
- European Commission 2012. Energy roadmap 2050.
- EWEA 2009. Wind Energy - The Facts.
- Fadl, M. S. and Karadelis, J. 2013. CFD Simulation for Wind Comfort and Safety in Urban Area: A Case Study of Coventry University Central Campus. *International Journal of Architecture, Engineering and Construction*, 2(2):131–143.
- Flores, F., Garreaud, R., and Muoz, R. C. 2014. OpenFOAM applied to the CFD simulation of turbulent buoyant atmospheric flows and pollutant dispersion inside large open pit mines under intense insolation. *Computers Fluids*, 90:72 – 87.
- Franke, J., Hellsten, A., Schlünzen, H., and Carissimo, B. 2007. *Best practice guideline for the CFD simulation of flows in the urban environment*. European Science Foundation COST Office.
- Franke, J., Hellsten, A., Schlunzen, K. H., and Carissimo, B. 2011. Best practice guideline for cfd simulation of flows in the urban environment: a summary. *International Journal of Environment and Pollution*, 44(1-4):419–427.

- Franke, J., Hirsch, C., Jensen, A., Krüs, H., Schatzmann, M., Westbury, P., Miles, S., Wisse, J., and Wright, N. 2004. *Recommendations on the use of CFD in wind engineering*. European Science Foundation COST Office.
- Gagliano, A., Nocera, F., Patania, F., and Capizzi, A. 2013. Assessment of micro-wind turbines performance in the urban environments: an aided methodology through geographical information systems. *International Journal of Energy and Environmental Engineering*, 4(1):43.
- Garcia-Sanchez, C., Beeck, J. V., and Gorle, C. 2015. Inflow uncertainty quantification within urban environments: wind fields and dispersion patterns. In *WINERCOST Workshop ‘Trends and Challenges for Wind Energy Harvesting’*, number March, pages 105–115, Coimbra, Portugal.
- Garg, N. and Srikanth, N. 2013. Wind resource and wind safety assessment in an urban complex. In *International conference on Alternative energy in developing countries and Emerging Economies (AEDCEE)*, Bangkok.
- Garratt, J. 1983. Surface influence upon vertical profiles in the nocturnal boundary layer. *Boundary-Layer Meteorology*, 26(1):69–80.
- Garratt, J. R. 1994. *The atmospheric boundary layer*. Cambridge : Cambridge U. P, 1st paperback (with corrections) edition. p. 294-310.
- Ghione, A. 2012. Development and validation of a two-phase cfd model using open-foam. Master’s thesis, KTH, Stockholm.
- Grimmond, C. S. B. and Oke, T. R. 1999. Aerodynamic properties of urban areas derived from analysis of surface form. *Journal of Applied Meteorology*, 38(9):1262–1292.
- Grotzbach, G. *Direct numerical and large eddy simulation of turbulent channel flow*. In *Encyclopedia of Fluid Mechanics*, volume 6.

- Hall, T. C., Britter, R. E., and Norford, L. K. 2012. Predicting velocities and turbulent momentum exchange in isolated street canyons. *Atmospheric Environment*, 59:75–85.
- Haupt, S. E., Zajaczkowski, F. J., and Peltier, L. J. 2011. Detached Eddy Simulation of Atmospheric Flow About a Surface Mounted Cube at High Reynolds Number. *Journal of Fluids Engineering*, 133(3):031002.
- He, J. and Song, C. C. 1999. Evaluation of pedestrian winds in urban area by numerical approach. *Journal of Wind Engineering and Industrial Aerodynamics*, 81(13):295 – 309.
- Heath, M. a., Walshe, J. D., and Watson, S. J. 2007. Estimating the potential yield of small building-mounted wind turbines. *Wind Energy*, 10(3):271–287.
- Holmes, N. and Morawska, L. 2006. A review of dispersion modelling and its application to the dispersion of particles: An overview of different dispersion models available. *Atmospheric Environment*, 40(30):5902–5928.
- Hong, T., Chang, W.-k., and Lin, H.-w. 2013. A Fresh Look at Weather Impact on Peak Electricity Demand and Energy Use of Buildings Using 30-Year Actual Weather Data. Technical Report May, Ernest Orlando Lawrence - Berkeley National Laboratory.
- Hooff, T. V. and Blocken, B. 2010. On the effect of wind direction and urban surroundings on natural ventilation of a large semi-enclosed stadium. *Computers & Fluids*, 39(7):1146–1155.
- Hossain, J. 2015. Wind Energy 2050 - On the shape of near 100 % RE grid. Technical Report October.
- Huang, S. and Li, Q. 2010. Numerical simulations of wind-driven rain on building

- envelopes based on eulerian multiphase model. *Journal of Wind Engineering and Industrial Aerodynamics*, 98(12):843 – 857.
- IEC 2006. *International Standard 61400-2. Wind Turbines - Part 2: Design requirements for small turbines*.
- Irshad, W. 2012. *Wind Resource Assessment : Statistical and Computational Fluid-Dynamic Analysis*. PhD thesis.
- Ishugah, T., Li, Y., Wang, R., and Kiplagat, J. 2014. Advances in wind energy resource exploitation in urban environment: A review. *Renewable and Sustainable Energy Reviews*, 37:613 – 626.
- James, P., Sissons, M., Bradford, J., Myers, L., a.S. Bahaj, Anwar, a., and Green, S. 2010. Implications of the UK field trial of building mounted horizontal axis micro-wind turbines. *Energy Policy*, 38(10):6130–6144.
- Janssen, W., Blocken, B., and van Hooff, T. 2013. Pedestrian wind comfort around buildings: Comparison of wind comfort criteria based on whole-flow field data for a complex case study. *Building and Environment*, 59(0):547 – 562.
- Jasak, H., Jemcov, A., and Tukovic, Z. 2007. Openfoam: A C++ library for complex physics simulations. *International workshop on coupled methods in numerical dynamics*, 1000:1–20.
- Jiang, Y., Alexander, D., Jenkins, H., Arthur, R., and Chen, Q. 2003. Natural ventilation in buildings: measurement in a wind tunnel and numerical simulation with large-eddy simulation. *Journal of Wind Engineering and Industrial Aerodynamics*, 91(3):331 – 353.
- Jones, P. and Whittle, G. 1992. Computational fluid dynamics for building air flow prediction current status and capabilities. *Building and Environment*, 27(3):321 – 338.

- Jones, P. J., Alexander, D., and Burnett, J. 2004. Pedestrian wind environment around high-rise residential buildings in hong kong. *Indoor and Built Environment*, 13(4):259–269.
- Jonkman, B. J. 2009. *TurbSim User’s Guide: Version 1.50*. National Renewable Energy Laboratory.
- Jothiprakasham, V. D. 2014. *Downscaling wind energy resource from mesocale to local scale by nesting and data assimilation with a CFD model*. PhD thesis, University of Paris-Est.
- Kaimal, J. C. and Finnigan, J. J. 1994. *Atmospheric boundary layer flows: their structure and measurement*. Oxford University Press, New York.
- Kaiser, K., Langreder, W., Hohlen, H., and Hjstrup, J. 2007. Turbulence correction for power curves. In Peinke, J., Schaumann, P., and Barth, S., editors, *Wind Energy*, pages 159–162. Springer Berlin Heidelberg.
- Kalmikov, A., Dupont, G., Dykes, K., and Chan, C. 2010. Wind power resource assessment in complex urban environments : MIT campus case-study using CFD Analysis. In *AWEA WINDPOWER Conference*.
- Karthikeya, B., Negi, P. S., and Srikanth, N. 2016. Wind resource assessment for urban renewable energy application in singapore. *Renewable Energy*, 87, Part 1:403 – 414.
- Katz, P. C. and Ag, S. Use of Computational Fluid Dynamics in Civil Engineering.
- Khayrullina, A., Hooff, T. V., and Blocken, B. 2013. A study on the wind energy potential in passages between parallel buildings. In *Proceedings of the 6th European-African Conference on Wind Engineering (EACWE)*, pages 1–8, Cambridge, UK.

- King, K. 2009. Interim Report: Wind Speed and Energy Yield Analysis of Small Wind Turbines on a 45m High-rise Building in the Built Environment. Technical report, Loughborough University.
- Kneifel, J. and O'Rear, E. 2014. An Assessment of Typical Weather Year Data Impacts vs. Multi-year Weather Data on Net-Zero Energy Building Simulations. Technical report, National Institute of Standards and Technology.
- Kono, T., Kogaki, T., and Kiwata, T. 2016. Numerical Investigation of Wind Conditions for Roof-Mounted Wind Turbines: Effects of Wind Direction and Horizontal Aspect Ratio of a High-Rise Cuboid Building. *Energies*, 9(11):907.
- Landberg, L., Myllerup, L., Rathmann, O., Petersen, E. L., Jorgensen, B. H., Badger, J., and Mortensen, N. G. 2003. Wind Resource Estimation-An Overview. *Wind Energy*, 6(3):261–271.
- Lateb, M., Meroney, R., Yataghene, M., Fellouah, H., Saleh, F., and Boufadel, M. 2016. On the use of numerical modelling for near-field pollutant dispersion in urban environments a review. *Environmental Pollution*, 208, Part A:271 – 283. Special Issue: Urban Health and Wellbeing.
- Launder, B. and Spalding, D. 1974. The numerical computation of turbulent flows. *Computer Methods in Applied Mechanics and Engineering*, 3(2):269 – 289.
- LEAPs Computational Fluid Dynamics. Turbulence part 3 - selection of wall functions and  $y^+$  to best capture the turbulent boundary layer. <http://www.computationalfluidynamics.com.au/>. [Online; accessed 2016-02-07].
- Ledo, L., Kosasih, P., and Cooper, P. 2011. Roof mounting site analysis for micro-wind turbines. *Renewable Energy*, 36(5):1379 – 1391.
- Li, X., Sun, H., Gao, W., Shi, Y., Liu, G., and Wu, Y. 2016. Wind speed and

- direction measurement based on arc ultrasonic sensor array signal processing algorithm. *ISA Transactions*.
- Lubitz, W. D. 2014. Impact of ambient turbulence on performance of a small wind turbine. *Renewable Energy*, 61:69–73.
- Lysenco, D., Ertesvag, I. S., and Rian, K. E. 2011. Turbulent bluff body flows modeling using OpenFOAM technology. In *MekIT11-Sixth National Conference on Computational Mechanics*, pages 189–208, Trondheim.
- Lysenko, D. A., Ertesvg, I. S., and Rian, K. E. 2013. Modeling of turbulent separated flows using openfoam. *Computers Fluids*, 80:408 – 422.
- Malkawi, A. and Augenbroe, G. 2004. *Advanced Building Simulation*. Taylor & Francis.
- Manwell, J., McGowan, J., and Rogers, A. 2010. *Wind Energy Explained: Theory, Design and Application*. Wiley.
- Mathew, S. 2006. *Wind Energy Fundamentals, Resource Analysis and Economics*.
- Mattuella, J., Loredou-Souza, A., Oliveira, M., and Petry, A. 2016. Wind tunnel experimental analysis of a complex terrain microsite. *Renewable and Sustainable Energy Reviews*, 54:110 – 119.
- McAlpine, J. D. 1985. Computational fluid dynamics or wind tunnel modeling.
- McDonough, J. M. 2007. Introductory lectures on turbulence - Physics , Mathematics and Modeling.
- Meng, Y. and Hibi, K. 1998. Cooperative project for CFD prediction of pedestrian wind environment in the architectural institute of japan. *Journal of Wind Engineering, Japan*, 76:55–64.



- Menter, F., Hemstrom, B., Henriksson, M., Karlsson, R., Latrobe, A., Martin, A., Muhlbauer, P., Scheuerer, M., Smith, B., Takacs, T., and Willemssen, S. 2002. CFD Best Practice Guidelines for CFD Code Validation for Reactor-Safety Applications.
- Menter, F. R. 1994. Two-equation eddy-viscosity turbulence models for engineering applications. *AIAA Journal*, 32(8):1598–1605.
- Meroney, R. N., d Neff, D. E., Chang, C.-h., and Pradoto, R. 2001. Computational Fluid Dynamics and Physical Model Comparisons of Wind Loads and Pedestrian Comfort Around a High Rise Building. In *Inaugural Meeting of Wind Engineering Research Center, Tokyo Institute of Polytechnics, (TIP), Atsugi, Japan*, page 2.
- Met Office. Met office surface data users guide. [http://badc.nerc.ac.uk/data/ukmo-midas/ukmo\\_guide.html#5.5](http://badc.nerc.ac.uk/data/ukmo-midas/ukmo_guide.html#5.5). [Online; accessed 2016-03-22].
- Milanese, M., de Risi, A., and Laforgia, D. 2011. Experimental and fluid-dynamic analysis of a micro wind turbine in urban area. In *Proceedings of Worlds Renewable Energy Congress, Sweden*, pages 4106–4113.
- Millward-Hopkins, J., a.S. Tomlin, Ma, L., Ingham, D., and Pourkashanian, M. 2013a. Assessing the potential of urban wind energy in a major UK city using an analytical model. *Renewable Energy*, 60:701–710.
- Millward-Hopkins, J., a.S. Tomlin, Ma, L., Ingham, D., and Pourkashanian, M. 2013b. Mapping the wind resource over UK cities. *Renewable Energy*, 55:202–211.
- Millward-Hopkins, J., Tomlin, A., Ma, L., Ingham, D., and Pourkashanian, M. 2012a. Improving estimates of roughness length in a road weather prediction model using airborne lidar data. *Meteorological Applications*, 19(4):420–426.

- Millward-Hopkins, J., Tomlin, A., Ma, L., Ingham, D., and Pourkashanian, M. 2012b. The predictability of above roof wind resource in the urban roughness sublayer. *Wind Energy*, 15(2):225–243.
- Millward-Hopkins, J., Tomlin, A., Ma, L., Ingham, D., and Pourkashanian, M. 2013c. Aerodynamic parameters of a UK city derived from morphological data. *Boundary-Layer Meteorology*, 146(3):447–468.
- Millward-Hopkins, J. T., Tomlin, a. S., Ma, L., Ingham, D., and Pourkashanian, M. 2011. Estimating Aerodynamic Parameters of Urban-Like Surfaces with Heterogeneous Building Heights. *Boundary-Layer Meteorology*, 141(3):443–465.
- Mochida, A., Murakami, S., Ojima, T., Kim, S., Ooka, R., and Sugiyama, H. 1997. CFD analysis of mesoscale climate in the greater tokyo area. *Journal of Wind Engineering and Industrial Aerodynamics*, 67 - 68:459 – 477.
- Mochida, A., Tominaga, Y., Murakami, S., Yoshie, R., Ishihara, T., and Ooka, R. 2002. Comparison of various k-  $\epsilon$  model and DSM applied to flow around a high-rise building - report on AIJ cooperative project for CFD prediction of wind environment -. *Wind and structures an international journal*, 5(January 2016):227–244.
- Moeng, C.-H. and Sullivan, P. 2015. Numerical models: Large-eddy simulation. In Zhang, G. R. N. P., editor, *Encyclopedia of Atmospheric Sciences*, pages 232 – 240. Academic Press, Oxford, second edition.
- Mohotti, D., Mendis, P., and Ngo, T. 2014. Application of computational fluid dynamics (cfd) in predicting the wind loads on tall buildings- a case study. In *23rd Australasian Conference on the Mechanics of Structures and Materials, Byron Bay, Australia*.
- Moin, P. and Mahesh, K. 1998. Direct numerical simulation: A tool in turbulence research. *Annual Review of Fluid Mechanics*, 30(1):539–578.

- Murakami, S. 1993. Comparison of various turbulence models applied to a bluff body. *Journal of Wind Engineering and Industrial Aerodynamics*, 46:21 – 36.
- Murakami, S., Zeng, J., and Hayashi, T. 1999. {CFD} analysis of wind environment around a human body. *Journal of Wind Engineering and Industrial Aerodynamics*, 83(13):393 – 408.
- Nangolo, C. and Musingwini, C. 2011. Empirical correlation of mineral commodity prices with exchange-traded mining stock prices. *Journal of the Southern African Institute of Mining and Metallurgy*, 111:459 – 468.
- Neofytou, P., Venetsanos, A., Vlachogiannis, D., Bartzis, J., and Scaperdas, A. 2006. CFD simulations of the wind environment around an airport terminal building. *Environmental Modelling & Software*, 21(4):520 – 524.
- Nicholas, N. and Lewis, J. 1970. *Relationships between aerodynamic roughness and land-use, land-cover in Baltimore, Maryland*.
- Nicoud, B. F. and Baggett, J. 1999. On the use of the optimal control theory for deriving wall models for LES. pages 329–341.
- NY Solar Map. <https://nysolarmap.com/>. [Online; accessed 2016-08-20].
- Oberkampf, W. L. and Trucano, T. G. 2002. Verification and validation in computational fluid dynamics. *Progress in Aerospace Sciences*, 38(3):209–272.
- OpenFOAM User Guide. Chapter 6 solving. <http://www.openfoam.com/documentation/user-guide/solving.php>. [Online; accessed 2016-09-20].
- Orszag, S. A. 2006. Analytical theories of turbulence. *Journal of Fluid Mechanics*, 41(2):363–386.
- Óskarsdóttir, M. O. 2014. *A General Description and Comparison of Horizontal Axis Wind Turbines and Vertical Axis Wind Turbines*. PhD thesis.

- Pagnini, L. C., Burlando, M., and Repetto, M. P. 2015. Experimental power curve of small-size wind turbines in turbulent urban environment. *Applied Energy*, 154:112–121.
- Paiva, L. M., Bodstein, G. C., and Menezes, W. F. 2009. Numerical simulation of atmospheric boundary layer flow over isolated and vegetated hills using {RAMS}. *Journal of Wind Engineering and Industrial Aerodynamics*, 97(910):439 – 454.
- ParaView. Public wiki. <http://www.paraview.org/Wiki/ParaView>. [Online; accessed 2016-04-22].
- Patil, S. and Tafti, D. 2011. *Wall Modeled Large Eddy Simulation of Flow over a Backward Facing Step with Synthetic Inlet Turbulence*. Aerospace Sciences Meetings. American Institute of Aeronautics and Astronautics.
- Pearson, E. S. 1929. Some notes on sampling tests with two variables. *Biometrika*, 21(1-4):337–360.
- Pearson, E. S. 1931. The test of significance for the correlation coefficient. *Journal of the American Statistical Association*, 26(174):128–134.
- Peterka, J., Meroney, R., and Kothari, K. 1985. Wind flow patterns about buildings. *Journal of Wind Engineering and Industrial Aerodynamics*, 21(1):21 – 38.
- Petry, A. P., Loredou-Souza, A. M., Filho, D. G. R. D. F., Mattuella, J. M. L., and Gusberti, F. W. 2015. Evaluation of Experimental Wind Tunnel, RANS and LES Analysis of Wind Flow Over a Complex Terrain. In *The European Wind Energy Association, Paris-France*.
- Planning and Building Department 2014. Wind Comfort and Safety Studies.
- Plate, E. J. 1999. Methods of investigating urban wind fieldsphysical models. *Atmospheric Environment*, 33(2425):3981 – 3989.

- Power Curve Working Group 2014. Turbulence Correction Method. Technical report.
- Probst, O. and Cardenas, D. 2010. Probst, Cárdenas - 2010 - State of the Art and Trends in Wind Resource Assessment-annotated.pdf. *Energies*, (3):1087–1141.
- Radhakrishnan, S. and Piomelli, U. 2008. Large-eddy simulation of oscillating boundary layers: Model comparison and validation. *Journal of Geophysical Research: Oceans*, 113.
- Rasouli, A., Romanic, D., and Hangan, H. 2014. Wind resource assessment in complex urban environments: case study. In *Offshore Energy & Storage Symposium, Windsor, Ontario, Canada UWCAES Society July 10-11*.
- Raupach, M. R., Antonia, R. A., and Rajagopalan, S. 1991. Rough-wall turbulent boundary layers. *Applied Mechanics Reviews*, 44(1):1–25.
- Richards, P. and Hoxey, R. 1993. Appropriate boundary conditions for computational wind engineering models using the k- $\epsilon$  turbulence model. *Journal of Wind Engineering and Industrial Aerodynamics*, 4647:145 – 153.
- Rodi, W. 1997. Comparison of LES and RANS calculations of the flow around bluff bodies. *Journal of Wind Engineering and Industrial Aerodynamics*, 69:55 – 75.
- Rodriguez-Hernandez, O., del Ro, J., and Jaramillo, O. 2016. The importance of mean time in power resource assessment for small wind turbine applications. *Energy for Sustainable Development*, 30:32 – 38.
- Romanic, D., Rasouli, A., and Hangan, H. 2015. Wind resource assessment in complex urban environment. *Wind Engineering*, 39(2):193–212.
- Rudman, M. and Blackburn, H. 2006. Direct numerical simulation of turbulent non-newtonian flow using a spectral element method. *Applied Mathematical Modelling*, 30(11):1229 – 1248.

- Saad, M. M. M. and Asmuin, N. 2014. Comparison of Horizontal Axis Wind Turbines and Vertical Axis Wind Turbines. *IOSR Journal of Engineering (IOSRJEN)*, 04(08):27–30.
- Sabatino, S., Solazzo, E., Paradisi, P., and Britter, R. 2008. A simple model for spatially-averaged wind profiles within and above an urban canopy. *Boundary-Layer Meteorology*, 127(1):131–151.
- Sadiki, A., Maltsev, A., Wegner, B., Flemming, F., Kempf, A., and Janicka, J. 2006. Unsteady methods (URANS and LES) for simulation of combustion systems. *International Journal of Thermal Sciences*, 45(8):760 – 773.
- Salim, S. M., Ong, K. C., Cheah, S. C., and Ntroduction, I. I. Comparison of RANS , URANS and LES in the Prediction of Airflow and Pollutant Dispersion. In *World Congress on Engineering and Computer Science 2011 Vol II*, volume II, San Francisco, USA.
- Schatzmann, M. and Leitl, B. 2011. Issues with validation of urban flow and dispersion CFD models. *Journal of Wind Engineering and Industrial Aerodynamics*, 99(4):169 – 186.
- Schatzmann, M., Rafailidis, S., and Pavageau, M. 1997. Some remarks on the validation of small-scale dispersion models with field and laboratory data. *Journal of Wind Engineering and Industrial Aerodynamics*, 6768:885 – 893.
- Schumann, U. 1975. Subgrid scale model for finite difference simulations of turbulent flows in plane channels and annuli. *Journal of Computational Physics*, 18(4):376 – 404.
- Shih, T.-H., Liou, W. W., Shabbir, A., Yang, Z., and Zhu, J. 1995. A new  $k\epsilon$  eddy viscosity model for high reynolds number turbulent flows - model development and validation. *Computers & Fluids*, 24(3):227–238.

- Simoës, T. and Estanqueiro, A. 2016. A new methodology for urban wind resource assessment. *Renewable Energy*, 89:598 – 605.
- Sissons, M., James, P., Bradford, J., Myers, L., a.S. Bahaj, Anwar, a., and Green, S. 2011. Pole-mounted horizontal axis micro-wind turbines: UK field trial findings and market size assessment. *Energy Policy*, 39(6):3822–3831.
- Smagorinsky, J. 1963. General circulation experiments with the primitive equations. *Monthly Weather Review*, 91(3):99–164.
- Smith, J., Forsyth, T., Sinclair, K., Oteri, F., Smith, J., Forsyth, T., Sinclair, K., and Oteri, F. 2012. Built-Environment Wind Turbine Roadmap. Technical Report November, National Renewable Energy Laboratory.
- Spalart, P. and Allmaras, S. 1992. *A one-equation turbulence model for aerodynamic flows*. Aerospace Sciences Meetings. American Institute of Aeronautics and Astronautics.
- Spalart, P. R., Deck, S., Shur, M. L., Squires, K. D., Strelets, M. K., and Travin, A. 2006. A New Version of Detached-eddy Simulation, Resistant to Ambiguous Grid Densities. *Theoretical and Computational Fluid Dynamics*, 20(3):181–195.
- Spalart, P. R., Jou, W., Strelets, M., and Allmaras, S. R. 1997. Comments on the Feasibility of LES for Wings, and on a Hybrid RANS/LES Approach.
- Spalding, D. B. 1961. A Single Formula for the ‘Law of the Wall’. 27:5–8.
- Spera, D. 1994. *Wind Turbine Technology: Fundamental Concepts of Wind Turbine Engineering*. ASME Press.
- Stathopoulos, T. 2006. Pedestrian level winds and outdoor human comfort. *Journal of Wind Engineering and Industrial Aerodynamics*, 94(11):769 – 780.

- Stathopoulos, T. and Baniotopoulos, C. 2007. *Wind Effects on Buildings and Design of Wind-Sensitive Structures*. CISM International Centre for Mechanical Sciences. Springer.
- Stathopoulos, T. and Storms, R. 1986. Wind environmental conditions in passages between buildings. *Journal of Wind Engineering and Industrial Aerodynamics*, 24(1):19 – 31.
- Sunderland, K., Woolmington, T., Blackledge, J., and Conlon, M. 2013. Small wind turbines in turbulent (urban) environments: A consideration of normal and weibull distributions for power prediction. *Journal of Wind Engineering and Industrial Aerodynamics*, 121:70 – 81.
- Svenningsen, L. 2010a. Proposal of an improved power curve air-density correction. In *European Wind Energy Conference Exhibition, Warsaw, Poland*.
- Svenningsen, L. 2010b. WindPRO / Energy - Power Curve Air Density Correction And Other Power Curve Options.
- Tabrizi, A. B., Whale, J., Lyons, T., and Urmee, T. 2014a. Performance and safety of rooftop wind turbines: Use of CFD to gain insight into inflow conditions. *Renewable Energy*, 67:242–251.
- Tabrizi, A. B., Whale, J., Lyons, T., and Urmee, T. 2014b. Performance and safety of rooftop wind turbines: Use of CFD to gain insight into inflow conditions. *Renewable Energy*, 67:242–251.
- The Scottish government. Planning for micro renewables. <http://www.gov.scot/Publications/2006/10/03093936/2>. Online; accessed 2016-01-19.
- Thogersen, M. L. 2000. WindPRO / ENERGY Modelling of the Variation of Air Density with Altitude through Pressure, Humidity and Temperature.



- Tindal, A., LeBlanc, M., Harman, K., and Rareshide, E. 2008. Site-specific adjustments to wind turbine power curves. In *AWEA Wind Power Conference, Houston*.
- Toja-Silva, F., Peralta, C., Lopez-Garcia, O., Navarro, J., and Cruz, I. 2015a. Effect of roof-mounted solar panels on the wind energy exploitation on high-rise buildings. *Journal of Wind Engineering and Industrial Aerodynamics*, 145:123 – 138.
- Toja-Silva, F., Peralta, C., Lopez-Garcia, O., Navarro, J., and Cruz, I. 2015b. Roof region dependent wind potential assessment with different RANS turbulence models. *Journal of Wind Engineering and Industrial Aerodynamics*, 142:258 – 271.
- Tominaga, Y., Mochida, A., Murakami, S., and Sawaki, S. 2008a. Comparison of various revised k- $\epsilon$  models and LES applied to flow around a high-rise building model with 1:1:2 shape placed within the surface boundary layer. *Journal of Wind Engineering and Industrial Aerodynamics*, 96(4):389–411.
- Tominaga, Y., Mochida, A., Shirasawa, T., Yoshie, T., Kataoka, H., Harimoto, K., and Nozu, T. 2004. Cross comparisons of CFD results of wind environment at pedestrian level around a high-rise building and within a building complex. *Journal of Asian Architecture and Building Engineering*, 3(1):63 – 70.
- Tominaga, Y., Mochida, A., Yoshie, R., Kataoka, H., Nozu, T., Yoshikawa, M., and Shirasawa, T. 2008b. AIJ guidelines for practical applications of CFD to pedestrian wind environment around buildings. *Journal of Wind Engineering and Industrial Aerodynamics*, 96(10):1749 – 1761.
- Tominaga, Y., Okaze, T., and Mochida, A. 2011. CFD modeling of snowdrift around a building: An overview of models and evaluation of a new approach. *Building and Environment*, 46(4):899 – 910.

- Tominaga, Y., Yoshie, R., Mochida, A., Kataoka, H., Harimoto, K., and Nozu, T. 2005. Cross Comparisons of CFD Prediction for Wind Environment at Pedestrian Level around Buildings. In *The Sixth Asia-Pacific Conference on Wind Engineering (APCWE-VI)*, Seoul, Korea.
- Tomlin, A. S., Ma, L., Ingham, D. B., and Pourkashanian, M. 2012. Mapping the Urban Wind Resource over UK Cities using an Analytical Downscaling Method. In *Proceedings of the EWEA Annual Conference*.
- Tsuchiya, M., Murakami, S., Mochida, A., Kondo, K., and Ishida, Y. 1997. Development of a new k- $\epsilon$  model for flow and pressure fields around bluff body. *Journal of Wind Engineering and Industrial Aerodynamics*, 6768:169 – 182.
- U.S. Department of Energy 2008. 20% Wind Energy by 2030 Increasing Wind Energy’s Contribution to U.S. Electricity Supply. Technical report.
- User Manual 2016. *WindMaster Pro*.
- Vafaeihosseini, E., Sagheb, A., and Ramancharla, P. K. 2013. Computational Fluid Dynamics Approach for Wind Analysis of Highrise Buildings. In *A3C-12 : AWARDS, CONVENTION CONSULTANTS COLLOQUIUM*, Hyderabad, India.
- Van der Vorst, H. A. 1992. Bi-cgstab: A fast and smoothly converging variant of bi-cg for the solution of nonsymmetric linear systems. *SIAM Journal on Scientific and Statistical Computing*, 13(2):631–644.
- van Hooff, T., Blocken, B., Aanen, L., and Bronsema, B. 2011a. A venturi-shaped roof for wind-induced natural ventilation of buildings: Wind tunnel and CFD evaluation of different design configurations. *Building and Environment*, 46(9):1797–1807.

- van Hooff, T., Blocken, B., and van Harten, M. 2011b. 3d CFD simulations of wind flow and wind-driven rain shelter in sports stadia: Influence of stadium geometry. *Building and Environment*, 46(1):22 – 37.
- Vardoulakis, S., Fisher, B. E., Pericleous, K., and Gonzalez-Flesca, N. 2003. Modelling air quality in street canyons: a review. *Atmospheric environment*, 37(2):155–182.
- Vermeir, J. J. and Runacres, M. C. 2015. Effect of averaging time in wind speed measurements on energy production estimates. pages 8–11.
- Veronesi, F., Grassi, S., and Raubal, M. 2016. Statistical learning approach for wind resource assessment. *Renewable and Sustainable Energy Reviews*, 56:836 – 850.
- Versteeg, H. and Malalasekera, W. 2007. *An Introduction to Computational Fluid Dynamics: The Finite Volume Method*. Pearson Education Limited.
- Villiers, E. 2006. *The Potential of Large Eddy Simulation for the Modeling of Wall Bounded Flows*. PhD thesis, Imperial College of Science.
- Vliet, E. <http://www.cfd-online.com/Forums/openfoam-programming-development/>. [Online; accessed 2016-04-22].
- Von Kármán, T. 1931. *Mechanical similitude and turbulence*. National Advisory Committee for Aeronautics, Washington D.C.
- Wagenaar, J. W. and Eecen, P. J. 2011. Dependence of Power Performance on Atmospheric Conditions and Possible Corrections. (March):14–17.
- Wagner, R., Antoniou, I., Pedersen, S. M., Courtney, M. S., and Jrgensen, H. E. 2009. The influence of the wind speed profile on wind turbine performance measurements. *Wind Energy*, 12(4):348–362.

- Walker, S. L. 2011. Building mounted wind turbines and their suitability for the urban scale-A review of methods of estimating urban wind resource. *Energy and Buildings*, 43(8):1852–1862.
- Wan, Y.-h., Ela, E., and Orwig, K. 2010. Development of an Equivalent Wind Plant Power-Curve. (June).
- Wang, B., Cot, L., Adolphe, L., Geoffroy, S., and Morchain, J. 2015. Estimation of wind energy over roof of two perpendicular buildings. *Energy and Buildings*, 88:57 – 67.
- Wang, B., Etheridge, D., and Ohba, M. 2011. Wind tunnel investigation of natural ventilation through multiple stacks. part 1: Mean values. *Building and Environment*, 46(7):1380 – 1392.
- Weekes, S. M. and Tomlin, A. S. 2013. Evaluation of a semi-empirical model for predicting the wind energy resource relevant to small-scale wind turbines. *Renewable Energy*, 50:280–288.
- Weller, H. G., Tabor, G., Jasak, H., and Fureby, C. 1998. A tensorial approach to computational continuum mechanics using object-oriented techniques. *Comput. Phys.*, 12(6):620–631.
- Wendt, J., Anderson, J., and for Fluid Dynamics, V. K. I. 1996. *Computational fluid dynamics: an introduction*. Von Karman Institute book. Springer.
- White, F. 2003. *Fluid Mechanics*. McGraw-Hill international editions.
- Wieringa, J. 1992. Updating the davenport roughness classification. *Journal of Wind Engineering and Industrial Aerodynamics*, 41(13):357 – 368.
- Wilcox, S. and Marion, W. 2008. Users Manual for TMY3 Data Sets.

- Willemsen, E. and Wisse, J. a. 2007. Design for wind comfort in The Netherlands: Procedures, criteria and open research issues. *Journal of Wind Engineering and Industrial Aerodynamics*, 95(9-11):1541–1550.
- WINDPOWER software. Wind turbine power curves. [http://www.wind-power-program.com/turbine\\_characteristics.htm](http://www.wind-power-program.com/turbine_characteristics.htm). [Online; accessed 2016-01-19].
- Woo, H., Peterka, J., and Cermak, J. 1977. *Wind Tunnel Measurements in the Wakes of Structures*. NASA contractor report. National Aeronautics and Space Administration.
- Xie, Z.-T. and Castro, I. P. 2009. Large-eddy simulation for flow and dispersion in urban streets. *Atmospheric Environment*, 43(13):2174–2185.
- Yang, A.-S., Su, Y.-M., Wen, C.-Y., Juan, Y.-H., Wang, W.-S., and Cheng, C.-H. 2016. Estimation of wind power generation in dense urban area. *Applied Energy*, 171:213–230.
- Yersel, M. and Goble, R. 1986. Roughness effects on urban turbulence parameters. *Boundary-Layer Meteorology*, 37(3):271–284.
- Yoshie, R., Mochida, A., Tominaga, Y., Kataoka, H., Harimoto, K., Nozu, T., and Shirasawa, T. 2007a. Cooperative project for CFD prediction of pedestrian wind environment in the architectural institute of japan. *Journal of Wind Engineering and Industrial Aerodynamics*, 95(911):1551 – 1578.
- Yoshie, R., Mochida, A., Tominaga, Y., Kataoka, H., Harimoto, K., Nozu, T., and Shirasawa, T. 2007b. Cooperative project for CFD prediction of pedestrian wind environment in the Architectural Institute of Japan. *Journal of Wind Engineering and Industrial Aerodynamics*, 95(9-11):1551–1578.

Zhang, M. 2015. *Wind Resource Assessment and Micro-siting: Science and Engineering*. Wiley.



# Appendix A

## Near wall treatment - Wall functions

The near-wall flowfield is composed by three layers (Figure A.1):

1. The inner layer,  $y^+ < 5$ , where viscous forces are dominant and the flow is considered laminar, i.e.  $y^+ = u^+$ .
2. The outer layer,  $y^+ > 30$ , where inertial forces dominate over viscous forces and the flow is fully turbulent. It is known as the log-law region, since it can be applied the law of the wall that states that the average velocity of a turbulent flow at a certain point close to the wall is proportional to the logarithmic distance from that point to the wall [Von Kármán, 1931].
3. The buffer layer (intermediate layer),  $5 < y^+ < 30$ , where viscous and inertial forces are both important.

In order the turbulence models to calculate the near wall region, the grid should be fine enough, such as the first computational cell off-the-wall to be located within the viscous sublayer, i.e.  $y^+ \approx 1$ . To avoid the fine grid requirements and hence the excessive computer resources, the wall functions have been introduced. They



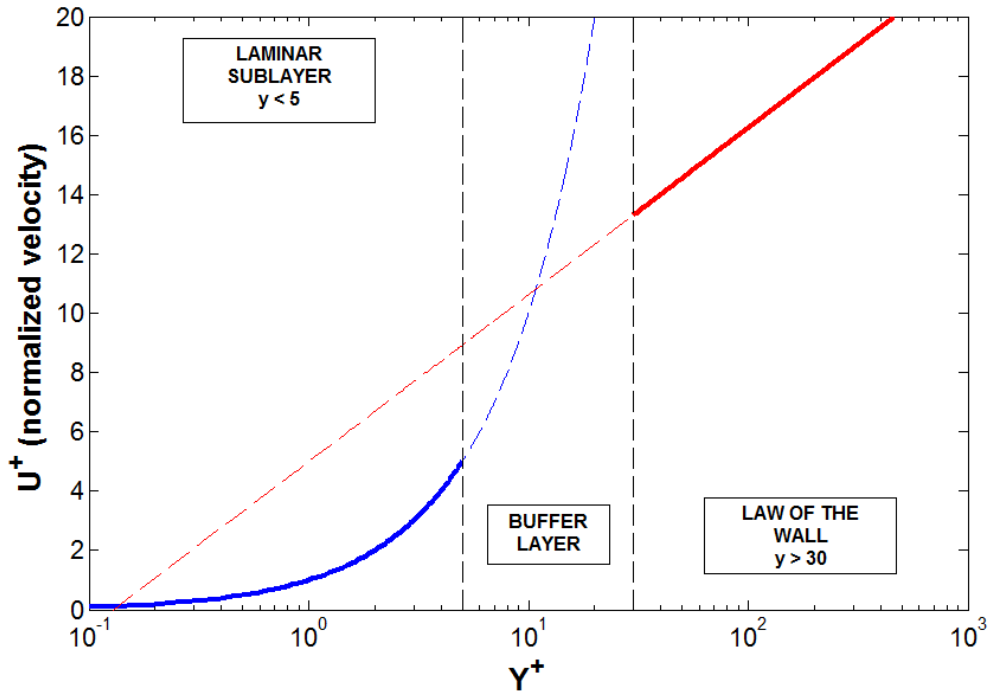


Figure A.1: Composite regions of the turbulent boundary layer [LEAPs Computational Fluid Dynamics].

are based on the universal character of the law of the wall which claims that the flowfield between the wall and the outer edge of the logarithmic layer is invariant. This results in considerable savings, justifying the use of wall functions. However, the first developed wall functions required the first off the wall point to lie in the logarithmic layer i.e.  $y^+ > 30$  and are known as log-layer wall functions. This condition is a stringent restraint and violation (i.e. the grid point lies in the viscous sublayer) results in inaccurate solutions. For this reason, adaptive wall functions have been developed which do not demand the first of the wall grid point to lie in the log layer.

## A.1 Log-law wall functions

### A.1.1 Smooth surfaces

They are based on equilibrium assumption between pressure and viscous forces and the use of logarithmic law of the wall based functions [Patil and Tafti, 2011]. Grotzbach approach, which is a variant of Schumann [1975] wall model, is the one used in our study. It calculates the mean wall shear ( $\tau_w$ ), from the logarithmic law:

$$U^+ = \frac{1}{\kappa} \log(y^+ E) \quad (\text{A.1})$$

where:

$$U^+ = \frac{u}{u_\tau} \quad (\text{A.2})$$

$$y^+ = \frac{y u_\tau}{\nu} \quad (\text{A.3})$$

$$u_\tau = \sqrt{\frac{t_w}{\rho}} \quad (\text{A.4})$$

Hence, it imposes that the first off-the-wall point should be in the logarithmic layer, typically  $30 < y^+ < 300$ . In OpenFoam the viscous sublayer lies under  $y^+ \leq 10.97$  and the OpenFoam imposes the laminar stress-strain relationship:

$$U^+ = y^+ \quad (\text{A.5})$$

When the point lies in the area beyond the logarithmic region, the calculated velocity is underestimated, while in the viscous sublayer it is overestimated [Nicoud and Baggett, 1999].

### A.1.2 Rough surfaces

The surface roughness is considered by defining two variables:

1. the dimensionless roughness height:

$$K_s^+ = \frac{\rho K_s u_t}{v} \quad (\text{A.6})$$

2. the roughness constant ( $C_s$ ).

Cebeci and Bradshaw [1977] have proposed that a boundary layer for rough surfaces is divided in three regimes depending on the size of  $K_s^+$  and  $C_s$ :

1. Hydro-dynamically smooth, for  $K_s^+ \leq 2.25$ ,
2. Transitional, for  $2.5 < K_s^+ \leq 90$ ,
3. Fully rough, for  $K_s^+ > 90$ ,

and they have modified the universal log-law to account for the roughness characteristics:

$$U^+ = \frac{1}{\kappa} \log(y^+ E) - \Delta B \quad (\text{A.7})$$

where  $\Delta B$  is expressed in terms of roughness variables ( $K_s$ ,  $C_s$ ), which for the three flow regimes is given by:

1. In smooth regime:

$$\Delta B = 0 \quad (\text{A.8})$$

2. In transitional regime:

$$\Delta B = \frac{1}{\kappa} \ln \left( \frac{K_s^+ - 2.25}{87.75} + C_s K_s^+ \right) \sin[0.425(\ln K_s^+ - 0.811)] \quad (\text{A.9})$$

3. In fully-rough regime:

$$\Delta B = \frac{1}{\kappa} \ln(1 + C_s K_s^+) \quad (\text{A.10})$$

Although the modifications of the log-law account for the non equilibrium effects of roughness, the accuracy of the approach depends on the nature of the case [[Armenio et al., 2010](#)]. So, in separated flows the error is significant, while in oscillated boundary layers studied by [Radhakrishnan and Piomelli \[2008\]](#) the error introduced is negligible.



# Appendix B

## Two-equation turbulence models

### B.1 Boussinesq approximation

The basis for the two-equation models is the Boussinesq eddy viscosity assumption [Boussinesq, 1877], which relates the Reynolds stress tensor ( $\tau_{ij} = -\overline{u_i' u_j'}$ ) to the mean velocity gradients and is expressed as follows:

$$\tau_{ij} = 2\nu_t S_{ij} - \frac{2}{3}\rho k \delta_{ij} \quad (\text{B.1})$$

where  $\nu_t$  is the kinetic eddy viscosity and  $S_{ij}$  the mean strain-rate tensor:

$$S_{ij} = \frac{1}{2} \left( \frac{\partial U_j}{\partial x_i} + \frac{\partial U_i}{\partial x_j} \right) \quad (\text{B.2})$$

## B.2 Standard k- $\epsilon$ turbulence model

In this model the kinetic eddy viscosity is calculated by means of turbulence kinetic energy ( $k$ ) and its dissipation rate ( $\epsilon$ ):

$$\nu_t = C_\mu \frac{k^2}{\epsilon} \quad (\text{B.3})$$

This is a semi-empirical model; the model transport equation for  $k$  (Equation B.4) is derived from the exact equation, while the model equation for  $\epsilon$  (Equation B.5) is empirical.

$$\frac{\partial k}{\partial t} + U_j \frac{\partial k}{\partial x_j} = \frac{\partial}{\partial x_j} \left[ \left( \nu + \frac{\nu_T}{\sigma_k} \right) \frac{\partial k}{\partial x_j} \right] + \tau_{ij} \frac{\partial U_i}{\partial x_j} - \epsilon \quad (\text{B.4})$$

$$\frac{\partial \epsilon}{\partial t} + U_j \frac{\partial \epsilon}{\partial x_j} = \frac{\partial}{\partial x_j} \left[ \left( \nu + \frac{\nu_T}{\sigma_\epsilon} \right) \frac{\partial \epsilon}{\partial x_j} \right] + C_{\epsilon 1} \frac{\epsilon}{k} \tau_{ij} \frac{\partial U_i}{\partial x_j} - C_{\epsilon 2} \frac{\epsilon^2}{k} \quad (\text{B.5})$$

The closure coefficients are listed in Table B.1.

$C_\mu$	$C_{\epsilon 1}$	$C_{\epsilon 2}$	$\sigma_k$	$\sigma_\epsilon$
0.09	1.44	1.92	1.0	1.3

Table B.1: Standard k- $\epsilon$  constants

## B.3 Realizable k- $\epsilon$ turbulence model

The realizable k- $\epsilon$  model differs from the standard k- $\epsilon$  model in two aspects:

1. A new transport equation for the dissipation rate  $\epsilon$ , derived from an exact

equation for the transport of the mean-square vorticity fluctuation:

$$\frac{\partial \epsilon}{\partial t} + U_j \frac{\partial \epsilon}{\partial x_j} = \frac{\partial}{\partial x_j} \left[ \left( \nu + \frac{\nu_T}{\sigma_\epsilon} \right) \frac{\partial \epsilon}{\partial x_j} \right] + C_2 \frac{\epsilon^2}{k + \sqrt{\nu \epsilon}} \quad (\text{B.6})$$

where:

$$C_2 = 1.9 \quad (\text{B.7})$$

2. The  $C_\mu$  in eddy viscosity formula (Equation B.3) is no longer constant and is given by:

$$C_\mu = \frac{1}{A_0 + A_s \frac{kU^*}{\epsilon}} \quad (\text{B.8})$$

where:

$$U^* \equiv \sqrt{S_{ij}S_{ij} + \tilde{\Omega}_{ij}\tilde{\Omega}_{ij}} \quad (\text{B.9})$$

$$\tilde{\Omega}_{ij} = \Omega_{ij} - 2\epsilon_{ijk}\omega_k \quad (\text{B.10})$$

$$\Omega_{ij} = \overline{\Omega_{ij}} - \epsilon_{ijk}\omega_k \quad (\text{B.11})$$

where  $\overline{\Omega_{ij}}$  is the mean rate-of-rotation tensor. The constants  $A_0$  and  $A_s$  are given by:

$$A_0 = 4.04 \quad (\text{B.12})$$

$$A_s = \sqrt{6}\cos\phi \quad (\text{B.13})$$

where:

$$\phi = \frac{1}{3}\cos^{-1}(\sqrt{6}W), \quad (\text{B.14})$$



$$W = \frac{S_{ij}S_{jk}S_{ki}}{\tilde{S}^3}, \quad (\text{B.15})$$

$$\tilde{S} = \sqrt{S_{ij}S_{ij}}, \quad (\text{B.16})$$

## B.4 Standard k- $\omega$ turbulence model

The eddy viscosity is calculated by means of the turbulent kinetic energy ( $k$ ) and the the specific rate of dissipation ( $\omega$ ):

$$\nu_t = \frac{k}{\omega} \quad (\text{B.17})$$

To calculate the new variables, the transport equations are expressed in terms of the turbulence kinetic energy ( $k$ ) and the specific rate of dissipation ( $\omega$ ) as follows:

$$\frac{\partial k}{\partial t} + U_j \frac{\partial k}{\partial x_j} = \frac{\partial}{\partial x_j} ((\nu + \sigma^* \nu_T) \frac{\partial k}{\partial x_j}) + \tau_{ij} \frac{\partial U_i}{\partial x_j} - \beta^* k \omega \quad (\text{B.18})$$

$$\frac{\partial \omega}{\partial t} + U_j \frac{\partial \omega}{\partial x_j} = \frac{\partial}{\partial x_j} ((\nu + \sigma \nu_T) \frac{\partial \omega}{\partial x_j}) + \alpha \frac{\omega}{k} \tau_{ij} \frac{\partial U_i}{\partial x_j} - \beta \omega^2 \quad (\text{B.19})$$

where:

$$\beta = \beta_0 f_\beta \quad (\text{B.20})$$

$$\beta^* = \beta_0^* f_{\beta^*} \quad (\text{B.21})$$

$$f_\beta = \frac{1 + 70\chi_\omega}{1 + 80\chi_\omega} \quad (\text{B.22})$$

$$\chi_\omega = \left| \frac{\Omega_{ij}\Omega_{jk}S_{ki}}{(\beta_0^*\omega)^3} \right| \quad (\text{B.23})$$

$$f_{\beta^*} = \begin{cases} 1, & \chi_k \leq 0 \\ \frac{1+680\chi_k^2}{1+400\chi_k^2}, & \chi_k > 0 \end{cases} \quad (\text{B.24})$$

$$\chi_k = \frac{1}{\omega^3} \frac{\partial k}{\partial x_j} \frac{\partial \omega}{\partial x_j} \quad (\text{B.25})$$

The closure coefficients are listed in Table B.2.

$\alpha$	$\sigma$	$\sigma^*$	$\beta_0$	$\beta_0^*$
$\frac{13}{25}$	$\frac{1}{2}$	$\frac{1}{2}$	$\frac{9}{125}$	$\frac{9}{100}$

Table B.2: Standard k- $\epsilon$  constants



# Appendix C

## OpenFOAM settings

The user specifies the choice of finite volume discretisation schemes in the `fvSchemes` dictionary, in the `system` directory. The specification of the equation solvers and tolerances and other algorithm controls is made in the `fvSolution` dictionary, similarly in the `system` directory [[OpenFOAM User Guide](#)]. The following sections present the `fvSchemes` and `fvSolution` dictionaries for the DES models for the test cases investigated.

### C.1 Test Case A: High rise building

#### C.1.1 `fvSchemes`

```
FoamFile
{
    version    2.0;
    format     ascii;
    class      dictionary;
    object     fvSchemes;
```

```
}
```

```
ddtSchemes
```

```
{  
    default          backward;  
}
```

```
gradSchemes
```

```
{  
    default          Gauss linear;  
    grad(nuTilda)   cellLimited Gauss linear 1;  
    grad(U)         cellLimited Gauss linear 1;  
}
```

```
divSchemes
```

```
{  
    default          none;  
    div(phi,U)       Gauss LUST unlimitedGrad(U);  
    div(phi,k)       Gauss limitedLinear 1;  
    div(phi,nuTilda) Gauss limitedLinear 1;  
    div((nuEff*dev(T(grad(U)))))) Gauss linear;  
}
```

```
laplacianSchemes
```

```
{  
    default          Gauss linear limited corrected 0.33;  
}
```

```
interpolationSchemes
```

```
{  
    default      linear;  
}
```

```
snGradSchemes
```

```
{  
    default      limited corrected 0.33;  
}
```

```
fluxRequired
```

```
{  
    default      no;  
    P;  
}
```

### C.1.2 fvSolution

```
FoamFile
```

```
{  
    version      2.0;  
    format       ascii;  
    class        dictionary;  
    object       fvSolution;  
}
```

```
solvers
{
  p
  {
    solver          GAMG;
    tolerance       1e-6;
    relTol          0.1;
    smoother        GaussSeidel;
    nPreSweeps      0;
    nPostSweeps     2;
    cacheAgglomeration true;
    nCellsInCoarsestLevel 50;
    agglomerator    faceAreaPair;
    mergeLevels     1;
  };
  pFinal
  {
    solver          GAMG;
    tolerance       1e-6;
    relTol          0;
    smoother        GaussSeidel;
    nPreSweeps      0;
    nPostSweeps     2;
    cacheAgglomeration true;
    nCellsInCoarsestLevel 50;
    agglomerator    faceAreaPair;
    mergeLevels     1;
  };
};
```

```
U
{
    solver          PBiCG;
    preconditioner  DILU;
    tolerance       1e-08;
    relTol          0;
};
UFinal
{
    solver          PBiCG;
    preconditioner  DILU;
    tolerance       1e-08;
    relTol          0;
};
nuTilda
{
    solver          PBiCG;
    preconditioner  DILU;
    tolerance       1e-07;
    relTol          0;
};
nuTildaFinal
{
    solver          PBiCG;
    preconditioner  DILU;
    tolerance       1e-07;
    relTol          0;
};
```



```
}
```

```
PIMPLE
```

```
{
```

```
    nOuterCorrectors          2;  
    nCorrectors                2;  
    nNonOrthogonalCorrectors  0;  
    pRefCell                   1001;  
    pRefValue                   0;
```

```
}
```

```
residualControl
```

```
{
```

```
    p                          1e-6;  
    U                          1e-6;  
    nuTilda                    1e-6;  
    pFinal                     1e-6;  
    UFinal                     1e-6;  
    nuTildaFinal               1e-6;
```

```
}
```

```
relaxationFactors
```

```
{
```

```
    equations  
    {  
        "U.*"                    1;  
        "nuTilda.*"              1;  
    }
```

```
}
```

## C.2 Test Case B: Actual urban area

### C.2.1 fvSchemes

FoamFile

```
{  
    version    2.0;  
    format     ascii;  
    class      dictionary;  
    object     fvSchemes;  
}
```

ddtSchemes

```
{  
    default    backward;  
}
```

gradSchemes

```
{  
    default    Gauss linear;  
    grad(nuTilda)  cellLimited Gauss linear 1;  
    grad(U)    cellLimited Gauss linear 1;  
}
```

divSchemes

```
{  
    default    none;  
    div(phi,U) Gauss LUST unlimitedGrad(U);  
}
```

```

    div(phi,k)                Gauss limitedLinear 1;
    div(phi,nuTilda)          Gauss limitedLinear 1;
    div((nuEff*dev(T(grad(U)))) Gauss linear;
}

```

laplacianSchemes

```

{
    default                Gauss linear limited corrected 0.33;
}

```

interpolationSchemes

```

{
    default                linear;
}

```

snGradSchemes

```

{
    default                limited corrected 0.33;
}

```

fluxRequired

```

{
    default                no;

    p;
}

```

### C.2.2 fvSolution

FoamFile

```

{
    version                2.0;
}

```

```

    format    ascii;
    class     dictionary;
    object    fvSolution;
}

solvers
{
    p
    {
        solver            GAMG;
        tolerance         1e-6;
        relTol            0.1;
        smoother          GaussSeidel;
        nPreSweeps        0;
        nPostSweeps       2;
        cacheAgglomeration true;
        nCellsInCoarsestLevel 50;
        agglomerator      faceAreaPair;
        mergeLevels       1;
    };
    pFinal
    {
        $p;
        tolerance         1e-6;
        relTol            0;
    };
    "(U—B—nuTilda)"
    {

```

```

        solver                smoothSolver;
        smoother              GaussSeidel;
        tolerance              1e-07;
        relTol                 0;
    };
    "(U nuTilda)Final"
    {
        $U;
        tolerance              1e-05;
        relTol                 0;
    }
}

```

PIMPLE

```

{
    nOuterCorrectors          2;
    nCorrectors                2;
    nNonOrthogonalCorrectors  0;
    pRefCell                   1001;
    pRefValue                  0;
}
relaxationFactors
{
    "U.*"                      1;
    "nuTilda.*"                1;
}

```

## C.3 Case study: DMU campus

### C.3.1 fvSchemes

FoamFile

```
{  
    version    2.0;  
    format     ascii;  
    class      dictionary;  
    object     fvSchemes;  
}
```

ddtSchemes

```
{  
    default    backward;  
}
```

gradSchemes

```
{  
    default    Gauss linear;  
    grad(nuTilda)  cellLimited Gauss linear 1;  
    grad(U)     cellLimited Gauss linear 1;  
}
```

divSchemes

```
{  
    default    none;
```

```

    div(phi,U)                Gauss LUST unlimitedGrad(U);
    div(phi,k)                Gauss limitedLinear 1;
    div(phi,nuTilda)         Gauss limitedLinear 1;
    div((nuEff*dev(T(grad(U)))) Gauss linear;
}

```

laplacianSchemes

```

{
    default                Gauss linear limited corrected 0.33;
}

```

interpolationSchemes

```

{
    default                linear;
}

```

snGradSchemes

```

{
    default                limited corrected 0.33;
}

```

fluxRequired

```

{
    default                no;
    p;
}

```

### C.3.2 fvSolution

FoamFile

```
{  
    version    2.0;  
    format     ascii;  
    class      dictionary;  
    object     fvSolution;  
}
```

solvers

```
{  
    p  
    {  
        solver          GAMG;  
        tolerance       1e-6;  
        relTol          0.1;  
        smoother        GaussSeidel;  
        nPreSweeps      0;  
        nPostSweeps     2;  
        cacheAgglomeration true;  
        nCellsInCoarsestLevel 50;  
        agglomerator     faceAreaPair;  
        mergeLevels     1;  
    };  
    pFinal  
    {  
        $p;  
        tolerance       1e-6;  
        relTol          0;  
    };  
}
```



```

“(U—B—nuTilda)”
{
    solver                smoothSolver;
    smoother              GaussSeidel;
    tolerance             1e-07;
    relTol                0;
};
“(U—nuTilda)Final”
{
    $U;
    tolerance             1e-05;
    relTol                0;
}
}

```

PIMPLE

```

{
    nOuterCorrectors     2;
    nCorrectors          2;
    nNonOrthogonalCorrectors 0;
    pRefCell             1001;
    pRefValue            0;
}
relaxationFactors
{
    “U.*”                1;
    “nuTilda.*”         1;
}

```

# Appendix D

## Mean Absolute Error

The Mean Absolute Error (MAE) is used in statistics to measure how close the predicted values are to the true (experimental) outcomes and is given by:

$$MAE = \frac{1}{n} \sum_{i=1}^n |f_i - y_i| = \frac{1}{n} \sum_{i=1}^n |e_i| \quad (\text{D.1})$$

where  $f_i$  is the prediction and  $y_i$  the true value.

The MAE is a common measure in time series analysis and as its name suggests it is the average of the absolute errors  $|e_i|$ .